An Examination of the Effects of Neutral Particles on the Edge Plasma in Tokamaks

A Dissertation
Presented to
The Academic Faculty
of the Nuclear and Radiological
Engineering Program

by

Zachary Ward Friis

In Partial Fulfillment
of the Requirements for the Degree
Doctorate in the
Nuclear and Radiological Engineering Program

Georgia Institute of Technology
May 2010

An Examination of the Effects of Neutral Particles on Plasma Edge Phenomena

Approved by:

Dr. Weston Stacey, Advisor
Nuclear and Radiological
Engineering Program
Georgia Institute of Technology

Dr. Farzad Rahnema
Nuclear and Radiological
Engineering Program
Georgia Institute of Technology

Dr. Nolan Hertel
Nuclear and Radiological
Engineering Program
Georgia Institute of Technology

Dr. C.-K. Chris Wang
Nuclear and Radiological
Engineering Program
Georgia Institute of Technology

Dr. Thomas Barker
School of Biomedical Engineering
Georgia Institute of Technology

Dr. Richard Groebner
General Atomics

Dr. Yunfeng Liang
Institut für Plasmaphysik
Forschungszentrum Jülich GmbH

Date Approved: May 19th 2010

“Technological advance is an inherently iterative process. One does not simply take sand from the beach and produce a Dataprobe. We use crude tools to fashion better tools, and then our better tools to fashion more precise tools, and so on. Each minor refinement is a step in the process, and all of the steps must be taken.”

Chairman Sheng-ji Yang
"Looking God in the Eye"

For TD

I am sorry it's not a rocket pack.

ACKNOWLEDGEMENTS

I would like to extend my deepest gratitude for all those who in one way or another guided and supported me during the completion of this thesis. To my research advisor, Dr. Weston M. Stacey, Jr., I am thankful for his guidance and useful insight during the course of this work. I am also grateful to Dr. Richard Groebner who was willing to help me whenever possible or guide me to the right people when it was not. I am eternally grateful to Dr. Tom Rognlien for helping me to learn the nuances of UEDGE in a very short amount of time. Without his assistance, none of this would have been possible. I would also like to thank Dr. Tony Leonard and Dr. Marv Rensink for providing me with the data used in the primary analysis of this work and Dr. Dingkang Zhang for his help in setting up and running the GTNEUT code. I would also like to thank Dr. Yunfeng Liang and the entire TEXTOR team for their guidance and hospitality while I was a guest in their lands. Additionally, I would like to thank my reading committee for their time and support throughout the thesis process.

I also wish to express my appreciation to my family and friends who have been a constant source motivation throughout the entire process. Many of whom helped in the revisions of this work: Craig, Judy, and Amber Friis, Shana Yorkey, Sarah Lynne Webb, Erin Sonderman, Meagan Scatterfield, Jessica Bryan Hughes, Justin Pounders, Benoit Forget, Stephane Dufresne, and Amanda Griffin Riggle.

TABLE OF CONTENTS

ACKNOWLEDGEMENTS VIII

LIST OF TABLES VIII

LIST OF FIGURES IX

SUMMARY XIII

1. INTRODUCTION 1

1.1 AREA OF RESEARCH 1

1.2 MOTIVATION 1

1.3 METHODS OF SOLVING THE NEUTRAL PARTICLE TRANSPORT EQUATION 25

2. TEXTOR EXPERIMENT AND MOTIVATION 33

2.1 OVERVIEW OF TEXTOR AND DIAGNOSTIC USED IN ANALYSIS 33

2.2 INTRODUCTION AND MOTIVATION FOR TEXTOR EXPERIMENTS 53

2.3 EXPERIMENTAL SETUP 55

2.4 RESULTS 64

2.5 CONCLUSION 74

3. THE GTNEUT CODE 75

3.1 DERIVATION OF TEP EQUATIONS 75

3.2 ADDITIONS TO THE TEP METHODOLOGY 91

4. APPLICATION OF THE GTNEUT CODE 94

4.1 GTNEUT INPUT FILE 94

4.2 BREAKDOWN OF THE TONEUT FILE 95

5. DIII-D ANALYSIS OF NEUTRAL PARTICLE RECYCLING AND PEDESTAL FUELING 100
5.1 DIII-D NEUTRAL PARTICLE RECYCLING MEASUREMENTS 100
6. NEUTRAL PARTICLE RECYCLING CALCULATIONS 108
6.1 GEOMETRIC MODEL 108
6.2 OVERALL PARTICLE BALANCE 112
6.3 NEUTRAL PARTICLE FLUXES RECYCLING FROM WALL SURFACE AND CROSSING SEPARATRIX 114
6.4 POLOIDAL DISTRIBUTIONS OF IONIZATION AND CHARGE-EXCHANGE RATES 118
6.5 NEUTRAL PENETRATION OF THE EDGE PEDESTAL 125
6.6 IMPORTANCE OF DIFFERENT NEUTRAL PARTICLE SOURCES IN FUELING PEDESTAL AND CORE 130
6.7 COMPUTATIONAL AND EXPERIMENTAL UNCERTAINTY 141
7. SUGGESTED IMPROVEMENTS TO GTNEUT 150
8. SUMMARY & CONCLUSIONS 151
APPENDIX A. PROCEDURE 152
APPENDIX B. DETACHED CASE 158
APPENDIX C. ATTACHED CASE 178
APPENDIX D. “MAKE_TONEUT” CODE 198
REFERENCES 217
VITA 220

LIST OF TABLES

Table 1: : P_{thresh}^{theory} and $P_{sep}^{\exp}$ evolution during three DIII-D discharges 19

Table 2: Breakdown of P_{thresh} 20

Table 3: Filterscope Channel 48

Table 4: Shot Plan for Rotation Scan 59

Table 5: Neutral sources from recycling ions. 103

Table 6: Ion global particle balance on CORE+PED 112

Table 7: Global neutral particle balance on entire computation domain 114

Table 8: Fraction of neutrals from each source ionized in PED+CORE 137

Table 9: Comparison of ionization rates 145

Table 10: make_toneut output files 155

Table 11: Routines created to plot data 157

LIST OF FIGURES

Figure 1: Simple Diagram of a Tokamak 2

Figure 2: A 2D cross section of single-null poloidal divertor plasma configuration..... 4

Figure 3: DIII-D Discharge 92976..... 17

Figure 4: TEXTOR CROSS SECTION..... 34

Figure 5: Top View of Neutral Beam Heating System in TEXTOR..... 36

Figure 6: Electric connections for the base modes the DED 38

Figure 7: Schematic view of the HCN-interferometer-polarimeter.. 41

Figure 8: A top view of a Tokamak 44

Figure 9: Experimental setup for observation of H_α. 45

Figure 10: Schematic Filterscope..... 47

Figure 11:LIMZ1 measures the H_α signal over the HFS 50

Figure 12: Bolometer Chords in TEXTOR..... 52

Figure 13: Dependence of Greenwald number on the heating power.. 54

Figure 14: Schematic of Shot Plan presented to BATEX committee. 57

Figure 15: Toroidal Flow Measurements..... 60

Figure 16: Centerline Electron Temperature for Rotation Scan Discharges 62

Figure 17: Maximum Edge Electron Density (m^{-3}) versus Co NBI (MW) beam power.. 65

Figure 18: H_α ratio versus Co NBI Power (MW). 66

Figure 19: Maximum edge electron density (m^{-3}) versus the requested total power. 68

Figure 20: Ratio of the H-alpha signals versus the requested total power (MW)..... 69

Figure 21: 2D Bolometer Shot 100178..... 71

Figure 22: Video of MARFE migration in TEXTOR..... 73

Figure 23: Schematic diagram for integral transport equation 76

Figure 24: Schematic diagram for TEP methodology 78

Figure 25: Geometry for calculation of transmission probability..... 81

Figure 26: 3D geometry for calculation of transmission probability..... 81

Figure 27: Geometry for calculating escape probability..... 83

Figure 28: Simplified Geometry of UEDGE Mesh 96

Figure 29: A) DIII-D geometry showing the divertor configuration. 101

Figure 30: Neutral mean free path distribution..... 106

Figure 31: 2D geometric model used in GTNEUT analysis. 109

Figure 32: Poloidal distribution of neutral fluxes recycling from the wall..... 116

Figure 33: Inward partial (in) and net (in minus out) neutral fluxes 117

Figure 34: Poloidal distribution of ionization rates per unit area along the separatrix... 120

Figure 35: Poloidal distribution of ionization rates per unit area along the separatrix... 121

Figure 36: Poloidal distribution of charge-exchange rates per unit area 123

Figure 37: Poloidal distribution of charge-exchange rates per unit area 124

Figure 38: Poloidal distribution of neutral density over flux surface in edge pedestal . 126

Figure 39: Poloidal distribution of neutral density over flux surface in edge pedestal . 127

Figure 40: Poloidal distribution of ionization density over flux surface 128

Figure 41: Poloidal distribution of ionization density over flux surface 129

Figure 42: Poloidal distribution of PED ionization rate per unit area 132

Figure 43: Poloidal distribution of PED ionization rate per unit area 133

Figure 44: Effectiveness of neutrals from different sources in fueling the pedestal 135

Figure 45: Effectiveness of neutrals from different sources in fueling the pedestal 136

Figure 46: Ionization fueling rates in the pedestal from different sources 139

Figure 47: Ionization fueling rates in the pedestal from different sources 140

Figure 48: Poloidal distributions of PED+CORE ionization rate..... 143

Figure 49: Poloidal distributions of PED+CORE ionization rate..... 144

Figure 50: Difference in HALO and Private Flux Region for GTNEUT and DEGAS2 146

Figure 51: Franck-Condon Energy Sensitivity Study (Attached Case)..... 148

Figure 52: Charge Exchange Fraction per Cell (Detached Case)..... 158

Figure 53: Charge Exchange Fraction per Cell divertor view (Detached Case)..... 159

Figure 54: Charge Exchange Rates per Cell (Detached Case) 160

Figure 55: Charge Exchange Rates per Cell divertor view (Detached Case)..... 161

Figure 56: Ionization Density per Cell (Detached Case)..... 162

Figure 57: Ionization Density per Cell divertor view (Detached Case)..... 163

Figure 58: Ionization Rate per Cell (Detached Case)..... 164

Figure 59: Ionization Rate per Cell divertor view (Detached Case)..... 165

Figure 60: Mean Free Path per Cell (Detached Case) 166

Figure 61: Mean Free Path per Cell divertor view (Detached Case)..... 167

Figure 62: Neutral Density per Cell (Detached Case) 168

Figure 63: Neutral Density per Cell divertor view (Detached Case)..... 169

Figure 64: Electron Density per Cell (Detached Case)..... 170

Figure 65: Electron Density per Cell divertor view (Detached Case) 171

Figure 66: Ion Density per Cell (Detached Case)..... 172

Figure 67: Ion Density per Cell divertor view (Detached Case) 173

Figure 68: Electron Temperature per Cell (Detached Case)..... 174

Figure 69: Electron Temperature per Cell divertor view (Detached Case) 175
Figure 70: Ion Temperature per Cell (Detached Case) 176
Figure 71: Ion Temperature per Cell divertor view(Detached Case) 177
Figure 72: Charge Exchange Fraction per Cell (Attached Case) 178
Figure 73: Charge Exchange Fraction per Cell divertor view (Attached Case) 179
Figure 74: Charge Exchange Rates per Cell (Attached Case) 180
Figure 75: Charge Exchange Rates per Cell divertor view (Attached Case) 181
Figure 76: Ionization Density per Cell (Attached Case) 182
Figure 77: Ionization Density per Cell divertor view (Attached Case) 183
Figure 78: Ionization Rate per Cell (Attached Case) 184
Figure 79: Ionization Rate per Cell divertor view (Attached Case) 185
Figure 80: Mean Free Path per Cell (Attached Case) 186
Figure 81: Mean Free Path per Cell divertor view (Attached Case) 187
Figure 82: Neutral Density per Cell (Attached Case) 188
Figure 83: Neutral Density per Cell divertor view (Attached Case) 189
Figure 84: Electron Density per Cell (Attached Case) 190
Figure 85: Electron Density per Cell divertor view (Attached Case) 191
Figure 86: Ion Density per Cell (Attached Case) 192
Figure 87: Ion Density per Cell divertor view (Attached Case) 193
Figure 88: Electron Temperature per Cell (Attached Case) 194
Figure 89: Electron Temperature per Cell divertor view (Attached Case) 195
Figure 90: Ion Temperature per Cell (Attached Case) 196
Figure 91: Ion Temperature per Cell divertor view(Attached Case) 197

SUMMARY

The recycling of neutral atoms in the plasma edge is an area of increasing interest in Tokamak plasma physics. Strong evidence has been presented recently that suggests there is a strong link between neutral particles and the overall confinement of the plasma. Experimental studies of neutral particle dynamics [1] and penetration into the core plasma [2] have stimulated investigations of the effects of neutrals upon edge phenomena such as MARFEs [3, 4] (Multifaceted Axisymmetric Radiation from the Edge), the L-H (Low-to-High Mode) transition [5-7], the structure of the edge pedestal [8, 9] in H-mode plasmas, and the interpretation of thermal transport coefficients from measurements of edge density and temperature gradients [10]. One such piece of evidence (and major motivation for our research) comes from a series of experiments carried out on the Tokamak TEXTOR that qualitatively demonstrates there is a direct link between density limits and neutral particle density in the plasma edge. The details of this experiment are found in Chapter 2 of this thesis.

Many studies have focused on the investigation of edge pedestal fueling by neutrals produced from ions recycling from edge plasma material surfaces. At issue is whether the edge pedestal is fueled primarily by neutrals recycling from ion fluxes incident on the divertor target plates, as has long been assumed, or by neutrals recycling from the main plasma chamber wall produced by radial convective ion fluxes in the SOL (scrape-off layer). Evidence for both divertor recycling [11, 12] and main chamber recycling [13-15] stimulated an extensive data collection, analysis and modeling effort for a series of DIII-D discharges [16], which concluded that divertor recycling was the primary fueling mechanism in DIII-D.

One purpose of this thesis is to make use of this extensive data compilation/analysis and background plasma calculation database that has been established for this series of DIII-D discharges for a detailed analysis of neutral particle recycling and edge pedestal fueling in an H-mode Tokamak plasma with the 2D neutral particle transport code GTNEUT [17, 18]. We have chosen the deterministic GTNEUT code instead of the more familiar Monte Carlo codes such as DEGAS2 [19] and EIRENE [20] which are frequently used with plasma fluid codes such as SOLPS [21] and UEDGE [22] for neutral recycling calculations in Tokamak plasmas because of the difficulty of obtaining sufficiently good statistics to calculate accurate neutral profiles with Monte Carlo (see e.g. Fig. 17 in Ref. [21]). The GTNEUT code is discussed in detail in Chapters 3 and 4. The ion flux measurements used in this analysis are discussed in Chapter 5. The neutral particle recycling and pedestal fueling calculations are discussed in Chapter 6. Analyses of the relative importance of neutrals recycled at different spatial locations and discussion of the calculational uncertainties are also presented in Chapter 6. Suggestions for improvements to the GTNEUT code are briefly discussed in Chapter 7. A brief summary and conclusions are presented in Chapter 8.

1. Introduction

1.1 Area of Research

This PhD dissertation is related to the fields of Plasma Physics and Fusion Technology. The main research topics are Edge Plasma Physics and Neutral Particle Transport Theory.

1.2 Motivation

Fusion is the process by which two nuclei are brought together to form a larger more massive nucleus. If the mass of the resulting nucleus is less than the sum of the two original nuclei, energy is released. This is the very process that powers our sun and every star in the night sky. In order for the fusion process to occur, very high temperatures are typically needed. The temperatures are so high in fact that no physical material can contain the reaction; instead, other means of confinement must be used. In stellar fusion, this is accomplished with gravity. The collective mass of all the nuclei in a star create a gravitational bottle that traps the hot atoms keeping them from escaping. While gravitational bottles are rather common throughout the known universe, they are impossible to replicate in the laboratory setting with today's technology. Here on earth, we must use more innovative means of confining the hot nuclei.

Fortunately, if a gas is heated to sufficiently hot temperatures, the electrons surrounding the nucleus of the gas atoms become unbound. This means the atoms are no longer microscopically neutral in charge; however, the system of ions and electrons are still macroscopically neutral. When the electrons are "vaporized" from the nucleus in this

fashion, we say that a gas has transitioned to the fourth state of matter which is called "plasma". Since the charged particles of the plasma spiral around magnetic field lines due to the Lorentz force, it is possible to utilize magnetic fields to confine the plasma.

There have been many magnetic field configurations used to create a "magnetic bottle" to confine the plasma, but one of the devices that holds the most promise is a device called the Tokamak. First developed in the former Soviet Union in the 1950s [23], the Tokamak is a donut shaped device that consists of three primary components: a vacuum vessel, an array of toroidal magnets, and a system of poloidal magnets as seen in the figure below.

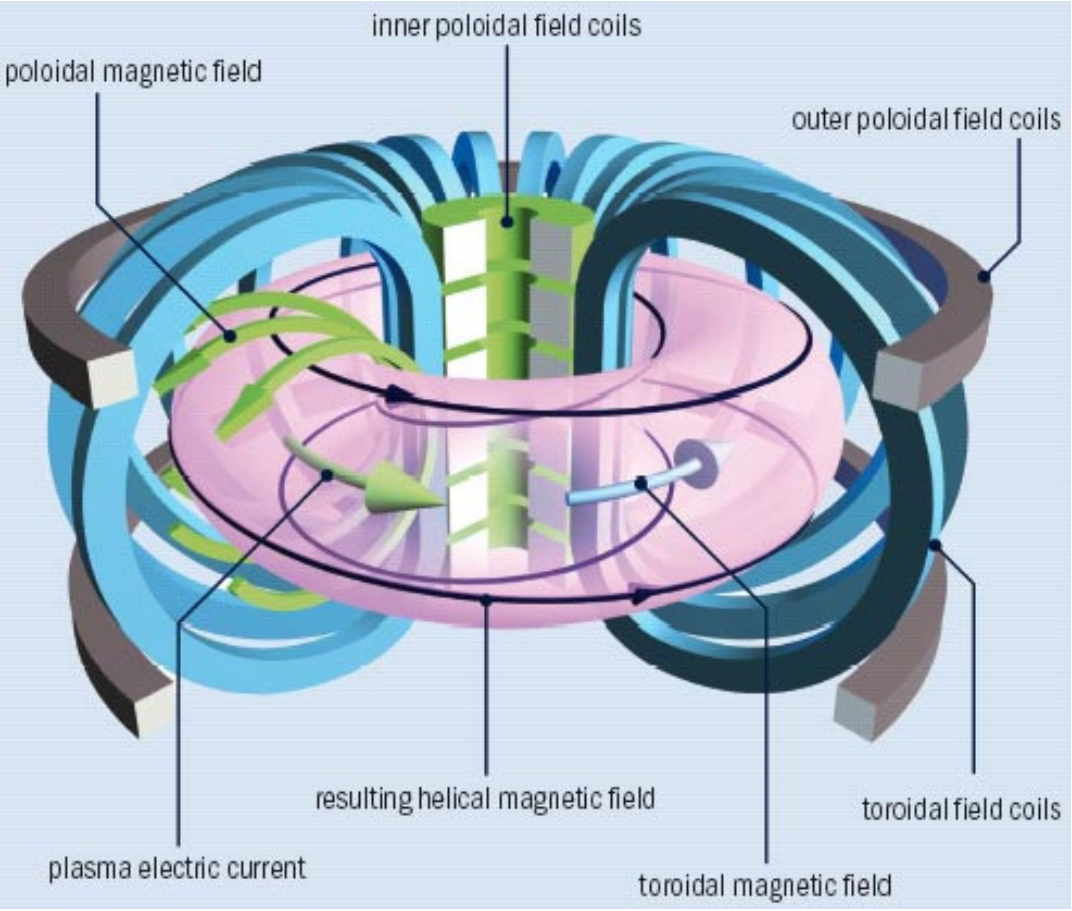

Figure 1: Simple Diagram of a Tokamak [24].

The vacuum vessel is used to confine the neutral gas and maintain optimal densities in order to create the plasma. The plasma itself is actually confined by the magnetic fields generated by the toroidal and poloidal field coils. The inner poloidal field coils (also called the central solenoid) are used to induce a current in the plasma. The current coursing through the plasma not only heats it, but also creates another magnetic field. The superposition of the toroidal and poloidal magnet fields creates a helical shaped magnetic field line for the plasma ions and electrons to orbit about.

The creation of the plasma particles begin in or around the core of the plasma. The core of the plasma is the hottest region inside the Tokamak. Temperatures exceed one million degrees Kelvin. The core is where most of the fusion occurs. A plasma particle cannot remain in the core indefinitely though. Ions will either fuse with other ions or escape. When the ion escapes the core of the plasma it crosses the Last Closed Flux Surface (LCFS) and then hits the wall of the vacuum vessel or another structure. The LCFS is the last of the helical field lines that creates a closed loop. Outside of the LCFS, the field lines are connected to the first wall of the vacuum vessel or another structure. Once a plasma ion hits the wall it recombines with an electron forming a neutral gas particle once again. This neutral gas is no longer confined by the magnetic field lines. Some neutral gas particles can be absorbed by the first wall of the vacuum vessel while others are injected back into the core to refuel it. However, in order for the neutral particle to refuel the plasma, it must first cross the LCFS once more and enter a region of the plasma called the edge.

The plasma edge is a small region inside of the Tokamak plasma that extends inward from the LCFS for only a few centimeters, as shown in the figure below.

Mathematically, this is the region that determines the boundary conditions for core plasma physics solutions. Physically, this is the region through which particles and energy from within the core must be transported through in order to pass to the unconfined plasma in the Scrape Off Layer (SOL). It is also the region in which the neutral particles re-entering the core from the SOL are ionized.

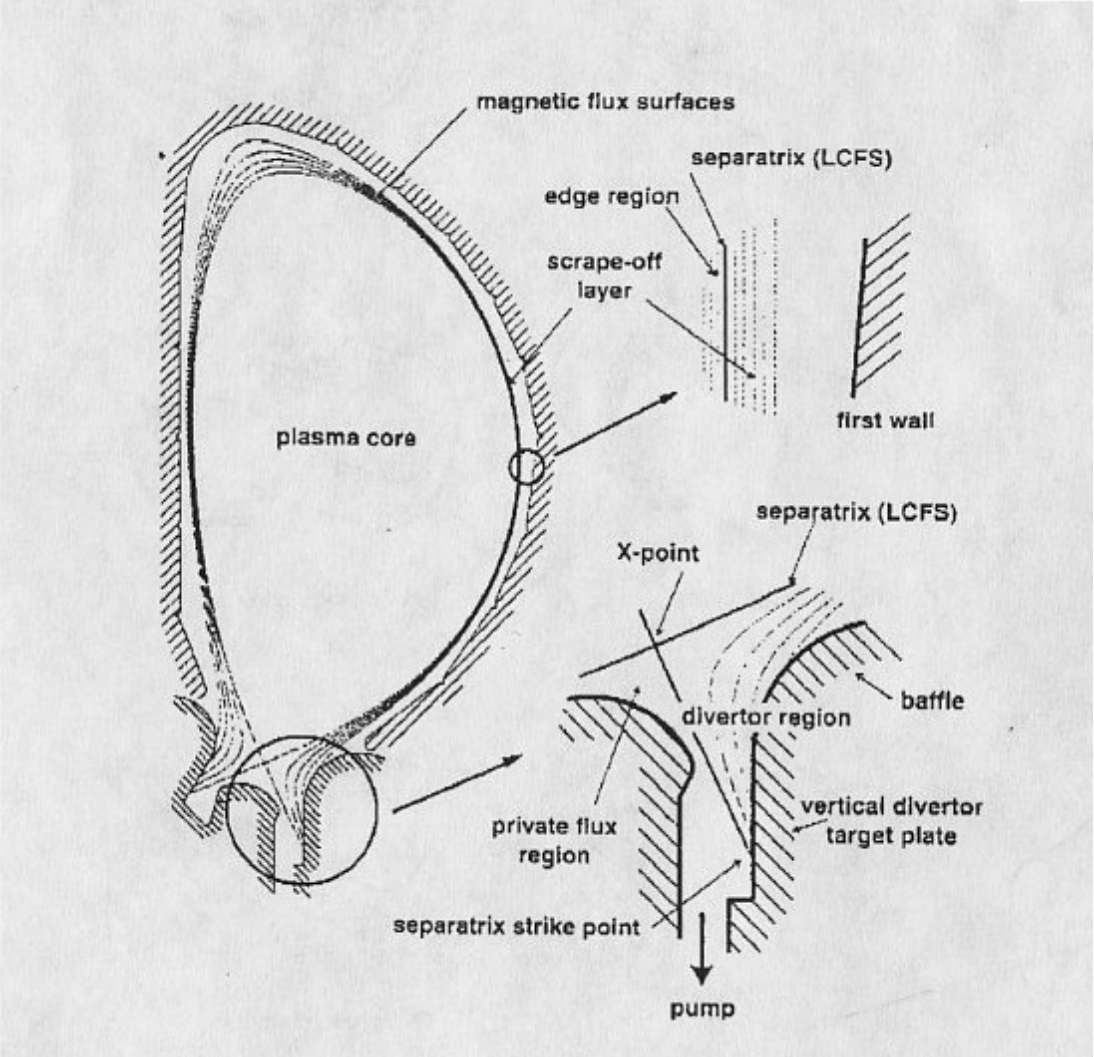

Figure 2: A 2D cross section of single-null poloidal divertor plasma configuration [25].

In the past, many plasma physicists concentrated research efforts on the exploration of core and SOL plasma physics with little attention given to the edge region

[25]. However, it has been known for some time that neutral atoms could travel deep into a hot plasma by repeated charge exchange [26, 27]. Strong evidence has been presented recently that suggests there is a strong link between neutral particles and the overall plasma power and particle balances, temperature and density profiles, plasma confinement, particle and energy fluxes to the wall of the device, erosion of the first wall, and the performance of the pumping systems [27-30]. The primary objective of this dissertation is to examine how neutral particles affect the plasma edge under various operating conditions; however, it is important to first discuss what has already been done.

It is known that recycling neutral particles cool the plasma edge, provide a source of ions, and alter the plasma momentum balance. By doing so, neutral particles may have profound effects on the plasma edge. Some of these effects may be due to the neutral particles altering the particle or power balance of the plasma [31]. Neutral particles may also influence the plasma velocity via momentum balance [32, 33] or simply alter the temperature and densities in the region [5, 34]. Regardless of how the plasma has been affected, the primary mechanisms by which neutral particles affect the plasma are through charge-exchange, ionization, and elastic scattering. Furthermore, neutrals may cool the plasma to the point where recombination occurs. Another primary effect is that the charge-exchange of neutral particles with partially ionized impurity atoms followed by recombination can increase substantially the impurity radiation cooling [31, 35].

One mechanism by which neutral particles may affect the plasma is by affecting thermal instabilities. Thermal instabilities are those instabilities in the particle and power balances driven primarily by the unfavorable temperature (and density) dependence of the plasma heating and cooling rates [31]. These instabilities have been identified by

many researchers as the probable cause for numerous abrupt-transition phenomena in Tokamaks. Such phenomena include (but are not limited to) transport barrier formation, Multifaceted Asymmetric Radiation From the Edge (MARFE), radiative collapse, divertor MARFEs, etc.

One of the most important discoveries in recent Tokamak history has been the observation of a new confinement regime called H-mode. It has been observed that when a particular non-radiative power through the LCFS exceeds a certain threshold value, a transport barrier sets up in the edge of the plasma causing steep density and temperature gradients to form. There are a number of theories on why this transport barrier forms, but the reigning paradigm is that an increase in the $E \times B$ velocity shear stabilizes edge turbulence. Regardless of how the transport barrier forms, there is a significant enhancement of the steep gradients signifying that more of the plasma remains hotter for a longer period of time thereby increasing the chance a fusion reaction will occur. This enhanced confinement regime is called High Mode (H-mode), and it can improve the confinement by a factor of two or more over that of the Low Mode (L-mode) confinement. The inner edge of the steep gradients is referred to as the "pedestal" [5]. From the many experiments in which the L-H transition has been observed, an empirical equation has been formulated to approximate the non-radiative power flowing outward across the last closed flux surface required for this transition to occur [25].

$$P_{LH}^{(MW)} = (2.84 / A_i)\bar{n}_{20}^{0.58} B^{0.82} R a^{0.81} \tag{1}$$

The above equation is based solely on the Tokamak machine parameters (aspect ratio, density, magnetic field, major, and minor radius) and can vary widely from device to device. In order to compensate, additional scaling factors are sometimes used.

Stacey has suggested [31, 36] how the suppression of thermal instabilities could act as a trigger mechanism in the formation of the steep temperature gradient region that is referred to as the edge transport barrier. He has developed a model for the power required to cross the separatrix in order to suppress thermal instabilities in the edge. His model is one of the few "non-empirical" formulations to achieve such a feat.

$$P_{thresh} = \frac{5}{4}\Gamma_{\perp} T A_{sep}\left[\sqrt{1+\frac{\left(\chi^0\left(\alpha-\chi^0 k_r^2/\nu\right)\right)}{\left(\frac{5}{4}\frac{\Gamma_{\perp}}{n}\right)^2}}+1\right] \tag{2}$$

The equation above is the simplified mathematical formularization of the model. χ^0 is the thermal conductivity and A_{sep} is the area of the separatrix. $\Gamma_{\perp}$ is the convective particle flux. n and T are density and temperature respectively. ν is the collision frequency and k_r^{-1} is the radial wavelength. Eq. (2) is similar in function to Eq. (1), except that it works for both the L-H transition and the H-L transition. It is based on fundamental physics rather than empirical correlations. P_{thresh} is equivalent to $P_{LH}^{(MW)}$, in that both are the non-radiative powers required to cross the separatrix in order for the plasma to transition to H-mode.

We should also note that the model formulated in Eq. (2) provides compelling theoretical evidence that neutral particles can strongly influence the L-H transition. This will become abundantly clear as we highlight the development of the model.

To develop his model [36], Stacey assumes that once thermal instabilities in the edge have been suppressed, the turbulent transport in the edge is suppressed by the sheared $E\times B$ flow. Then he couples the most basic particle, momentum, and energy

balance equation to density-velocity-temperature instabilities with a short k_r^{-1} in the edge. The coupling is done by performing an expansion of the solution of the time dependent balance equations in the vicinity of a given equilibrium solution as a small perturbation in density, velocity and temperature about a given equilibrium solution. This course of action yields a dispersion relationship for the growth rates and wavelengths of the thermal instabilities in the edge.

$$\omega = -\frac{2}{3}\left(\chi\left(\nu L_T^{-2} + k_r^2\right) + \frac{5}{2}\nu\frac{\Gamma_\perp}{n}L_T^{-1} - \alpha \right) \tag{3}$$

When ω of Eq. (3) goes to zero, thermal instabilities in the plasma edge are suppressed, thus enabling the transitioning of the plasma from L-mode to H-mode. It is by setting Eq. (3) to zero that Eq. (2) may be derived; however, it is easier to study the effects of neutral particles on thermal instabilities by looking at Eq. (3). The first two terms in Eq. (3) are the stabilizing effects of heat conduction and convection respectively. The α-terms encompass the destabilizing atomic physics process and the stabilizing effects of heating in the edge. For ions the α-term is given by

$$\alpha_i = \frac{5}{2}(\nu - 1)\nu_{ion} + \frac{3}{2}\nu_{at}^c\left(\nu - \left[1 + \frac{T_i}{\nu_{at}^c}\frac{\partial \nu_{at}^c}{\partial T_i} \right] \right) - \frac{1}{n}\left(\nu\frac{H_i}{T_i} - \frac{\partial H_i}{\partial T_i} \right) \tag{4}$$

and for the electrons

$$\alpha_e = n_z\left(\frac{\nu L_z}{T_e} - \frac{\partial L_z}{\partial T_e} \right) + \nu_{ion}\left\{ \frac{5}{2}(\nu - 1) + \nu\frac{E_{ion}}{T_e} - \left(\frac{3}{2} + \frac{E_{ion}}{T_e} \right)\frac{T_e}{\nu_{ion}} - \frac{1}{n}\left(\nu\frac{H_e}{T_e} - \frac{\partial H_e}{\partial T_e} \right) \right\}. \tag{5}$$

In these equations, $\chi \sim T^\nu$ is the radial thermal diffusivity, $L_T^{-1} = -(dT/dr)/T$, $\Gamma_\perp$ is the average radial particle flux flowing outward through the plasma edge region (as in Eq. 2), ν_{ion} is the neutral ionization frequency, ν_{at}^c is the frequency of charge exchange plus

elastic scattering reactions with ‘‘cold’’ neutrals, E_{ion} is the ionization energy, n_z and L_z are the density and radiation emissivity of impurity ions, and H is any external heating that may be present. All quantities are in the plasma edge [36].

It is from the α terms that we can see how the presence of neutral particles can enhance the excitation thermal instabilities in the edge. In the ion α term, $\nu_{at}^{c} = n_0^{cold}\left(\langle\sigma\nu\rangle_{cx} + \langle\sigma\nu\rangle_{elast}\right)$. This term encompasses the charge exchange and elastic scattering rates. As the neutral particle density in the edge increases, so do these rates. This means the edge is cooling faster causing ω to increase. The same is true for the ionization rate ($\nu_{ion} = n_o\langle\sigma\nu\rangle_{ion}$) in both α terms. Additionally in α_e, the first term represents impurities in the edge. As the impurity density in the edge increases, the edge to further cools by radiation which further increases ω.

Further theoretical evidence for the effect of neutrals on the L-H transition has been provided by Carreras. He examined a wide range of plasma discharges to study the effects that neutral particles have on the L-H transition [37]. Carreras finds that neutrals may in fact play multiple roles in the transition. As previously stated in Stacey’s analysis, Carreras also finds that the neutrals clearly affect the particle and energy fluxes as well as the ion momentum loss through charge exchange friction. From here, he suggests that due to the poloidal localization of the charge exchange damping, neutrals may modify not only the magnitude, but also the topology of the $E\times B$ flow shear. This suggest that neutrals can play a dual role in the L-H transition by having both positive or negative effects [37].

Carreras uses a different approach to examine the effects of the neutrals on the L-H transition. He starts with the assumption that the L-H transition occurs by the sudden

amplification of the poloidal shear through the Reynolds stress which suppresses turbulence in the edge. With this assumption, he suggest that one must examine the main physics effects of the poloidal momentum balance in order to obtain a clear picture of what effects the neutrals have on the suppression of the edge turbulence. This is done by looking at a simplified form for the evolution of the poloidal ion velocity shear, $\langle V_\theta \rangle_s^{'}$, given by:

$$\frac{d\langle V_{\theta i}\rangle_s^{'}}{dt} = -\left(\beta \frac{\left\langle (\tilde{n}/n)^2 \right\rangle}{W_k^2} + \mu_{neo} + \langle n_n \rangle_s \langle \nu\sigma \rangle_{cx} \right) \times \langle V_{\theta i} \rangle_s^{'} + \alpha_3 f\left(N_n, N_T\right) \left\langle (\tilde{n}/n)^2 \right\rangle \langle V_{\theta E} \rangle_s^{'}. \tag{6}$$

The first and last terms on the right hand side of Eq. (6) are contributions due to the Reynolds Stress Tensor, and the second term is the neoclassical flow damping term. The third term is a simplified form of the friction between ions and neutrals induced by charge exchange. Using Eq. (6), Carreras formulates a transition criterion [37].

$$\alpha_3 f\left(N_n, N_T\right) \left\langle (\tilde{n}/n)^2 \right\rangle > \mu_{neo} + \beta \left\langle (\tilde{n}/n)^2 \right\rangle / W_k^2 + \langle n_n \rangle_s \langle \nu\sigma \rangle_{ex} \tag{7}$$

The left hand side of the equation can be equated related to power through transport and temperature gradients. It is therefore straight forward to see how one of the possible roles of neutrals is impeding the transition. The enhanced poloidal flow damping due to charge-exchange friction increases the power threshold.

He also suggests that neutrals may also increase the ion energy loss through charge exchange and ionization, but that this contribution to the increase in the power threshold would be weak. From the model discussed, Carreras suggest that the increase of the transition threshold by neutrals goes beyond the particular model just discussed. In

fact, he says this carries over to all transition models that incorporate the $E \times B$ shear flow suppression of turbulence as the basic transition mechanism [37].

Using the phase transition model, Carreras suggest that the effects of the neutrals on the transition could possibly be described by taking the ratio of the charge exchange damping rate, ν_{cx}, to the neoclassical flow damping rate, n_{ceo}. Carreras produces a semi-empirical formula based on experimental correlations from DIII-D for the power required to cross the separatrix in order to transition from L mode to H mode.

$$P_{sep} = \overline{n}\left(0.37 + 0.63 \frac{\left(\nu_{cx}\right)_M^2}{\mu_{neo}^2} \right) \tag{8}$$

Here Carreras correlates $P_{sep}/\overline{n}$ to $\left(\nu_{cx}\right)_M / \mu_{neo}$. This equation is similar to Stacey's formula in Eq. (2) in that both predict an increasing power flow across the separatrix is required for H-mode as the neutral density in the edge increases and in that both indicate that the value of this power flux depends on local edge parameters. Carreras finds that this fit is rather poor, especially if the density dependence is eliminated. He suggests a better fit to experimental data is produced when he correlates $P_{sep}/\overline{n}$ to λ_n / r_s, where λ_n is the poloidally averaged neutral profile radial decay length and r_s is the averaged minor radius of the separatrix.

$$P_{sep} = \overline{n}\left(0.179 + 3148.8 \left(\frac{\lambda_n}{r_s} \right)^{2.56} \right) \tag{9}$$

From his experimental analysis, Carreras concluded that there was significant correlation between neutrals at the plasma edge and the power threshold for L-H transitions which is quite clear from Eq. (8) and Eq. (9). Additionally, it was observed experimentally, that neutral densities in the SOL can be misleading when estimating the

neutral population inside of the separatrix. This is because an increase in the neutral population in the SOL increases the plasma density, which in turn increases the opacity to the neutrals. This reduces the neutral penetration, which reduces the neutral density [37]. In fact, Carreras suggest this could be a reason that in some experiments with very strong gas puffing in DIII-D, the power threshold actually decreases.

Fukuda [38] points out that the DIII-D observations directly contradict observations in JT-60U. In JT-60U (as well as other Tokamaks) excessive gas puffing can either quench H-mode or inhibit its formation altogether, but he goes on to suggest neutrals are still extremely significant factors. It should be noted that while those such as Fukuda suggest that neutrals are in fact important "hidden" variables in scaling laws such as Eq. (1), there is some experimental evidence that may suggest the impact that neutrals have on the L-H transition is small. Suttrop [39] made comparisons of matching sets of experiments on JET and ASDEX-upgrade. The comparisons consisted of a set of similarity tests; from which, he concluded that it is unlikely that atomic physics processes dominated the H-mode threshold scaling at the parameters of the experiment. The reason for these conclusions was that while I_p, $\bar{n}_e$, and B_t matched for each comparable discharge between the machines, there was no consistency between some other factors such as ν^*.

In addition to the H-mode regime, neutral particles may influence a regime known as detachment. Detachment is useful because it may decrease the heat and particle loads to the wall of the confinement vessel and the divertor (effectively decreasing the damage to both respectively). Detachment occurs when the plasma just above the divertor strike plate is radiatively cooled. Detachment can reduce the temperature in the divertor region

to extremely low temperatures (~ 1 eV). Lowering the temperature in this region also increases the number of neutrals by increasing the amount of recombination of ions and electrons [40, 41]. Some have indicated that increase of neutrals from this region in the detached regime may influence the H-mode transition [1, 36, 42]. It has also been shown that by continuing to fuel the plasma via gas puffing after detachment has occur, the onset of a Multifaceted Asymmetric Radiation from the edge (MARFE) may occur [3, 36, 42].

MARFEs are essentially poloidally localized, relatively cool, dense, and strongly radiating regions in the plasma edge [43]. They were first observed in the early 1980's in DIII, FT, ASDEX, and PDX [43-46]. MARFEs were observed to have threshold density limits slightly lower than that of the disruption density limits. It was observed that if the MARFE density limit were reached the plasma still remained stable, but if the density of the plasma was further increased, the MARFE would grow until the heat lost by the ionization of the neutrals exceeded the heat flow from the plasma. Once this occurred a plasma disruption was imminent. This is one reason that many have studied the MARFEs on a number of devices.

Petrie [47] observed distinct differences in the accumulation of neutral particles in the private flux region between single-null (SN) and double-null (DN) divertor discharges. He observed that in SN discharges, MARFE formation was more likely to take place than with DN divertor configuration. Petrie suggests that one reason for the decreased neutral particle accumulation in the double-null discharges was that DN divertors are 'more detached' on their inboard legs than are single-null divertors. Petrie states that in the DN divertor case there is a higher probability that a neutral particle will recycle and directly fuel the core as opposed to being pumped by the graphite tiles [47].

Others have shown how localized neutral particle accumulation may precede MARFE formation in several limiter Tokamaks [4, 34, 35, 48]. In a series of ohmic discharges with an actively cooled limiter carried out on Tore Supra, Guirlet observed an increase in the D_α radiation line just above the alt limiter [34]. The D_α line is usually proportional to the neutral particle flux in the region. Just prior to the MARFE formation, this radiating region left the area above the limiter and migrated to the HFS of the Tokamak. This could be similar to the phenomena observed by Petrie in the single-null case where a radiating region forms in the private flux region then crosses the X-point during MARFE formation. Friis and Liang [49] have observed several cases similar to Guirlet's observations under different operating conditions in TEXTOR. Friis and Liang were investigating the effect that plasma flow has on the MARFE density limit when they discovered that different auxiliary heating methods can affect the neutral particle distribution in the edge. More of Friis and Liang's analysis will be presented in the next section of this thesis as it is a primary motivation for this body of work.

While many have experimentally studied MARFEs, Drake [50] was one of the first to explain them theoretically. Using astrophysical precedents, he expressed the driving mechanism behind MARFEs as "Radiative Condensation" which is quite easy to explain qualitatively. First, there must be a local increase in the plasma density in the edge. This increase in density causes an increase in the radiation rate in the region, reducing the local plasma temperature. For the plasma to maintain constant pressure, more density must flow along field lines into the cooler radiating region ("condensing"). This process continues as the plasma is fueled, ultimately leading to a plasma disruption. Using this concept, Drake was able to formulate a model for threshold conditions for

MARFE onset. Many have expanded upon Drake's work, and Stacey has developed a comprehensive theoretical conditions for MARFE onset [51, 52].

Stacey [53] performed a stability analysis for the $k_{\|} = \left(m + nqB_\theta / B\right)/qR \approx 0$ two-dimensional edge-localized modes. These modes are the first modes to become unstable in MARFE formation, because of the stabilizing effect of parallel heat conduction for finite $k_{\|}$ modes. When the linear analysis of stability is carried out over a poloidally uniform plasma edge density and temperature distribution in the limit $k_{\|} \to 0$, a conservative estimate for the maximum density for which the uniform equilibrium solution is stable may be obtained. This is referred to as the MARFE onset density limit and is given by [3]

$$
\begin{aligned}
n_{MARFE} = \left[\chi_r \left(\nu L_T^{-2} + \left(C^{(2)} - 1\right) L_T^{-1} L_n^{-1}\right)\right] / \Bigg\{ & f_z \left(\nu + 1 - C^{(2)} \frac{L_z}{T} - \frac{\partial L_z}{\partial T}\right) \\
& + f_0 \left[\frac{E_{ion}}{T}\left(\nu - \frac{T}{\langle\sigma\nu\rangle_{ion}} \frac{\partial \langle\sigma\nu\rangle_{ion}}{\partial T}\right)\right] + f_0^{cold} \left[\frac{3}{2}\left(\langle\sigma\nu\rangle_{cx} + \langle\sigma\nu\rangle_{el}\right)\right. . \\
& \left. \times \left(\nu - 1 - T \frac{\partial\left(\langle\sigma\nu\rangle_{cx} + \langle\sigma\nu\rangle_{el}\right)/\partial T}{\left(\langle\sigma\nu\rangle_{cx} + \langle\sigma\nu\rangle_{el}\right)}\right)\right] \Bigg\}
\end{aligned}
\tag{10}
$$

When the experimental density (n_{exp}) exceeds this theoretical prediction, a MARFE forms. Therefore, higher values of n_{MARFE} are desirable. From Eq. (10) it becomes abundantly clear of how important neutrals are in determining MARFE onset. f_0 and f_z are the neutral and impurity concentrations in the edge, respectively. The "cold" refers to uncollided neutrals recycling from the wall. In Eq. (10), if either f_0 or f_z increases, then n_{MARFE} will decrease. Additionally, as the charge-exchange and elastic scattering rates

($<\sigma v>_{cx}$ and $<\sigma v>_{el}$) increase with increasing neutral particle concentration, n_{MARFE} will decrease.

It is often easy to predict MARFE onset by dividing n_{MARFE} by n_{exp}. This is referred to as the MARFE Index (MI). When MI is greater than 1, a MARFE has formed. The theoretical MARFE index has been compared with experimental results many times. One example is shown below.

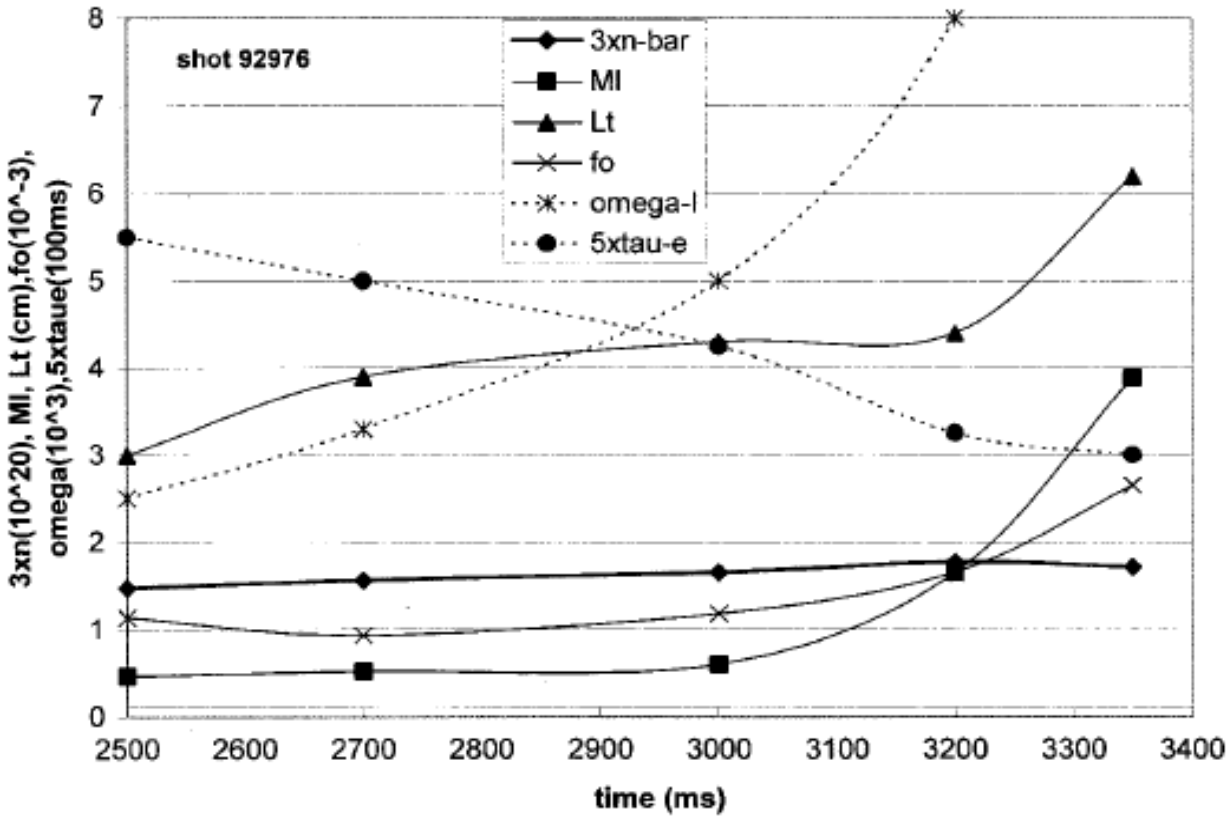

Figure 3: DIII-D Discharge 92976 (B=2.1T, I=1.03MA, P_{NBI}=5MW, f_{carbon}=0.028-0.012). Several parameter versus time[3].

Experimental data from discharge 92976 indicates a MARFE occurred between 3050-3100 ms. In Fig. 3, at around 3000 ms, we see the MI beginning to rise. At around 3100 ms, the MI increases to above 1. By examining the components of Eq. (10), it becomes easy to see how neutral particles in the edge can influence this theoretical onset prediction. f_0 is also plotted in figure 1, and as we can see, at around 3000 ms it steadily increases with the MI [3].

Stacey is not the only one to describe the role neutrals play in the theoretical prediction for MARFE onset. Tokar [4, 54-56] has extensively studied the subject using simple heat balance equations. In his predictive model, the plasma edge becomes thermally unstable if $\partial q_{loss} / \partial \langle T \rangle < 0$. Therefore, the destabilizing terms become the heat lost due to convection-recycling and radiation. Both of these losses are directly proportional to the neutral particle fluxes in Tokar's models.

It has been observed in a number of Tokamaks that when a MARFE forms in the H-Mode confinement regime, the plasma will transition back to L-mode [42]. This has been attributed to the loss of non-radiative power crossing the separatrix due to the increase in radiation losses associated with the MARFE. Recently, however, Stacey and Friis analyzed the relation between MARFEs and the H-L transition using the models outlined in Eqs. (2) and (10), and they have shown that this is not the only reason for the back transition. Their analysis showed that while the increase in the radiating power could contribute to the H-L transition, it was primarily the increase in the neutral particles associated with the MARFE formation that changed the conditions required to maintain H-mode (Eq. (2)).

Table 1: : P_{thresh}^{theory} and $P_{sep}^{\exp}$ **evolution during three DIII-D shots that underwent H-L transitions following core MARFE. (All Units are in MW)**

TIME ↓	92976 TIME(ms)	P_{rad}	P_{NBI}	$\frac{dW}{dt}$	P_{OH}	P_{sep}^{exp}	P_{thresh}
	2500	.54	5	0	.30	**4.8**	**2.5**
	2962-3000	DIVERTOR MARFE					
	3000	.39	5	0	.58	**5.2**	**3.0**
	3050-3100	CORE MARFE					
	3212	1.4	5	0	.63	**4.2**	**4.1**
	3230	H-to-L TRANSITION					
TIME ↓	**92972** TIME(ms)	P_{rad}	P_{nbi}	$\frac{dW}{dt}$	P_{OH}	P_{sep}^{exp}	P_{thresh}
	2500	.62	5.2	0	.35	**4.9**	**3.5**
	2750-2790	DIVERTOR MARFE					
	3000	.87	5.2	0	.45	**4.8**	**3.7**
	3190	CORE MARFE					
	3325	1.29	5.2	0	.55	**4.5**	**4.6**
	3323	H-to-L TRANSITION					
TIME ↓	**96887** TIME(ms)	P_{rad}	P_{nbi}	$\frac{dW}{dt}$	P_{OH}	P_{sep}^{exp}	P_{thresh}
	2390	DIVERTOR MARFE					
	2500	.8	8.5	0	.21	**7.9**	**6.1**
	3200	1.09	8.5	-.46	.37	**8.2**	**6.8**
	3240	CORE MARFE					
	3650	1.2	8.5	-.23	.95	**8.5**	**8.8**
	3653	H-to-L TRANSITION					

Table 1 shows a "snapshot" time progression analysis of three similar DIII-D density limit discharges with continuous gas fueling. $P_{sep}^{\exp}$ is the experimentally observed non-radiative power crossing separatrix. It was calculated using the power balance equation, $P_{sep}^{\exp} = P_{OH} + P_{NBI} - dW/dt - P_{rad}$. P_{thresh} was then calculated using Eq. (2). According to Table 1, we do generally see P_{rad} increase as fueling continues, but more importantly it seems that P_{thresh} increases sharply after MARFE formation. When we break down P_{thresh} into its components to ascertain the reason for the sharp increase, we find some interesting results.

Table 2: Breakdown of P_{thresh}

92976 *TIME(ms)*	$S_{recyc}(10^{20}/s)$	n_{ped} $(10^{20}m^{-3})$	T_{eped}(eV)	f_0 (%)	α_i $(10^3 s^{-1})$	α_e $(10^3 s^{-1})$	$\Gamma_\perp(10^{20}/s)$
2500	.64	.41	218	.84	.37	.40	1.6
2962-3000	DIVERTOR MARFE						
3000	1.4	.43	212	1.7	.88	1.3	3.0
3050-3100	CORE MARFE						
3212	3.9	.44	187	3.7	2.3	2.4	6.9
3230	H-to-L TRANSITION						
92972 *TIME(ms)*	$S_{recyc}(10^{20}/s)$	n_{ped} $(10^{20}m^{-3})$	T_{eped}(eV)	f_0 (%)	α_i $(10^3 s^{-1})$	α_e $(10^3 s^{-1})$	$\Gamma_\perp(10^{20}/s)$
2500	.40	.59	414	.48	.26	.29	1.1
2750-2790	DIVERTOR MARFE						
3000	1.1	.62	212	.91	.48	1.0	2.7
3190	CORE MARFE						
3325	7.2	.55	168	2.3	1.6	1.6	12
3323	H-to-L TRANSITION						
96887 *TIME(ms)*	$S_{recyc}(10^{20}/s)$	n_{ped} $(10^{20}m^{-3})$	T_{eped}(eV)	f_0 (%)	α_i $(10^3 s^{-1})$	α_e $(10^3 s^{-1})$	$\Gamma_\perp(10^{20}/s)$
2390	DIVERTOR MARFE						
2500	2.1	.99	440	.46	.45	.46	5.3
3200	2.5	.96	450	.56	.54	.55	6.1
3240	CORE MARFE						
3650	6.7	1.13	231	.70	.90	1.1	13
3653	H-to-L TRANSITION						

The quantities in Eq. (2) for P_{thresh}, which change with time during the shots, are tabulated in Table 2. It is clear from the table that the neutral influx ($S_{recyc}(10^{20}/s)=\Gamma_0^{in} A_{sep}$), hence the neutral concentration in the edge (f_0) increases with time in general and increases sharply at the time of core MARFE formation. . The increase in neutral influx produces an increase in the ion out-flux across the separatrix, as given by Eq. (2), and causes an increase in both the neutral and electron densities in the pedestal. The increased neutral density in the pedestal increases the ionization, charge-exchange and scattering rates in the pedestal, $\nu_{ion} = n_o \langle \sigma v \rangle_{ion}$ and $\nu_{at}^c = n_0^{cold} \left(\langle \sigma v \rangle_{cx} + \langle \sigma v \rangle_{elast} \right)$, which generally causes an increase in the atomic physics

terms α_i and α_e. An increase in neutral concentration in the edge also causes an increase in the carbon radiation emissivity, which causes an increase in α_e [6, 42].

Stacey and Friis concluded from these results that the increased neutral influx associated with the MARFE formation, causing a sharp increase in the threshold non-radiative power crossing the separatrix that is required for the plasma to remain in H-mode, is a principal mechanism triggering the back H-L transitions that are observed to follow MARFE formation in DIII-D [6, 42].

We have previously discussed the MARFE density limit in some detail, so now we will discuss some of the other density limits that may be of interest in this study. Probably the most important density limit for fusion power reactors will be the "disruption density limit". A disruption refers to a total loss of confinement, and it can be one of the most destructive events that can take place in a Tokamak. Plasma disruptions in smaller devices are generally considered minor nuisances. A disruption can "dirty" the next plasma discharge with impurities vaporized from the first wall leading to unfavorable plasma conditions, and could also offset sensitive diagnostic settings. In either case, time would be lost while cleaning the containment vessel or recalibrating the diagnostics took place. In larger Tokamaks such as JET or ITER, disruptions are no longer minor nuisances but crippling events that can cause substantial damage to diagnostic equipment, diverters, the vacuum vessel, and even the support structure.

The overall physics behind a disruption are generally well understood [57]. Cooling of the plasma at the q=2 surface will eventually contract the current profile increasing the destabilizing current gradient. In some cases (not all), the cooling at the q=2 surface may be caused by phenomena directly influenced by neutral particles from

the edge. This unstable current profile will subsequently destabilize the m = 2 tearing mode. The non-linear growth of this tearing mode ultimately leads to a collapse of the plasma temperature and a total loss of particle confinement.

Greenwald [58] compiled a database of discharges from several machines that had undergone a plasma disruption which he used to create an empirical correlation between the plasma current and maximum attainable density.

$$n_{GW} = \frac{I_P}{\pi a^2} \tag{11}$$

This correlation is often used as a guideline, as numerous experiments on many Tokamaks have shown that the "Greenwald Density Limit" may be exceeded by up to a factor of 2. In most Tokamaks, additional scaling terms are added because other factors may either increase or decrease n_{GW} [31, 59]. In has been postulated by some that this variation in the Greenwald scaling may be due to some of the effects neutrals have on the plasma [49].

While they represent the absolute maximum limit, disruption density limits are often preceded by one of two other density limits [59]. In moderately heated discharges that have relatively high amounts of Low-Z impurities, a disruption will usually be preceded by a symmetric radiation belt around the plasma and a shrinking of the plasma column. This is referred to as radiative detachment [31]. This is due to the radiative cooling power equaling the heating power. Consequently, the destabilization at the "detachment density limit" is not caused by the high density but by the low temperatures in the edge or to high of radiation levels. As with the MARFEs, the low temperatures in the edge can cause recombination of ions. Through atomic physics processes, the recombination ions and electrons causes increased radiation, which further decreases the

temperature. To increase the "detachment density limit", more auxiliary heating is required.

As previously stated, the inner edge of the steep gradients in an H-mode plasma is referred to as the "pedestal". The height of the pedestal and the width of the transport barrier can have a significant influence on the overall performance of the Tokamak, especially in the "next step" machines. It is for this reason, the H-mode pedestal has been well scrutinized for the last several years [9]. The mechanisms responsible for controlling the characteristics of the transport barrier are still a topic of great debate. There are several competing models that claim magneto-hydrodynamic (MHD) stability, transport, and sources of heat, particles, and momentum are responsible for controlling the H-mode transport barrier widths, but one model in particular predicts that transport barriers are driven by fluxes of heat and particles [60].

To derive the model [61], the assumption is made that the electron and neutral densities obey the continuity equation. The two continuity equations are then coupled to derive a steady state expression for the neutral density.

$$n_0(x) = n_0(a)\exp\left[-\frac{<\sigma v>}{V_n}\int_x^a n_e(x)dx\right] \tag{12}$$

The assumption is made that $n_e(a) = 0$, where a is the radius of the base of the pedestal and is also assumed to be the location of the separatrix. From here the electron density can be described as the following differential equation:

$$D\frac{\partial n_e}{\partial x} = V_n n_0(a)\exp\left[\frac{<\sigma v>}{V_n}\int_x^a n_e(x)dx\right] \tag{13}$$

Solving Eq. (13) for n_e, the familiar hyperbolic tangent function with width and height given by:

$$W_{ne} = 2\sqrt{\frac{D}{2\nu_i(a)}} \tag{14}$$

$$H_{ne} = n_0(a)\sqrt{\frac{2V_n^2}{D\nu_i(a)}} \tag{15}$$

where D is the usual particle diffusion coefficient, $\nu_i(a) = n_o(a)\langle\sigma\nu\rangle_{ion}$ is the ionization frequency evaluated at the base of the pedestal, $V_n(a)$ is the average neutral velocity originating from outside the plasma, and $n_0(a)$ is the neutral density at the base of the pedestal. Numerical simulations [60] of this model have shown that the particle barrier is driven by the large edge particle source and the resulting width of the barrier is approximately equal to the neutral penetration length; which to this begs the question, "Is the width of the transport barrier for the electron density equal to the characteristic penetration length for neutrals?" Luckily, this can be studied experimentally. On Alcator C-Mod, good agreement was seen between this model and experiment [61]. Observations on DIII-D have shown remarkable agreement as well. They showed neutral penetration as well as particle transport can play an important role in setting the width of the electron density transport barrier in H-mode. However, Groebner further expanded on this model by showing that there is a canonical shape to the density profile so that the height and width of the barrier have a relationship that is nearly independent of transport and depends primarily on the neutral penetration length [5, 60].

Stacey [10, 62] has theoretically investigated the extent to which the structure and other features of the edge density pedestal can be accounted for by (1) the requirements of plasma ion particle and momentum balance and (2) the penetration of recycling neutrals. He considers only steady-state balance equations, so his investigation is only

applicable in between ELMs. The results from his investigation was a first principles model for the self-consistent calculation of the edge density pedestal structure–radial profiles of plasma ion and neutral densities, radial electric field, poloidal and toroidal velocities, radial pinch velocity, and related quantities in the plasma edge of Tokamaks all of which had varying degrees of dependence on the neutral particles in the edge region [62].

It is very clear from these studies that the transport of neutral particles in the plasma edge is very important for the overall performance of the plasma. And, as varied as the effects of neutrals on the plasma edge, so are the methods by which they are studied. While the primary focus of this paper utilizes but one of these methods, it is important to list some of the other methods used.

1.3 Methods of Solving the Neutral Particle Transport Equation

One of the first methods used to study neutral particles was the spherical harmonics method (or P_n method) which can be traced back to 1926 [63]. The P_n approximation is the theoretical basis for the diffusion equation [64]. Utilizing the P_n method to find a solution to the one-dimensional transport equation can be done as follows. If ψ, the neutral flux distribution, is defined as $\psi = nv$ and μ as the cosine of the angle made by the velocity vector v of the neutral particle and the x-axis; then the one-dimensional and time independent Boltzmann equation can be written as [65]:

$$\mu \frac{\partial \psi(x,\mu,E)}{\partial x} + \Sigma_t(x,E)\ \psi(x,\mu,E) = S(x,\mu,E) \quad + \\ \tfrac{1}{2}\int_0^\infty dE' \int_{-1}^{1} d\mu'\, \Sigma_s(x:\mu',E' \to \mu,E) \tag{16}$$

The basic concept of the P_n method is to write the unknown $\psi(x, \mu, E)$ as an expansion of a finite number of known functions of angle. The most convenient expansion functions are the Legendre Polynomials, because the integration over μ ranges from 1 to -1. Using the Legendre Polynomials, we can rewrite $\psi(x, \mu, E)$ as [65]:

$$\psi(x,\mu,E) = \sum_{n=0}^{N} \left(\tfrac{2n+1}{2}\right)\ \psi_n(x,E)\ P_n(\mu) \tag{17}$$

Since the scattering term (i.e., Σ_s (x:μ' , $E' \rightarrow \mu$, E) usually depends only on the scattering angle, this term can be written as:

$$\Sigma_s(x,\mu_0,E' \rightarrow E) = \sum_{n=0}^{N} \left(\tfrac{2n+1}{2}\right)\ \Sigma_{sl}(x,E' \rightarrow E)\ P_l(\mu_0) \tag{18}$$

where $\mu_0 = \cos\theta = \mu' \cdot \mu$ represents the scattering angle.

Now these expressions can be placed in the original transport equation, then multiplied by Legendre polynomials of various orders, namely, P_l, l = 1, 2, ...N, and integrated over the angular variable. At this point the orthogonality, recurrence relations, and additive properties of the spherical harmonics [63-71] can be used to obtain the expressions [65]:

$$\frac{d\psi_1(x,E)}{dx} + \Sigma_t(x,E)\ \psi_0(x,E) = S(x,E) + \int_0^{\infty} dE'\, \Sigma_{s0}(x : E' \rightarrow E) \tag{19}$$

for l = 0, and

$$\frac{(l+1)}{(2l+1)}\frac{\partial \psi_{l+1}}{\partial x} + \frac{l}{(2l+1)}\frac{\partial \psi_{l-1}}{\partial x}\Sigma_t(x,E)\ \psi_l(x,E) = \int_0^{\infty} dE'\, \Sigma_{sl}(x,E' \rightarrow E)\ \psi_l(x,E') \tag{20}$$

for l = 1, 2, 3, ...

The angular components of the differential scattering cross section are defined as

$$\Sigma_{sl}\left(x, E' \rightarrow E\right) = \int_{-1}^{1} d\mu_0 \; \Sigma_s\left(x, E' \rightarrow E, \mu_0\right) \; P_l\left(\mu_0\right) \tag{21}$$

The boundary conditions, which cannot be imposed exactly due to previous approximations, can still be approximated by Marshak-type boundary conditions. For instance a vacuum condition, which otherwise can be represented as ψ(a, μ, E) = 0, can be represented as

$$\sum_{n=0}^{N}\left(\tfrac{2n+1}{2}\right) \; \psi_l\left(a, E\right) \int_0^1 P_l\left(\mu\right) \; P_n\left(\mu\right) \; d\mu = 0 \tag{22}$$

for l = 1, 3, ... N. Similar expressions can be found for reflective, incident flux, and other boundary conditions [65].

In order to force closure of the equations, and thus obtain the P_n approximation, the last term ψ_{N+1} is dropped and what is left is a set of N + 1 coupled integrodifferential equations in space and energy. These equations can be solved numerically by approximating the spatial derivatives with finite difference schemes, and the energy dependence can be implemented with multigroup techniques [65].

While the P_n approximation is very useful and has been extended to 2 and 3 dimensions, it is very difficult to model complex geometries such as a Tokamak plasma. The same can be said for the discrete ordinates method (S_n method), which generally more preferable when dealing with higher dimensions [65].

The S_n method had its origin in radiation transport calculations in stellar atmospheres [65]. Since then, the method has evolved and is primarily used in reactor analysis calculations where the diffusion theory has proved to be inadequate [64]. It has become the dominant method for obtaining numerical solutions to the integrodifferential form of the transport equation. The S_n method consists of evaluating the angular

distribution of the neutral flux at discrete angular directions or ordinates. This is the prime characteristic that differentiates this method from the spherical harmonics method, in which the angular variable is treated as continuous. In theory, the solution of the transport equation can be found to a high degree of accuracy by taking enough discrete ordinates; however, in practice it is very complicated. The method requires careful tracking in order to preserve particles; however, the method can lead to computer algorithms of high efficiency [64].

In the most general case, the total angular dependence of ψ(r, μ, E) is eliminated by taking a discrete number of directions, i.e., μ_v (n = 1, 2, 3,..., N) where $\mu_v = i\mu_{xn} + j\mu_{yn} + k\mu_{zn}$ where *i, j, k* represent the unit vectors in the x, y, and z direction. Therefore, the unknown function becomes ψ(r, μ_n,E). In this way the integral over μ is now represented by a summation

$$\int_{-1}^{1} d\mu\, \psi(r, \mu', E') \cong \sum_{n=1}^{N} w_n\ \psi(r, \mu, E) \tag{23}$$

where the w_n are quadrature weights for the particular numerical integration scheme used to handle the angular integrals. Since the values of the μ_{in} are not unique, the main factors that determine the choice of directions are the physical insights of the problem and the experience. For the one-dimensional and the time independent transport equation, this treatment leads to

$$\mu_{xn}\frac{\partial\psi(x,\mu_n,E)}{\partial x}+\Sigma_t(x,E)\ \psi(x,\mu_n,E)=S(x,\mu_n,E)+\frac{1}{2}\sum_{n'=1}^{N}\int_0^{\infty}dE'\ w_n\ \Sigma_s(x,\mu_{n'}\rightarrow\mu_n,E'\rightarrow E)\ \psi(x,\mu_{n'},E') \tag{24}$$

This forms a set of N-coupled differential equations which, with the corresponding boundary conditions, can be solved by replacing the energy variable with a sum over a finite number of energy groups, and by making use of finite difference approximations to approximate the spatial derivatives. Implementation of the method is rather long and involved; however, the N-coupled differential equations can be solved on almost any computer.

The selection of the quadrature weights, w_n, and of the directions cosines, μ_n, are important when assessing the accuracy of the solutions of these equations. It is customary to obey the following requirements when selecting these quantities [66]:

1. w_n must always be positive. This requirement arises from the intrinsic nature of the integral term in Boltzman transport equation. Simply put, its value is always positive.
2. Since particle flow is equally important in both positive and negative directions, then it is the norm to make a symmetric choice of quadrature weights and of directions about $\mu = 0$. Thus $\mu_n = -\mu_{N+1-n}$ and $w_n = w_{N+1-n}$

If N is even, then at a reflective boundary, (e.g. at x = 0, $\psi_n(0) = \psi_{N+1-n}(0)$ for n = 1, 2, ... N/2) and at a vacuum boundary (e.g. at x = a, $\psi_n(a) = 0$, for n = N/2 + 1, N/2 + 2, ... N). Therefore, an even value for N will automatically provide the correct number of boundary conditions for the set of N-coupled differential equations. If N is odd then the

direction cosine, μ = 0, would be perpendicular to the x axis, which implies that the derivative term vanishes.

It is important to note that the P_n and S_n methods can be fairly accurate, but they require that the mesh spacing be smaller than the mean free path. Additionally, they are not well suited for treating regions with long mean free paths [65]. As will be shown later in this study, both of these conditions are prevalent in close proximately to one another near the private flux and divertor regions of a Tokamak.

Quite different from the discrete ordinates and spherical harmonics technique, the integral transport method is based on integrating out the angular dependence of the transport equations rather than discretizing the angular dependence. The angular variable can in principle be treated with perfect accuracy by eliminating the angular dependence. The level of accuracy is essentially determined by the methods used to numerically evaluate the expressions resulting from the angular integration [64]. One such method implies the transport equation can be integrated making use of an integrating factor

$$\frac{\partial\left(\psi\, e^{\int_0^l \Sigma_t\, dl}\right)}{\partial l} = e^{\int_0^l \Sigma_t\, dl}\ \overline{S}\left(x, E, \mu\right) \tag{25}$$

where *S* represents the scattering term and the external source term. Integration leads to

$$\psi\left(l, E, \mu\right) = \int_0^l dl'\, e^{-\int_{l'}^{l} \Sigma_t\, dl}\ \overline{S}\left(l', E, \mu\right) \quad + \quad e^{-\int_0^l \Sigma_t\, dl} \psi\left(0, E, \mu\right) \tag{26}$$

From this point on the solution is an iterative procedure such that

$$\psi = \sum_{n=1}^{\infty} \psi_n\left(l, E, \mu\right) \tag{27}$$

where

$$\psi_n(l,E,\mu) = \int_0^l dl' \; e^{-\int_{l'}^{l} \Sigma_t \, dl} \; \overline{S}(l',E,\mu) + S_{sc}(\psi_{n-1}) \tag{28}$$

in which S_{sc}, the secondary source, is the n-1 iteration solution.

In practice, particles of a given source going in a particular direction are exponentially attenuated as the integral of the inverse mean free path along the direction of flight. This implies that for a fixed source, the solution to the flux distribution is simply dependent on the geometry of the problem. However, if one of the processes by which the neutrals are attenuated (such as recombination) gives rise to another neutral with a different energy and direction, the process is in itself a secondary neutral source which is uniquely distributed in space [65].

This means the solution must be obtained via an iterative process. This process can be very time-consuming because couplings exist among all spatial points. In order to speed up the iteration process, it has become customary to solve for the flux distribution of fixed sources and to neglect all secondary sources. This procedure is good in just a few cases, in particular when the ionization rate is greater than the charge-exchange rate. The method becomes impractical for complex geometries and when the rate of processes that result in secondary sources becomes large (such as charge exchange near the wall and divertor plates) [64-66, 69, 72]. Despite this limitation, the integral transport method has been applied in the edge region of fusion plasmas for simple one-dimensional problems [73].

In order to circumvent the short comings of the Pn, Sn, and integral transport methods, the standard method used to study neutral particles in the plasma edge today is the Monte Carlo method. Monte Carlo methods are essentially the brute force simulations

in which large numbers of particle histories created by a random number generator and tracked. In each history created, random numbers are used to sample probability distributions for energy, angles, path lengths, reactions, etc. The overall accuracy of the Monte Carlo method is ultimately determined by the accuracy of the reaction rates used in the simulation and the number of particles tracked [65]. The great advantage of Monte Carlo simulation is that they can model nearly any geometry with a great deal of accuracy. The greatest draw back to Monte Carlo techniques though is that they can require great amounts of computational time in order to decrease the statistical errors inherent to the method. Variance reduction schemes can be utilized to decrease the amount of computational time and increase accuracy. Monte Carlo techniques are considered by some to be computationally expensive and also have the disadvantage of being prone to statistical noise.

In an attempt to solve the transport equation for complicated geometries in a computationally efficient manner devoid of statistical noise, the Transmission/Escape Probability (TEP) formulation of integral transport theory was developed by extending the interface-current balance method used in fission reaction calculations [64, 65, 68, 72, 74]. The TEP method is based on the balancing of particle fluxes/currents across surfaces and internal sources. It has the advantages of being computationally efficient, ability to model complex geometries, as well as function in regions with both long and short mean free paths. For the analysis that follows, the TEP method is the principle method used in the Georgia Tech Neutrals Code which is the primary tool used in the analysis presented at end of this work. A more in depth look into the formulation of the TEP method used in the Georgia Tech Neutrals Code will be presented in a chapter 3 of this thesis.

2. TEXTOR Experiment and Motivation

In the introduction, we briefly covered many instances (both computational and theoretical) in which the plasma edge was influenced by neutral particles. In this chapter we will be discussing a series of experiments that are in large part a direct motivation for the topic of this dissertation. In March of 2006, a rotation scan analysis was performed for the author of this work on the Tokamak TEXTOR in order to determine if plasma rotation influenced the MARFE density limit. This chapter discusses what TEXTOR is, the relevant diagnostics used in the experiment, the motivation for the experiment, the experimental setup, and the analysis of the results.

2.1 Overview of TEXTOR and Diagnostic Used in Analysis

The Tokamak Experiment for Technology Oriented Research (TEXTOR) is a Tokamak located in Juelich, Germany that is optimized for studying plasma wall interaction. TEXTOR is a medium size toroidal pumped limiter Tokamak belonging to the class of moderate field but large volume (approximately 7 cubic meters) devices having a circular cross section of the plasma and an iron core. The plasma major radius is 1.75 m and the minor radius is 0.47 m [75].

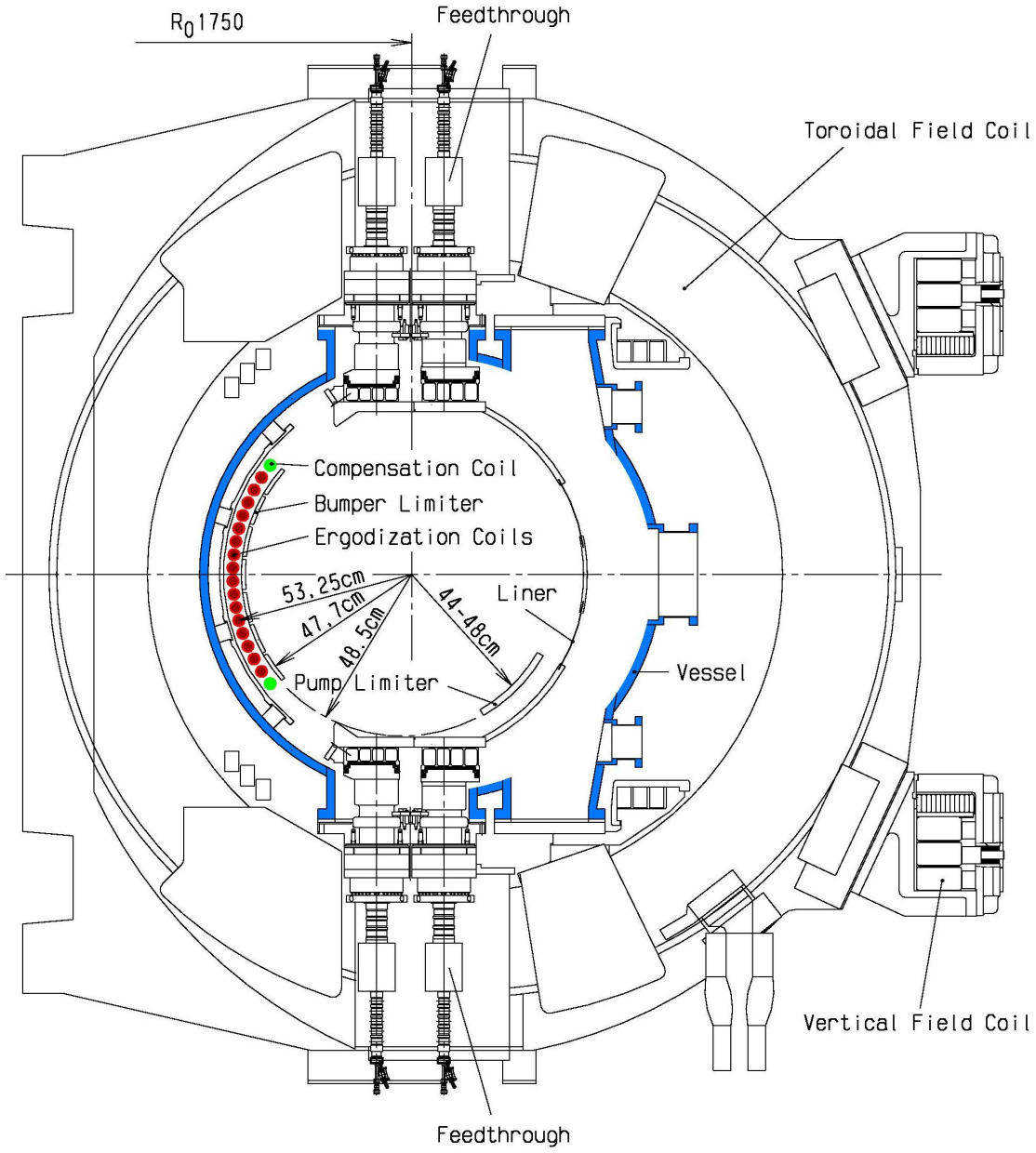

Figure 4: TEXTOR CROSS SECTION

TEXTOR can have a maximum plasma current of 0.8 MA, and its 16 toroidal field coils can provide a maximum magnetic field of 3 Tesla. It has had a sustained pulse length of 10 s with optimal cooling conditions. TEXTOR is fed directly from the 110 kV grid using an installed converter power of about 300 MVA. The inner wall of TEXTOR is equipped with several specially shaped limiters being partly remotely movable.

TEXTOR has several auxiliary heating systems. The neutral beam injection (NBI) system can provide up to 3 MWs. There are two beam lines that can each supply up to 1.5 MWs of power. The two beams are injected into the system in different ways. The co- beam is directed in the same direction as the plasma current. The other beam (ctr-) is injected against direction of the plasma current as illustrated in the figure below. The beam direction is very important to the analysis presented later in this chapter.

In addition to NBI, TEXTOR can also be heated by ion cyclotron resonance plasma heating (ICRH). There are two ICRH antennas that can supply up to 4 MWs of power. TEXTOR can also be heated with electron cyclotron resonance plasma heating (ECRH). The contributions to plasma heating via the ECRH are limited to about 0.8 MWs. In total, TEXTOR is capable of being heated by approximately 9 MW of auxiliary power.

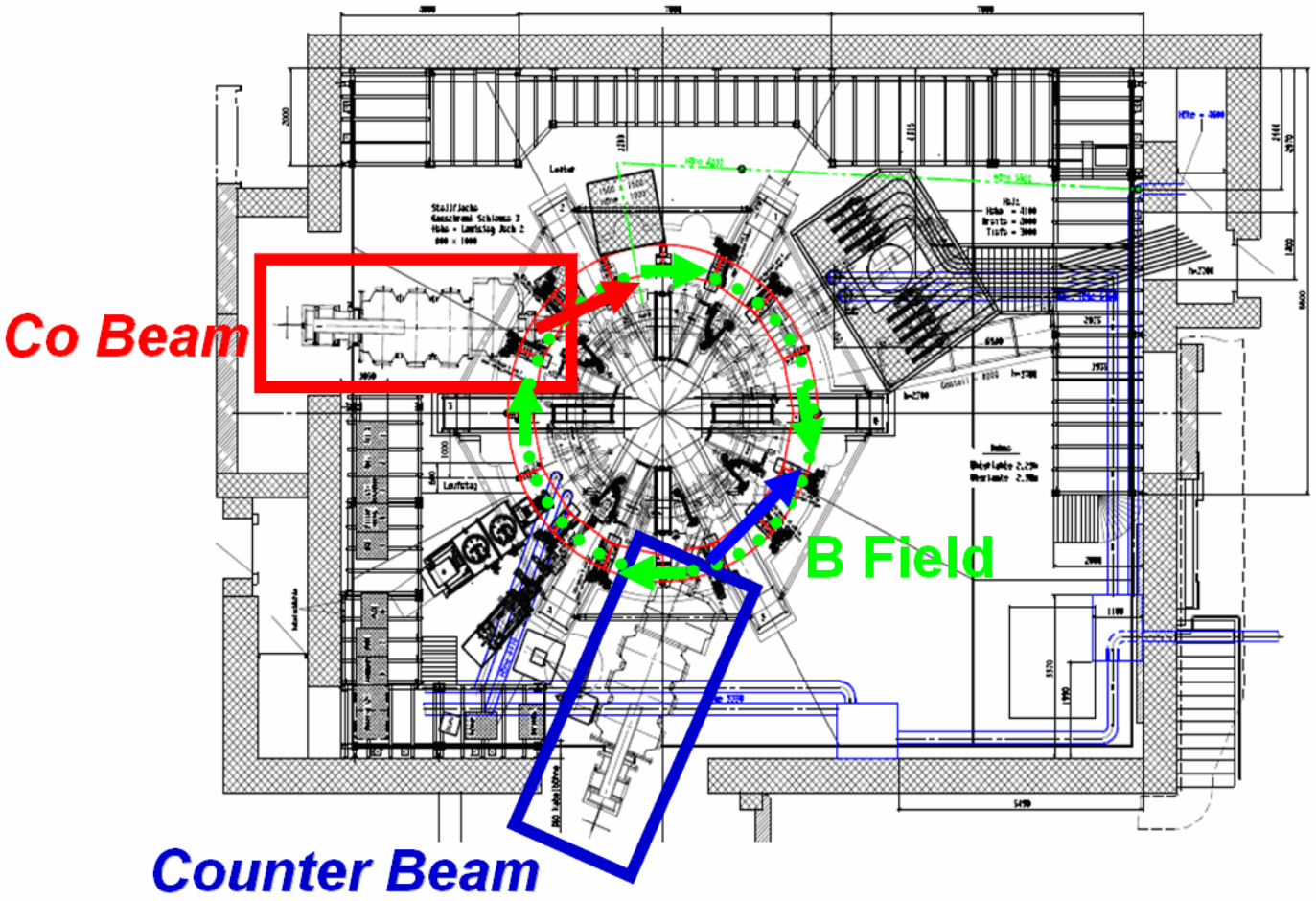

Figure 5: Top View of Neutral Beam Heating System in TEXTOR

One of the most unique features of TEXTOR is the Dynamic Ergodic Divertor (DED). The DED is a novel flexible tool used to influence transport parameters at the plasma edge and to study the resulting effects on heat exhaust, edge cooling, impurity screening, plasma confinement and stability [75].

The main component of the DED is a set of magnetic perturbation coils whose purpose is to ergodize the magnetic field structure in the plasma edge region. These coils are located inside the vacuum vessel at the high field side of the torus. The set consists of 16 individual coils (4 quadruples) plus two compensation coils. The compensation coils above and below the proper DED coils are required because the coils do not have the most symmetric feeding every 22.5° but every 90°. The compensation coils prevent a vertical force from acting on the plasma. The individual perturbation coils follow the direction of the equilibrium magnetic field of the plasma edge (i.e. helically) [76].

Using the DED, a resonant effect of the external perturbation field is obtained on the edge plasma at a pre-selected radius. The inputs and outputs of the individual windings from the DED are fed through the vacuum vessel to the outside where they are connected in different ways to the power supplies. There are three primary modes of operation. The figure below depicts these. In each mode, the DED can be operated either in dc or in ac with frequencies of up to 10 kHz. In the ac-operation, the neighboring sets of coils have a phase difference of 90◦. In dc-operation, the maximum perturbation is obtained and reached if two neighboring sets of coils have the full current in one direction and the next set in the opposite direction. We call these configurations (a) 12/4, (b) 6/2 and (c) 3/1 base modes because the coils would form this configuration if the coils

were continued poloidally over the whole torus. Each corresponding mode configuration has been illustrated in the figure below [76].

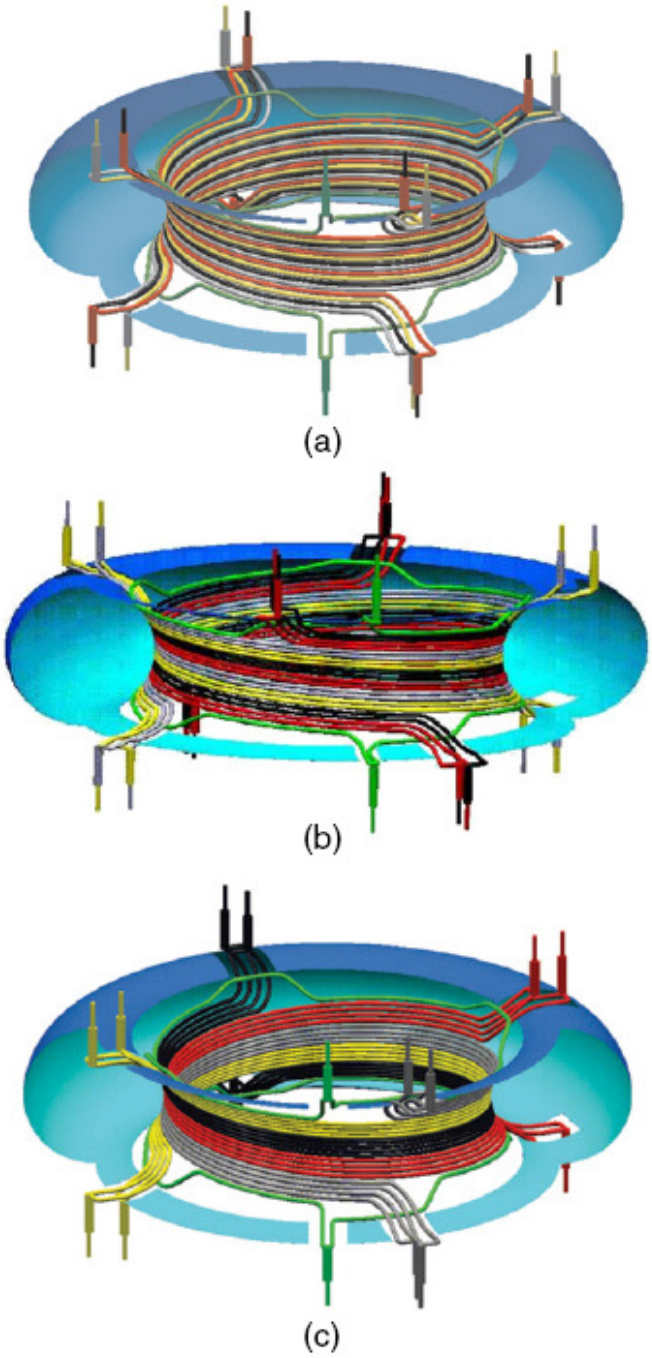

Figure 6: Electric connections for the base modes (a) m/n = 12/4, (b) 6/2 and (c) 3/1. The coils are plotted in different colors which indicate different phases in the ac-configuration of the DED. In the 12/4 base mode, neighboring coil has a different phasing while in the 3/1 base mode 4 neighbors are switched in parallel. The top and bottom coils are compensation coils which are necessary for vertical plasma stability [76].

TEXTOR is outfitted with glow discharge system. Glow discharge cleaning (GDC) has proven to be useful for both hydrogen recycling control and impurity removal. It is routinely used in many fusion devices [77]. GDC uses a direct current anode (sometimes with RF bias) inserted into the torus to produce a steady-state low-pressure 'cathode glow' discharge that covers the torus/wall surface. The GDC in TEXTOR is used for initial removal of oxygen and other volatile impurities. Helium glow cleaning decreases the hydrogen content of graphite walls by particle induced desorption processes [77]. GDC is often used between discharges that have experienced a disruption in order to decrease the amount of impurities that would be present in subsequent discharges otherwise.

TEXTOR's glow discharge system is operated at a pressure of about 10^{-3} mbar. The apparatus consists of four antennae. The output of an RF-amplifier and a positive DC voltage are applied simultaneously to these structures making them anodes in the discharge. The wall is grounded and thus cathode. The cleaning method is completed by a residual gas analysis [75].

TEXTOR is outfitted with a myriad of diagnostic tools. The most important diagnostics used in the analysis presented below are: the Hydrogen Cyanide (HCN) Interferometer used to ascertain the electron density, Electron Cyclotron Emission (ECE) diagnostic used to measure electron temperature, charge exchange spectroscopy used to measure ion velocity, filterscopes used to measure the intensity of photonic emissions from hydrogen, and the bolometer array used to measure the power being radiated from the plasma.

The HCN interferometer used in TEXTOR works the same way as most other far infrared (FIR) interferometers used to measure the electron density. A laser beam generated by a FIR laser (Hydrogen Cyanide in the case of TEXTOR) crosses the plasma column and undergoes a phase shift relative to a reference beam outside of the plasma. This phase shift $\triangle\varphi$, depends on the electron density of the plasma which amounts to

$$\Delta\varphi = r_e \lambda \int n_e dl \tag{29}$$

where r_e denotes the classical electron radius and λ the wavelength of the laser. The integral is taken along the line of sight of the laser beam. When characterizing the fusion plasma it is typical to take the line averaged density which is defined as

$$\overline{n_e} = \frac{1}{L}\int n_e dl = \frac{C}{L}\Delta\varphi \tag{30}$$

with L being the length of the intersection of the laser beam with the plasma. $C = 1/r_e\lambda$ depends only on the wavelength of the laser. The phase shift $\Delta\varphi$, is determined by superposing the probing wave with a reference wave whose frequency is slightly shifted and detecting the resulting intensity with a square law detector. In TEXTOR $\Delta\gamma \simeq 10khz$. Thus the output signal of the detector is a sine wave with the difference frequency $\Delta\omega$, and the plasma-induced phase shift of the probing wave is transferred to an equal phase shift of the oscillating beat signal. By comparing it with a reference signal of equal frequency but constant phase, the line integrated electron density is obtained [78]. A schematic view of TEXTOR's HCN interferometer can be seen in the figure below.

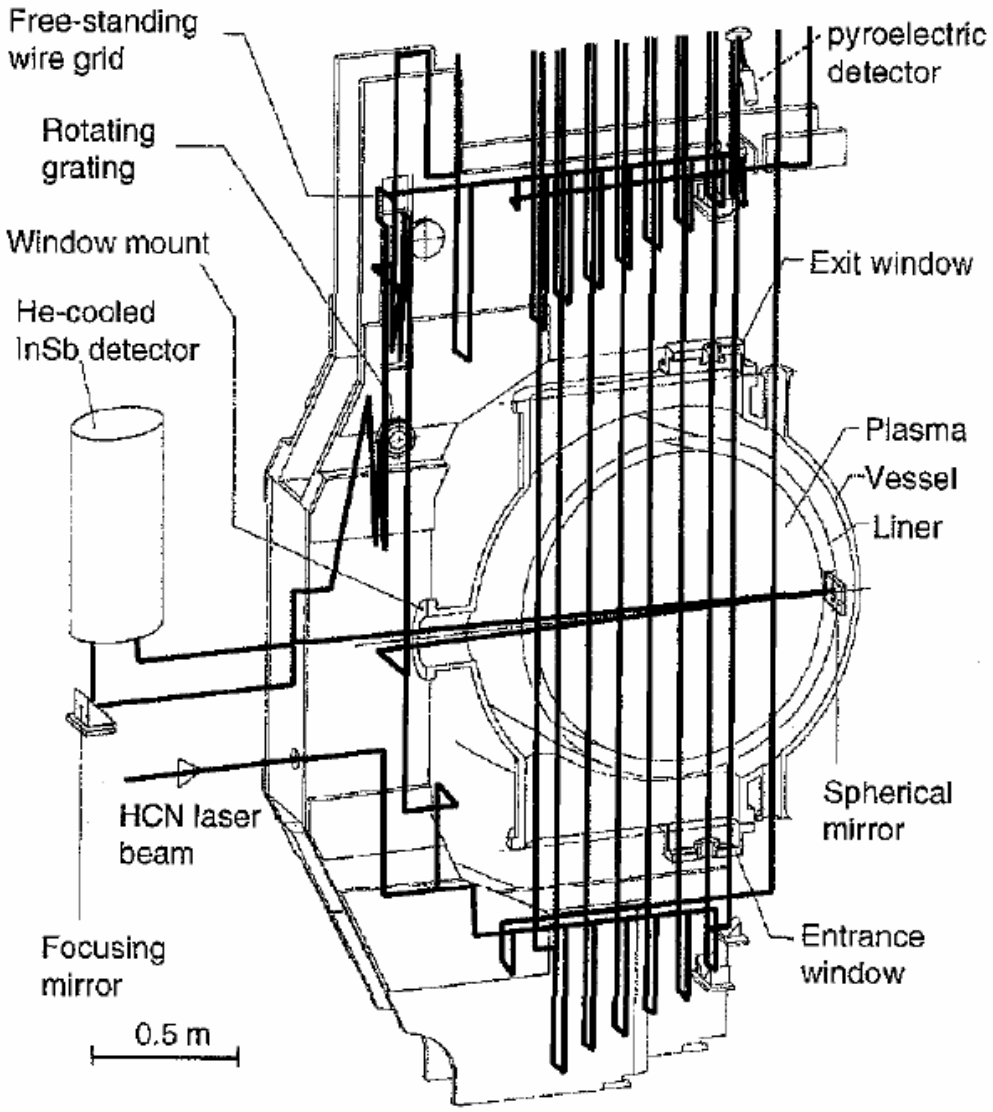

Figure 7: Schematic view of the HCN-interferometer-polarimeter. The line-integrated electron density is measured along nine vertical and one horizontal lines of sight [79].

In an external magnetic field electrons will gyrate around magnetic field lines. The gyromotion caused by the magnetic field gives rise to electron cyclotron emission (ECE) at harmonics of the electron cyclotron frequency. The emissions are proportional to the local magnetic field. If the plasma is optically thick (the electrons are sufficiently

hot and sufficiently dense), the electron cyclotron emission (ECE) is directly proportional to the electron temperature and independent of all other plasma parameters [80].

Because of the circular cross section in TEXTOR, the magnetic field decreases monotonically with radius. The emissions at a given frequency are emitted from a very specific layer of the plasma corresponding to a given magnetic field. By measuring the ECE power as a function of frequency, the electron temperature can be computed as a function of plasma radius. Typically, ECE radiometry employs a single wideband receiver to resolve multi-frequency ECE into a spatially varying temperature profile. This has been a standard diagnostic for magnetic fusion plasmas for over thirty years. These systems are generally limited to one dimensional horizontal measurement along the major radius [81].

For the set of discharges analyzed later in this dissertation, a method of establishing the total momentum input into was needed. Using charge exchange spectroscopy (CXS), we can locally measure the ion velocity distribution. From the local ion velocity distribution, the random thermal velocity (or ion temperature) and the fluid velocity may be derived. CXS works by analyzing the Doppler shift and broadening of the line-emission spectrum by ions in the plasma core. Due to the high temperature the ions in the center of the plasma are fully stripped of electrons (except for heavy impurities); hence, the line-emission from ions in the plasma core does not occur spontaneously [81].

In order to emit light, the ions must receive at least one electron, which can happen when they undergo a charge exchange reaction. Typically, when neutral atoms (via Neutral Beam Injection) are shot into the plasma, they will usually provide one of the

electrons with which the ions to charge exchange. The ion receives this electron in a high quantum level. It will return from its excited state to the ground state, losing its excess energy through line-emission. Throughout the charge exchange process a neutral atom loses an electron to a plasma ion [82]. The electron is most likely to be transferred to a specific, preferential quantum level of the plasma ion. The probability for electron transfer to both higher and lower levels decreases monotonically. In case of a charge exchange reaction $H^+ + C^{6+} \rightarrow H^+ + C^{5+}$ the C^{5+} level most likely to be populated is n = 4, but also for the n = 7 and n = 8 levels the chances of population are significant [83]. These quantum levels differ from the ground state, which means that a charge exchange reaction will yield a plasma ion in an excited state. It will return to the ground state through a cascade of transitions. The radiation emitted by the transitions varies over a wide wavelength range, depending on the populated states. For diagnostic use of charge exchange, especially transitions that emit visible light, are of interest. The advantage of visible light is that it can be easily collected by common optical elements and also plenty spectroscopical methods are available for the analysis of visible light [81].

In the Tokamak TEXTOR, the $n:8 \rightarrow 7$ transition of C^{5+} is used. It has a wavelength of 529 nm. This is in the visible range. The reason for analyzing the charge exchange light of an impurity like carbon instead of the charge exchange light of the bulk ions of deuterium or hydrogen is the high complexity of the hydrogen-deuterium spectrum. Usually the bulk plasma is a mixture of deuterium and hydrogen, where the charge exchange (CX) emission lines of deuterium and hydrogen overlap. Apart from CX emission, neutral deuterium and hydrogen in the plasma edge have a strong line-emission due to excitation by electrons. This emission lies in the same wavelength range as the

charge exchange emission. Finally the neutral beam species is commonly hydrogen as well, resulting in a beam spectrum on top of the charge exchange spectrum. As a result one gets a spectrum that is the sum of two charge exchange lines, electron excited emission and beam emission. The spectrum is decomposed into its components in order to regain the charge exchange line that results in large error bars on the derived quantities. A schematic representation of the CXS diagnostic used in TEXTOR can be seen below [81].

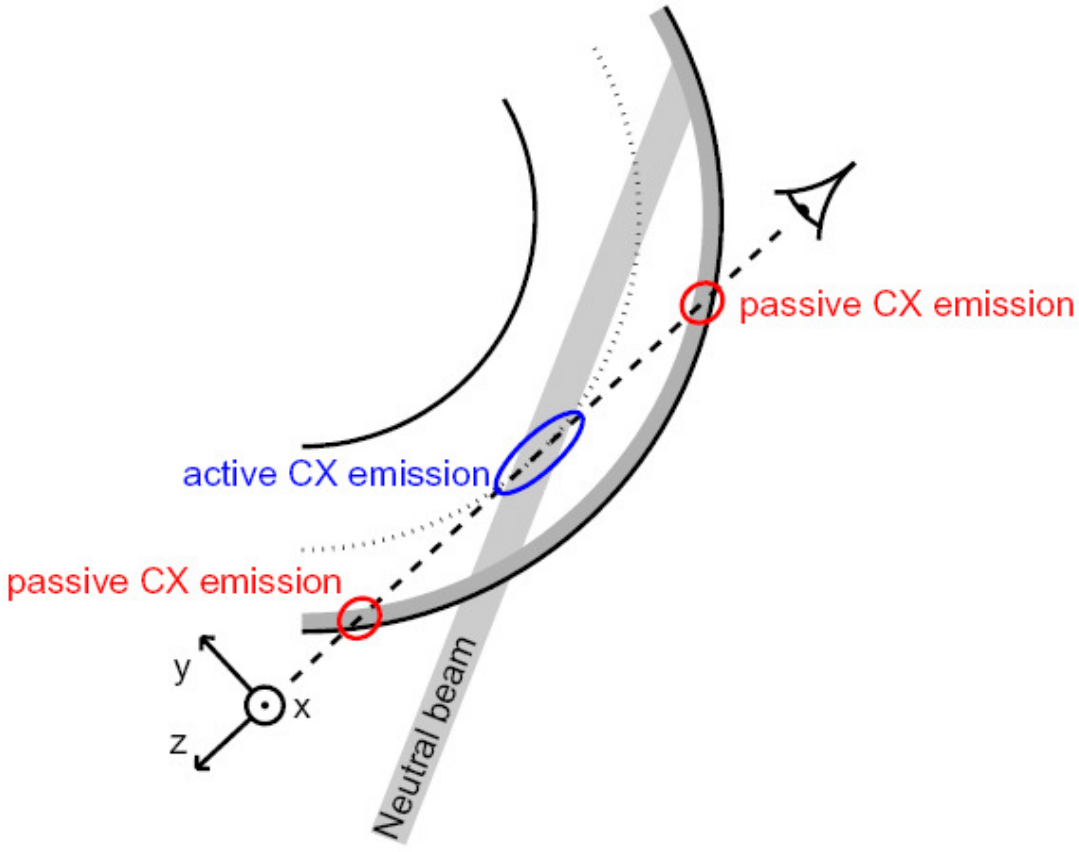

Figure 8: A top view of a Tokamak with a CX line-of-sight. The passive component of the CX spectrum is caused by neutral particles in the edge, the active CX signal is emitted where the line-of-sight crosses the neutral beam [81].

The fliterscopes in TEXTOR are an array of light sensitive diodes positioned around the walls of the vacuum chamber. As discussed previously when ions recombine with electrons, photons are emitted. Depending on what ions recombine and at what energy levels they recombine too, different wavelengths of light are emitted. Light emitted from a location such as limiter is focused through a lens to a diode as depicted in the figure below.

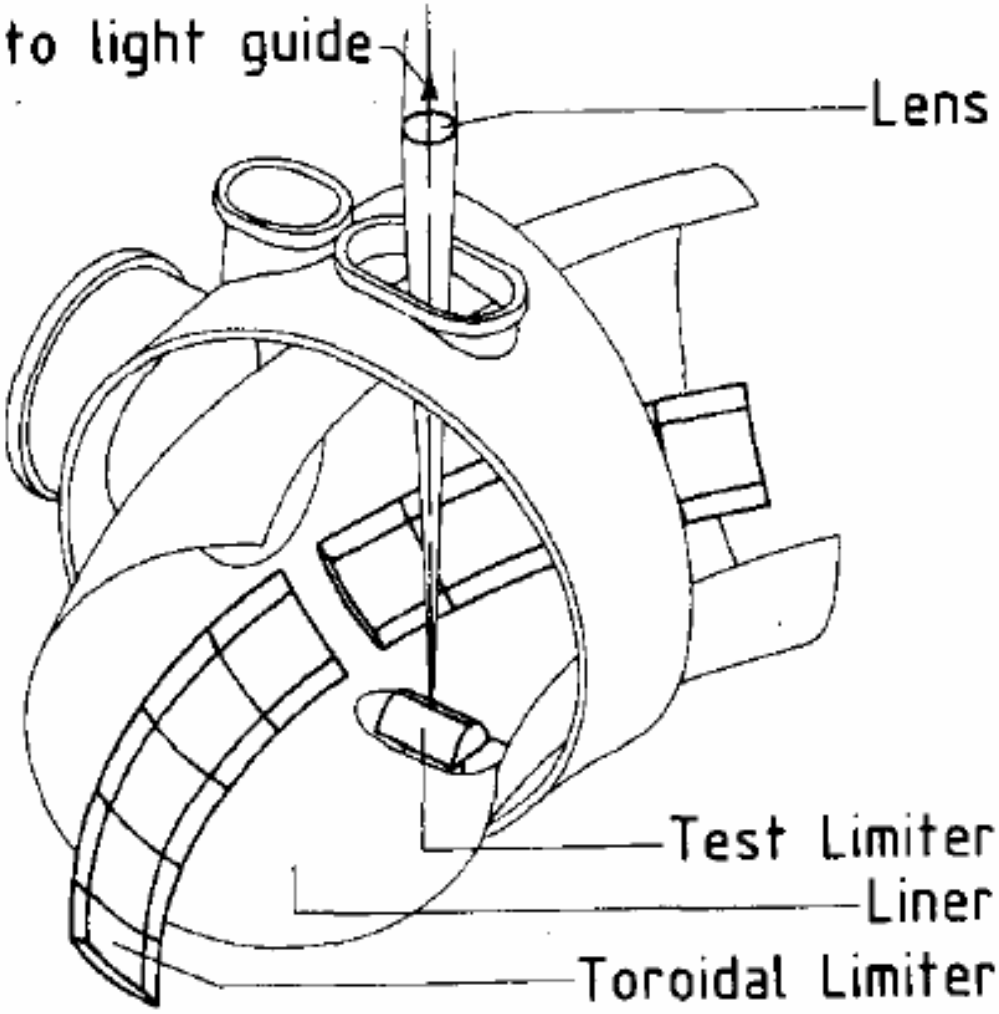

Figure 9: Experimental setup for observation of H_α.

The light being emitted by the recombination of ions is then focused through a lens to a photodiode detector. Electrical signals produced by the diode are then amplified through a circuit such as the one below, where D1 is the light sensitive diode [84].

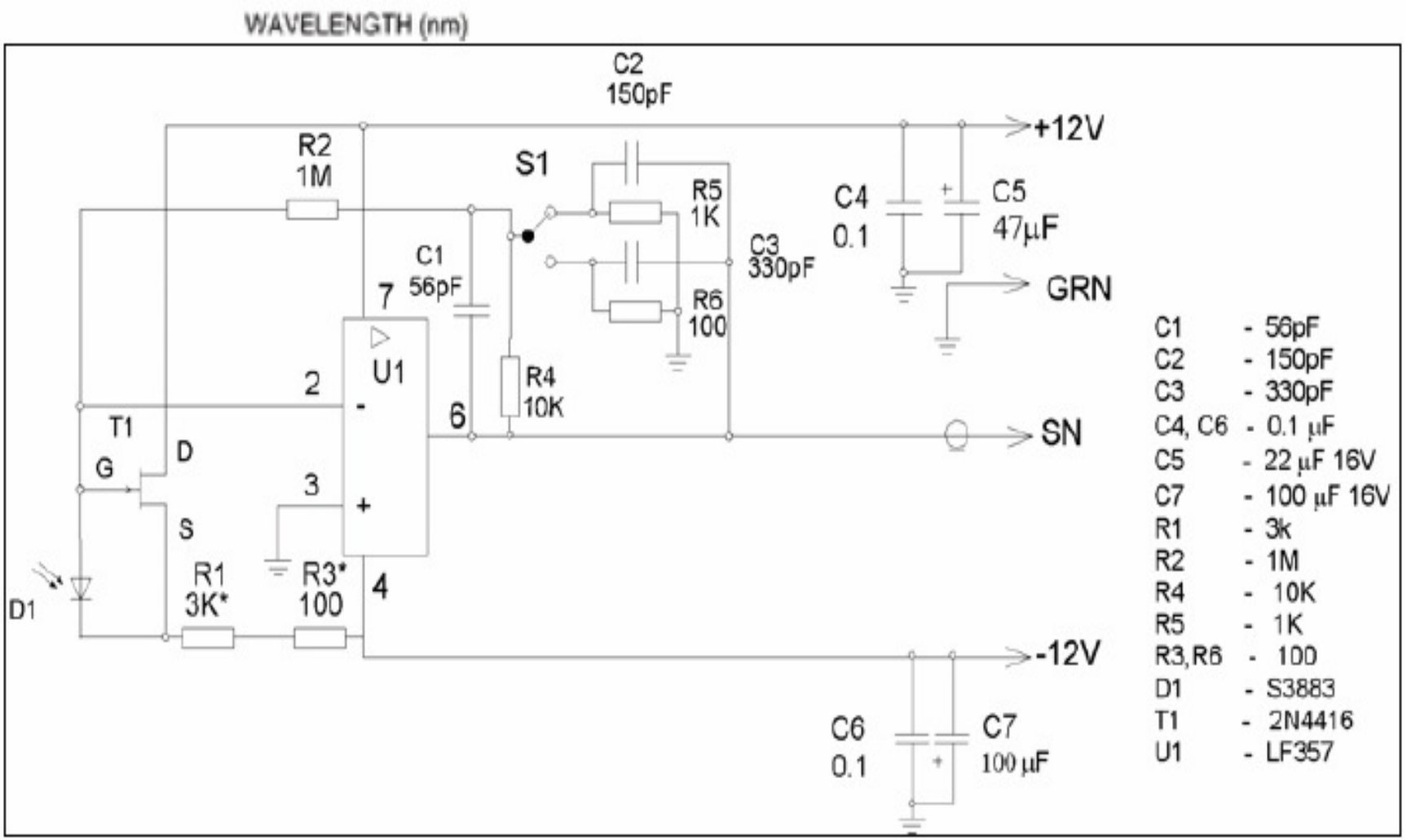

Figure 10: Schematic Filterscope

For the Hα signal, the system has a quantum efficiency of about 0.85. Its sensitivity is roughly 10^8 V/A. This means that for every 1 Volt measured by the photodiode $5.3 * 10^{10}$ photons per second are being produced in that line of sight [84].

The photodiodes are sensitive to a number of wavelengths that emerge from the recombination spectrum of hydrogen, carbon, and other atoms that might be present in the line of sight. The table below shows which spectrum lines certain diode arrays are sensitive to and the corresponding element. The designations LIMV, LIMW, and LIMZ correspond to the line of sight at different positions. The different positions will be discussed later in this chapter as they pertain to the analysis.

Table 3: Filterscope Channel

Channel	λ,nm	Δλ,nm	Element	Channel	λ,nm	Δλ,nm	Element
LIMV1	427.0	3.6	CII+CrI	LIMW1	656.2	3.6	H_α
LIMV2	844.5	5.0	OI	LIMW2	909.4	1.76	CI
LIMV3	909.4	5.0	CI	LIMW3	844.5	3.0	OI
LIMV4	412.0	1.0	BII	LIMW4	468.6	1.5	HeII
LIMV5	656.2	5.0	H_α	LIMW5	640.2	1.5	NeIII
LIMV6	514.0	1.5	CII	LIMW6	434.0	1.5	Hγ
LIMZ1	656.2	5.4	H_α	LIMW7	412.2	1.5	BII
LIMZ2	486.1	5.4	H_β	LIMW8	486.1	2.0	Hβ
LIMZ3	434.0	1.8	H_γ				
LIMZ4	426.3	1.0	CII				

Of particular importance to our analysis later in this chapter are the filterscopes located at certain positions. Looking at the image below, in our analysis we were most interested in the filterscope channels LIMZ1 and LIMW1. We also used LIMZ3 in determining the discharge at which the MARFE occurred.

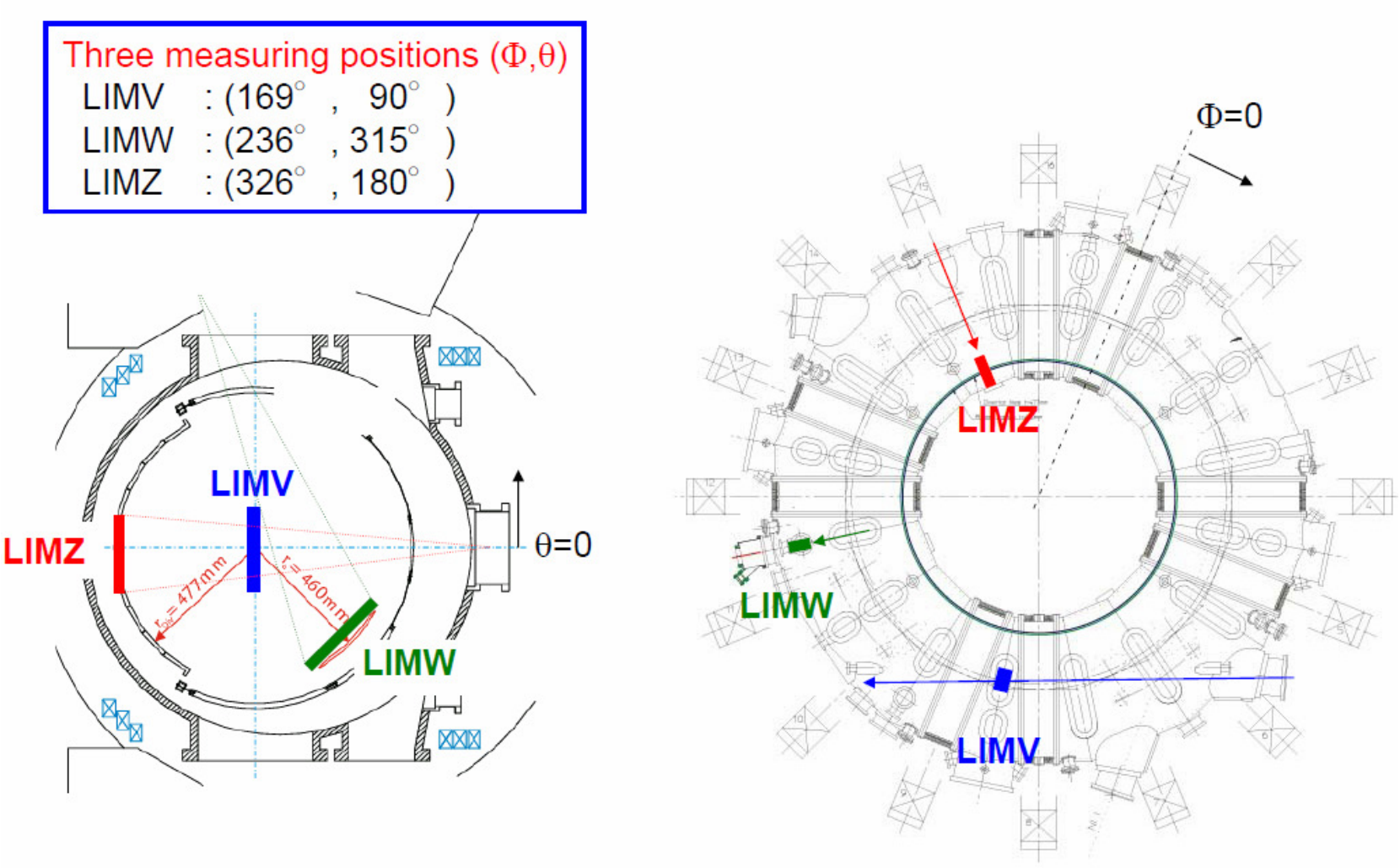

Figure 11:LIMZ1 measures the H_α signal over the HFS and LIMW1 measures the H_α signal just above the alt toroidal limiter [84]

In addition to the filterscope array, bolometers are also a useful tool for measuring incident photons on the vessel wall. Unlike the filterscope array though, bolometers are non-discriminatory in which wavelengths of light they sense. Bolometers utilize thermocouples to convert the radiant energy into electrical signals. These signals can be used to determine the total amount of energy being lost from the plasma due to radiative mechanisms [85]. The figure below shows a schematic diagram of the bolometer array in TEXTOR. Four cameras are used to measure incident heat fluxes on 36 surface locations. Computational models can be used to create a 2D representation of the heat being lost due to radiation.

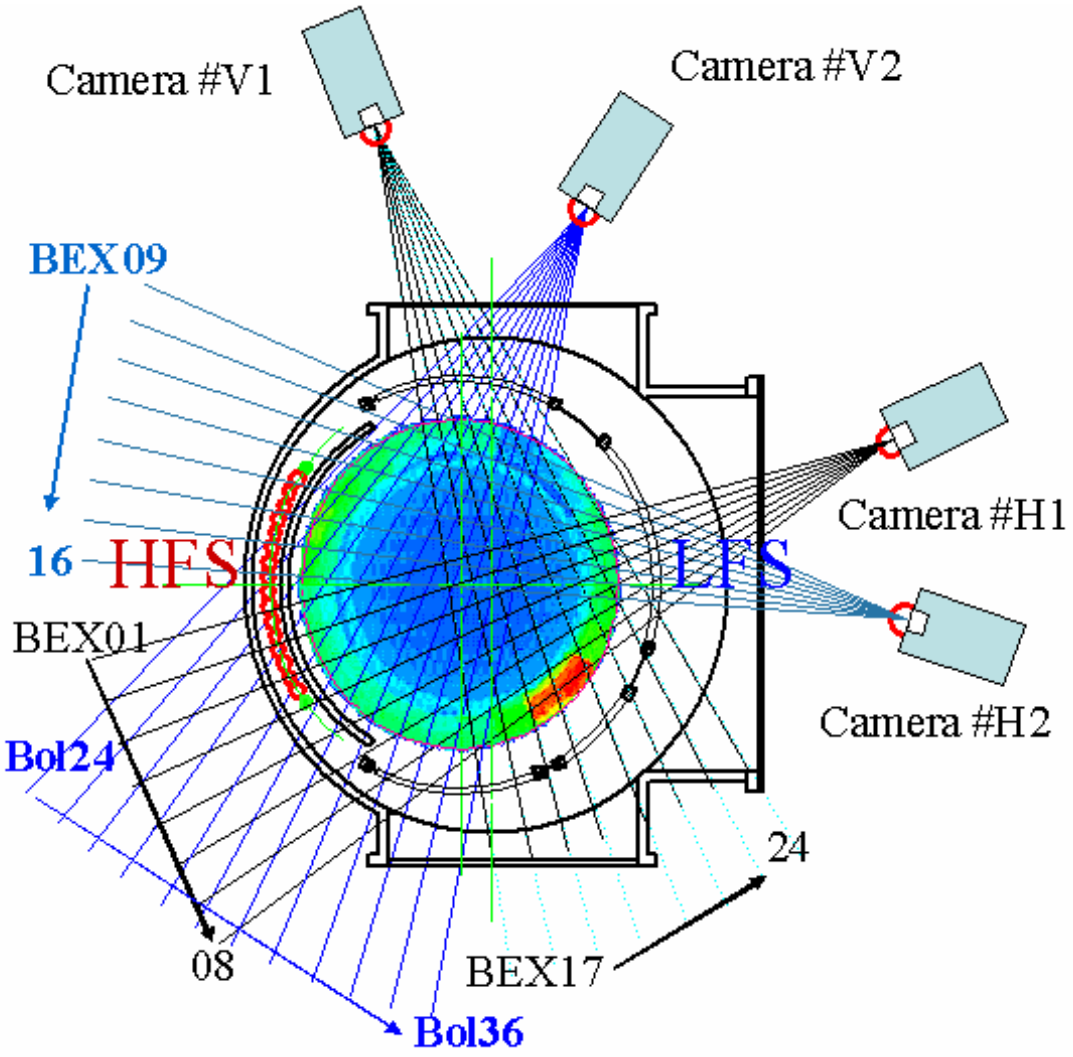

Figure 12: Bolometer Chords in TEXTOR [49]

The bolometer arrays are often very useful in tracking radiative phenomena, such as MARFEs. Two dimensional representations of the radiant power profiles can be compiled from data provided by the bolometers. The results from one of these analyses is shown later in this chapter.

2.2 Introduction and Motivation for TEXTOR Experiments

In a series of density limit discharges on TEXTOR, it was shown that the Greenwald number (as seen in Eq. 11) varies with auxiliary heating power by $P^{0.44}$ as illustrated in Fig. 13 [59]. However, in the same illustration, the edge density limit seems to plateau towards the upper heating levels.

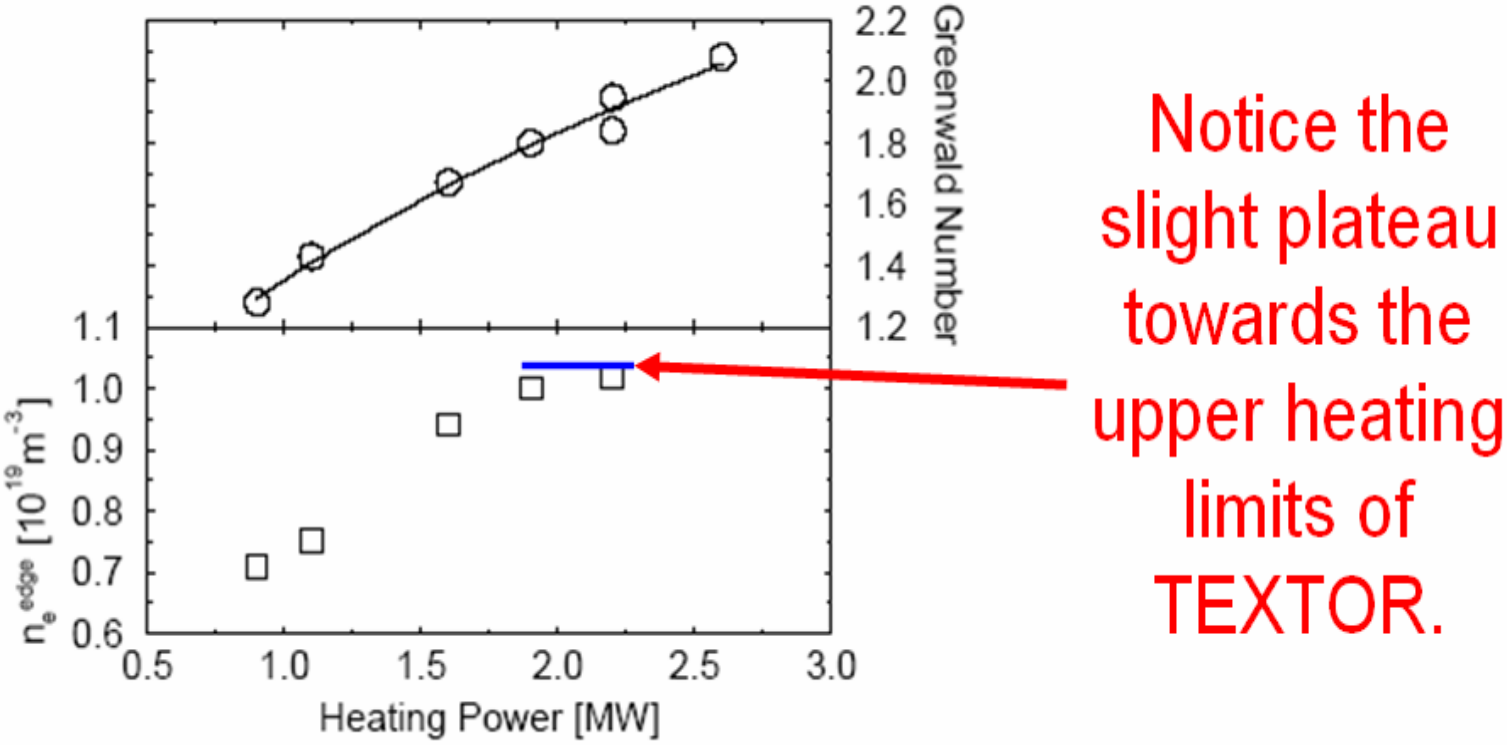

Figure 13: Dependence of Greenwald number on the heating power. The regression yields $P^{0.44}$. Dependence of the edge electron density (a + 1 cm) on the heating power (I_p = 230 kA) [49].

In order to reach the power levels used in the experiment in Fig. 13, both co- and counter- neutral beam injections must be used in nearly equal parts. When the beam powers were balanced towards the upper heating limits of the device, the total momentum input should have been reduced. This would in-turn decrease the poloidal velocity in the edge [49].

From a different set of experiments, it has also been shown that the poloidal flow in the edge induced by the Dynamic Ergotic Divertor (DED) could "smooth" the distribution of the neutral particle recycle. The "smoothing" of the neutral particle flux helped to extend the MARFE density limit [48]. To test whether flow might have an effect on the MARFE density limit, a series of Rotation Scan Density Limit discharges has been carried out on the Tokamak TEXTOR [49]. The reason these experiments could be important is because the neutral beam injectors in ITER are directed into the plasma in such a way that plasma rotation should be fairly low. It is important to assess whether or not low rotation could affect the MARFE density limit. TEXTOR was an ideal machine for this particular experiment given its size and the availability of both co- and counter-neutral beam injection.

2.3 Experimental Setup

To perform the Rotation Scan Density Limit discharges, all of the main plasma parameters (I_P, B, a, etc.) where kept constant. Bt=1.9T, Ip=250kA, plasma position was kept constant, and NBI co and counter used deuterium beams with an energy of 50kV. Throughout the series, we ramped up the density starting from $2.5*10^{19}m^{-3}$ until a MARFE formed or the plasma disrupted. To determine the exact moment at which

MARFE form, a ration of the Hα to Hγ signals were taken from the filterscope array position over the High Field Side of TEXTOR. As discussed previously, these signals correspond to the amount of photons being emitted at the respective spectrum lines. The H_γ transmission line occurs are higher temperatures than the H_α line, so when there is an increase in the ratio of H_α to H_γ this means there must be a temperature drop in the line of sight. The temperature drop along this view chord is indicative of a MARFE. All density limits discussed later in this analysis are taken at a time slice just prior to when a MARFE occurred. If no MARFE formed, the density limit was taken to be the maximum density achieved prior to disruption.

Due to the frequency of high density disruption, helium glow discharges were used between each shot to clean the vessel. The total input power was maintained at 1.3 MW for each discharge varying only the method at which it was obtained in order to vary the total input momentum. The figure below shows the basic outline of the shot plan.

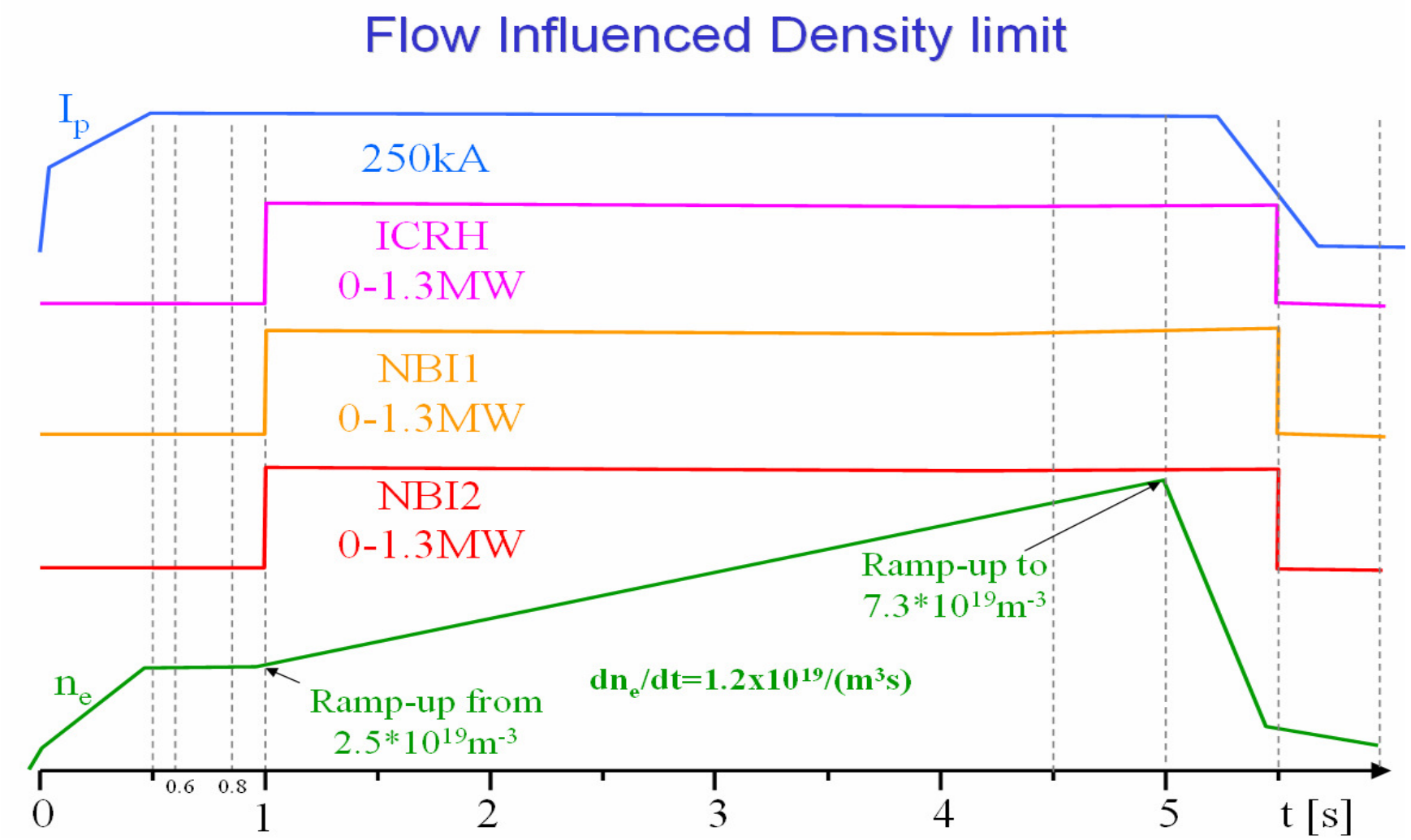

Figure 14: Schematic of Shot Plan presented to BATEX committee.

To vary the momentum input, we used two methods. In the first method, only co and counter beam were used. The shot sequence started with pure co beam injection. In the next discharge, the co beam power was decreased slightly, while the counter beam was turned on to compensate. In the third shot, the co beam was decreased again, and the counter beam increased to match the co beam. We continued this for two more discharges, ending with pure counter beam and no co beam. The table below is the actual shot plan for the rotation scan.

The second method used to vary the momentum input comprised of using a combination of co beam injection and ICRH. ICRH deposits very little momentum into the plasma, so it was thought that by keeping the total input power the same, but varying the amount of ICRH and co beam injection we could also vary the poloidal flow in the edge. The table below show the actual shot plans for the campaign. V-Target/cm in the table below corresponds to the size of the target for the neutral beam injectors and thus the amount of power being beamed into the plasma. When V-Target/cm = 40 this corresponds to 1.3 MW of neutral beam power being deposited into the plasma. Shots 1 through 9 in the table below are the actual rotation scan. Discharges 10 through 15 where part of a power scan analysis. In those discharges, we where testing the limits of TEXTOR. Fortunately, some of the data obtained from these additional discharges proved valuable for the analysis discussed in a later section.

Table 4: Shot Plan for Rotation Scan

#	ICRH(MW)	NBI1 V-Target/cm	NBI2 V-Target/cm
1	0	40	0
2	0	20.5	4.6
3	0	11.4	11.4
4	0	4.6	20.5
5	0	0	40
6	.325	20.5	0
7	.65	11.4	0
8	.975	4.6	0
9	1.3	0	0
10	0	40	11.4
11	0	40	20.5
12	0	40	40
13	.65	40	0
14	.975	40	0
15	1.3	40	0

The figure below shows the experimental measurements of the toroidal flow in the edge for both the rotation scan discharges. Shot 100179 corresponds to #1 in the table above. Discharges 100185 and 100189 correspond to #5 and #9. Both of these discharges only used counter beam injection or ICRH. The CXS system requires the co- beam injectors to function; therefore no rotation measurements exist for those two shots.

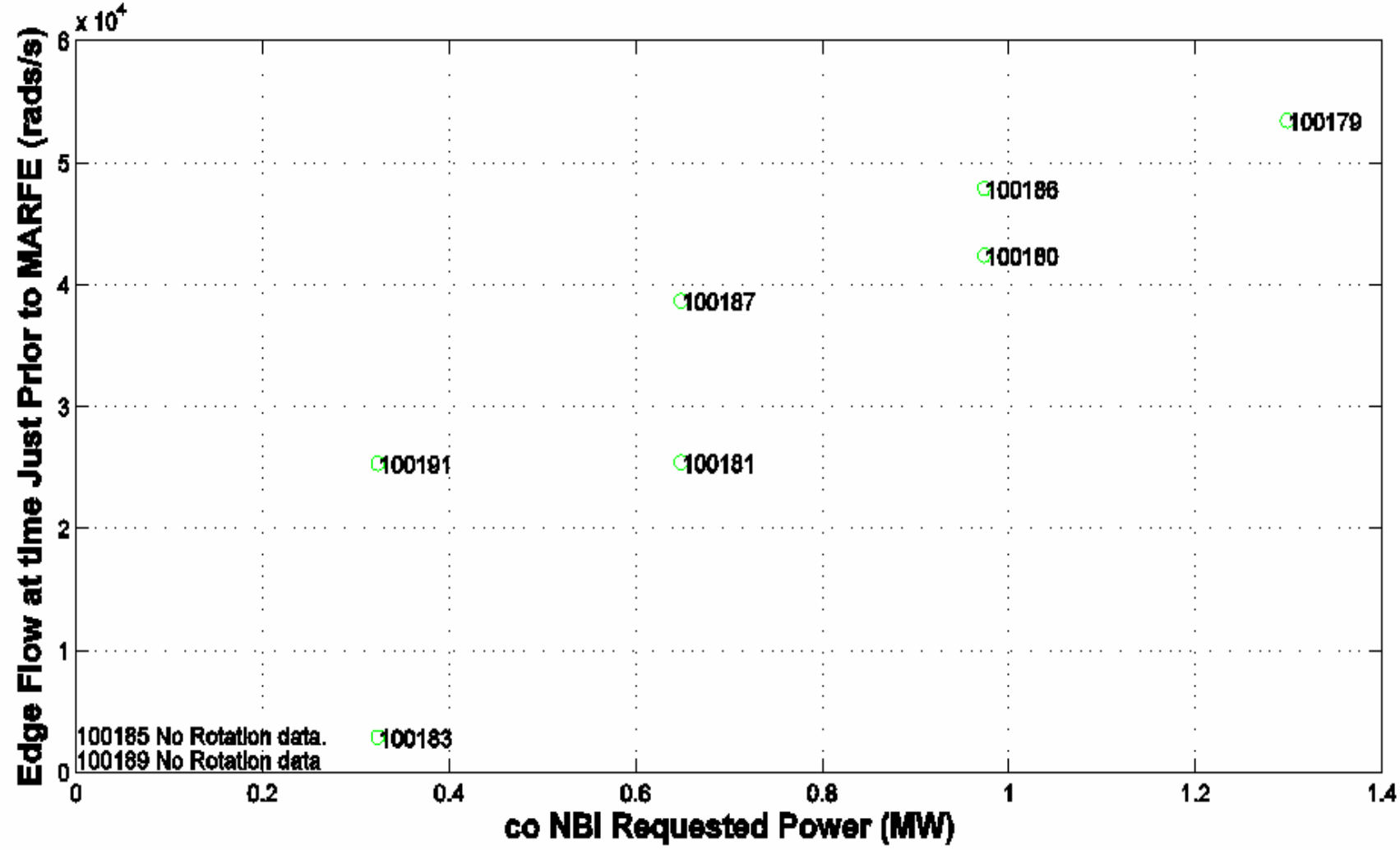

Figure 15: Toroidal Flow Measurements

As one can see, the toroidal rotation does indeed decrease as the co- beam power decreases. Since no diagnostic was available to measure the poloidal velocity, we estimate that the poloidal velocities should be approximately an order of magnitude lower than above measured toroidal velocities. To show that the discharge had roughly the same input parameters as requested, the center line electron temperature was measured at a time just prior to MARFE formation.

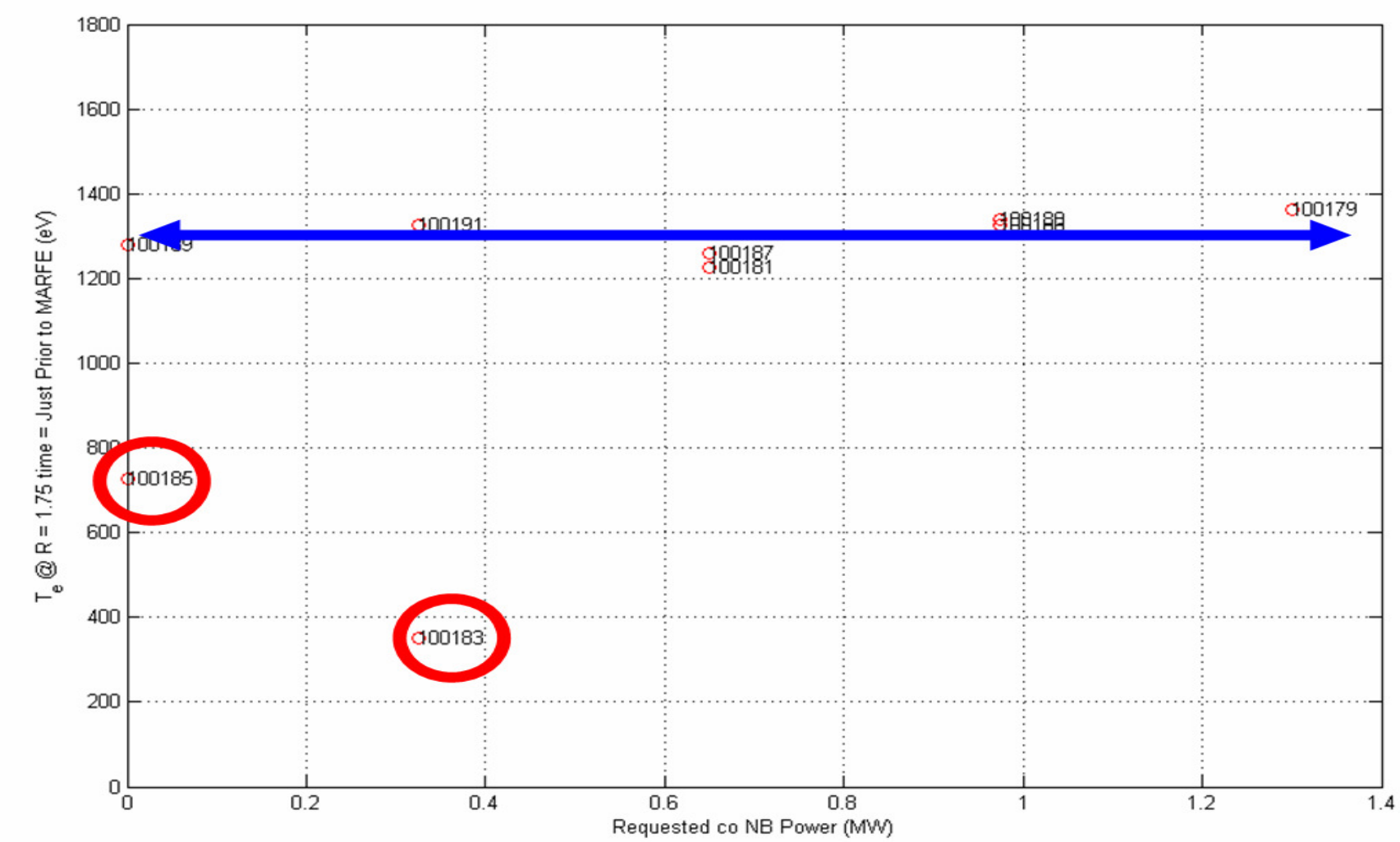

Figure 16: Centerline Electron Temperature for Rotation Scan Discharges

Shots 100185 and 100183 did not experience a MARFE prior to a disruption. Instead, the disruptions occurred early in the time progression due to the onset of the 2-1 tearing mode. The rest of the discharges had roughly the same center line electron temperature just prior to MARFE formation which indicated that the experiment was set up properly. The toroidal velocity measurements show that variation of the toroidal velocity was achieved and the center line electron temperature indicates that we heated the plasma to roughly the same temperature throughout the campaign.

Initially from the motivation for this set of experiments, it was postulated that enhanced poloidal flow in the plasma edge may "smooth" the neutral particle recycle. To see if this indeed happened for this experiment, the maximum edge density limit at the edge was recorded at a time just prior to MARFE formation. This was then compared with the ratio of the H_α line from the High Field Side (HFS) over the Low Field Side (LFS) at a time shortly after the heating scenario was set up.

The H_α signal is a measure of the amount of light coming from hydrogen undergoing an atomic transition. This signal is often proportional to the neutral particle flux in the region. A ratio of these signals from the HFS to the LFS is a "quick and dirty" way of estimating the distribution of the neutral particle flux in the edge. Because there is usually a much higher neutral particle flux just above the LFS due to the alt limiter, it is thought that an increase in the ratio illustrates a smoothing of the neutral particle flux.

2.4 Results

The comparison of the Edge Density Limit to the H_α ratios yielded some interesting results. The results do not conclusively show that the edge density is influenced by edge rotation; however, this could be due to the fact that the maximum edge velocity measured is at least an order of magnitude lower than the ion sound speed. At such low velocities, the effects of the distribution of neutrals occurring outside of the SOL would much lower than those created from ions streaming into the wall from the inside the SOL.

There are, however, significant differences in the edge density limit versus the methods of heating used. Figs. 18 are plots of the ratio of the H_α signal versus the co beam input power. Fig. 17 shows the maximum edge density versus the co beam input power.

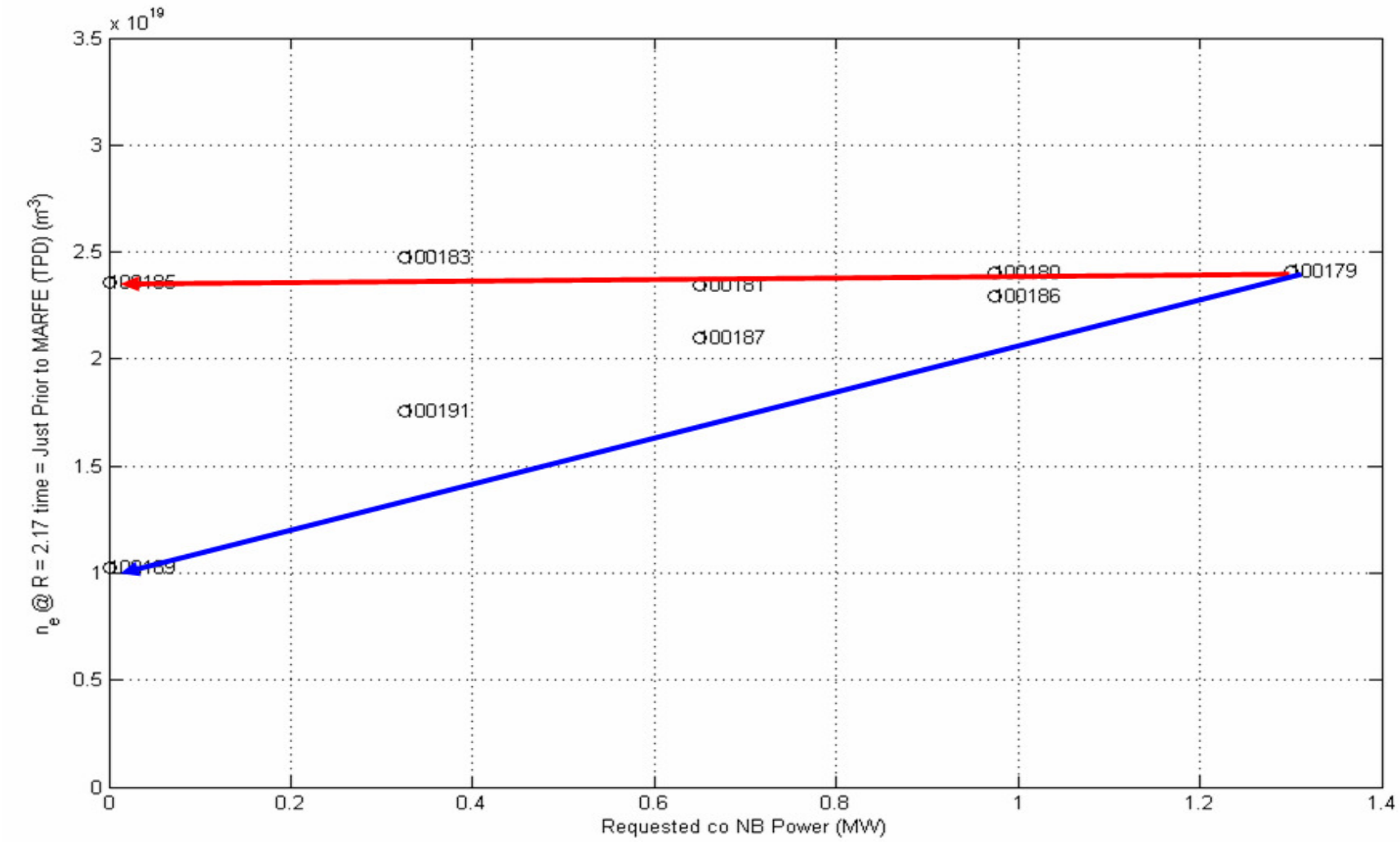

Figure 17: Maximum Edge Electron Density (m^{-3}) versus Co NBI (MW) beam power.

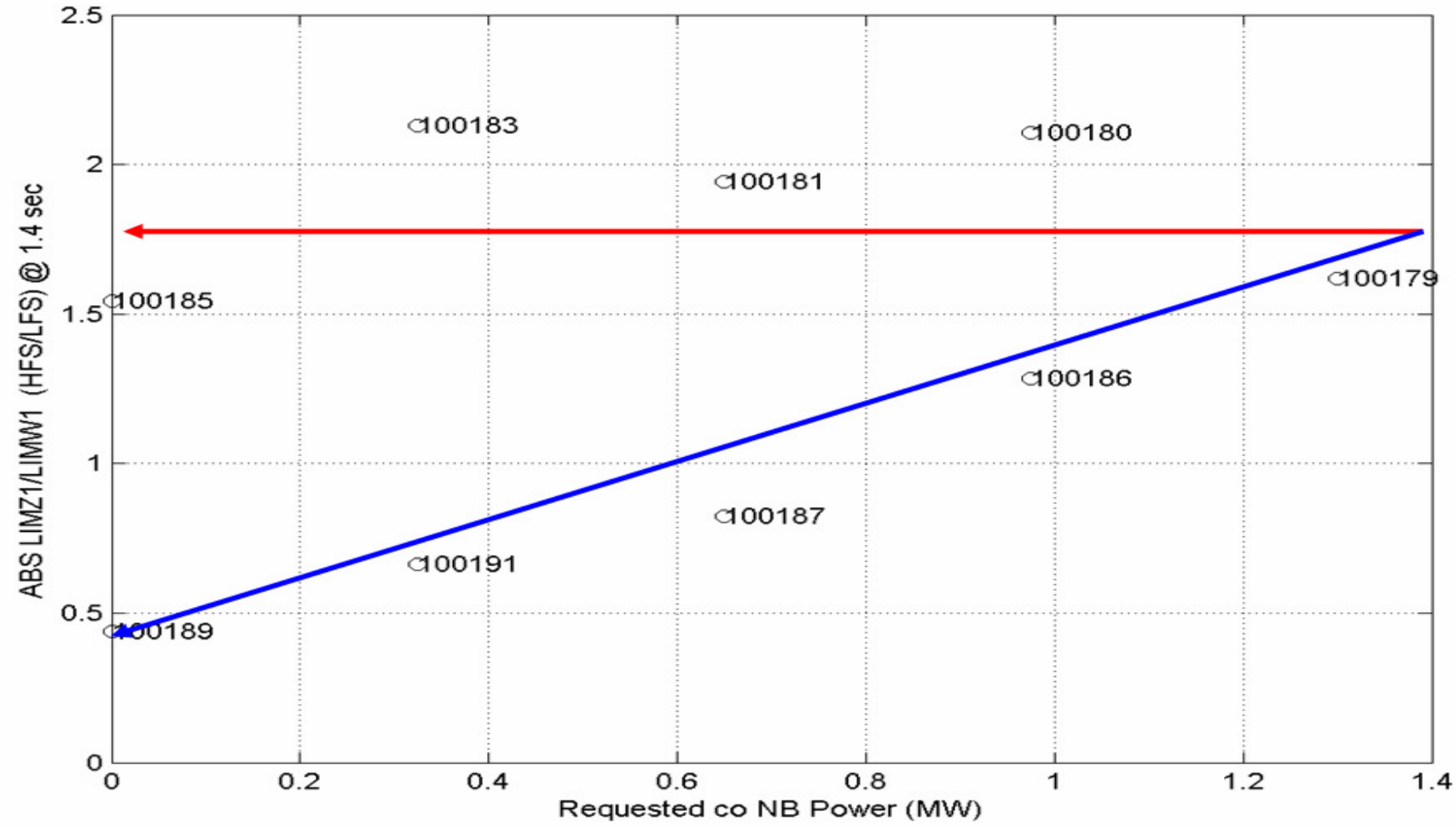

Figure 18: H_α ratio versus Co NBI Power (MW).

Surprisingly, the two plots seem to synch with one another. Discharges with the higher edge density limit had a higher ratio of the H_α signals, which would imply that the neutral particle flux in the edge may be more distributed.

A similar pattern was found later the same day in a power scan series of discharges. In Figs. 19 and 20, the main plasma parameters were the same as the rotation scan. The only difference in the discharges was that the power was increased in each discharge using several different types of heating methods. The amount of power being deposited into the system can be ascertained from table 2. Three separate trends can clearly be seen.

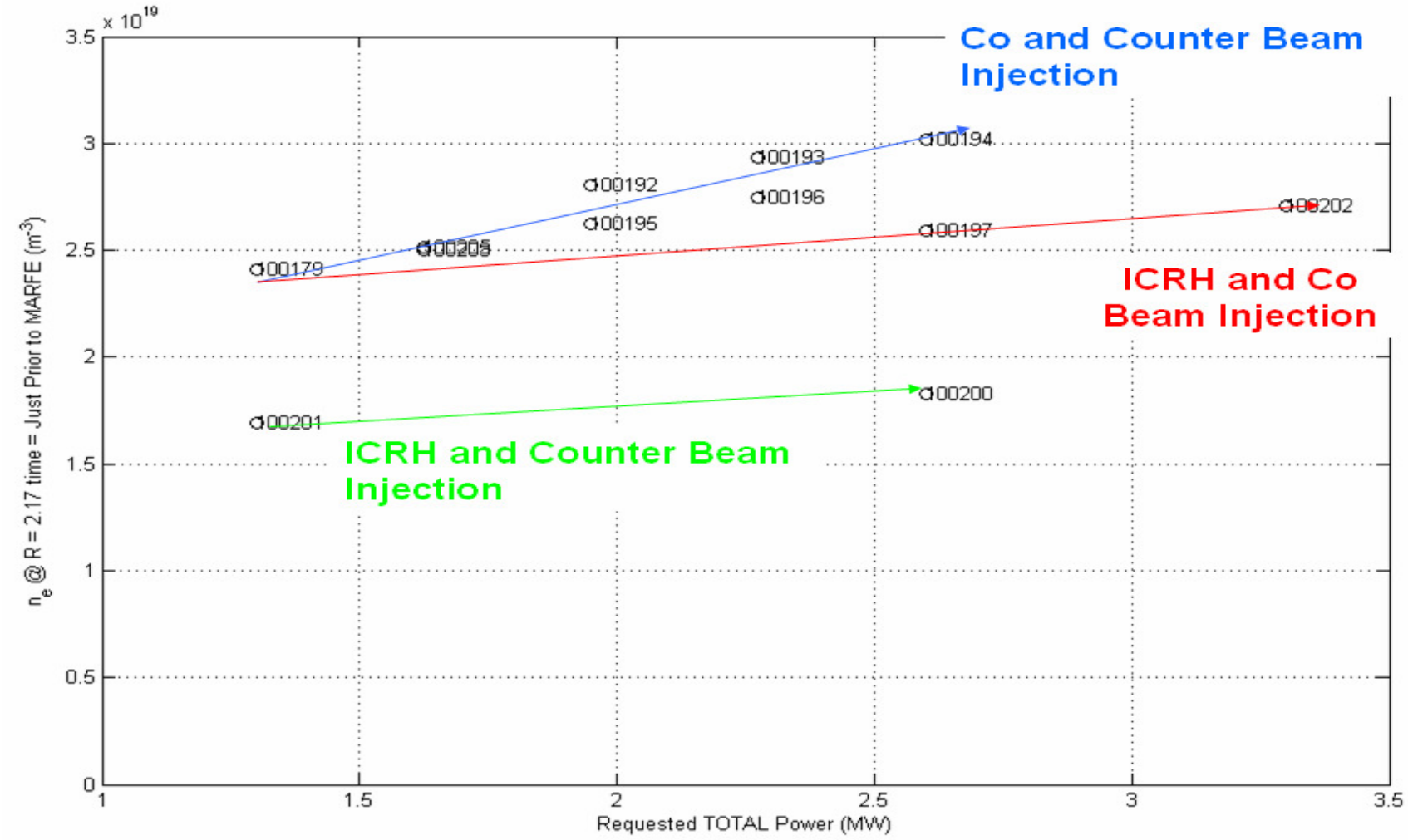

Figure 19: Maximum edge electron density (m^{-3}) versus the requested total power (MW).

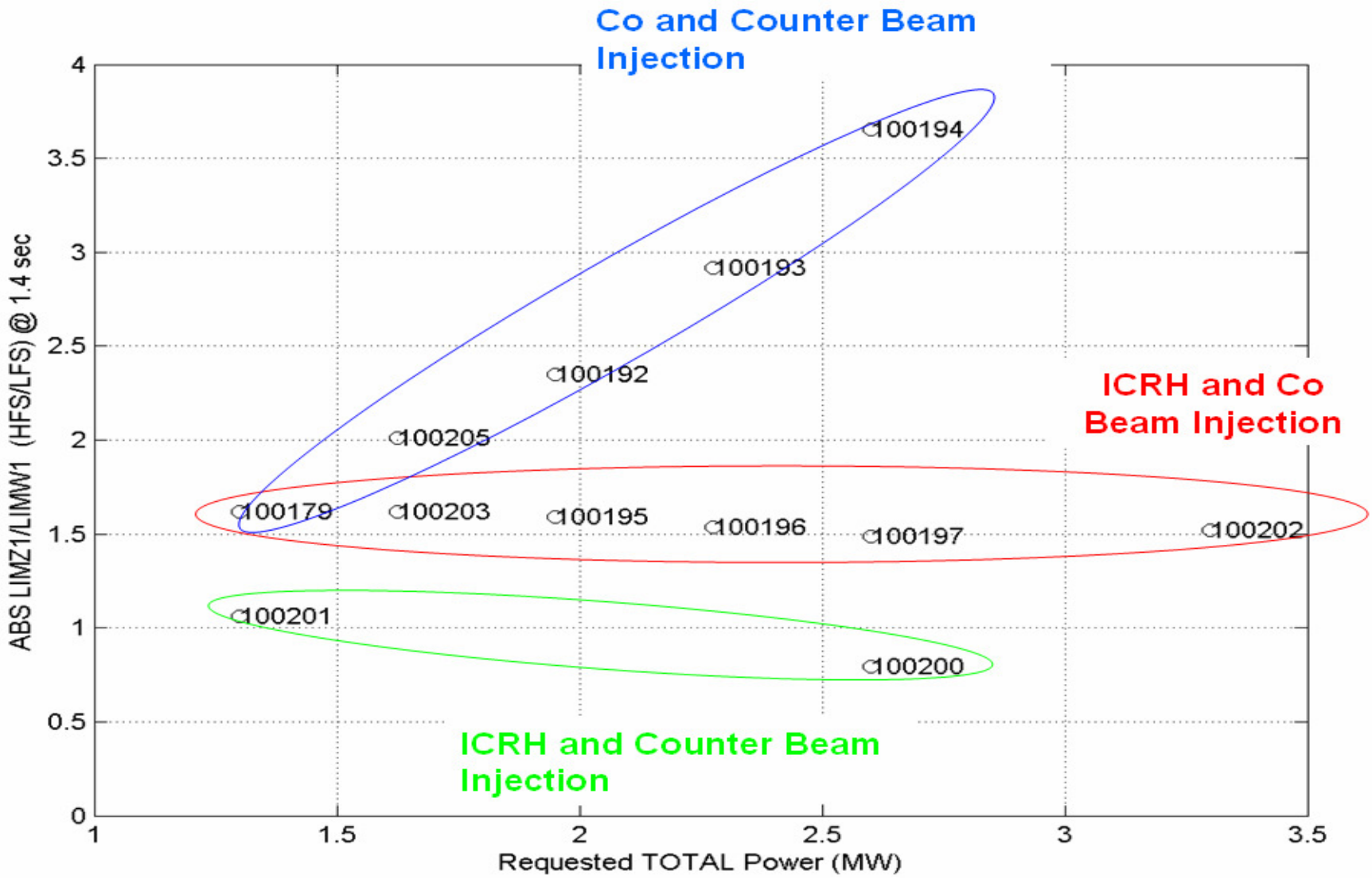

Figure 20: Ratio of the H-alpha signals versus the requested total power (MW).

Figs. 19 and 20 show results similar to the rotation scan. In predominately co- and counter- beam heated discharges, the maximum edge density is higher than discharges heated with a mixture of ICRH and co- beam injection. Figure 20 displays how the maximum edge density synchs with the ratio of the H_α signals.

In addition to the rotation and power scans, the very first shot of the discharge sequence had an additional experiment piggy backed onto it. In the power scan and rotation scan analysis, we were only interested in the actual MARFE density limit. The additional experiment dealt with control of the MARFE position. After the MARFE had occurred, neutral gas was puffed into the vacuum chamber near the top of the vessel. Once the gas was puffed in, the MARFE migrated to the top of the vessel. Using the bolometer array, a 2D representation of the radiant power profile from the plasma was compiled.

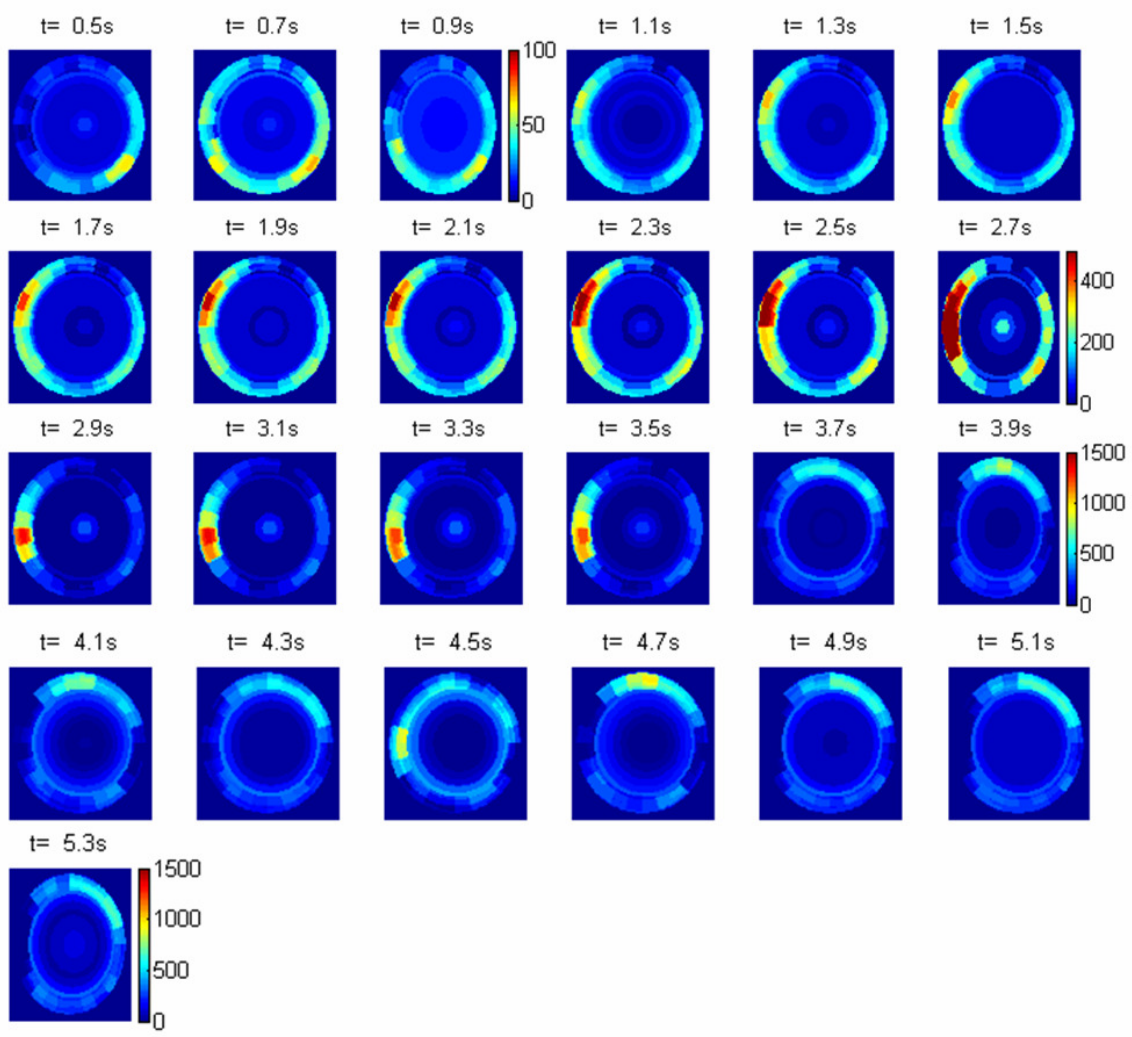

Figure 21: 2D Bolometer Liang Shot 100178 [86]

The figure shows an increase in the power being radiated on the high field side of TEXTOR at around 1.1s indicating a MARFE has started to form. The density was continuously ramped up until about 2.7s. One can see power is being radiated from the core at this time also. Using gas puffing at an alternate location near the top of the vessel, the MARFE was moved to the top of the vessel as can be seen in subsequent time slices such as 3.9 ms. Gas puffing was turned off at the top of the vessel, and the MARFE subsequently moved back to the High Field Side of the TEXTOR.

A less quantitative (but far more visually stunning) representation of this induced MARFE migration can be seen by observing a video of the D_α light. We have discussed previously that the intensity of D_α light is inversely proportional to the temperature and directly proportional to the neutral particle density. In the video below, you can clearly see a very bright "pinkish" ball of plasma (the MARFE itself) forming on the high field side (right hand middle side for the video) of TEXTOR close to the inner wall. The brightness is misleading to those unfamiliar with plasma physics. In thermonuclear physics, visually bright regions such as the one shown in the video are in fact very "cool" regions within the plasma. The very hot regions remain invisible to the naked eye. These cool regions are radiating immensely releasing their energy in the form of visible light.

As the time progresses in the discharge depicted in the video below, gas is puffed into the plasma vessel at the top of TEXTOR and the MARFE migrates to the location of the gas puffing. This is clear evidence and undisputable evidence that two dimensional effects are extremely important in MARFE dynamics.

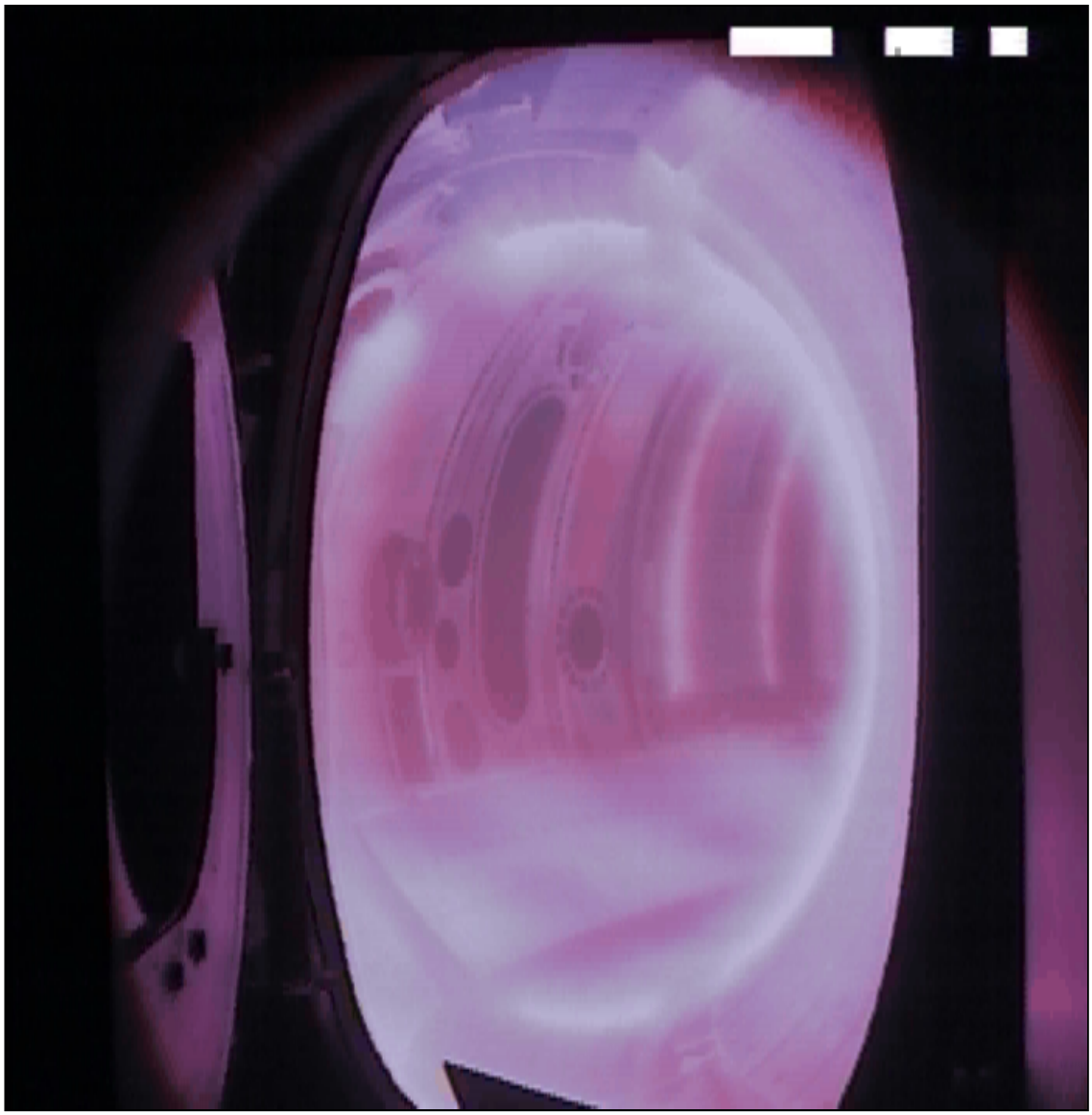

Figure 22: Video of MARFE migration in TEXTOR.

2.5 Conclusion

From the analysis, we have essentially shown that plasma rotation induced by the neutral beam injection does not significantly alter the MARFE density limit as we had thought plausible. However, the experiments did reveal there is a distinct difference in the neutral particle distributions due to the various methods of heating. The varying distribution of the neutral particles coincides with the change in the MARFE density limit. The prevailing theory for why the ICRH heated discharges have a much earlier MARFE onset is that there is some localized cooling source near the antenna. The ICRH antennas are located in positions above the alt-limiter on the low field side. If a localized cooling source were present, this could increase the amount of neutral particles and initiate conditions for MARFE onset [4, 34]. Shot 100178 somewhat backs up this possibility.

The neutrals analyses for these experiments should be done using more quantitative techniques. The ratios of the H_α signals for these discharges are useful in determining the influence of neutral particles on the MARFE density limit; however, they provide little quantitative information. A more detailed analysis of neutral particles in the plasma edge would be useful for this study. However, at this time, edge and SOL data for these sets of experiments are very sparse. Additionally, a 2D grid based off of an equilibrium fitting code is not readily available. In order to carry out a neutral particle analysis using the methods that will be outlined in later chapters, this information is necessary.

3. The GTNEUT Code

In the previous chapter, we utilized experimental data to perform an "ad hoc" neutral particle analysis for the Tokamak TEXTOR. In the following chapter, we will be performing an in depth neutral particle analysis from experiments performed on the DIII-D Tokamak in San Diego California. For this analysis, we have chosen to use the Georgia Tech Neutrals Code (GTNEUT) [87].

The GTNEUT code is based on the TEP method of solving the Boltzman transport equation. In this chapter we will outline the basic formulation of the TEP equations used in GTNEUT and discuss what upgrades have been added to the GTNEUT code. Along the way, we will discuss computational methods used to solve certain aspects of the TEP in GTNEUT. Towards the end of the chapter, we will discuss previous comparisons between GTNEUT code and Monte Carlo simulations. To begin, we should start with the derivation of the TEP equations. This originates with the integral transport equation [87].

3.1 Derivation of TEP Equations

The one-speed steady-state integral transport equation for a domain D_i with boundary ∂D_i, as shown in Fig. 23, can be written as [87]:

$$\psi(\mathbf{r},\mathbf{\Omega}) = \psi_{in}(\mathbf{r}_S,\mathbf{\Omega})\exp\left(-\tau(\mathbf{r},\mathbf{r}_S)\right) + \int_0^{R_s} dlq\left(\mathbf{r}-l\mathbf{\Omega},\mathbf{\Omega}\right)\exp\left(-\tau\left(\mathbf{r},\mathbf{r}-l\mathbf{\Omega}\right)\right) \qquad (31)$$

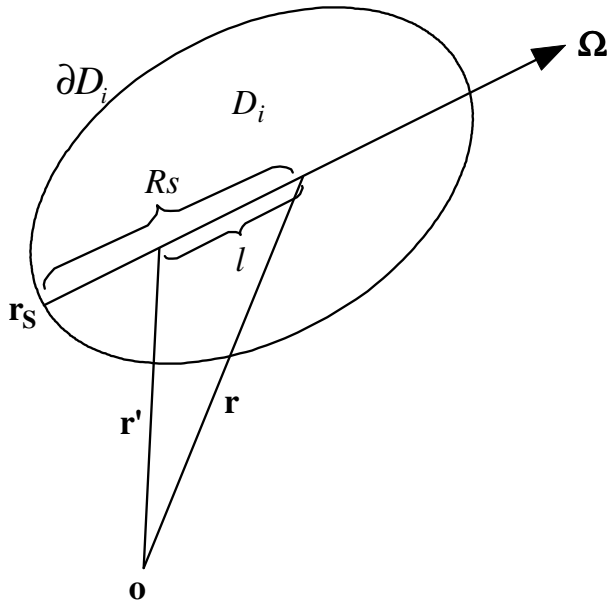

Figure 23: Schematic diagram for integral transport equation [87]

Where $\psi(\mathbf{r},\mathbf{\Omega})$ is the angular flux at point $\mathbf{r}$ in direction $\mathbf{\Omega}$ and $\mathbf{\Omega}=\frac{\mathbf{r}-\mathbf{r}_S}{|\mathbf{r}-\mathbf{r}_S|}$; $\psi_{in}(\mathbf{r}_s,\mathbf{\Omega})$ is the incoming flux at boundary; R_S is the distance between point $\mathbf{r}$ and the starting point $\mathbf{r}_S$ on the boundary and $R_S=|\mathbf{r}-\mathbf{r}_S|$; $\tau(\mathbf{r},\mathbf{r}')$ is the optical length between $\mathbf{r}$ and $\mathbf{r}'$ defined by the following equation;

$$\tau(\mathbf{r},\mathbf{r}')=\int_0^{|\mathbf{r}-\mathbf{r}'|}dl\Sigma_t\left(\mathbf{r}'+l\frac{\mathbf{r}-\mathbf{r}'}{|\mathbf{r}-\mathbf{r}'|}\right) \tag{32}$$

Here, Σ_t is the total macroscopic cross section and $q(\mathbf{r},\mathbf{\Omega})$ is the total volumetric source defined as:

$$q(\mathbf{r},\mathbf{\Omega})=\int_{4\pi}d\mathbf{\Omega}'\Sigma_{cx}(\mathbf{r},\mathbf{\Omega}'\to\mathbf{\Omega})\psi(\mathbf{r},\mathbf{\Omega}')+S_{ext}(\mathbf{r},\mathbf{\Omega}) \tag{33}$$

where $S_{ext}(\mathbf{r},\mathbf{\Omega})$ is external volumetric source and Σ_{cx} is the macroscopic charge-exchange cross section.

With isotropic sources and charge-exchange scattering, integral transport equation becomes:

$$\psi(\mathbf{r},\mathbf{\Omega}) = \psi_{in}(\mathbf{r}_S,\mathbf{\Omega})\exp\left(-\tau(\mathbf{r},\mathbf{r}_S)\right) + \int_0^{R_S} dl\,\frac{q(\mathbf{r}-l\mathbf{\Omega})}{4\pi}\exp\left(-\tau(\mathbf{r},\mathbf{r}-l\mathbf{\Omega})\right) \tag{34}$$

Integrating over $\mathbf{\Omega}$ over 4π solid angle, we obtain scalar flux $\phi(\mathbf{r})$.

$$\phi(\mathbf{r}) = \int_{D_i} d\mathbf{r}'\,\frac{q(\mathbf{r}')\exp\left(-\tau(\mathbf{r},\mathbf{r}')\right)}{4\pi|\mathbf{r}-\mathbf{r}'|^2} + \int_{\partial D_i} dS\,\psi_{in}(\mathbf{r}_S,\mathbf{\Omega})\frac{\exp\left(-\tau(\mathbf{r},\mathbf{r}_S)\right)}{|\mathbf{r}-\mathbf{r}_S|^2}(\mathbf{\Omega}\cdot\mathbf{n}_-) \tag{35}$$

Where $\mathbf{n}_-$ is the inward normal unit vector at the boundary [87].

To begin deriving the TEP equations from the integral transport equation shown above, we must start by subdividing the region of interest into convex polygons or cells. The background plasma is treated as uniform in each individual cell. From here a neutral particle balance is applied to each single. In the figure below, we consider an arbitrary cell *i* bounded by surface $\partial D_i = \sum_j \partial D_{ij}$, where ∂D_{ij} is the interface between cell *i* and adjacent cell *j*. The schematic below illustrates the neutral particle balance performed on the cell [87].

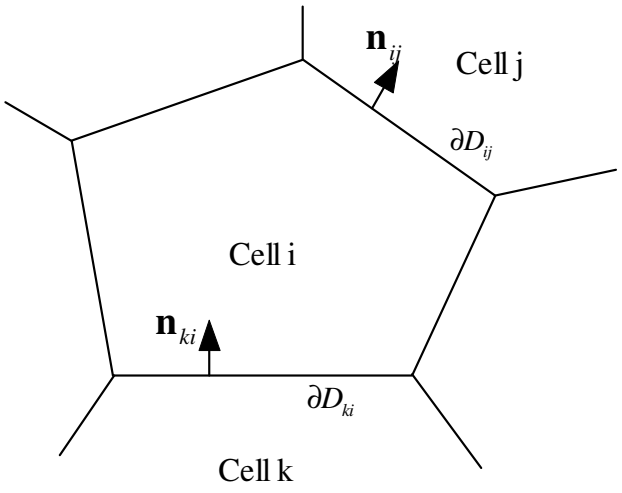

Figure 24: Schematic diagram for TEP methodology [87]

First we define the total partial current from cell *i* into adjacent cell *j*, $\Gamma_{i,j}$ as:

$$\Gamma_{i,j} = \int_{\partial D_{ij}} dS_{ij} \int_{\mathbf{\Omega}\cdot\mathbf{n}_{ij}>0} d\mathbf{\Omega}\left(\mathbf{\Omega}\cdot\mathbf{n}_{ij}\right)\psi\left(\mathbf{r}_{ij},\mathbf{\Omega}\right) \tag{36}$$

where $\mathbf{n}_{ij}$ is the outward normal (out of cell i) at interface ∂D_{ij}. It should be noted here that $\Gamma_{i,j}$ is a current, and it is a particle flow rate across the interface. It has units of particles/sec. Unfortunately, throughout the work leading up to this thesis, the term "flux" has been applied to $\Gamma_{i,j}$ by many. Keep in mind that all sources used in GTNEUT are currents or particle rates regardless of rather or not the term "flux" is used. There is NO spatial component to $\Gamma_{i,j}$.

Continuing with the derivation, we insert the integral transport equation into the equation for the total partial current and obtain [87]:

$$\begin{aligned}\Gamma_{i,j} &= \int_{\partial D_{ij}} dS_{ij} \int_{\mathbf{\Omega}\cdot\mathbf{n}_{ij}>0} d\mathbf{\Omega}\left(\mathbf{\Omega}\cdot\mathbf{n}_{ij}\right)\Big[\psi_{in}\left(\mathbf{r}_S,\mathbf{\Omega}\right)\exp\left(-\Sigma_t\left|\mathbf{r}_{ij}-\mathbf{r}_S\right|\right) \\ &\quad +\int_0^{R_S} dl\,\frac{q\left(\mathbf{r}_{ij}-l\mathbf{\Omega}\right)}{4\pi}\exp\left(-\Sigma_t l\right)\Big] \\ &= \sum_k \int_{\partial D_{ij}} dS_{ij} \int_{\partial D_{ik}} dS_{ik}\left(\mathbf{\Omega}\cdot\mathbf{n}_{ij}\right)\frac{\left(\mathbf{\Omega}\cdot\mathbf{n}_{ki}\right)}{\left|\mathbf{r}_{ij}-\mathbf{r}_{ik}\right|^2}\psi\left(\mathbf{r}_{ik},\mathbf{\Omega}\right)\exp\left(-\Sigma_t\left|\mathbf{r}_{ij}-\mathbf{r}_{ik}\right|\right) \\ &\quad + \int_{\partial D_{ij}} dS_{ij}\int_{D_i} d\mathbf{r}\,\frac{q\left(\mathbf{r}\right)}{4\pi\left|\mathbf{r}-\mathbf{r}_{ij}\right|^2}\exp\left(-\Sigma_t\left|\mathbf{r}-\mathbf{r}_{ij}\right|\right)\left(\mathbf{\Omega}\cdot\mathbf{n}_{ij}\right)\end{aligned} \tag{37}$$

This can be written in the more concise form.

$$\Gamma_{i,j} = \sum_k \Gamma_{k,i} T^i_{k,j} + Q_i P_{0,i} \Lambda_{ij} \tag{38}$$

Where we define coefficients $T^i_{k,j}$, $P_{0,i}$, Λ_{ij} and total volumetric source Q_i as:

$$T^i_{k,j} = \frac{1}{\Gamma_{k,i}} \int_{\partial D_{ij}} dS_{ij} \int_{\partial D_{ik}} dS_{ik}\left(\mathbf{\Omega}\cdot\mathbf{n}_{ij}\right)\frac{\left(\mathbf{\Omega}\cdot\mathbf{n}_{ki}\right)}{\left|\mathbf{r}_{ij}-\mathbf{r}_{ik}\right|^2}\psi\left(\mathbf{r}_{ik},\mathbf{\Omega}\right)\exp\left(-\Sigma_t\left|\mathbf{r}_{ij}-\mathbf{r}_{ik}\right|\right) \tag{39}$$

$$P_{0,i} = \frac{1}{Q_i}\int_{\partial D_i} dS_i \int_{D_i} d\mathbf{r}\,\frac{q(\mathbf{r})}{4\pi\left|\mathbf{r}-\mathbf{r}_i\right|^2}\exp\left(-\Sigma_t\left|\mathbf{r}-\mathbf{r}_i\right|\right)\left(\mathbf{\Omega}\cdot\mathbf{n}_+\right) \tag{40}$$

$$\Lambda_{ij} = \frac{1}{Q_i P_{0,i}}\int_{\partial D_{ij}} dS_{ij} \int_{D_i} d\mathbf{r}\,\frac{q(\mathbf{r})}{4\pi\left|\mathbf{r}-\mathbf{r}_i\right|^2}\exp\left(-\Sigma_t\left|\mathbf{r}-\mathbf{r}_{ij}\right|\right)\left(\mathbf{\Omega}\cdot\mathbf{n}_{ij}\right) \tag{41}$$

and

$$Q\left(\mathbf{r}\right) = \int_{D_i} d\mathbf{r} q\left(\mathbf{r}\right) \tag{42}$$

The first term in the right hand side of the concise form represents uncollided flux from all adjacent cells. The second term is contribution from volumetric sources [87].

$T_{k,j}^{i}$ is the probability that particles going from cell k to cell j through cell i will do so without making a collision. We call this the transmission probability. In order to evaluate $T_{k,j}^{i}$, we make the following assumptions: 1) the angular distribution of flux at interface ∂D_{ik} is isotropic in the inward hemisphere; 2) the spatial distribution of angular flux at interface is uniform. When we evaluate transmission probabilities for cell *k*, we again need to assume that the outward angular flux (actually it is inward direction for cell *k*) at interface ∂D_{ik} is isotropic, but it may have different magnitude from inward direction. Thus the first assumption is usually called Double P_0 or DP_0 approximation [87].

Noting that $\psi(\mathbf{r}_{ik},\mathbf{\Omega})=\psi_0$, the total incoming partial current at interface ∂D_{ik} can be written as:

$$\Gamma_{k,i}=\int_{\partial D_{ik}} dS_{ik}\int_{\mathbf{\Omega}\cdot\mathbf{n}_{ki}>0} d\mathbf{\Omega}\left(\mathbf{\Omega}\cdot\mathbf{n}_{ki}\right)\psi(\mathbf{r}_{ki},\mathbf{\Omega})=\pi\psi_0 L_{ik} \tag{43}$$

From here the transmission probability, $T_{k,j}^{i}$, may be simplified as:

$$\begin{aligned} T_{k,j}^{i} &= \frac{1}{\pi\psi_0 L_{ik}}\int_0^{L_{ik}} dx_{ik}\int_{\phi_{\min}(x_{ik})}^{\phi_{\min}(x_{ik})} d\phi\int_0^{\frac{\pi}{2}} d\theta\psi_0\left(\mathbf{\Omega}\cdot\mathbf{n}_{ki}\right)\exp\left(-\frac{\Sigma_t l\left(x_{ik},\phi\right)}{\sin\theta}\right) \\ &= \frac{2}{\pi L_{ik}}\int_0^{L_{ik}} dx_{ik}\int_{\phi_{\min}(x_{ik})}^{\phi_{\max}(x_{ik})} d\phi\cos\phi Ki_3\left(\Sigma_t l\left(x_{ik},\phi\right)\right) \end{aligned} \tag{44}$$

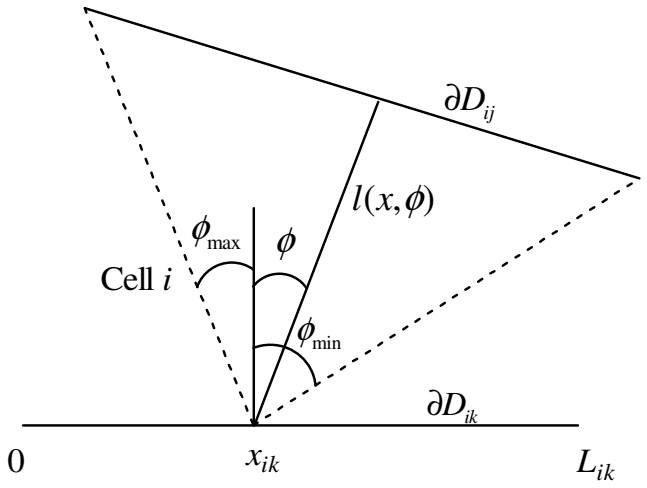

Figure 25: Geometry for calculation of transmission probability

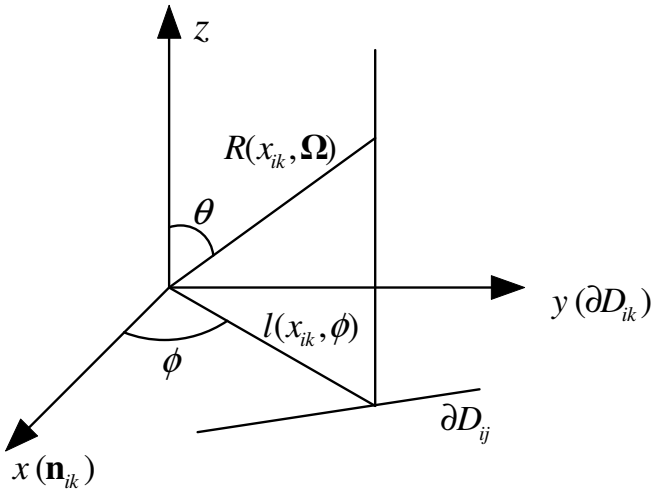

Figure 26: 3D geometry for calculation of transmission probability

Where, as shown in the figure above, L_{ik} is the length of interface ∂D_{ik}, $\phi_{\min}(x_{ik})$ and $\phi_{\max}(x_{ik})$ are integral limits for angular variable, and $l(x_{ik},\phi)$ is just distance traveled by a neutral in the 2D plane and Ki_3 is the third order Bickley-Naylor function [87].

$$Ki_n(x) = \int_0^{\frac{\pi}{2}} d\theta \sin^{n-1}\theta \exp\left(-\frac{x}{\sin\theta}\right) \tag{45}$$

In the actual coding of GTNEUT, this third order Bickley-Naylor function is the cause of some trouble. Approximately 85% of the computation time is spent solving the Bickley-Naylor functions. Additionally, the Bickley–Naylor function, in GTNEUT is evaluated from an approximate fit [17]. The performance of GTNEUT could be improved by utilizing other methods of integral evaluation of the transmission coefficients.

The coefficient, $P_{0,i}$, is defined as the probability that neutrals born (volumetric sources) in cell *i* will escape from cell *i* without collision with cell *i*. Similarly, the coefficient, Λ_{ij} , is the directional escape probability that a neutral born in and escaping from cell *i* will escape into adjacent region *j* [87].

Using the assumption that volumetric sources are uniformly distributed in cell i, we obtain the following for the escape probability:

$$\begin{aligned} P_{0,i} &= \frac{1}{4\pi S_i}\int_{D_i} d\mathbf{r}\int_{4\pi} d\boldsymbol{\Omega}\exp\left(-\frac{\Sigma_t l(\mathbf{r},\phi)}{\sin\theta}\right) \\ &= \frac{1}{4\pi S_i}\int_{D_i} d\mathbf{r}\int_0^{2\pi} d\phi\int_0^{\pi} d\theta\sin\theta\exp\left(-\frac{\Sigma_t l(\mathbf{r},\phi)}{\sin\theta}\right) \\ &= \frac{1}{2\pi S_i}\int_{D_i} d\mathbf{r}\int_0^{2\pi} d\phi Ki_2\left(\Sigma_t l(\mathbf{r},\phi)\right) \end{aligned} \tag{46}$$

and

$$\begin{aligned}\Lambda_{ij} &= \frac{1}{4\pi S_i P_{0,i}} \int_{D_i} d\mathbf{r} \int_{\phi_{\min}^j(\mathbf{r})}^{\phi_{\max}^j(\mathbf{r})} d\phi \int_0^{\pi} d\theta \sin\theta \exp\left(-\frac{\Sigma_t l(\mathbf{r},\phi)}{\sin\theta}\right) \\ &= \frac{1}{4\pi S_i P_{0,i}} \int_{D_i} d\mathbf{r} \int_{\phi_{\min}^j(\mathbf{r})}^{\phi_{\max}^j(\mathbf{r})} d\phi Ki_2\left(\Sigma_t l(\mathbf{r},\phi)\right)\end{aligned} \tag{47}$$

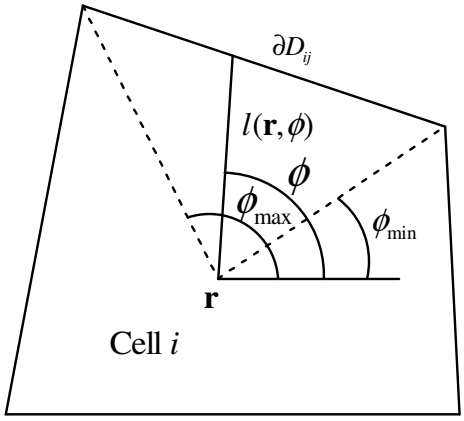

Figure 27: Geometry for calculating escape probability

However, it is computationally expensive to calculate these first flight escape probabilities and directional escape probabilities. Usually, a rational approximation for calculation of $P_{0,i}$ can achieve both high efficiency and accuracy [87].

$$P_{0,i} = \frac{1}{X}\left[1-\left(1+\frac{X}{n}\right)^{-n}\right] \tag{48}$$

In the equation above, $X = 4S_i\Sigma_t / L_i$, S_i is the area of cell i and L_i is the perimeter of cell i and exponent $n = 2.09$ is resulted from comparisons with Monte Carlo calculations [65]. The directional escape probability is assumed to be proportional to L_{ij}, the length of interface ∂D_{ij}, i.e.

$$\Lambda_{ij} = \frac{L_{ij}}{L_i} \tag{49}$$

The total volumetric source Q_i used the equation for the total partial current is still unknown. To eliminate Q_i, one must first determine its relation with S_{ext}^i, the total external volumetric source and $\left\{\Gamma_{k,i}, k = 1, \cdots\right\}$, the incoming total partial current from all the adjacent cells. If we keep in mind that the source term is equal to [87]:

$$q(\mathbf{r}) = \Sigma_{cx}\phi(\mathbf{r}) + S_{ext}(\mathbf{r}) = \Sigma_{cx}\phi(\mathbf{r}) + \frac{S_{ext}^i}{S_i} \tag{50}$$

we may insert the equation for the scalar flux into the source term and integrate over D_i

$$\begin{aligned} Q_i &= \int_{D_i} d\mathbf{r} q(\mathbf{r}) = \int_{D_i} d\mathbf{r}\left(\Sigma_{cx}\phi(\mathbf{r}) + \frac{S_{ext}^i}{S_i}\right) \\ &= S_{ext}^i + \int_{D_i} d\mathbf{r}\Sigma_{cx}\left[\int_{D_i} d\mathbf{r}' \frac{q(\mathbf{r}')\exp\left(-\Sigma_t|\mathbf{r}-\mathbf{r}'|\right)}{4\pi|\mathbf{r}-\mathbf{r}'|^2}\right. \\ &\quad \left. + \int_{\partial D_i} dS\psi_{in}(\mathbf{r}_S, \mathbf{\Omega})\frac{\exp\left(-\Sigma_t|\mathbf{r}-\mathbf{r}_S|\right)}{|\mathbf{r}-\mathbf{r}_S|}(\mathbf{\Omega}\cdot\mathbf{n}_-)\right] \end{aligned} \tag{51}$$

Using DP_0 and flat flux assumptions, we may rewrite the total volumetric source as:

$$\begin{aligned} Q_i &= S_{ext}^i + Q_i\frac{\Sigma_{cx}}{\Sigma_t}\frac{\Sigma_t}{S_i}\int_{D_i} d\mathbf{r}\int_{D_i} d\mathbf{r}' \frac{\exp\left(-\Sigma_t|\mathbf{r}-\mathbf{r}'|\right)}{4\pi|\mathbf{r}-\mathbf{r}'|^2} \\ &\quad + \sum_k \Gamma_{k,i}\frac{\Sigma_{cx}}{\Sigma_t}\frac{\Sigma_t}{\pi L_{ki}}\int_{D_i} d\mathbf{r}\int_{\partial D_{ik}} dS_{ik}\frac{\exp\left(-\Sigma_t|\mathbf{r}-\mathbf{r}_{ik}|\right)}{4\pi|\mathbf{r}-\mathbf{r}_{ik}|^2}(\mathbf{\Omega}\cdot\mathbf{n}_{ki}) \\ &= S_{ext}^i + Q_i c_i P1_{ii} + \sum_k \Gamma_{k,i} c_i P2_{ki} \end{aligned} \tag{52}$$

Where coefficients $P1_{ii}$, $P2_{ki}$ and c_i are defined in the following equations.

$$P1_{ii} = \frac{\Sigma_t}{S_i} \int_{D_i} d\mathbf{r} \int_{D_i} d\mathbf{r}' \frac{\exp\left(-\Sigma_t \left|\mathbf{r}-\mathbf{r}'\right|\right)}{4\pi \left|\mathbf{r}-\mathbf{r}'\right|^2} \tag{53}$$

$$P2_{ki} = \frac{\Sigma_t}{\pi L_{ki}} \int_{D_i} d\mathbf{r} \int_{\partial D_{ik}} dS_{ik} \frac{\exp\left(-\Sigma_t \left|\mathbf{r}-\mathbf{r}_{ik}\right|\right)}{\left|\mathbf{r}-\mathbf{r}_{ik}\right|^2} \left(\mathbf{\Omega} \cdot \mathbf{n}_{ki}\right) \tag{54}$$

$$c_i = \frac{\Sigma_{cx}}{\Sigma_t} \tag{55}$$

Now we change dummy variables in the integral of Eq. 2.21a by $d\mathbf{r}' = R^2 dR d\mathbf{\Omega} = \left(l/\sin\theta\right)^2 \cdot \left(dl/\sin\theta\right) d\mathbf{\Omega}$, then integrate along neutral trajectory, we obtain [87]

$$\begin{aligned} P1_{ii} &= \frac{\Sigma_t}{4\pi S_i} \int_{D_i} d\mathbf{r} \int \int_{4\pi} \frac{dl}{\sin\theta} d\mathbf{\Omega} \exp\left(-\frac{\Sigma_t l}{\sin\theta}\right) \\ &= \frac{\Sigma_t}{2\pi S_i} \int_{D_i} d\mathbf{r} \int_{2\pi} d\phi \int dl Ki_1\left(\Sigma_t l\right) \\ &= \frac{\Sigma_t}{2\pi S_i} \int_{D_i} d\mathbf{r} \int_{2\pi} d\phi \left(1 - Ki_2\left(\Sigma_t l\right)\right) \\ &= 1 - \frac{1}{2\pi S_i} \int_{D_i} d\mathbf{r} \int_{2\pi} d\phi Ki_2\left(\Sigma_t l\left(\mathbf{r},\phi\right)\right) \\ &= 1 - P_{0,i} \end{aligned} \tag{56}$$

During derivation we used the differential property $dKi_n(x)/dx = -Ki_{n-1}(x)$ and $Ki_2(0) = 1$

Similarly,

$$
\begin{aligned}
P2_{ki} &= \frac{\Sigma_t}{\pi L_{ki}} \int_{D_i} d\mathbf{r} \int_{\partial D_{ik}} dS_{ik} \frac{\exp\left(-\Sigma_t \left|\mathbf{r}-\mathbf{r}_{ik}\right|\right)}{\left|\mathbf{r}-\mathbf{r}_{ik}\right|^2} \left(\mathbf{\Omega}\cdot\mathbf{n}_{ki}\right) \\
&= \frac{\Sigma_t}{\pi L_{ki}} \int_{\partial D_{ik}} dS_{ik} \int\int_{4\pi} \frac{dl}{\sin\theta} d\mathbf{\Omega} \exp\left(-\frac{\Sigma_t l}{\sin\theta}\right) \left(\mathbf{\Omega}\cdot\mathbf{n}_{ki}\right) \\
&= \frac{1}{\pi L_{ki}} \int_{\partial D_{ik}} dS_{ik} \int_{4\pi} d\mathbf{\Omega} \left[1-\exp\left(-\frac{\Sigma_t l\left(\mathbf{r}_{ki},\phi\right)}{\sin\theta}\right)\right] \left(\mathbf{\Omega}\cdot\mathbf{n}_{ki}\right) \\
&= 1-\frac{1}{\pi L_{ki}} \int_{\partial D_{ik}} dS_{ik} \int_{4\pi} d\mathbf{\Omega} \exp\left(-\frac{\Sigma_t l\left(\mathbf{r}_{ki},\phi\right)}{\sin\theta}\right) \left(\mathbf{\Omega}\cdot\mathbf{n}_{ki}\right) \\
&= 1-\frac{1}{\pi L_{ki}} \int_{\partial D_{ik}} dS_{ik} \int_{4\pi} d\mathbf{\Omega} \exp\left(-\frac{\Sigma_t l\left(\mathbf{r}_{ki},\phi\right)}{\sin\theta}\right) \left(\mathbf{\Omega}\cdot\mathbf{n}_{ki}\right) \\
&= 1-\frac{1}{\pi L_{ki}} \int_{\partial D_{ik}} dS_{ik} \int_{\partial D_i} \frac{dS_i\left(\mathbf{\Omega}\cdot\mathbf{n}_{+}\right)}{\left|\mathbf{r}_i-\mathbf{r}_{ik}\right|} \exp\left(-\Sigma_t \left|\mathbf{r}_i-\mathbf{r}_{ik}\right|\right) \left(\mathbf{\Omega}\cdot\mathbf{n}_{ki}\right) \\
&= 1-\sum_l \frac{1}{\pi L_{ki}} \int_{\partial D_{ik}} dS_{ik} \int_{\partial D_{il}} \frac{dS_{il}\left(\mathbf{\Omega}\cdot\mathbf{n}_{il}\right)}{\left|\mathbf{r}_{il}-\mathbf{r}_{ik}\right|} \exp\left(-\Sigma_t \left|\mathbf{r}_{il}-\mathbf{r}_{ik}\right|\right) \left(\mathbf{\Omega}\cdot\mathbf{n}_{ki}\right) \\
&= 1-\sum_l T^i_{k,l}
\end{aligned}
\tag{57}
$$

Substitute the two equations above into the equation for the total volumetric source, we have

$$
\left[1-c_i\left(1-P_{0,i}\right)\right] Q_i = S^i_{ext} + \sum_k \left(1-\sum_l T^i_{k,l}\right) \tag{58}
$$

or

$$Q_i = \frac{S_{ext}^i + \sum_k \left(1 - \sum_l T_{k,l}^i\right) c_i \Gamma_{k,i}}{1 - c_i \left(1 - P_{0,i}\right)} \tag{59}$$

If we insert Q_i back into the concise form of the total partial currents and define the total escape probability as:

$$P_i = \frac{P_{0,i}}{1 - c_i \left(1 - P_{0,i}\right)} \tag{60}$$

we can rewrite the TEP equations as [87]:

$$\Gamma_{i,j} = \sum_k \Gamma_{k,i} T_{k,j}^i + \sum_k \Gamma_{k,i} \left(1 - \sum_l T_{k,l}^i\right) c_i P_i \Lambda_{ij} + S_{ext}^i P_i \Lambda_{ij} \tag{61}$$

The first term of the TEP equation represents the sum of the partial currents entering cell *i* from all adjacent cells and being directly transmitted to region j without collision with cell i. The second term is the sum of the partial current entering cell i from all the adjacent cells and having one or more charge-exchange scattering with cell *i* and finally exiting into cell *j*. The third term is the contribution of external volumetric sources and their progenies. Since the exiting flux from a cell is only dependent on the incoming fluxes entering that cell from all the adjacent cells, the transmission matrix is sparse, with the number of nonzero elements growing linearly with the number of cells. In the actual coding of GTNEUT, the sparse matrices are solved using the UMFPACK Fortran version 2.2.1 [17]. UMFPACK is a set of routines for the direct solution of sparse linear systems using the unsymmetric multifrontal method [88]. In theory, any sparse matrix solver

could be used in the coding of GTNEUT, and as will be presented at the end of this work it may be necessary to upgrade the routines used to solve the sparse matrix.

A useful convenience in the TEP methodology is that the shape of cells is arbitrary [87]. Practically any shape could be used so long as it is convex in nature. By this we mean, the cell cannot be set up so that particles streaming from one interface can stream back into the same interface. In practice, GTNEUT generally only uses meshes that have cells with 3 or 4 sides.

Defining the TEP equations for the computational regions would not be complete without a brief discussion of the boundary conditions that may occur at certain cell faces. There are essentially two kinds of real world boundaries used in the neutrals analysis of Tokamak plasmas. The neutrals may either encounter the wall of the confinement vessel or they may enter the core plasma region. The wall of the confinement vessel is a physical boundary. The core plasma region is an area of the plasma that is so hot that neutral particles either scatter out of or get ionized in. The most computationally efficient method of handling the neutrals entering the core plasma boundary is to simply impose an albedo boundary condition [89].

Since the mean free path of neutrals in core plasma regions are extremely small, core plasma regions can be treated as semi-infinite half-space. Originally the one-speed diffusion theory was exploited to calculate the albedo coefficient [63].

$$\alpha = \frac{1 - \frac{2}{\sqrt{3}}\sqrt{c_i^{-1} - 1}}{1 + \frac{2}{\sqrt{3}}\sqrt{c_i^{-1} - 1}} \tag{62}$$

The diffusion approximation has been found to be accurate if charge-exchange fraction c is greater that 0.9. However, the results of the diffusion approximation would be significantly lower than the Monte Carlo calculations when c is smaller than 0.9, and could even become negative when c is smaller than 0.57. To compensate, an albedo coefficient was created using data from Monte Carlo simulations. It was found to be very accurate for the entire range of charge-exchange fraction c [63].

$$\alpha(c) = \frac{0.00059720174 + 0.2045041c - 0.3818644c^2 + 0.1769341c^3}{1 - 2.46848679c + 1.9744939c^2 - 0.505836c^3} \tag{63}$$

The wall boundary is a great deal more complicated than the core boundary. Ion and neutrals striking the first wall of the confinement vessel can either backscatter into the system or they may undergo desorption or absorption into the first wall. Neutrals backscattering into the system may do so with a significant fraction of the impact energy after encountering several elastic collisions with target material. In desorption or absorption, neutral particles are implanted in the near surface, where they will reach thermal equilibrium with wall material and subsequently be released as thermal molecules due to either direct particle-surface collisions or collisions of sputtered and backscattered particles. The "absorption means" of the neutrals means that the incident particles are permanently trapped inside the material wall. In the actual coding of GTNEUT, these particles are lost in the same manner as particles are lost to the core [87]. The neutrals; however, that are re-emitted back into the plasma typically have an energy of 1-5 eV since the molecules disassociate as Franck-Condon atoms [90, 91]. In previous sensitivity studies, varying the Franck-Condon energy in GTNEUT did little to impact

the neutral transport; however, a sensitivity study presented later in the thesis disputes those findings.

The particle and energy reflection coefficients R_N and R_E, which depend on the impact energy E_0, impact and substrate species, are two of the most important back-scattering data. The particle reflection coefficient R_N is defined as the ratio of the number *N* of all reflected particles to the total number N_0 of incident particles [87]:

$$R_N = \frac{N}{N_0} \tag{64}$$

The energy reflection coefficients R_E is defined as the total energy of the reflected particles divided by the total energy of the incident particles, so the average energy of the back-scattered particles is [87]:

$$\overline{E} = \frac{R_E}{R_N} E_0 \tag{65}$$

The total reflect flux from a wall segment can be written as:

$$\Gamma_{kw,i} = \Gamma_{ext}^{kw} + R_N^{kw}\Gamma_{i,kw} + \left(1 - R_N^{kw}\right)\left(1 - f_{abs}^{kw}\right)\Gamma_{i,kw} \tag{66}$$

Where R_N^{kw} is the particle reflection coefficient for wall segment *kw*, f_{abs}^{kw} is the fraction that particles are permanently trapped inside the wall material. In the equation above, the first term is the external flux, the second term represents back-scattered flux with energy $\overline{E}$, and the last terms represent the flux due to Franck-Condon atoms [87]. It should be noted that there is no one definitive number for $\overline{E}$. Several estimates place it to be

between 1-10 eV [17, 65, 90-92]. As will be revealed in Chapter 6, this range is actually very important for the penetration of neutral particles into the pedestal region. For all the results presented in Chapter 6, we will be assuming $\overline{E} = 2eV$.

Having derived the most basic 2D TEP equations used in the original GTNEUT code and discussed the most basic boundary conditions, it is important to discuss what additional work has been done in upgrading and implementing them.

3.2 Additions to the TEP Methodology

Many additions to the TEP Methodology have been made by Dingkang Zhang. One of the most important additions to the GTNEUT methodology is the incorporation of the DP_1 approximation for the particle distribution in the forward half-space at each successive interface. In the old methodology, only the DP_0 was used. The DP_0 approximation has a tendency to over-estimate the attenuation of neutral particles streaming between successive interfaces. The reason for this is that the DP_0 approximation does not account for the preferential attenuation of particles moving at large angles relative to the normal. The problem tends to be most prevalent in cases where the mean free path lengths are longer than the cell length [74]. This could be a major problem in realistic plasma backgrounds.

In reality, the mean free path lengths can be on the scale of meters (sometimes 10's of meters) and border cells with mean free paths of less than 1cm. This means that in regions where the mean free path is very long compared to the cell length, there could be an over estimation of particle flux across the cell with much less current streaming into the i-1 or i+1 locations. Fortunately, the most current version of GTNEUT has the ability

to use either DP_0 or DP_1. It should be noted that using the DP_1 method can increase the computational time of the problem substantially as the TEP equations become much longer and more complicated to solve. Even with DP_1, GTNEUT may have some regions of excessive forward scatter. DP_1 is a good approximation in most cases, but DP_2 might further increase the accuracy of GTNEUT by making the forward streaming more quadrilateral anisotropic. Still, this would add much more computational time (probably comparable with Monte Carlo).

The most recent addition to the TEP methodology has been the incorporation of the Average Neutral Energy (ANE) approximation. The ANE approximation assumes that the average neutral energy from a region is the weighted average of the energy of neutrals incident from contiguous regions and of the energy of neutrals resulting from charge-exchanged ions within the region. This can be expressed as [87]

$$\bar{E}_{ij} = \frac{\sum_{k,n} T^{n\to 0}_{i,k\to j}\Gamma^{n}_{i,k}\bar{E}_{ki} + \Gamma^{c,0}_{i,j}T_i}{\sum_{k,n} T^{n\to 0}_{i,k\to j}\Gamma^{n}_{i,k} + \Gamma^{c,0}_{i,j}} \tag{67}$$

It has been developed and implemented into the GTNEUT code. In GTNEUT, the ANE approximation is implanted by using the following algorithm [18]:

1. Assume $\bar{E}_{ij} = 3/2T_i$ the local ion temperature assumption
2. Calculate the neutral mean-free-path, transmission and escape probabilities, and solve the linear system to determine the interface currents
3. Calculate the collided and uncollided fluxes from the interface currents
4. Use the above equation to update the average neutral energy $\bar{E}_{ij}$

5. Repeat steps 2-4 until convergence, which is determined by the maximum fractional change of $\overline{E}_{ij}$ from the previous iteration
6. Calculate the final neutral densities and the ionization rates.

The average neutral energy approximation has been demonstrated to be more accurate than the original local ion temperature approximation for optically thin regions. The simulations of the refined GTNEUT code agree excellently with the DEGAS predictions in DIII-D Lmode and H-mode discharges, and the results of both codes are in good agreement with the experimental measurements [87].

4. Application of the GTNEUT Code

4.1 GTNEUT Input File

While the GTNEUT code has been used in the past for experimental analysis, most of the work has focused primarily on methods development. The GTNEUT code has never been used from a "start-to-finish" type of analysis of actual experimental data. A large part of this thesis was developing a method to utilize the GTNEUT in a "routine" type fashion.

In order to do this, two obstacles had to be overcome. First, GTNEUT does not possess intrinsic mesh generation capabilities for complex 2D geometries such as those found in a Tokamak plasma. Additionally, the GTNEUT methodology requires the use of a "region-free" grid structure. This means traditional grid points are not needed for GTNEUT and cannot be utilized in neutral particle transport calculations. Second, GTNEUT does not possess the ability to generate its own plasma background parameters. This means, GTNEUT is dependent on the use of other codes or directly observable experimental values for the ion and electron temperatures and densities, recombination neutrals, ion fluxes to the walls, gas puffing rates, and pumping locations.

In order to use GTNEUT for experimental analysis, a procedure for circumventing these two above issues we utilized the 2D fluid code UEDGE. UEDGE is a very powerful 2D fluid code that has the capability of generating very complex 2D meshes based off of equilibrium fitting data. Additionally, UEDGE calculates a plasma background throughout the 2D mesh [22]. We have created routines that can convert the 2D mesh generated by UEDGE into a format that can be directly imported into the

geometry section of the GTNEUT input file called “toneut”. Additionally, if UEDGE has already converged to a solution, it is possible to extract the plasma background information into a format usable by GTNEUT as well. Additionally, experimentally observed quantities may also be imported into the GTNEUT mesh.

4.2 Breakdown of the TONEUT file

GTNEUT requires an input file called “toneut” to run. In the toneut file there are essentially 4 sections: geometry, plasma background, sources for neutrals, and runtime options.

The geometry is arguably the most complicated section of the input file. The geometry section contains the geometric definition of the problem. The TEP method is unique in that it does not require a clearly defined coordinate system. Instead, cell information is made up of the lengths and angles of the cell interfaces. Additionally, neighboring cells must be tracked. The greatest challenge in this problem has been devising a way of tracking cell lengths, angles, and cell neighbors. GTNEUT has a built in routine that checks the geometry section of the input file. If the geometry is off at all, GTNEUT will halt and list the cells in which there is a problem.

The figure below is a very simplified version illustrating how we have decided to number our grid. The UEDGE mesh is essentially laid out in a poloidal and radial distribution.

The number of cells in the poloidal direction is referred to as NX. It is defined (starting at cell one and going in the clockwise direction) as nxleg(1,1) + nxxpt + nxxpt + nxcore(1,1) + nxcore(1,2) + nxxpt + nxxpt + nxleg(1,2).

A better explanation of these terms are located in the UEDGE manual ZWF, but nxleg(1,1) and nxleg(1,2) are the number of cells in the poloidal direction for the inner and outer divertor strike points respectively.

Likewise, nxcore(1,1) and nxcore(1,2) are the number of poloidal cells for the regions above the X-Point. One can add resolution to the X-Point region by adding nxxpt. The creates 4 * nxxpt number of cells around the X-Point. Various options are available to determine how closely these extra cells are clustered around the X-Point.

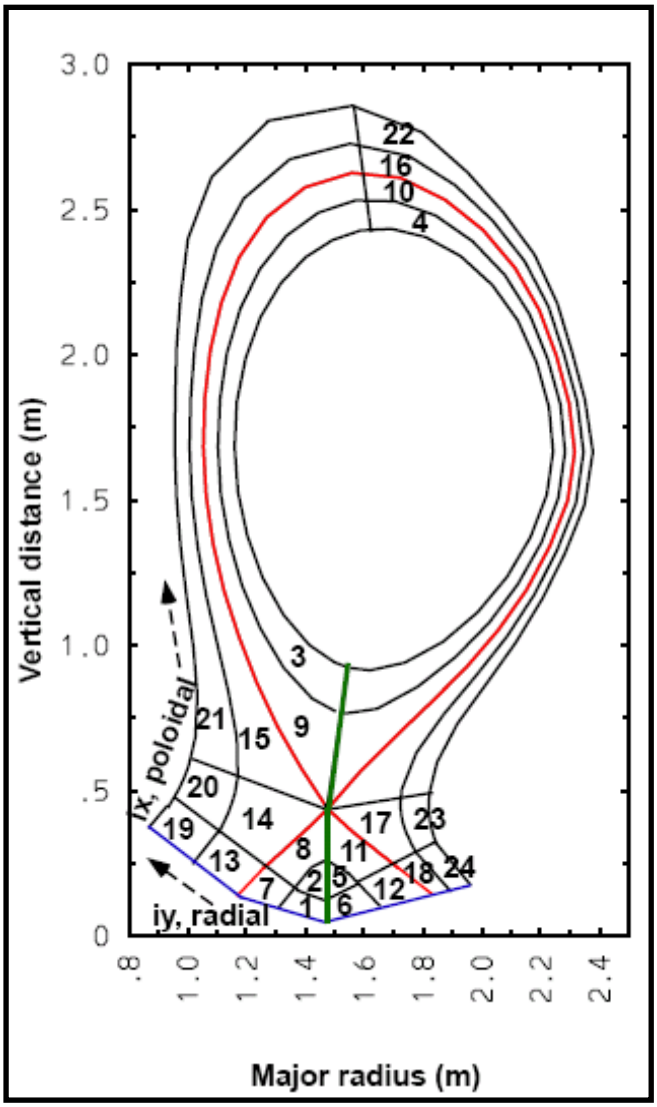

Figure 28: Simplified Geometry of UEDGE Mesh [93]

The number of cells in the radial direction (NY) is the summation of nycore(1) and nysol(1). nycore(1) is the number of poloidal layers within the separatrix. nysol(1) is the number of poloidal layers outside the separatrix.

The convention of numbering from the 2D array of UEDGE coordinates to the GTNEUT 1D array of cells is given by: icn = ix + NX*(iy-1)

In total, there are NX*NY cells in the UEDGE grid. The UEDGE grid, however, requires some modifications before it can be used in GTNEUT. First, the grid should be fit to the divertor [93] for all GTNEUT runs. Additionally, UEDGE imposes boundary conditions at the edge of the grid. The UEDGE mesh does not extend to the wall. The UEDGE grid does not extend to the walls of the confinement vessel. The routines created for our analysis extend the UEDGE mesh to the wall. Intrinsic to the UEDGE calculation, there is a dummy layer of cells along the last layer of cells in the SOL. We call this the HALO region. When GTNEUT utilizes this layer of cells, there are effectively (NY+1)*(NX) number of cells in the GTNEUT grid. The same formula as above can be used to locate cells in term of icn. NY is now given by NY = NY + 1.

Lastly, the GTNEUT mesh also needs to fill in the gap in the private flux region with computational cells. These cells are slightly different. All of the other NX*(NY+1) cells are 4 sided. The cells in the private flux region are 3 sided. The number of cells is determined by the sum of nxleg(1,1)+nxxpt+nxxpt+nxleg(1,2).

So, in total there are:

$$NX*(NY+1)+nxleg(1,1)+nxxpt+nxxpt+nxleg(1,2)$$

cells in a GTNEUT calculation. Additionally, the number of plasma regions and the number of wall locations must be tracked. The number of plasma regions is simply:

nxppt+nxcore(1,1)+nxcore(1,2)+nxxpt

The number of wall locations is given by:

NX + 2* NY + 2

The additional 2 wall segments are from the 2 cells touching the wall in the private flux region. The numbering scheme for the plasma and wall cells can appear complicated. However, it is fairly straight forward. The plasma number scheme starts from the total number of cells in GTNEUT. So, if there are

NX*(NY+1)+nxleg(1,1)+nxxpt+nxxpt+nxleg(1,2)

cells in the problem, the first plasma region is:

NX*(NY+1)+nxleg(1,1)+nxxpt+nxxpt+nxleg(1,2) +1

The first plasma location is located adjacent to the first internal cell bordering the plasma region. The numbering likewise goes in the clockwise fashion. The wall regions start at:

NX*(NY+1)+nxleg(1,1)+nxxpt+nxxpt+nxleg(1,2) +

nxppt+nxcore(1,1)+nxcore(1,2)+nxxpt

The numbering starts at the wall location immediately adjacent to internal cell 1. In many of the GTNEUT input options, the wall locations are labeled from 1 to # of wall segments. Be aware, in this numbering convention, wall segment 1 is located adjacent to cell 1. The wall segments increase linearly from 1 to # of wall locations in a clockwise

fashion until it gets to the wall segment bordering the first private flux region cell. This method was used to create the grids used in the experimental analysis. A more detailed version of this procedure with links to the code can be found in Appendix A. There we will show examples of the actual process as well as provide links to the code used to carry out the process.

5. DIII-D Analysis of Neutral Particle Recycling and Pedestal Fueling

5.1 DIII-D Neutral Particle Recycling Measurements

In recent DIII-D analyses, Leonard et al. [13, 16] developed techniques to experimentally determine ion fluxes to the wall. The principle technique used to find the ion flux to the divertor target plates was by integrating the ion saturation current profile over the surface mounted Langmuir probes along the divertor target. The location of the divertor Langmuir probes are depicted in the Fig. 29A.

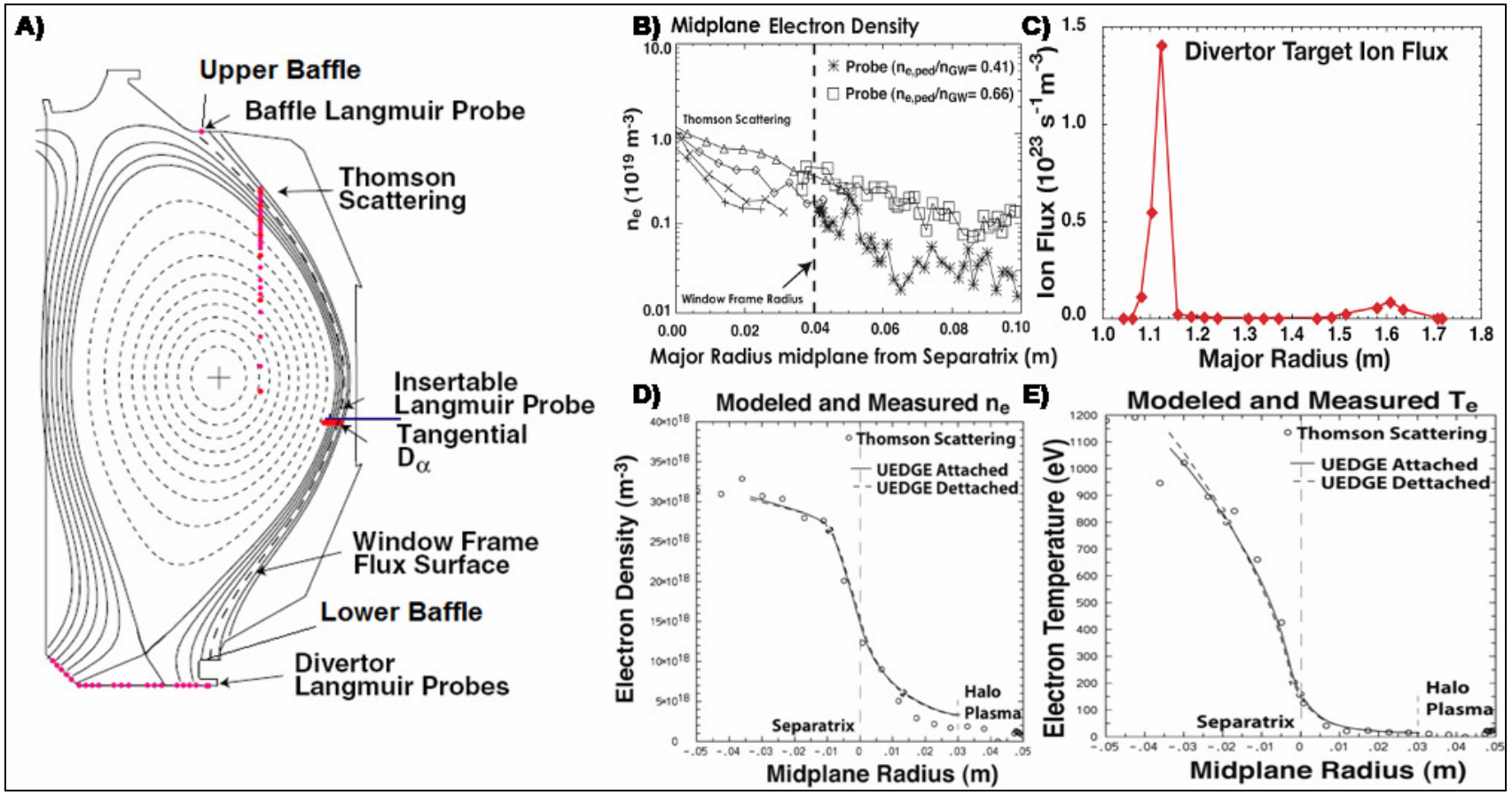

Figure 29: A) DIII-D geometry showing the divertor configuration and the location where most of the main chamber ion flux recycles as well as where most of the divertor ion flux recycles. B) midplane probe data. C) divertor target ion flux ascertained from the surface mounted Langmuir probes along the strike plates. Thomson scattering data for D) density and E) temperature (A and B reproduced with permission from Refs [13]and [16]).

Ion fluxes to the wall from main chamber recycling were inferred from a "window frame" analysis [13]. The window frame analysis utilizes data from the midplane insertable Langmuir probe, Thomson Scattering, and the Langmuir probe near the Upper Baffle. The locations of these diagnostics and their respective outputs are depicted in the figure above. The window frame analysis determines a global ion flux to the outboard chamber. The global radial particle flux to the outboard main chamber is 4 cm from the outboard midplane separatrix [13]. This is represented by the magnetic flux surface marked with the dashed line in the figure above. The main chamber is defined as surfaces outside of the horizontal divertor target tiles for the outboard divertor and the 45˚ tile for the inboard divertor. An important feature of this surface is that both ends of the field lines terminate on a toroidally symmetric surface. If one assumes parallel plasma flow to the surface with negligible recycling in the low density far SOL plasma, the particle flux through the window frame can be found from:

$$\Gamma_i = 2\pi n_e c_s \lambda \frac{B_p}{B_T}\left[\left(\langle R\rangle \xi\right)_1 + \left(\langle R\rangle \xi\right)_2\right] \tag{68}$$

where $n_e, c_s, \lambda,$ are density and sound speed and their convoluted e-folding scale length at the midplane probe, and B_p and B_T are the midplane window frame values of toroidal and poloidal magnetic field respectively. R is the average major radius of the upper and lower halves of the window frame flux surface, and ξ is the ratio of saturation current between the termination surfaces and the midplane, $\xi \sim 0.5$ [13]. For the midplane window frame plasma conditions, the probe profiles of electron density and temperature

and ion saturation current (I_{sat}) are fit to an exponential function from the window frame radius outward to the baffle limiters [13]. The window frame analysis provides global estimated particle flux, Γ_i, to the outboard midplain. In Ref. [16], it was noted that low midplane probe currents suggested the ion flux was mainly to the baffles, so that the recycling neutral source due to this ion flux is distributed evenly between the upper and lower baffles. A distribution of the ion current to the wall for both the divertor and baffle sources is presented later.

Table 5: Neutral sources from recycling ions obtained from surface mounted probes (divertor) and window frame analysis (baffles).

Ion Recycling Sources (#/s)	
UPPER BAFFLE	8.13E+20
LOWER BAFFLE	8.13E+20
INNER DIVERTOR	5.55E+21
OUTER DIVERTOR	6.04E+21

The 2D edge fluids code UEDGE [22], which has been used extensively [5, 8, 11-13, 16, 20] to interpret DIII-D edge plasma phenomena, was used to determine the background edge plasma parameters. This determination and reconciliation with spectroscopic data of the background plasma parameters is described in detail in earlier work [11, 13, 16]. The transport coefficients in the edge pedestal were adjusted to obtain agreement between calculated and measured densities and temperatures at the Thomson scattering diagnostic locations shown in Fig. 29A, thus validating the calculated background by comparison with experiment in the edge pedestal. Figs. 29D and 29E show that the UEDGE calculation matches well with the Thomson data.

There was not adequate experimental data in the divertor region to benchmark the UEDGE calculation to experimental data in this region [16]. Thus, two different sets of background plasma parameters were calculated [16] with UEDGE to bracket the actual experimental conditions (both benchmarked to the upstream Thomson data), by varying the wall recycling coefficients in UEDGE. Following these authors [16], we denote these two calculated background plasmas as 'attached' (high T) and 'detached' (low T). In the 'attached' case, the temperature near the inboard divertor plate is fairly high ($\sim 10eV$ within a cm of the plate). In the 'detached' case, the inboard divertor temperature is much lower ($\sim 1eV$ within a cm of the plate). We emphasize that we are analyzing a single DIII-D discharge using two different sets of previously calculated background plasma parameters in order to bracket the likely divertor plasma parameters.

We further note that the GTNEUT neutrals calculation and the UEDGE background plasma calculations have not been iterated to consistency. The UEDGE background plasma calculations include an approximate fluid neutrals calculation and are adjusted to match the measured 'upstream' plasma conditions in the outboard midplane edge pedestal and scrape-off layer. Then, the more geometrically detailed GTNEUT calculations (extending the neutral transport to the plasma chamber wall) are carried out on a fixed background plasma to investigate in detail the neutral particle recycling and core refueling.

Because of the different ranges of temperatures and densities in the SOL, divertor and pedestal regions, the neutral mean free paths can vary by large amounts, as shown in Fig.30 for the "detached" plasma background, for which neutral mean free paths (mfp) range from less than a cm at the divertor plate to close to 60 meters in the private flux

region. In the “attached” case, the mean free path lengths in the SOL-DIV region range from less than a cm to well over 30 meters in the private flux region.

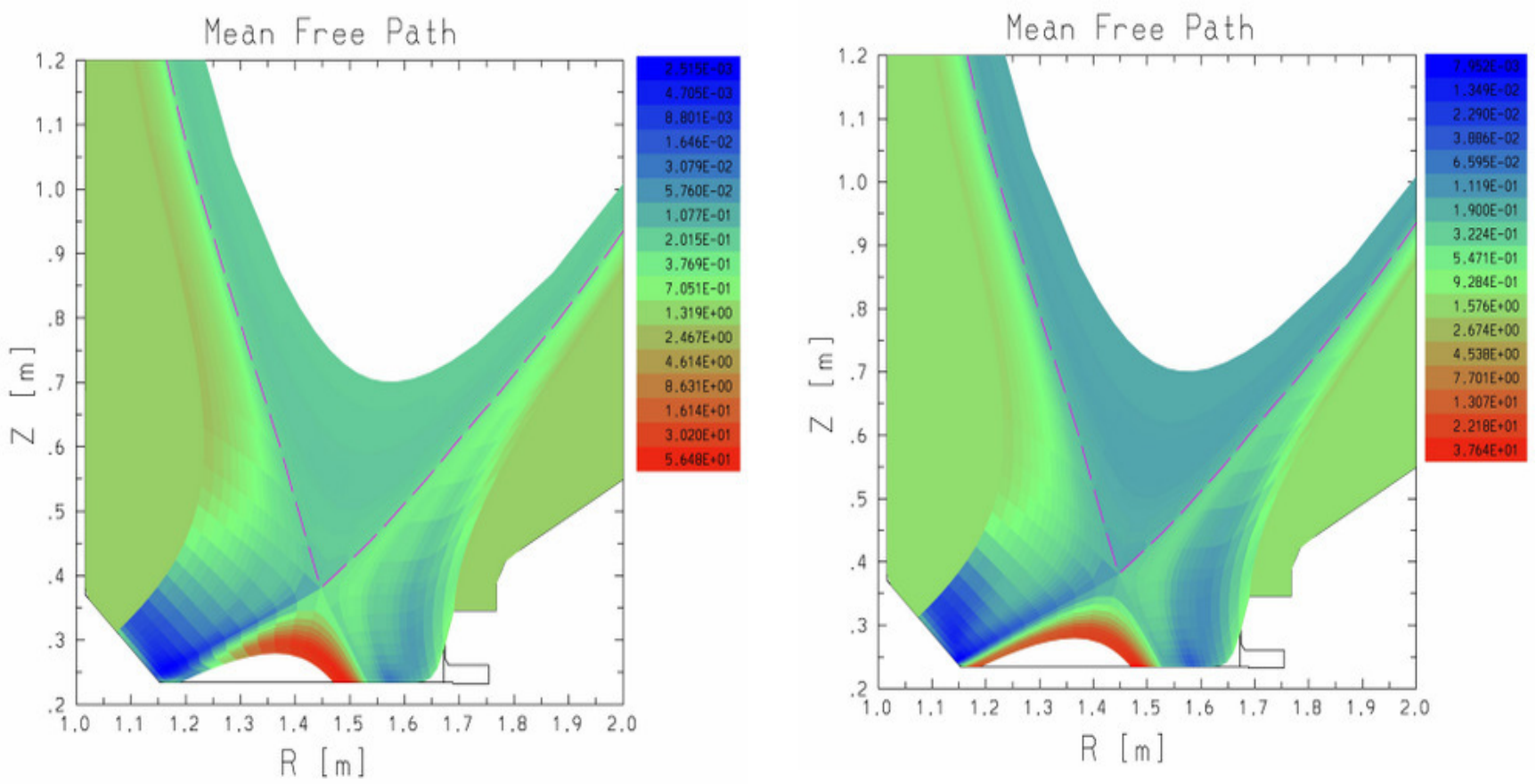

Figure 30: Neutral mean free path distribution (DETACHED left and ATTACHED right plasma background) calculated with the UEDGE code [22])

The recombination rates calculated with UEDGE ZWF are quite different for the 'attached' and 'detached' background plasmas. In the 'attached' case, the source of neutrals due to recombination is small (1.473×10^{20}/s in front of the inboard divertor plate); however, in the 'detached' background plasma case the temperatures are so low and the density is so high that the neutral atom source due to recombination becomes quite substantial (6.243×10^{21}/s in front of the inboard divertor plate) relative to the attached background plasma case.

The core ion particle source due to neutral beam injection for this discharge is known from experiment to be 3.86×10^{20}/s. Note that the neutral beam source is not included as a source in the neutrals calculations, but as a source of ions.

Since the UEDGE code does not calculate the core plasma transport, the ion out-flux must be determined from experiment. Using a method proposed by Porter [94], the ion outflow across the separatrix was estimated [16] from the density rise just after the L-H transition by assuming the separatrix ion flux was diffusive with a uniform diffusion coefficient equal to 25% of the effective heat diffusivity inferred from the experimental temperature gradient. This estimated ion outflux across the separatrix was 2.74×10^{21}/s, with an estimated uncertainty [94] of ± 30% due to experimental uncertainty. There are an additional modeling uncertainties associated with assumptions such as a diffusive ion particle flux and a constant diffusion coefficient over the separatrix which would increase this uncertainty in the ion outflux, but these can not be readily estimated.

6. Neutral Particle Recycling Calculations

6.1 Geometric model

The analysis presented in this paper was performed on a 2D mesh generated by the 2D fluids code UEDGE and extended to the walls of the confinement vessel, as discussed in the previous section. The computational grid shown in Fig. 31 consists of a pedestal (PED) region extending inward from the separatrix for a distance sufficient to attenuate the neutral density by a couple of orders of magnitude [about 7% of the normalized radius (rho)], a scrape-off layer (SOL) region extending outward from the separatrix to the outer edge of the UEDGE computational grid, a halo (HALO) region extending from the exterior of the UEDGE computation grid to the material wall, inner and outer divertor (DIV) regions extending from the X-point to the divertor targets, and a private flux (PFR) region. Also shown in the figure is a CORE region, which is represented in the GTNEUT calculation as an albedo (fractional reflection) boundary condition for the inner surface of the PED region.

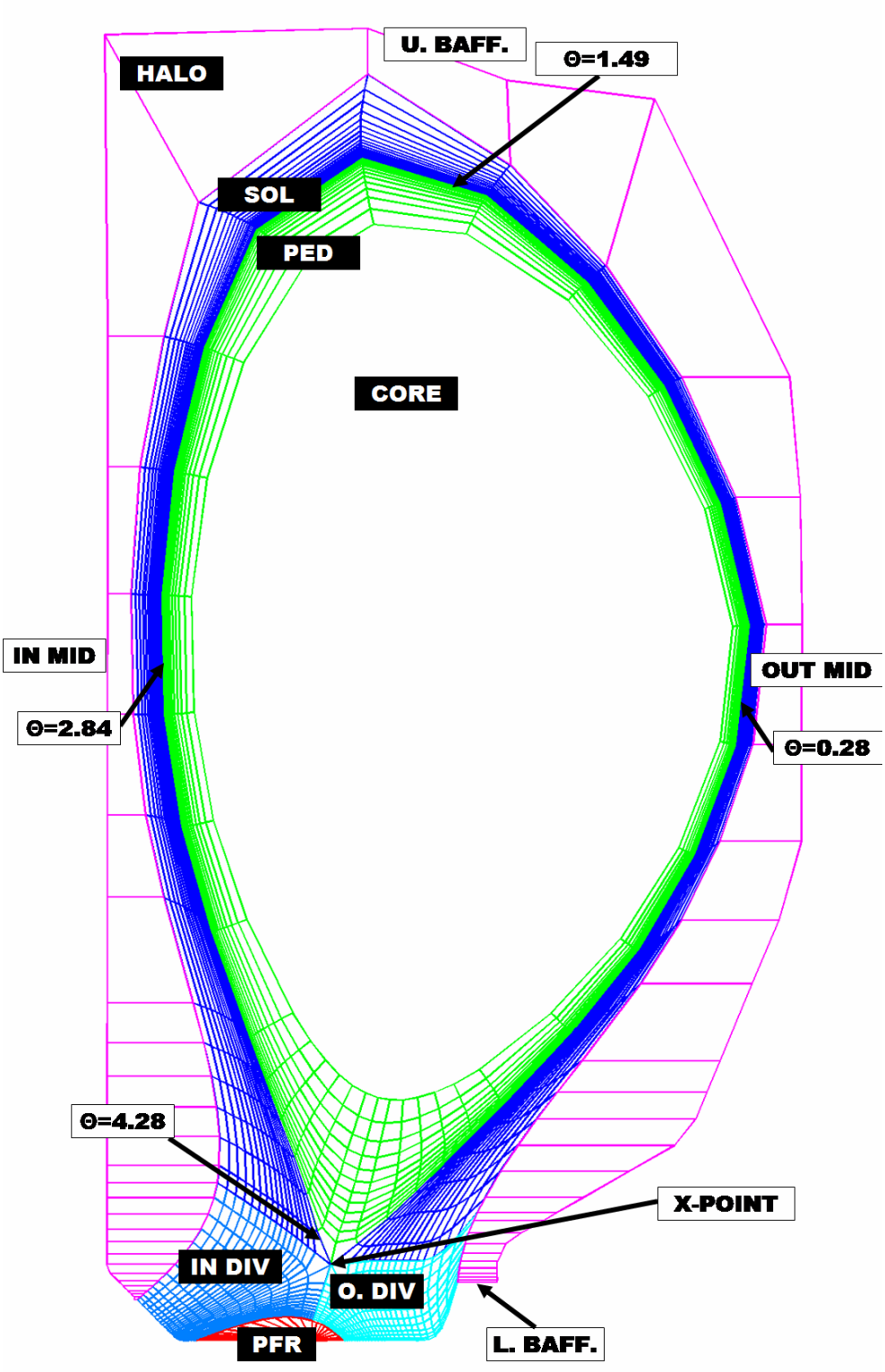

Figure 31: 2D geometric model used in GTNEUT analysis.

The lines going around the plasma in the poloidal direction in Fig. 31 are the flux surfaces produced from the EFIT. "Radial" lines crossing these flux surfaces extend inward from the separatrix across the PED region to the CORE region (at $\rho < 0.93$) and outward from the separatrix across the SOL to the outer edge of the UEDGE computational grid, and then across the surrounding HALO region to the material wall. The regions formed by these intersecting "poloidal" and "radial" line define the computation grid for the GTNEUT calculation. Neutral densities, ionization rates, etc. are calculated in the grid regions formed by the intersection of these "radial" and "poloidal" surfaces. Each of these grid regions can be identified by a "radial" location associated with the bounding flux surfaces and a "poloidal" location defined by where its bounding radial lines intersect the separatrix (this poloidal distance along the separatrix is measured in the clockwise direction with respect to an origin where the separatrix intersects the target plate in the inner divertor). For example, a poloidal distribution of ionization rates at $\rho = 0.96$ in the pedestal would be constructed by plotting the ionization rate in each grid region between the flux surfaces bounding $\rho = 0.96$ versus the poloidal location at which the "radial" lines bounding the grid region intersected the separatrix. The poloidal distribution of the total ionization in the pedestal would then be plotted by summing the ionization over all cells in the pedestal bounded by two "radial" lines intersecting the separatrix at a given poloidal distance along the separatrix.

The background plasma parameters in the upper PED, outboard PED and SOL were taken from the Thomson scattering data and used to benchmark the UEDGE calculation of the background plasma parameters throughout the PED, SOL and DIV regions [16]. The HALO region was assumed to have a uniform temperature and density

distribution (ne , ni = 0.13e19 #/m^3 and Te , Ti = 12 eV). The PFR is assumed to have a uniform temperature and density (ne , ni = 1e18 #/m^3 and Te , Ti = 3 eV). The plasma CORE is not included in the GTNEUT calculation, but the net number of neutrals crossing the boundary from the PED to the CORE are considered to be ionized in the core.

Several points of interest are also illustrated in Fig. 31. The lower and upper baffle locations (L. BAFF. and U. BAFF.) are where the recycling calculated by the Window Frame method and shown in Table 1 is assumed to take place.

In order to discuss the poloidal distribution of neutral particles and reaction rates, it is convenient to define certain 'poloidal' reference points. It is easiest to do this in terms of an angle θ. Starting at the outboard midplane (OUT MID), θ = 0. If we consider the separatrix in the 2D calculation model as a 1D strip starting at θ = 0, the midpoint of the first computation cell occurs at θ = 0.28. Thus, θ = 0.28 is the OUT MID reference point. Continuing along the 1D strip (separatrix) in the counterclockwise direction, the next reference point is the cell along the separatrix located at the upper baffle (U. BAFF.) location (θ = 1.49). The next reference point is the inner midplane (IN MID) location at θ = 2.84. Finally, the last reference point is at the X-Point. There are two sides of the X-Point, an inboard and an outboard side. For our figures showing the poloidal distributions, the SOL always starts at the inboard side of the X-Point (θ = 4.28) and continues in a clockwise fashion around the separatrix back to the outboard side of the X-Point. The divertor regions are represented as short extensions on both ends of the SOL.

6.2 Overall particle balance

The overall ion particle balance on the region inside the separatrix (CORE + PED) is shown in Table 6 for both sets of background plasma parameters.

Table 6: Ion global particle balance on CORE+PED

	'Attached'	'Detached'	Determined
Loss--Ion Outflow Across Separatrix (#/s)[a]	**2.74E+21**	**2.74E+21**	Experiment
Sources			
Neutral Beam Ion Source(#/s)	0.386E+21	0.386E+21	Known
Ionization of Recycling Neutrals (#/s)	0.927E+21	1.313E+21	GTNEUT[b]
Total Ion Source(#/s)	**1.316E+21**	**1.699E+21**	
Ion (Outflow – Sources) (#/s)	**1.424E+21**	**1.041E+21**	

[a] ***determine experimentally using the Porter method*** **[94]**
[b] ***see Refs*** **[17, 95-97]*for comparison of GTNEUT with Monte Carlo and experiment***

If the UEDGE solution for the background plasma parameters and the GTNEUT solution for the neutral particle ionization rates were self-consistent, and if the Porter method [94] for determining the experimental ion outflow across the separatrix was precise, then the experimental outflow of ions across the separatrix should be balanced at steady-state by the neutral beam ion source plus the ionization of recycling neutrals in the CORE+PED regions. As shown in Table 6, there is a significant discrepancy between the sources of ions in the core (due to neutral beams and to the calculated neutral inflow across the separatrix) and the experimental ion outflow across the separatrix determined by the Porter method [94]. This discrepancy is larger than the quoted ±30% uncertainty in the determination of the experimental ion outflow associated with uncertainty in the experimental data [94]. However, as discussed at the end of section II, there are other unquantified uncertainties in the determination of the experimental ion outflow across the separatrix.

As indicated by the last line in Table 6, the use of the "detached" UEDGE background plasma parameter (with the larger recombination neutral source) results in significantly better agreement between the ion sources and losses. In both cases the difference between ion sources and losses are larger than the estimated [94] 30% error in the determination of the ion outflow across the separatrix. This result is consistent with the earlier conclusion [16] that the plasma is probably detached at the inner divertor in this shot.

The overall neutral particle balance between sources (ion recycling and recombination) and sinks is shown in Table 7 for both the 'attached' and 'detached' background plasma parameters. The distribution of neutral particle ionization rates among the various regions is also given in Table 7. Clearly, the majority of the ionization (≈70%) takes place in the divertors, and only 7% of the recycling and recombined neutrals actually make it across the separatrix to fuel the pedestal and core. The percentage of the total neutral ionization that is in each region and the percentage of the total neutral source from recycling and from recombination is given in parentheses in Table 7.

Table 7: Global neutral particle balance on entire computation domain

	'Attached'	'Detached'	Determined
Ionization (Sinks) (#/s)			
CORE	0.129E+21 (1%)	0.193E+21 (1%)	GTNEUT
PED	0.798E+21 (6%)	1.120E+21 (6%)	"
SOL	1.910E+21 (15%)	2.670E+21 (14%)	"
HALO	1.120E+21 (9%)	2.020E+21 (11%)	"
IN DIV	4.380E+21 (33%)	7.390E+21 (39%)	"
OUT DIV	4.770E+21 (36%)	5.430E+21 (29%)	"
PFR	0.107E+19 (<<1%)	0.365E+19 (<<1%)	"
Total Ionization	**13.108E+21**	**18.827E+21**	
Sources (#/s)			
Ion recycling	13.217E+21 (99%)	13.217E+21 (66%)	experiment
Recombination	0.147E+21 (1%)	6.243E+21 (34%)	UEDGE
Total Sources	**13.364E+21**	**19.460E+21**	

6.3 Neutral particle fluxes recycling from wall surface and crossing separatrix

With reference to the poloidal locations identified in Fig. 31, the neutral particle fluxes recycling from the wall are shown in Fig. 32. Two types of recycling neutral particle fluxes are shown—those produced by the recycling of the experimental incident ion fluxes (which are inputs to the GTNEUT calculation) and those produced by the recycling of the calculated (GTNEUT) incident neutral fluxes. The incident ion fluxes measured by the probes at the divertor targets of course recycle as neutrals from those locations, but the incident ion fluxes determined from probe measurements on the outboard using the "window frame" technique are represented in the GTNEUT calculation as being localized at the upper and lower baffles, and are shown as single points in Fig. 32. The recycling neutral fluxes from incident ions are consistent with the measured ion fluxes to the wall—largest near the divertors but with a significant peaking at the upper and lower baffles.

These neutral fluxes from the wall resulting directly from the incident ion fluxes then charge-exchange somewhere in the edge plasma and produce neutral fluxes incident on the wall which in turn recycle as neutral fluxes, charge exchange and produce neutral fluxes to the wall, etc. The sum total of the recycling neutral fluxes from the wall due to charge exchange (and elastic scatter) incident neutral fluxes on the walls are also shown in Fig. 32, for the GTNEUT calculations using both the 'attached' and 'detached' background plasma parameters. The recycling fluxes produced by the recycling incident charge exchange neutral fluxes dominate the recycling fluxes produced by incident ion fluxes. The poloidal length along the chamber wall is measured clockwise from the point on the chamber wall in the lower left of Fig. 31 where the inner divertor and halo regions meet.

The recombination source is calculated in all regions but is only significant in the inner divertor region. As shown in Table 7, the recombination source is only 1% of the total neutral source for the "attached" background plasma, but is 34% of the neutral source for the "detached" background plasma.

The inward neutral fluxes across the separatrix are shown in Fig. 33. Both the partial inward flux and the net inward flux (when the outward flux of charge-exchanged and scattered neutrals is subtracted) across the separatrix are shown. The inward partial flux is directly related to the recycling source, while the net inward flux is the quantity relevant to particle balance inside the separatrix. The plasma is fueled primarily through the X-point region by neutrals recycling from the divertor targets or recombining in the inner divertor region. There is a strong secondary fueling due to ions recycling at the upper and lower baffles.

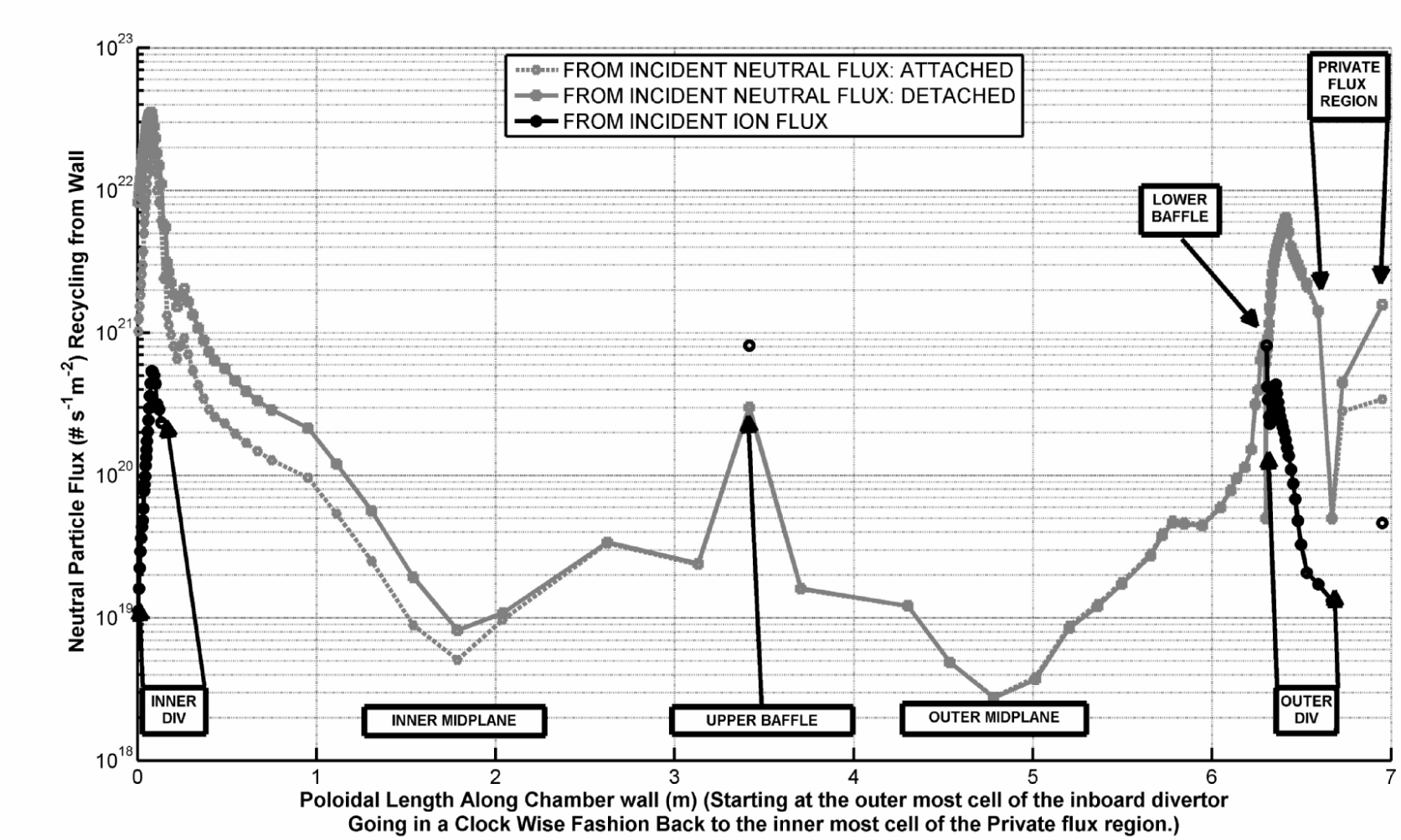

Figure 32: Poloidal distribution of neutral fluxes recycling from the wall

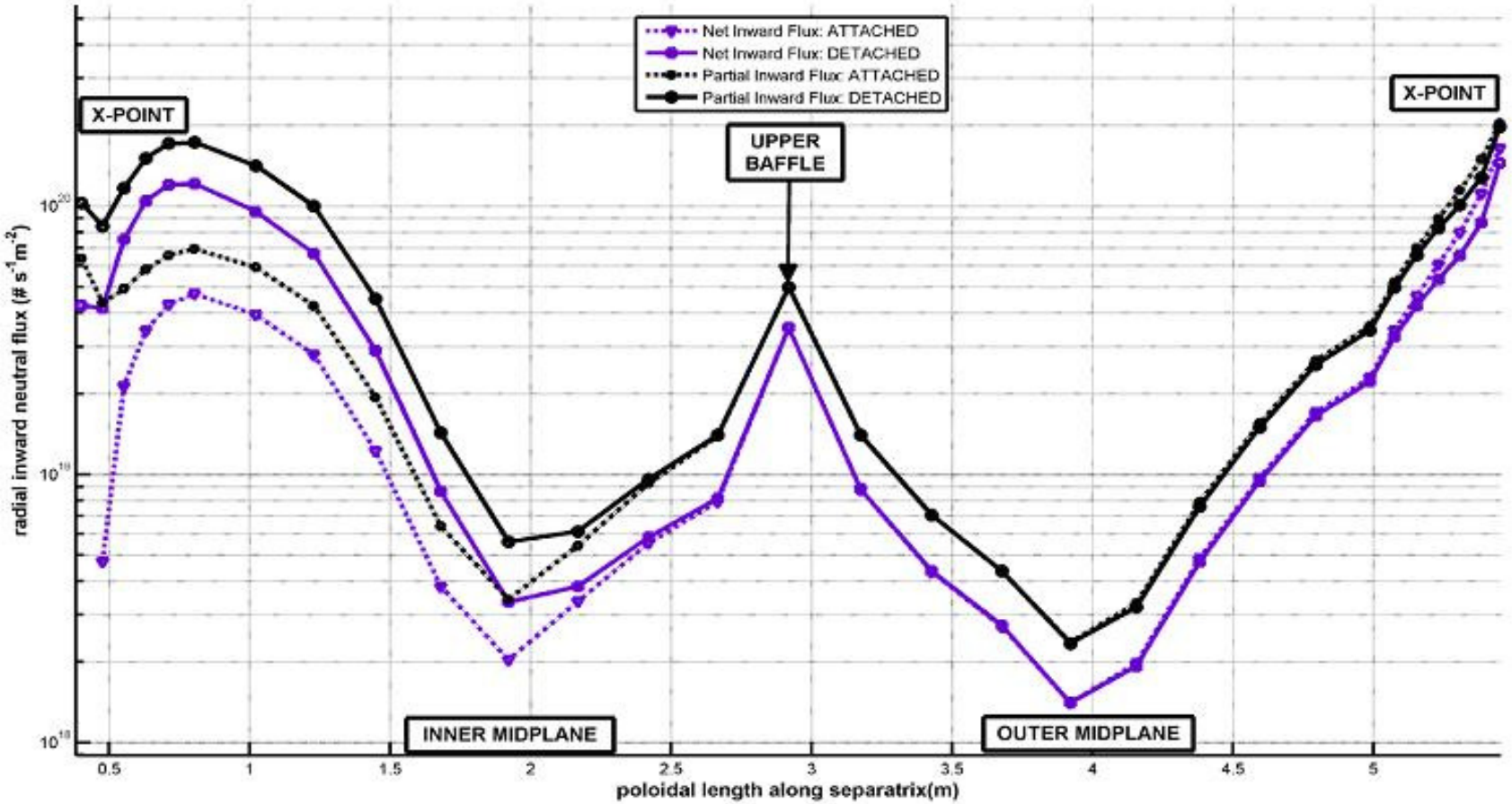

Figure 33: Inward partial (in) and net (in minus out) neutral fluxes across the separatrix

6.4 Poloidal distributions of ionization and charge-exchange rates

A neutral particle recycling from the wall or formed by recombination will ultimately be ionized. It is of interest to examine in which region this ionization will take place. The "radially-summed" ionization rate in the various regions defined in Fig. 31 is plotted as a function of poloidal location along the separatrix in Figs. 34 and 37.

With reference to Fig. 31, the computational grid is constructed so that for each segment along the separatrix there is a corresponding set of SOL regions extending outward, beyond which is a HALO region, and a corresponding set of PED regions extending inwards. In the previous Monte Carlo (DEGAS2) calculations[16] of this discharge, the total ionization in all the PED regions "behind" a given segment along the separatrix were summed and divided by the surface area of that separatrix segment (the segment length extended toroidally around the plasma chamber) in order to obtain a proxy for the poloidal distribution of the radial neutral particle flux crossing the separatrix (the statistical nature of the Monte Carlo solution leads to a rather erratic direct calculation of this quantity). In order to touch base with these Monte Carlo calculations, this same quantity calculated with GTNEUT is plotted in Figs. 34 and 35 as the PED ionization (with units of flux), for the detached and attached plasma background case. Similar quantities constructed from the ionization in the corresponding HALO region and summed "radially" over the corresponding SOL regions are also plotted. The computation grid extends almost perpendicular to the separatrix in the two divertor regions, and the summed ionization rates over the regions corresponding to a given segment along the separatrix (divided by the area of that segment extended toroidally) is

plotted as the INNER DIV and OUTER DIV ionization in Figs. 36 and 37. The main difference between the ionization rates shown in Fig. 34 and 35 for the detached case and those calculated with the attached background plasma parameters are factor of 2 lower ionization rates in the HALO, SOL and PED ionization vicinity of the inner divertor due to the lower recombination source for the attached case.

The major part of the ionization (≈70%) takes place in the divertor and, to a lesser extent, in the scrape-off layer (≈15%). The poloidal distribution of ionization roughly corresponds to the poloidal distribution of the recycling sources shown in Fig. 4 and the location of a strong recombination source in the inner divertor for the 'detached' background plasma parameters. The reduction in the inner divertor ionization rate just in front of the target, where the temperature is about 1 eV, is notable in Fig. 34 for the 'detached' background plasma parameters.

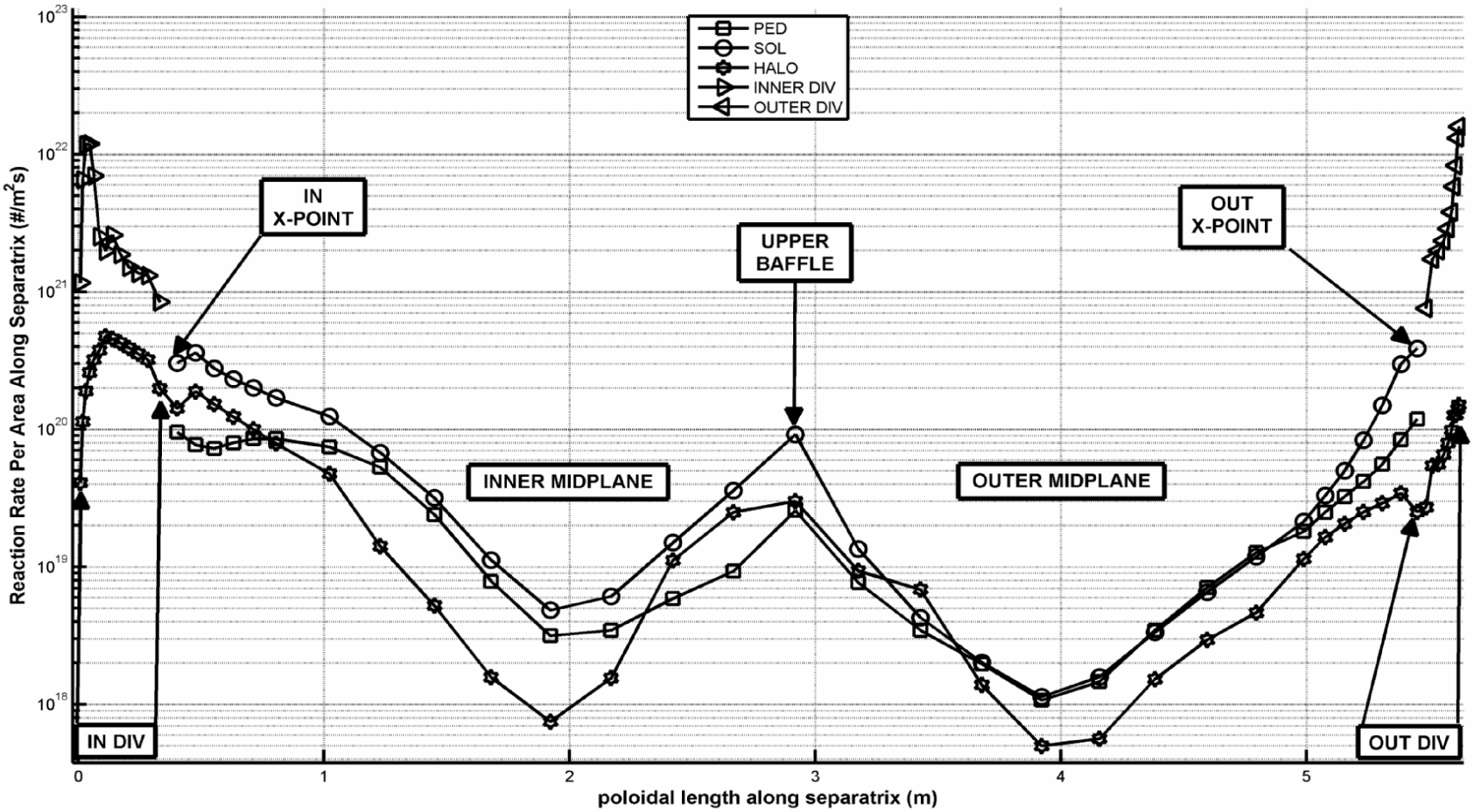

Figure 34: Poloidal distribution of ionization rates per unit area along the separatrix (DETACHED)

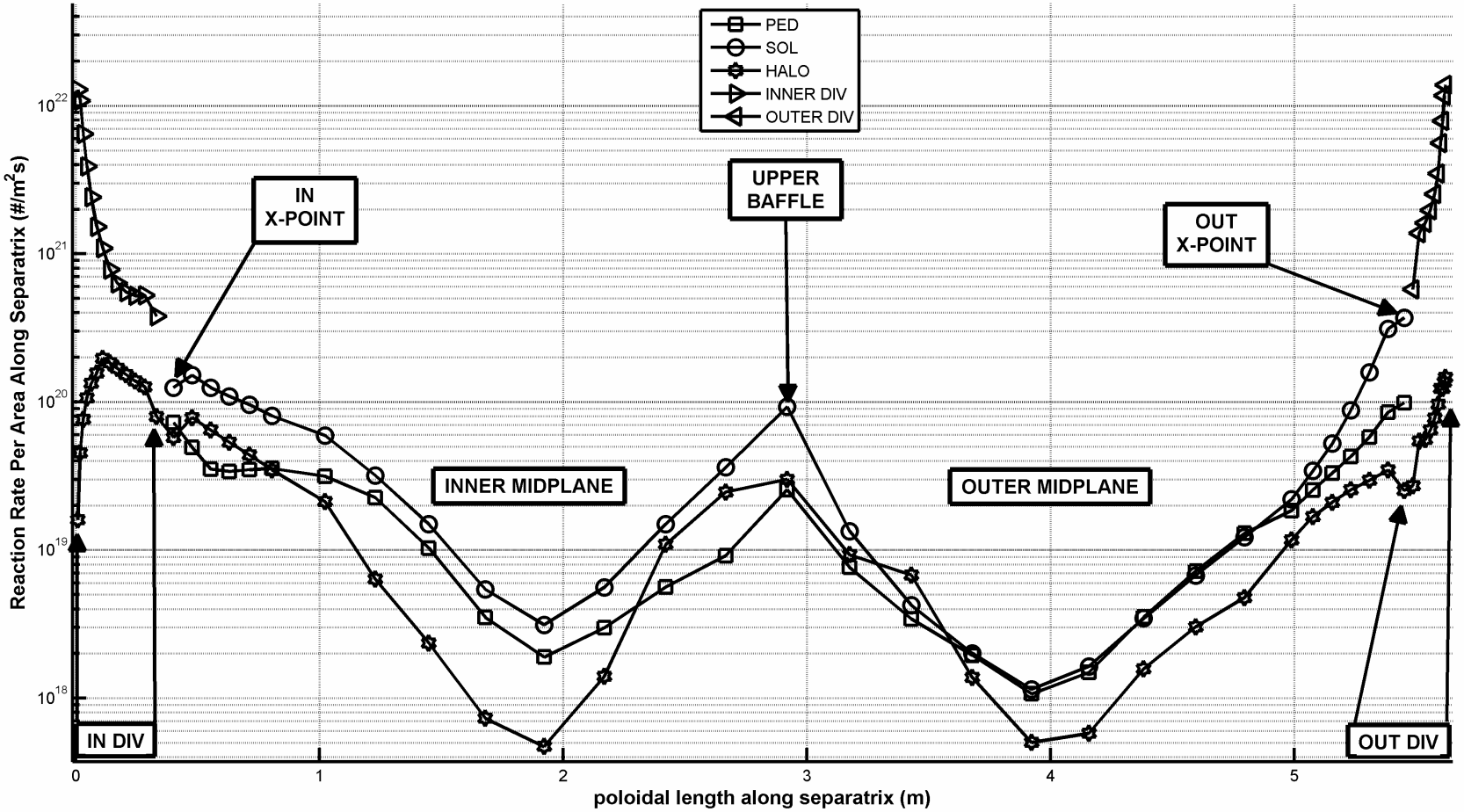

Figure 35: Poloidal distribution of ionization rates per unit area along the separatrix (ATTACHED)

Charge-exchange reaction rates, constructed in the same manner as discussed above for ionization, are shown in Fig. 36 for the detached plasma background and Fig. 37 for the attached. The poloidal distribution roughly corresponds to the poloidal distribution of the wall recycling neutral fluxes and recombination source in the inner divertor. The charge-exchange rates are generally comparable to or larger than the ionization rates; the enormous charge-exchange rate in the inner divertor for the "detached" background plasma is notable. For the "attached" background plasma the large peaking of the charge-exchange rate in the inner divertor is reduced by several orders of magnitude and the charge-exchange rates in the HALO, SOL, and PED in the vicinity of the inner divertor are reduced by a factor of 2.

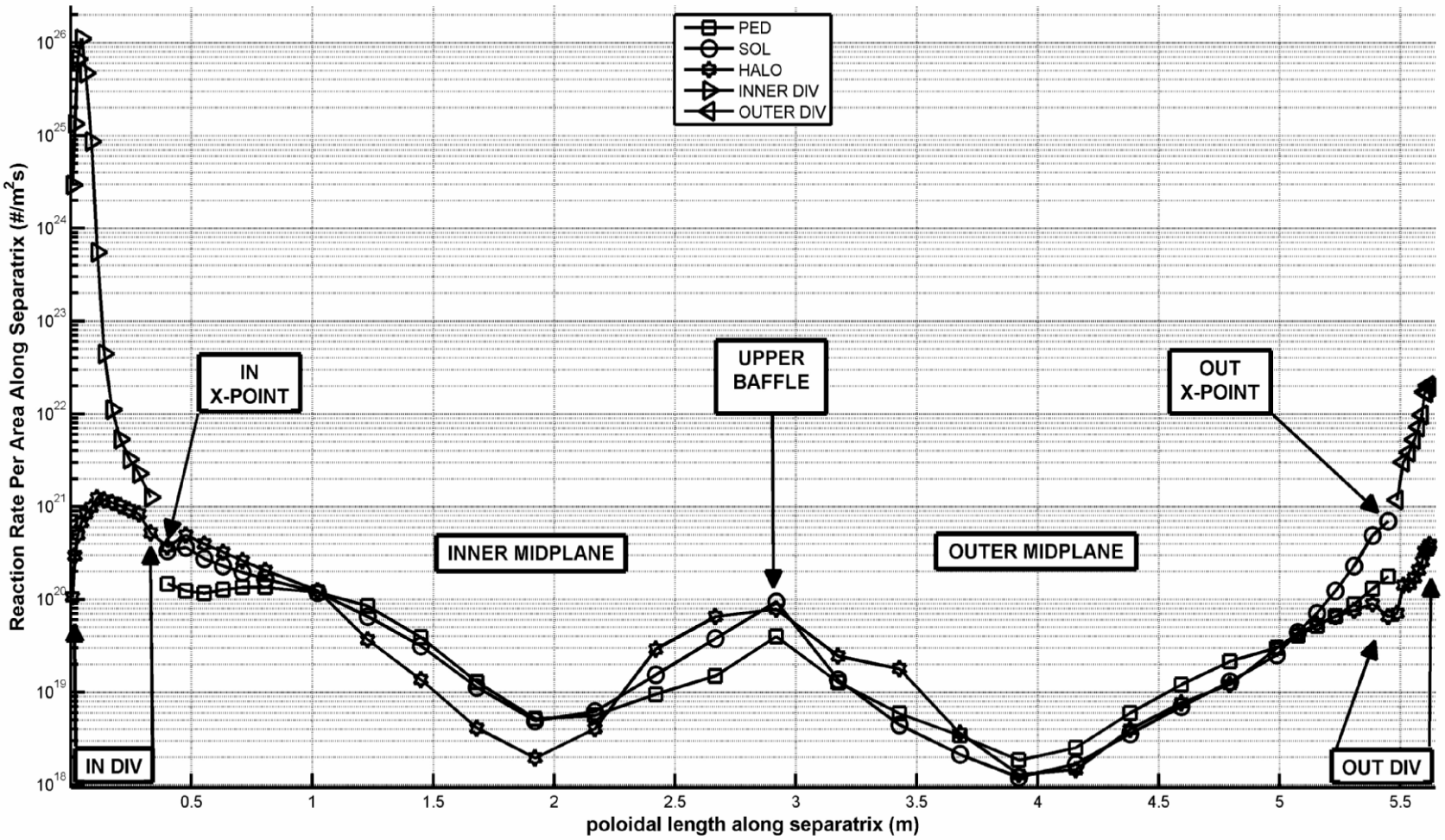

Figure 36: Poloidal distribution of charge-exchange rates per unit area along the separatrix (DETACHED)

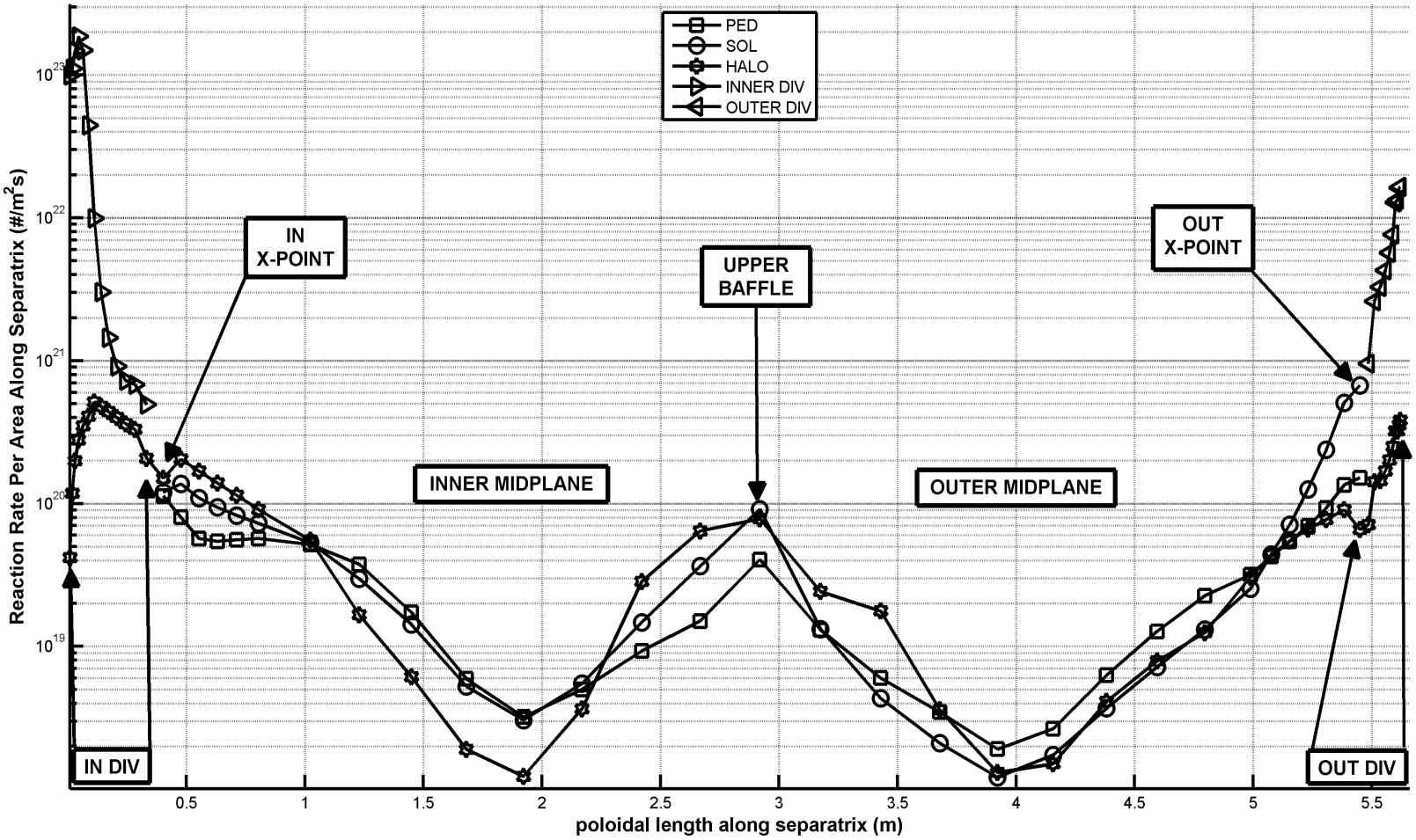

Figure 37: Poloidal distribution of charge-exchange rates per unit area along the separatrix (ATTACHED)

6.5 Neutral penetration of the edge pedestal

The poloidal distribution over the flux surface of the neutral atom density is plotted for several values of the normalized radius (rho) in Fig. 38, for the detached plasma background case. For the 'attached' plasma background (Fig. 38), the ionization rates were a factor of 2 lower in the vicinity of the inner divertor, because of the lower recombination source. Similar distributions were calculated for the ionization and recombination rates.

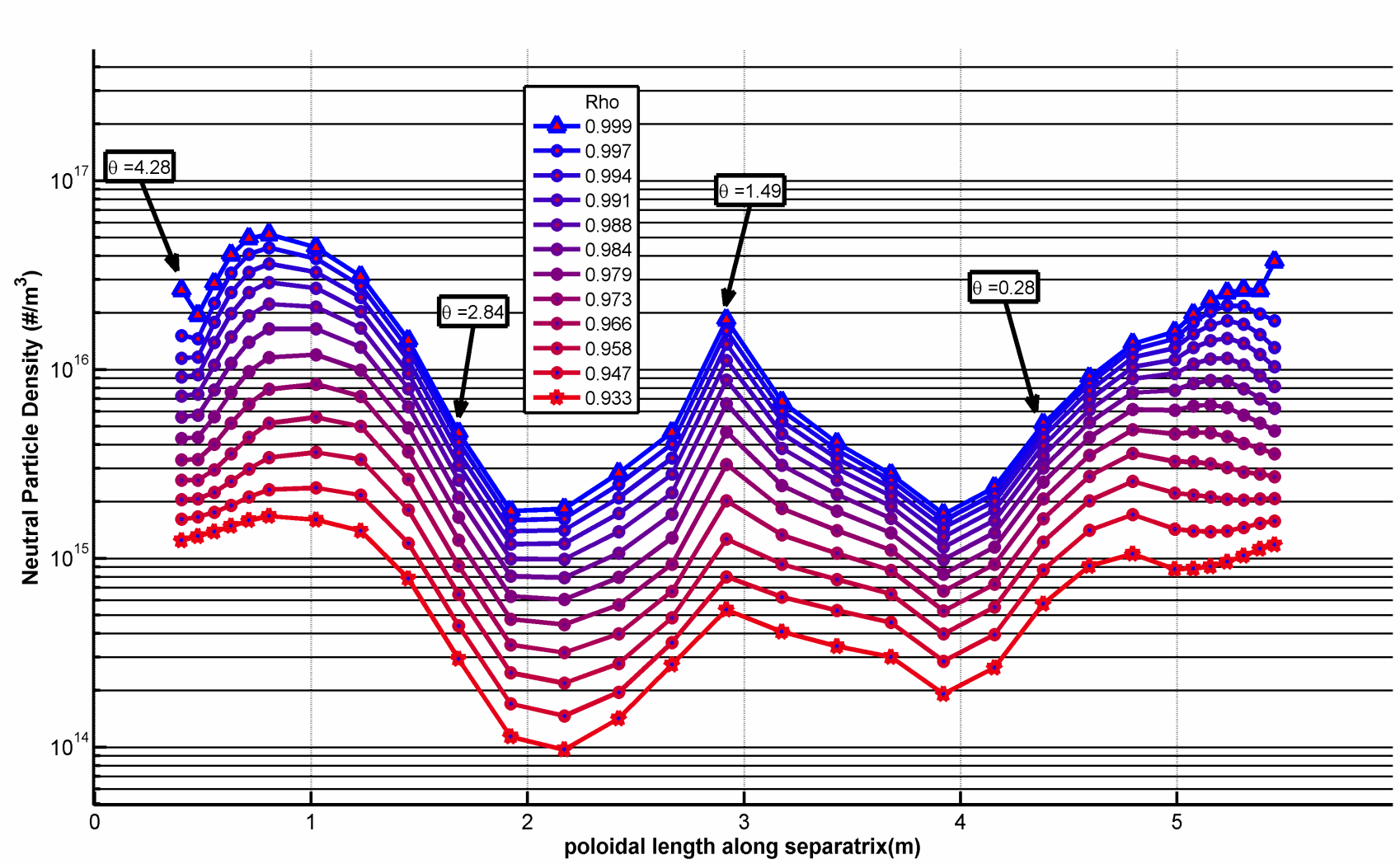

Figure 38: Poloidal distribution of neutral density over flux surface in edge pedestal (DETACHED). (see Fig. 31for locations corresponding to θs)

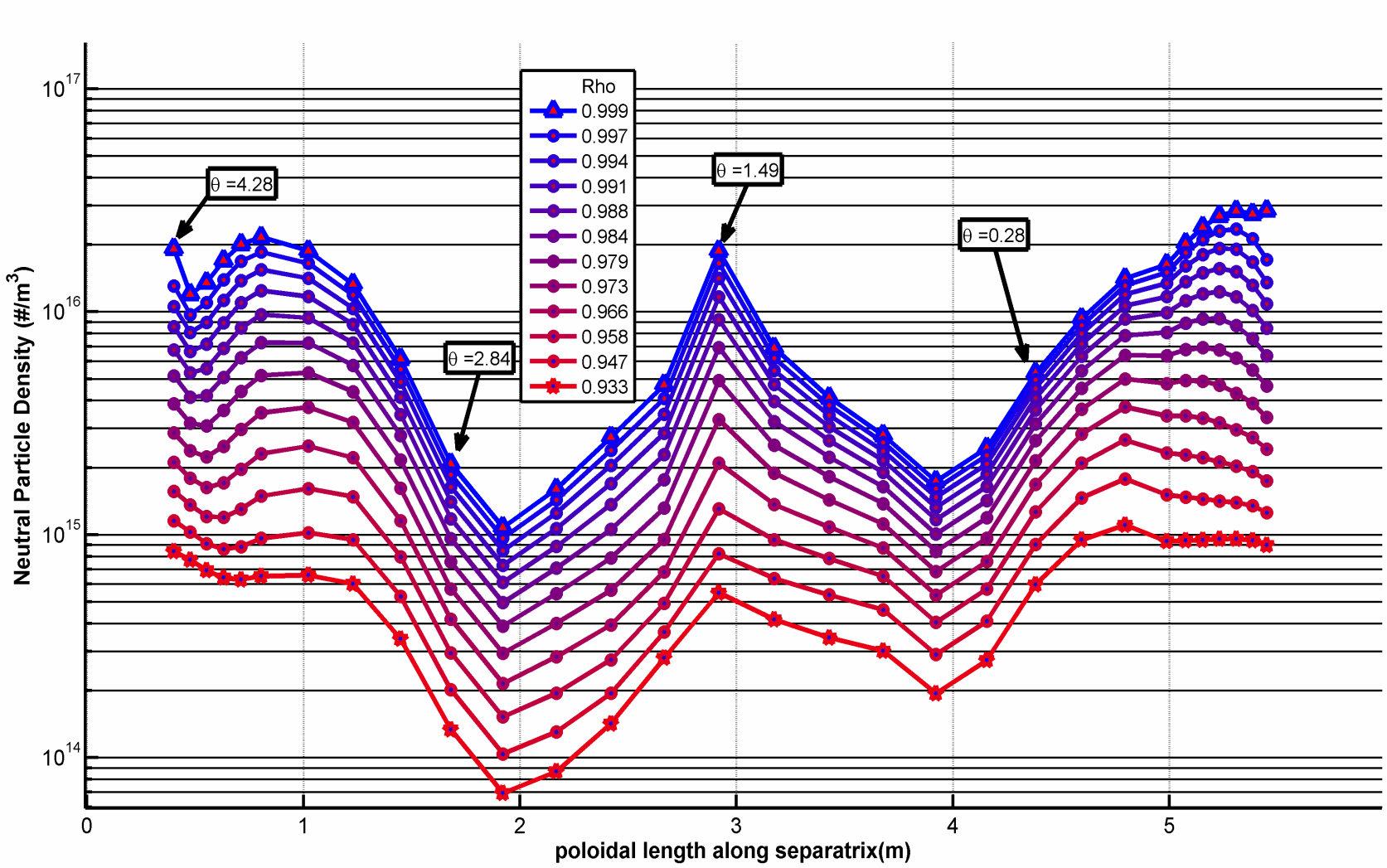

Figure 39: Poloidal distribution of neutral density over flux surface in edge pedestal (ATTACHED). (see Fig. 31 for locations corresponding to θs)

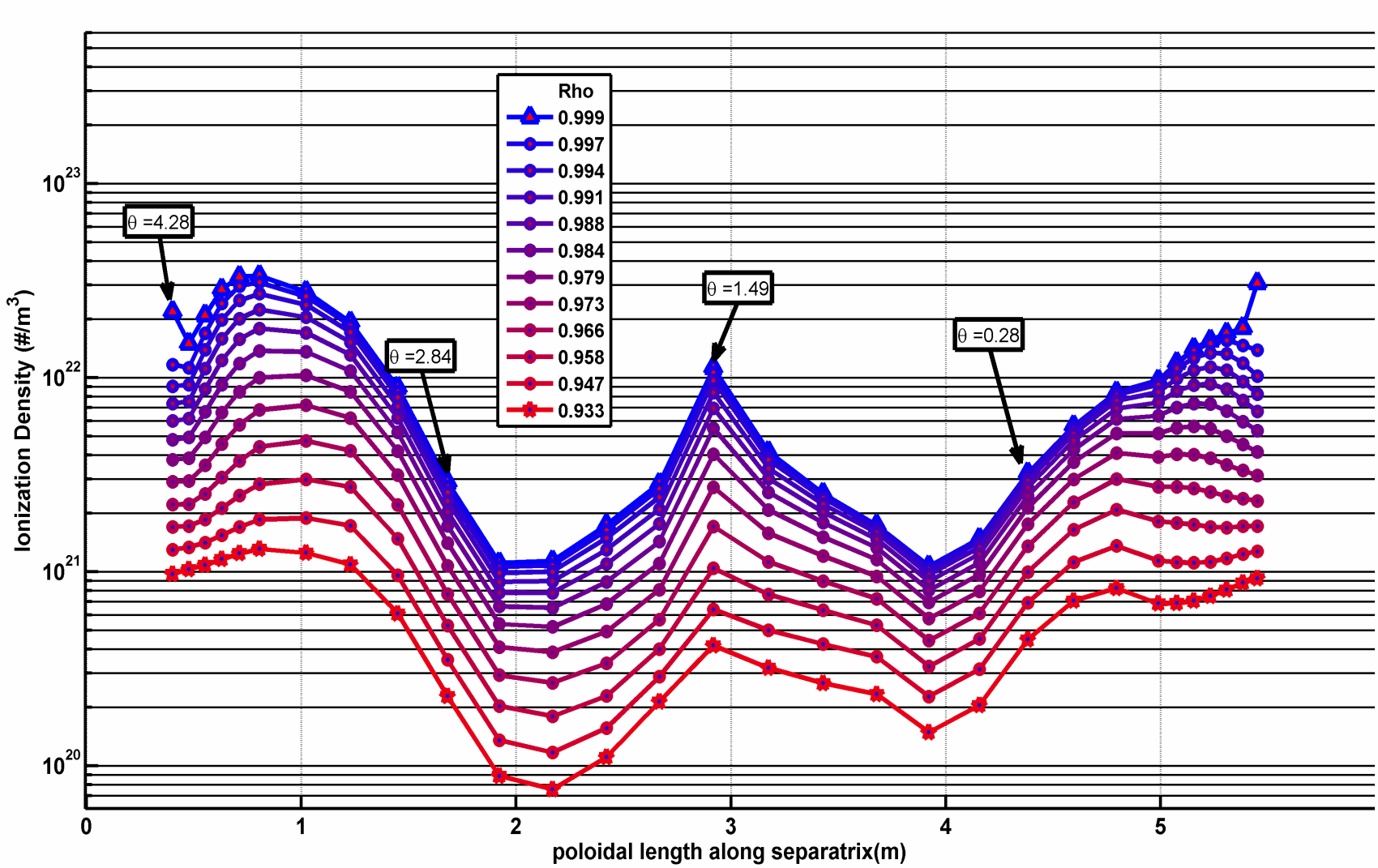

Figure 40: Poloidal distribution of ionization density over flux surface in edge pedestal (DETACHED). (see Fig. 31 for locations corresponding to θs)

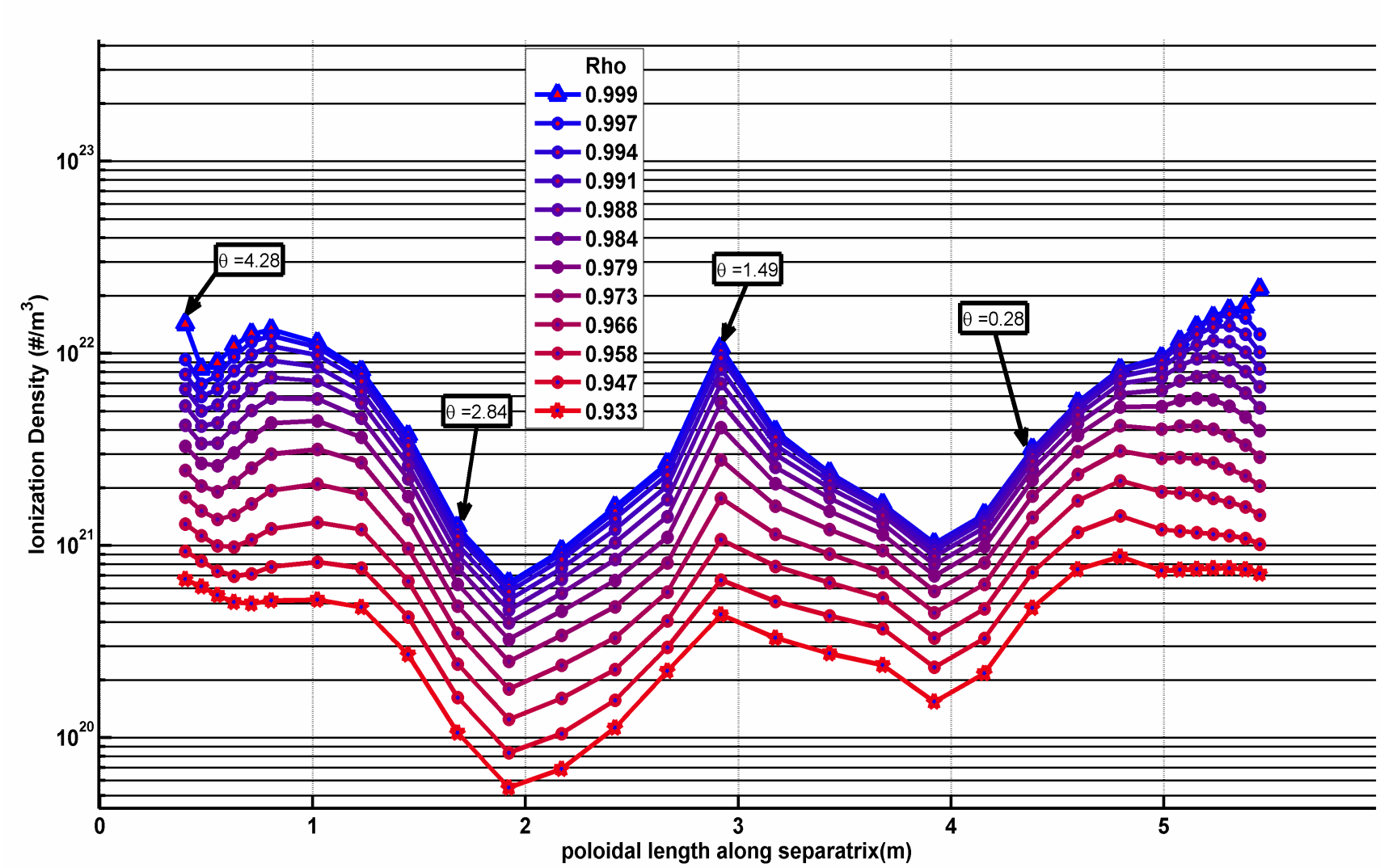

Figure 41: Poloidal distribution of ionization density over flux surface in edge pedestal (ATTACHED). (see Fig. 31 for locations corresponding to θs)

It is clear that there are orders of magnitude variations in the neutral atom density, the ionization fueling source, the electron ionization cooling and the ion charge-exchange cooling over the flux surface in the plasma edge pedestal. This raises questions about the adequacy of 1D ion particle and energy transport calculations that are frequently made (e.g. Ref. [10]) in the edge pedestal region in the presence of strong neutral recycling. For example, the more than two orders of magnitude difference between the ionization rate in the pedestal just above and to the left of the X-point (poloidal length ≈ 1) and the upper inboard quadrant (poloidal length ≈ 2) causes a similar variation in the ionization particle source and electron cooling rate which could drive edge thermal instabilities (e.g. MARFEs) that might not be predicted by a 1D radial calculation in which the poloidal variations were averaged out.

6.6 Importance of different neutral particle sources in fueling pedestal and core

The importance of a given neutral particle source (e.g. upper baffle recycling or inner divertor recombination) for fueling the pedestal and core depends on two factors—the strength of the source and the fraction of the particles from a given source that are transported inward across the separatrix. The poloidal distribution of the PED ionization rates (constructed by radially summing the ionization occurring in the PED regions inboard of a given segment along the separatrix and dividing by the area of that segment extended toroidally around the plasma, as previously described) resulting from each individual neutral particle source are shown for the 'attached' and 'detached' background plasmas in Figs. 42 and 43. Not surprisingly, the inner and outer divertor ion recycling sources are most important for fueling the region around the x-point, for the 'attached'

background plasma, and the upper baffle recycling ion source is most important for fueling the top of the plasma near the upper baffle. For the ‘detached’ background plasma, the recombination source (mostly in the inner divertor) is also an important contributor to the x-point fueling of the pedestal.

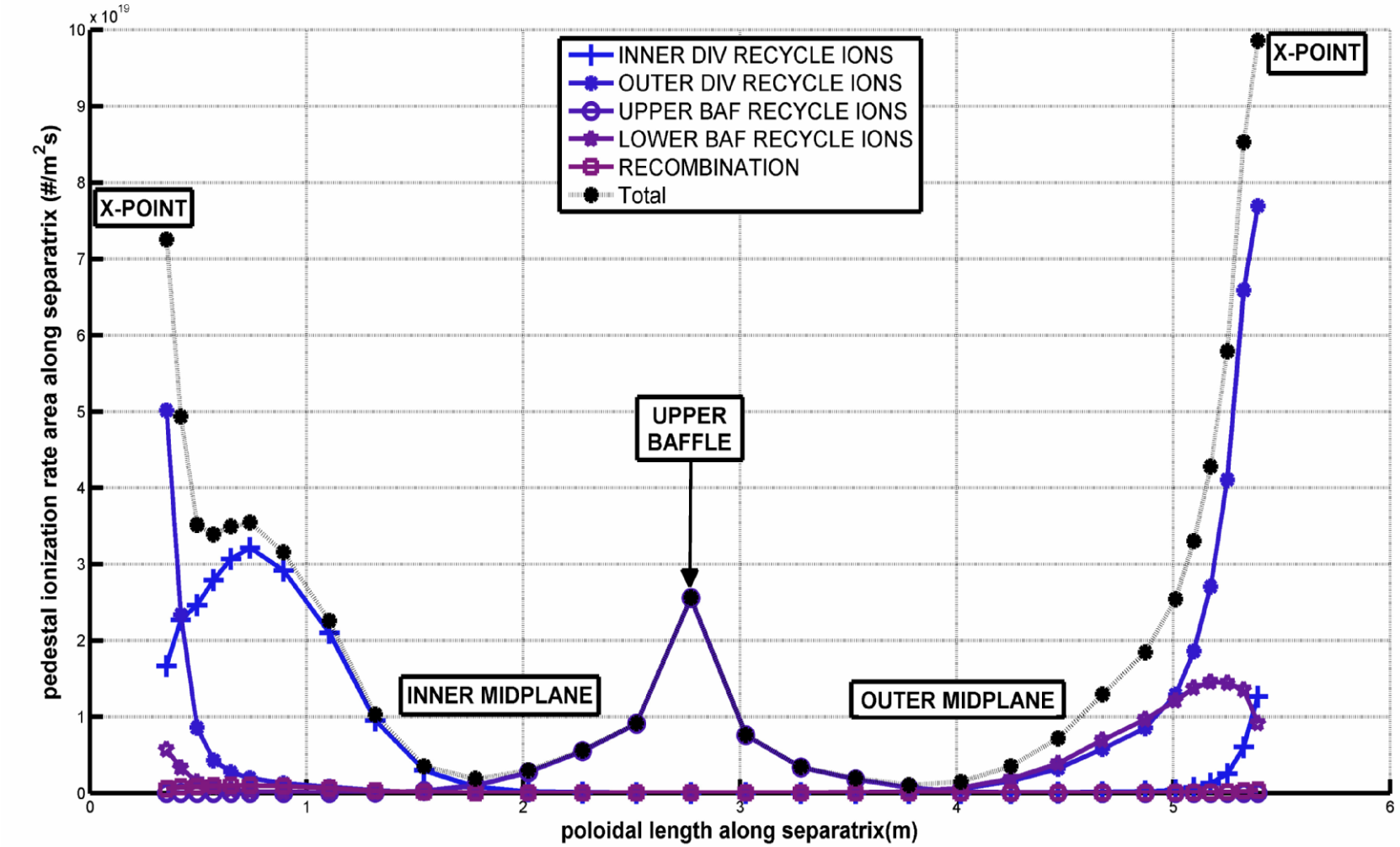

Figure 42: Poloidal distribution of PED ionization rate per unit area along the separatrix due to each recycling source separately. (ATTACHED)

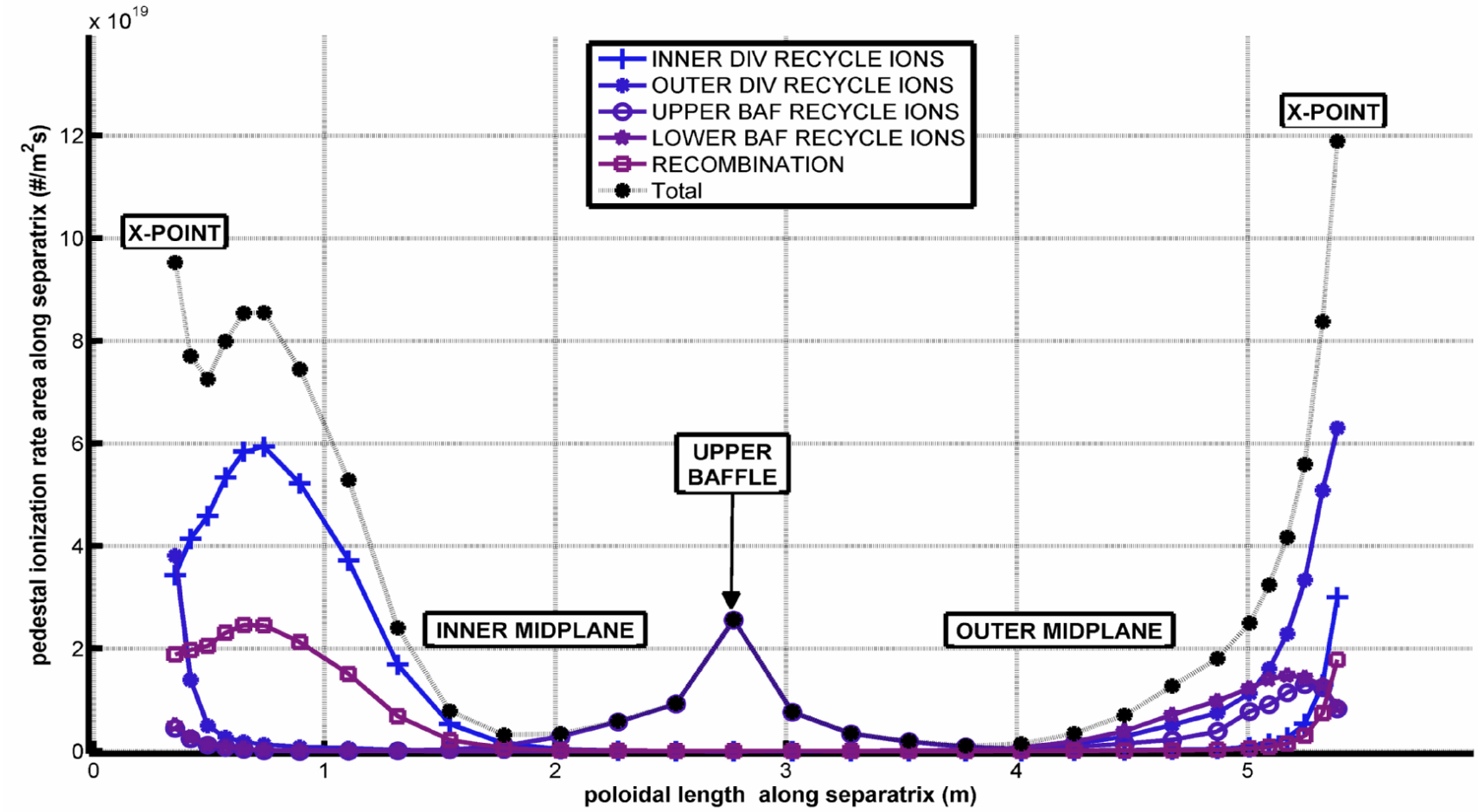

Figure 43: Poloidal distribution of PED ionization rate per unit area along separatrix due to each recycling source separately. (DETACHED)

In order to characterize the likelihood that a neutral particle from a given source would be transported across the separatrix and cause a fueling (ionization) event on a given flux surface (rho) in the pedestal, we first calculated ionization rates as a function of rho and theta, like those shown in Figs. 38 and 39, for each source. We then summed these plots poloidally to obtain the total ionization rate on each flux surface due to each source, then divided by the respective source strengths to obtain the fraction of neutrals from a given source that would cross the separatrix to refuel the pedestal on a given flux surface. This "fraction" is plotted vs. flux surfaces (rho) in Figs. 44 and 45 for the 'attached' and 'detached', respectively, background plasma parameters. Neutrals recycling from the upper and lower baffles are more effective at penetrating across the separatrix to fuel the pedestal than are neutrals recycling or recombining in the divertor. This is understandable because of the shorter distance (in mean free path) the neutrals must travel from the baffle to separatrix than from the divertor plates to the separatrix.

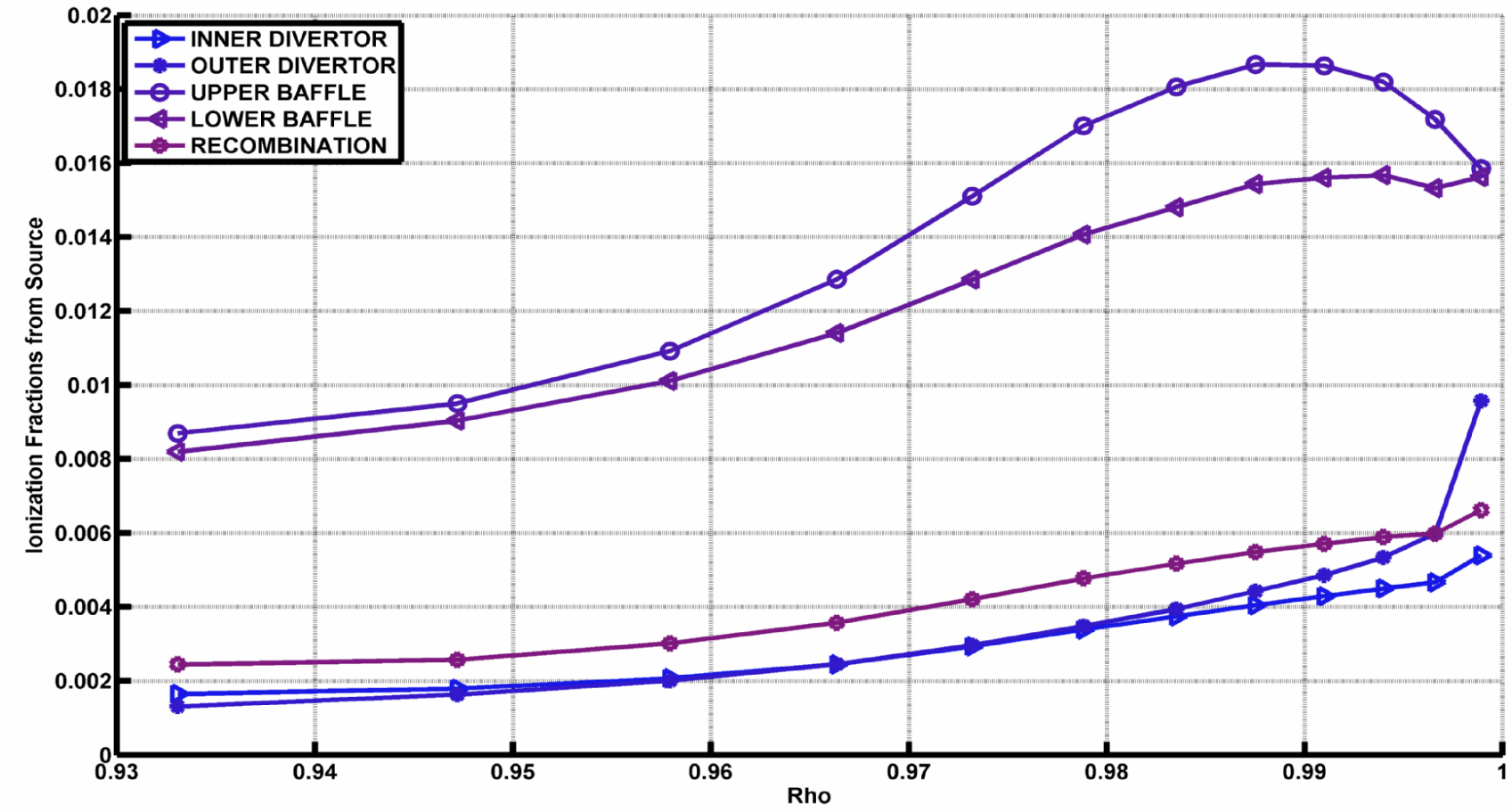

Figure 44: Effectiveness of neutrals from different sources in fueling the pedestal (fraction of source neutrals ionized on each flux surface in pedestal) (ATTACHED)

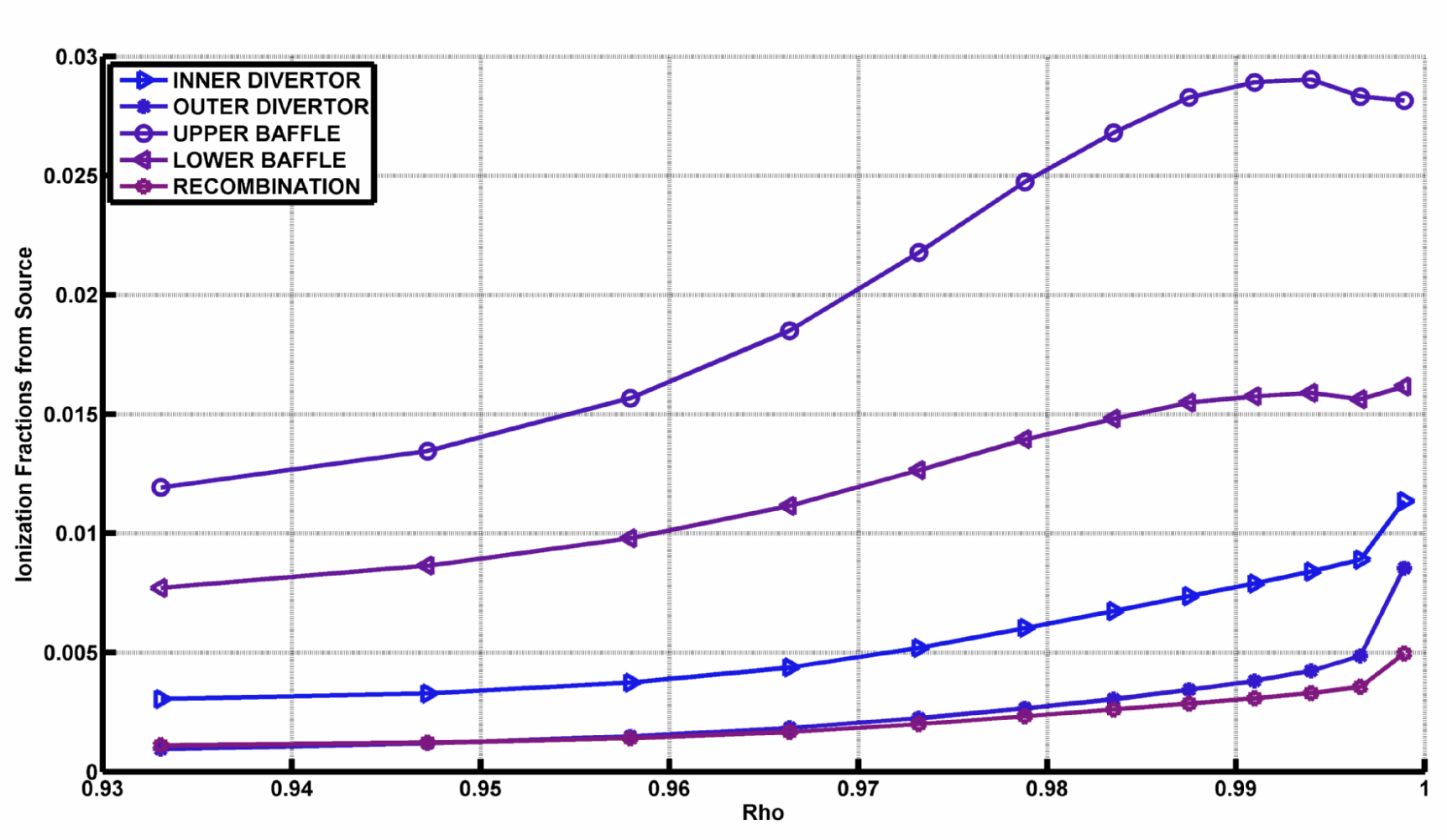

Figure 45: Effectiveness of neutrals from different sources in fueling the pedestal (fraction of source neutrals ionized on each flux surface in pedestal) (DETACHED)

Neutrals recycling from the inner divertor are more effective in fueling the pedestal than neutrals recycling from the outer divertor for the "detached" case in which the ionization mean free path in the cold inner divertor become longer.

Summing the ionization rate due to each source over the entire pedestal and core regions (basically integrating the pedestal integration of Figs. 44 and 45 over the radial extent of the pedestal), and then dividing by the strength of that source, yields the fraction of the neutrals produced by each source that crosses the separatrix to fuel (ionize in) the confined plasma shown in Table 8.

Table 8: Fraction of neutrals from each source ionized in PED+CORE

CASE	Fraction					
	ATTACHED			DETACHED		
	PED	CORE	PED+CORE	PED	CORE	PED+CORE
Upper baffle recycling	17.5%	4.0%	**21.50%**	27.6%	5.4%	**33.00%**
Lower baffle recycling	15.2%	3.7%	**18.90%**	15.8%	3.6%	**19.40%**
Inner divertor recycling	4.0%	0.7%	**4.70%**	7.6%	1.5%	**9.10%**
Outer divertor recycling	4.7%	0.4%	**5.10%**	3.8%	0.3%	**4.10%**
Recombination	2.4%	1.3%	**3.70%**	3.0%	0.5%	**3.50%**

It must be emphasized that, although individual neutrals recycling from the baffles have better chance of fueling the pedestal than do individual neutrals recycling from the divertor, the greater number of neutrals recycling or recombining in the divertor than recycling from the baffles results in the divertor being the principal source of neutrals refueling in this discharge, as shown in Figs 46 and 47, which were obtained by multiplying the curves in Figs. 44 and 45 by the respective source strengths given in

Table 5 and recombination strengths given in Table 7. These figures also show how the relative contributions of the various neutral sources to fueling the pedestal depends on the background plasma parameters (note that only the recombination neutral source calculated with UEDGE is different for the GTNEUT calculations with the "attached" and "detached" plasma backgrounds, since the ion recycling neutral sources are taken from experiment and are independent of the background plasma parameters).

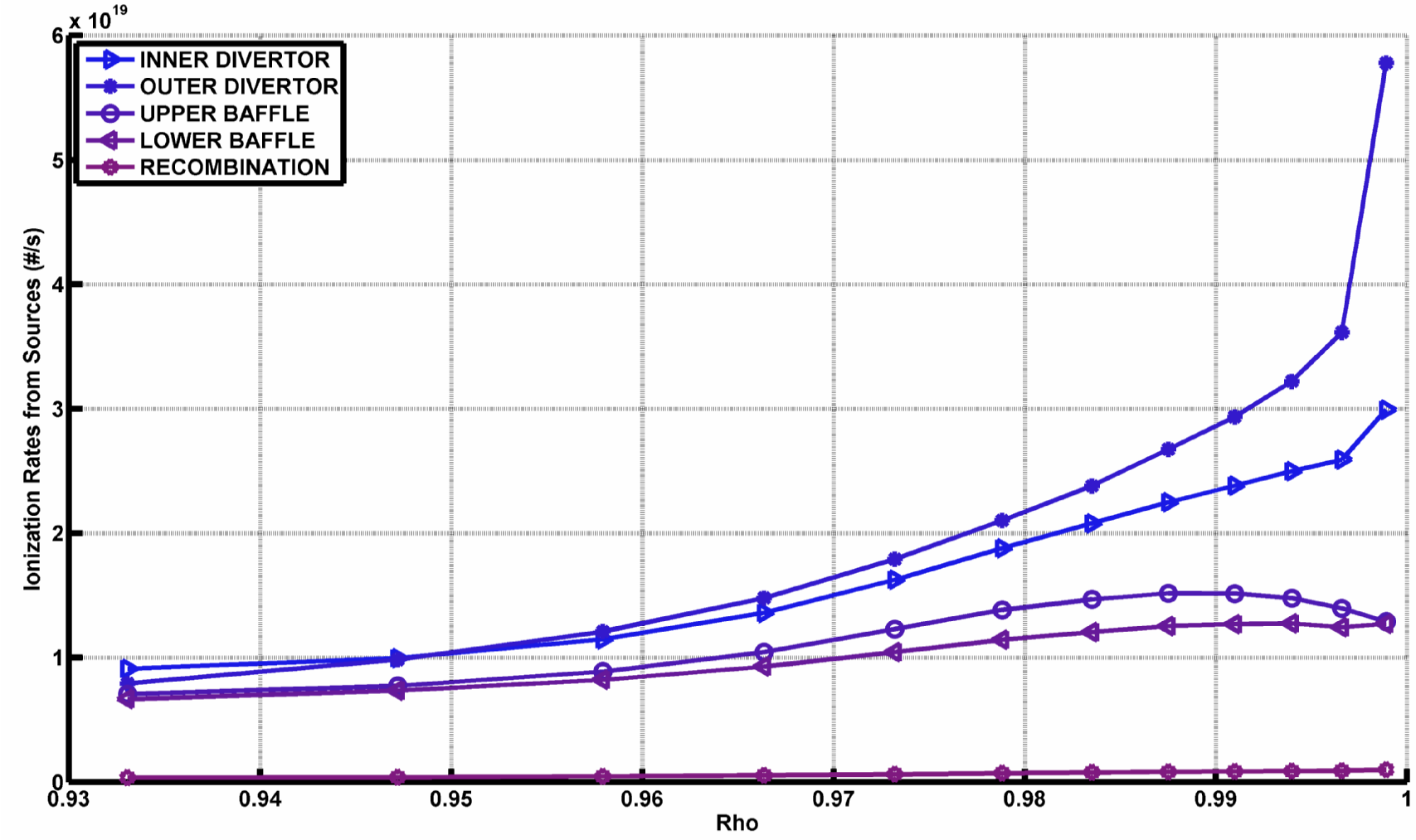

Figure 46: Ionization fueling rates in the pedestal from different sources (ATTACHED)

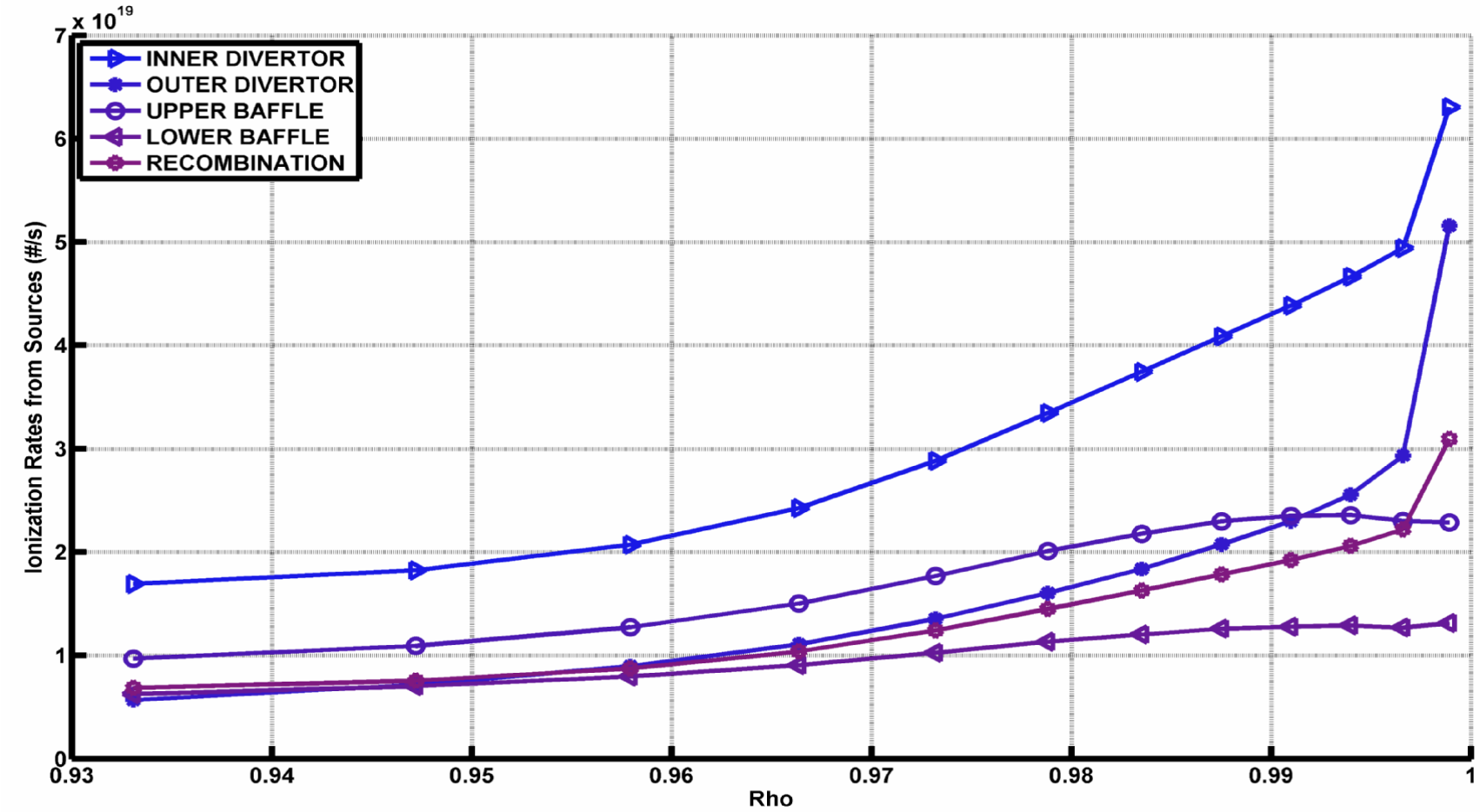

Figure 47: Ionization fueling rates in the pedestal from different sources (DETACHED)

6.7 Computational and experimental uncertainty

There is a fair amount of uncertainty in the analysis we have presented. As previously mentioned, the accuracy of the experimental determination of the ion outflow from the CORE+PED across the separatrix into the SOL, due to uncertainty in the experimental data, is judged to be about $\pm 30\%$ [94], but experimental uncertainties are not the only ones.

A measure of the computational uncertainty in the GTNEUT solution is obtained by performing an internal particle balance on the input sources minus the calculated sinks. The difference is a measure of the overall error in the calculation, and local errors could be greater or less. For the 'attached' background plasma, this error was about 1.8% and for the 'detached' background plasma it was about 3.2%. While GTNEUT has been extensively benchmarked against Monte Carlo calculations [17, 95-97], it has not previously been used for problems with so many (1560) regions, some of which have mean free paths in the tens of meters. The error in the internal particle balance may be due to errors in inverting such a large, albeit sparse, matrix. Additionally, some errors may be occurring in the evaluation of the transmission coefficients. There is some evidence [87] that the approximate evaluation of the Bickley functions used in the angular integration to obtain the transmission coefficients may be a source of error.

A Monte Carlo neutrals calculation for this same shot, using the same two sets of background plasma parameters, has been performed [13] with DEGAS2 [19]. The 2D mesh was identical except in the halo regions, where a different grid structure from that shown in Fig. 31 was used to extend the UEDGE mesh to the wall of the confinement vessel in the DEGAS2 calculation. With 10,000 histories each for the four wall recycling

sources and for the recombination source, the overall statistical uncertainty in the DEGAS2 calculation is estimated to be roughly $\pm 5\%$, but the statistical uncertainty in the calculation of ionization rates in individual small regions could be significantly larger.

The radially integrated PED+CORE ionization rates, determined as discussed above, calculated with GTNEUT and DEGAS2 are compared in Figs. 48 and 49. It is clear that the two calculations agree rather well except in the region on the inboard side just above the X-point. Possible causes of this disagreement are discussed below.

The GTNEUT and DEGAS2 calculations of the total ionization rate in the PED+CORE region are compared in Table 9. Also shown are the overall particle balance error from Table 7 in the GTNEUT calculation, which is a measure of the global calculational uncertainty in GTNEUT, and the estimated statistical uncertainty in the DEGAS2 calculation of the ionization in the PED+CORE region.

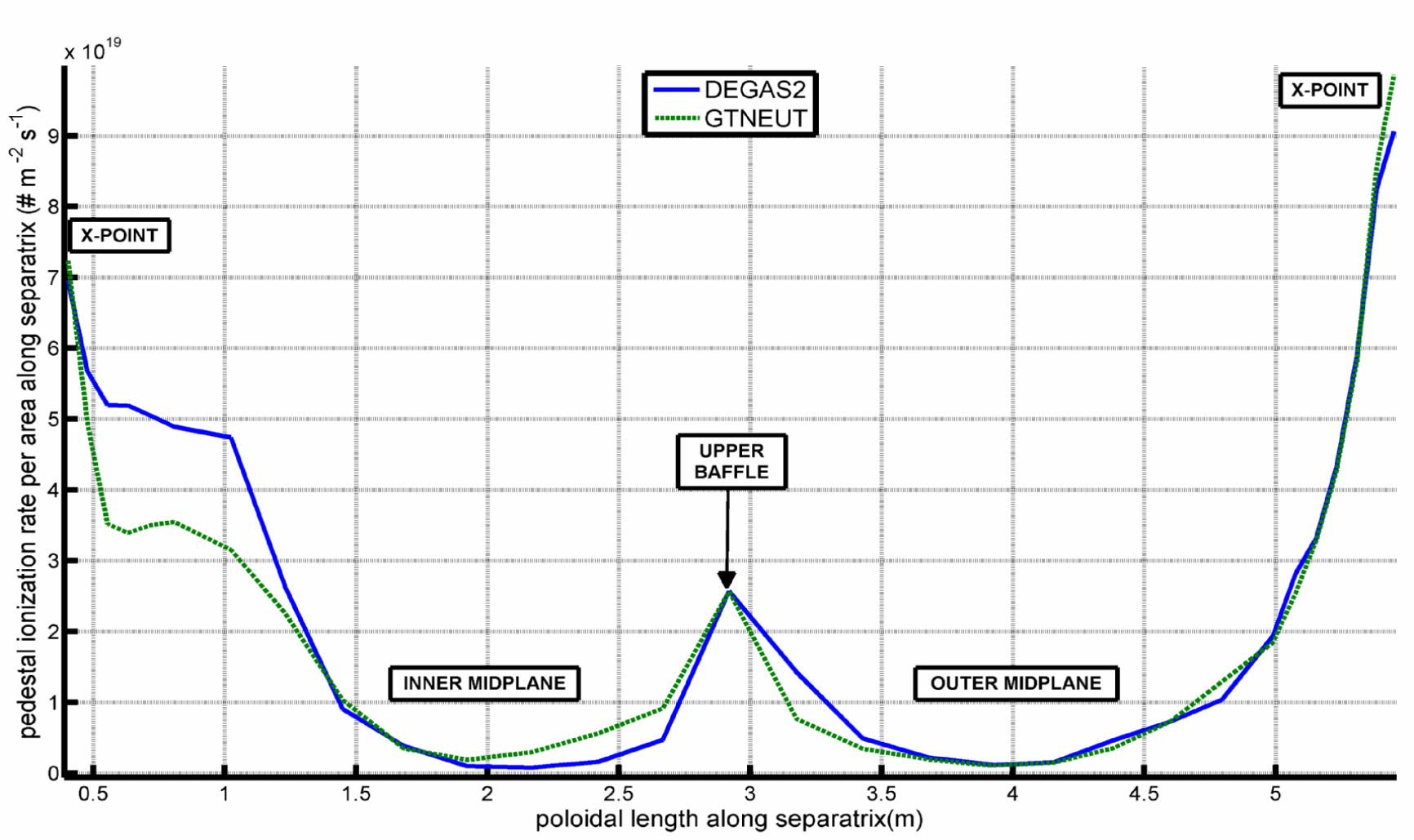

Figure 48: Poloidal distributions of PED+CORE ionization rate per unit separatrix area calculated by GTNEUT and DEGAS2. (ATTACHED)

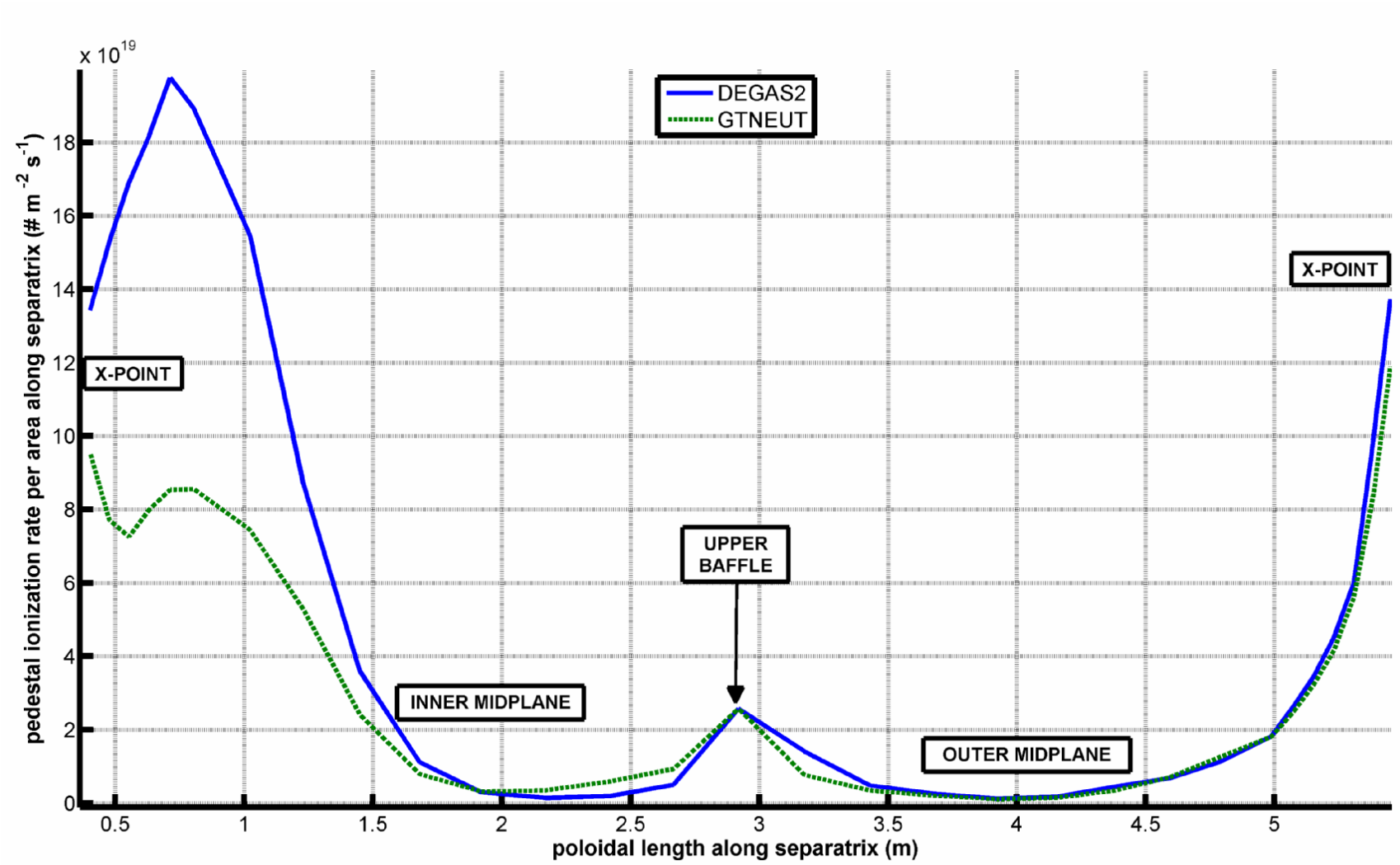

Figure 49: Poloidal distributions of PED+CORE ionization rate per unit separatrix area calculated by GTNEUT and DEGAS2. (DETACHED)

Table 9: Comparison of ionization rates in the PED+CORE calculated by GTNEUT and DEGAS2

	GTNEUT		DEGAS2	
	'Attached'	'Detached'	'Attached'	'Detached'
Source Strength (#/s)	1.34E+22	1.96E+22	1.34E+22	1.96E+22
Ionization Rate (#/s) PED + CORE	0.927E+21	1.313E+21	0.860E+21	1.77E+21
Percent of Source Neutrals Ionized in PED + CORE	6.9%	6.7%	6.4%	9.0%
Calculation Uncertainty	1.8%	3.2%	5%	5%

Calculations of pedestal fueling for the two codes agree reasonably well for the 'attached' background plasma parameters, but differ more significantly for the 'detached' background plasma parameters. Fig. 49 indicates that most of this disagreement arises from differences in neutral transport just above the x-point on the inboard side. For the 'attached' background plasma parameters, the disagreement between the two calculations is within the calculational uncertainty in the calculations. However, for the 'detached' background plasma calculations the disagreement would seem to be significantly larger than the calculational uncertainty, suggesting a discrepancy due to methods or data. There are several possible reasons for the discrepancies. The most obvious reason is the difference in the grid structure in the HALO and private flux region as seen in the figure below.

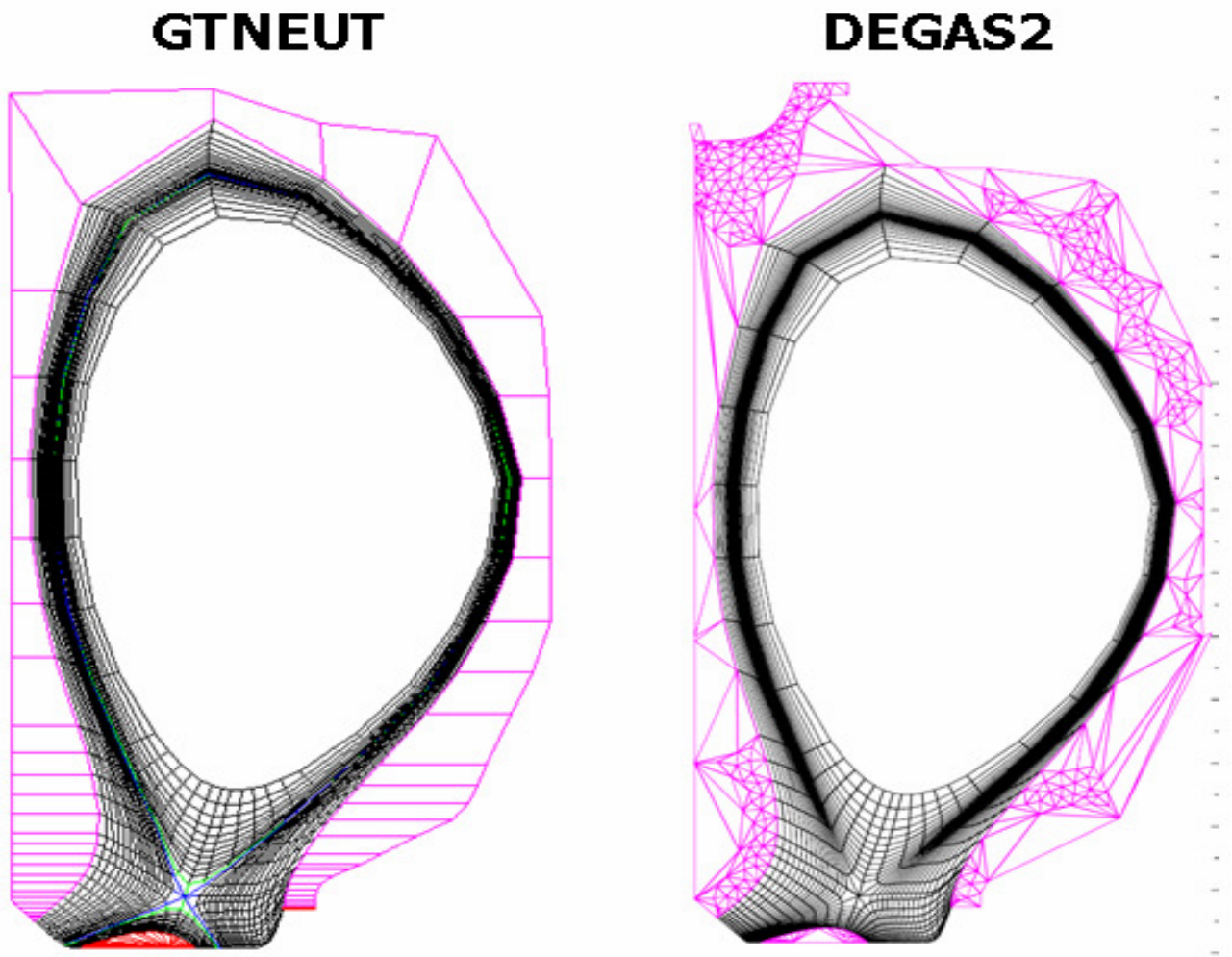

Figure 50: Difference in HALO and Private Flux Region for GTNEUT and DEGAS2 Calculation.

We conjecture that this discrepancy may be due to the different ways in which the two codes handle molecular transport. DEGAS2 fully models molecular transport with different species in the plasma edge. In GTNEUT molecules recycled from the wall are assumed to dissociate into Franck-Condon energy atoms in the first grid region in front of the wall and be transported with a mean free path corresponding to that energy until they have a collision. The regions that would be most affected by the different treatments of molecular transport would be the regions with very low temperature (e.g. the inner divertor regions with the 'detached' background plasma parameters). This conjecture is supported by a previous comparison [95] of GTNEUT and DEGAS for a different DIII-D shot, in which differences between calculated ionization rates between the two codes were reduced dramatically when the molecular transport calculation was turned off in the DEGAS calculation.

Additionally, in the figure below we can clearly see how varying the Franck-Condon energy can affect the penetration of the neutral particles into the core of the plasma. "twall" is the assumed Franck-Condon energy (eV) of the neutral atoms formed by the dissociation of molecules in the first region in front of the wall. In GTNEUT, this energy is specified by the user. For our analysis, we used a twall value of 2 eV for both the 'attached' and 'detached' cases. The twall = 2.0 value in the figure below corresponds to the green line in figure 48. Increasing twall can drastically increase the neutral particle penetration.

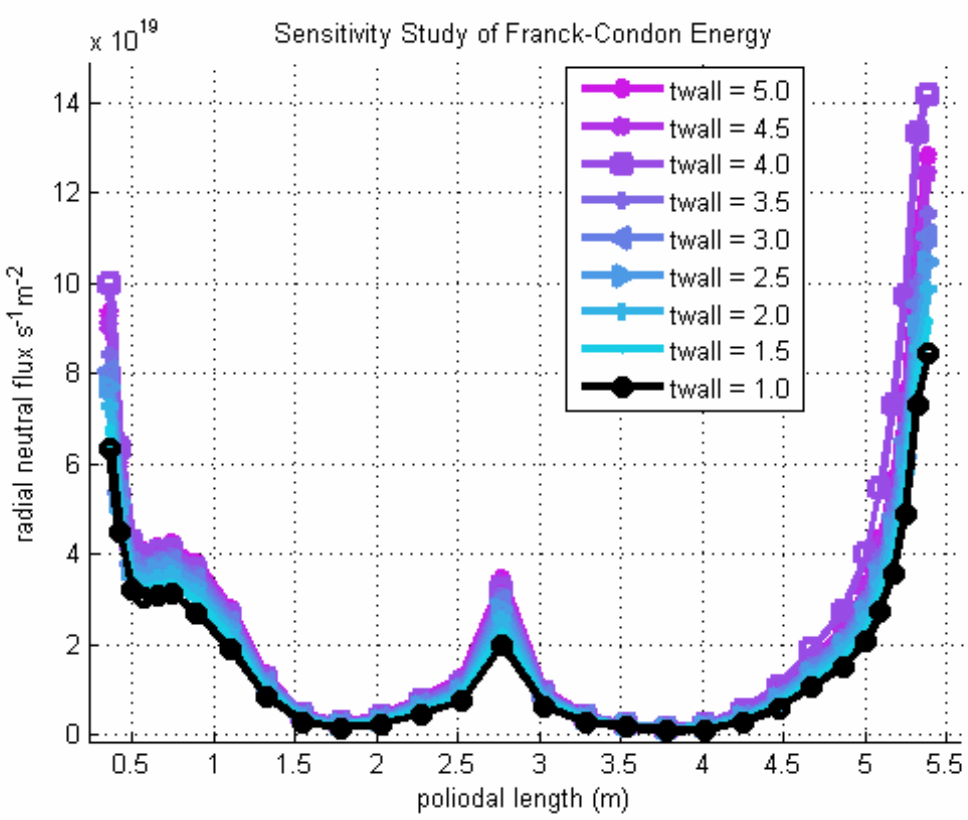

Figure 51: Franck-Condon Energy Sensitivity Study (Attached Case)

The figure above somewhat contradicts previous assumptions that the variance of "twall" did little to affect the outcome of results. However, the previous analysis used to test the importance of "twall" was primarily concerned with neutral particle densities outside of the separatrix [17, 87]. Here densities are very high. Small perturbations in the total number of neutral particles would be quite small. In the analysis we have done, we are concerned primarily with the neutral particles that have crossed the LCFS. In the table above, we see that this is typically less than 5 percent of the total number of neutral particles being tracked by GTNEUT. Since we are dealing with much smaller numbers, it is clear why the "twall" parameter can change the outcome of the problem.

In addition to the discrepancies that may have arisen from the lack of molecule transport, other possible causes of this discrepancy could arise from differences in atomic physics data used by the two codes (which we believe based on previous work to be small) and to the treatment of a plasma flow dependence of the direction of charge-exchanged neutrals in DEGAS2 which is not available in GTNEUT.

7. Suggested Improvements to GTNEUT

The TEP methodology results in a large matrix equation relating the two partial fluxes across each interface in the computational domain indicated in Fig. 31, which is solved using a standard sparse matrix routine. In previous applications to problems with many fewer interfaces the solution procedure went smoothly. However, with this large number of interfaces we did encounter some difficulty (which we attributed to round-off error) in obtaining a solution in some cases. For problems of this size and larger, it would be good to implement a better sparse matrix routine.

The differences between the GTNEUT and DEGAS2 calculation near the inner divertor shown in Figs. 48 and 49 are conjectured to be due to the differences in the treatment of molecules. As discussed at the end of Chapter 6, DEGAS2 explicitly accounts for molecular transport, whereas in GTNEUT the molecules are assumed to be dissociated in the region immediately adjacent to the wall and into atoms. Inclusion of molecular transport in GTNEUT would seem to be suggested.

We also suggest an improvements previously mentioned by Dingkang Zhang [87]. The method of angular integration used to find the transmission coefficients should be modified. The current routines take up approximately 85 percent of the computational time for a GTNEUT calculation. Additionally, there is reason to believe these routines could be responsible for round off errors in the calculations.

8. Summary & Conclusions

We have investigated in detail the neutral particle recycling and pedestal fueling from wall reflection and volumetric recombination sources in a DIII-D H-mode discharge. The investigation confirms previous studies [13, 16] that the edge pedestal in DIII-D is primarily fueled by recycling and recombination neutrals from the divertor region.

We find that the penetration of recycling neutrals into the pedestal region is highly non-uniform poloidally, both because the recycling and recombination sources are poloidally non-uniform and because neutral particles recycling from the upper baffle penetrate deeper into the pedestal (because the path length in mean free paths is shorter) than do neutrals recycling from the divertor region. Although the effects of poloidally asymmetric particle source and heat sinks will be ameliorated to some extent by rapid poloidal transport along the field lines, this result raises questions about the adequacy of one-dimensional plasma transport calculations that are sometime employed in the edge pedestal and suggests an area of further investigation.

Finally, comparison of DEGAS2 and GTNEUT calculations of neutral ionization rates indicates relatively good agreement between the two codes except in the immediate vicinity of the inner divertor, where the differences in treatment of molecular transport is thought to be responsible for the significant discrepancy in predicted neutral influxes across the separatrix.

Appendix A. Procedure

The following procedure is intended for those with previous knowledge of GTNEUT, EFIT, and some UEDGE experience. Access to the Linux Cluster at General Atomics is required to carry out this procedure. Before continuing, please study the GTNEUT and UEDGE manual founds in Refs. [17, 22].

The first step in creating the GTNEUT geometry section of the "toneut" file is obtaining the EFIT files required create a grid structure for GTNEUT. The steps are quite simple. At the UNIX command prompt:

1st: Run IDL.

2nd: From the IDL command prompt, generate the "a" and "g" EQDSK files by issuing the commands:

writea,shotnumber,timeslice,runid

writeg,shotnumber,timeslice,runid

Next, export the EQDSK into a directory of your choosing. UEDGE templates to generate the GTNEUT mesh can be found in my GA home directory:

/u4/friis/uedge/runs/UEDGE_DEMO

Several templates have the extension, ".template". Several of the files in this folder are needed in order to simply run UEDGE. As previously stated, all UEDGE runs need to be run with the divertor fitting option. It is up to the user to ensure the correct

divertor geometry files have been loaded. Remember new divertor shelves where installed on DIII-D, and different divertor geometries require different fitting files. The creators and custodians of UEDGE will have more information on this.

There are many options to modify in the templates provided. These are in the UEDGE manual also. It may be discovered, there are options not utilized in the routines provided that may cause the scripts to breakdown. It does however work for the cases used in this dissertation and should provide a basis for expansion. After the template files are set up in conjunction with the proper EFIT files, UEDGE may be run.

It should be noted that the versions of UEDGE and GTNEUT utilized for this analysis are all located on the linux cluster. For this analysis Zeus was primarily used; however, Zeus died several months into the analysis. To finish the analysis Delphi was used with success.

The version of UEDGE used is located in:

/d2/uedge/Ver_5.0b_linux/dev/lnx-2.3-i32/bin/xuedge

The version of GTNEUT used is located in:

/u4/friis/GTNEUT/

This is the most current and up to date version of GTNEUT in existence. **ALL MODIFICATIONS TO THE GTNEUT CODE SHOULD BE BASED OFF THIS VERSION.** The routine used to convert the UEDGE mesh into a GTNEUT mesh can be found in:

/u4/friis/uedge/runs/UEDGE_DEMO

and it is called:

make_toneut

Before the script make_toneut can be run, the UEDGE mesh must be created. This can be accomplished by running UEDGE using the executable provided above and then typing:

read "template file name"

This sets up the UEDGE file. Next, the actual UEDGE grid must be created. Instead of actually running UEDGE though, this is accomplished by typing:

call flxrun

call grdrun

This simply makes the UEDGE grid. One can view the mesh by typing

win on

followed by

read plotmesh

If mesh has been successfully created, make_toneut can be run by typing

read make_toneut

By running this, we have extended the mesh to the wall and generated several outputs.

To view the new GTNEUT mesh, type

read plotgtneutmesh

This routine is located in the post directory within the UEDGE directory. It will create a very color depiction of the new GTNEUT mesh.

The output files created from make_toneut are primarily the geometry files.

There are 5 output files. The table below breaks down the output files from make_toneut. The toneut-cells, toneut-cores, and toneut-walls contain all of the pertinent geometric data. toneut-flatflux create a uniform temperature and density distribution throughout the computational grid. This isn't really useful, except for making sure the geometry is set up properly. Lastly, toneut-rwall_gex are the run options.

Table 10: make_toneut output files

toneut-cells	**contains all iType(0) cells and needed information.**
toneut-cores	**contains all iType(1) regions and tracks neighboring cells**
toneut-walls	**contains all iType(2) regions and tracks neighboring cells.**
toneut-flatflux	**gives all of iType(0) and iType(1) cells a uniform temperature and density.**
toneut-rwall_gex	**generates the end of the toneut file with specified options.**

To test the geometry use the unix cat command to make the toneut file:

cat toneut-cells toneut-cores toneut-walls toneut-flatflux toneut-rwall_gex > toneut

GTNEUT can now be run using the executable provided previously. If there is a problem with the geometry, it will be instantly obvious. If GTNEUT starts running though, one can simply cancel the run using ctrl c. There is no point in running GTNEUT with the flatflux approximation. It may not converge to a solution.

If GTNEUT ran under the flatflux run, this means the geometry section should be correct. We know need the plasma background. The routine "gtneut_temp_dense_full" can extract ion and electron temperatures provided a UEDGE run has been made. The routine "gtneut_volume_source" can extract volumetric sources due to recombination provided a UEDGE run has been made. If one is using the recombination source from UEDGE, it is advised that ifrstcol = 0 in the GTNEUT runtime options. This treats all volumetric sources as first flight collisions. If ifrstcol=1, the volumetric neutrals have an initial energy of eneut_v. To create the actually GTNEUT input files use the linux "cat" command and merge the geometry, background plasma, source files, and run options files together and create the "toneut" file.

After gtneut has been successfully ran, use the command "read loadnd" from the UEDGE prompt. This will load the output from GTNEUT into uedge. Now type "win on" so the routines in Table 11 may be run. These routines can be found in "u4/friis/uedge/post". These routines were used to create the figures in Appendices B and C.

Table 11: Routines created to plot data.

read plotpoly_ir	**Plots Ionization Rates**
read plotpoly_id	**Plots Ionization Densities**
read plotpoly_nd	**Plots Neutral Particle Densities**
read plotpoly_cx	**Plots Charge Exchange Fractions**
read plotgtneutmesh4	**Zooms in on Divertor Region**

Appendix B. DETACHED CASE

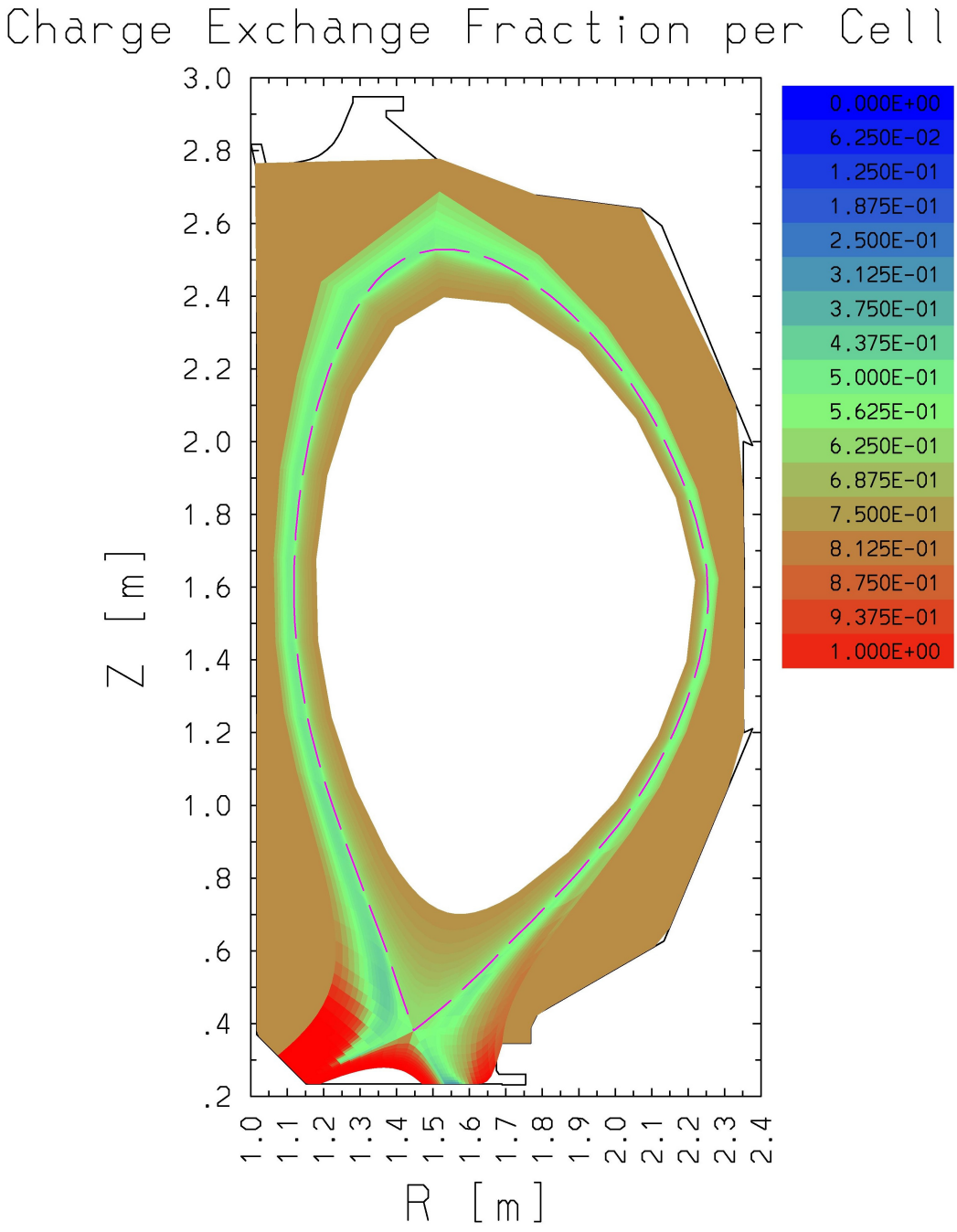

Figure 52: Charge Exchange Fraction per Cell (Detached Case)

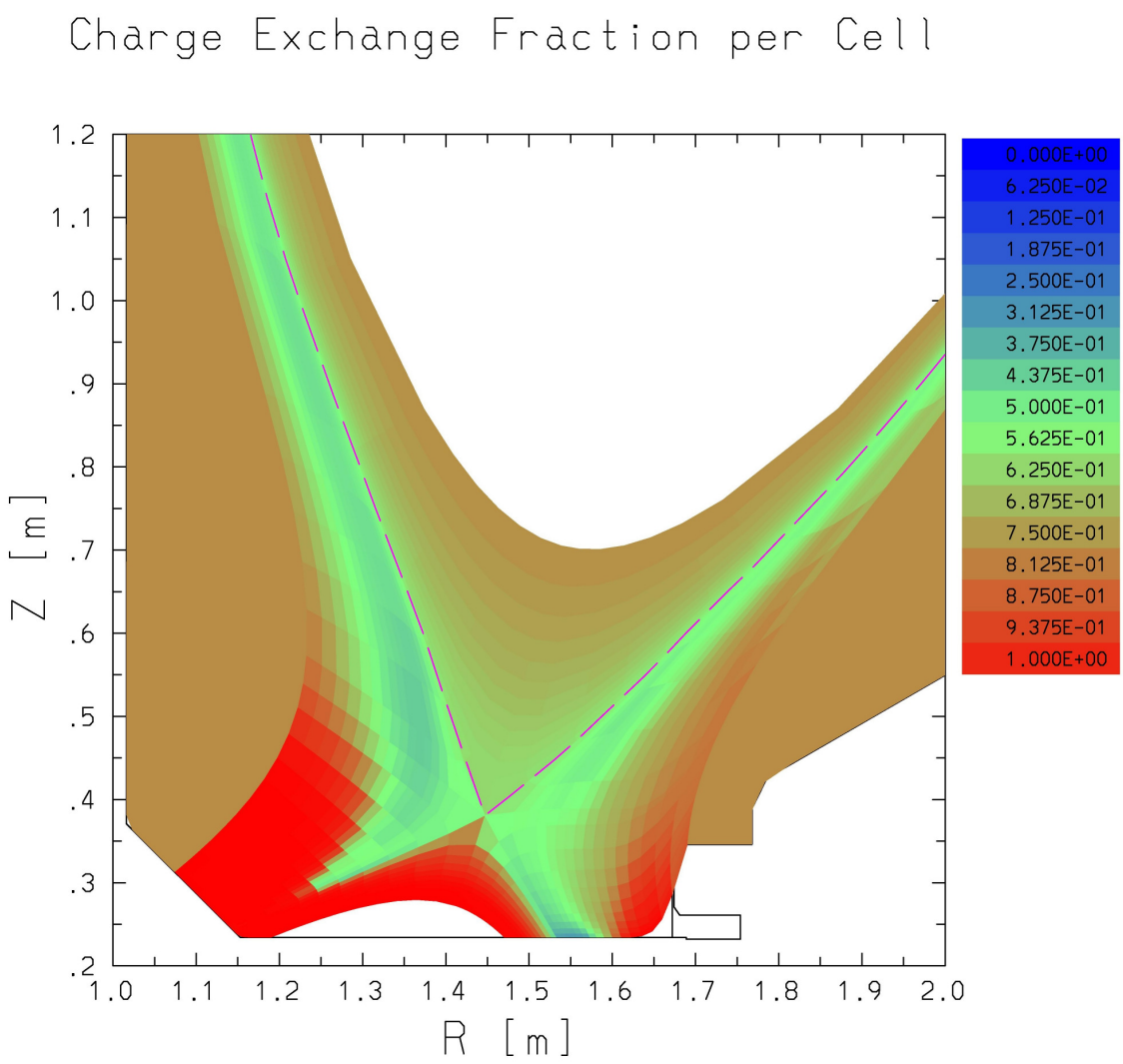

Figure 53: Charge Exchange Fraction per Cell divertor view (Detached Case)

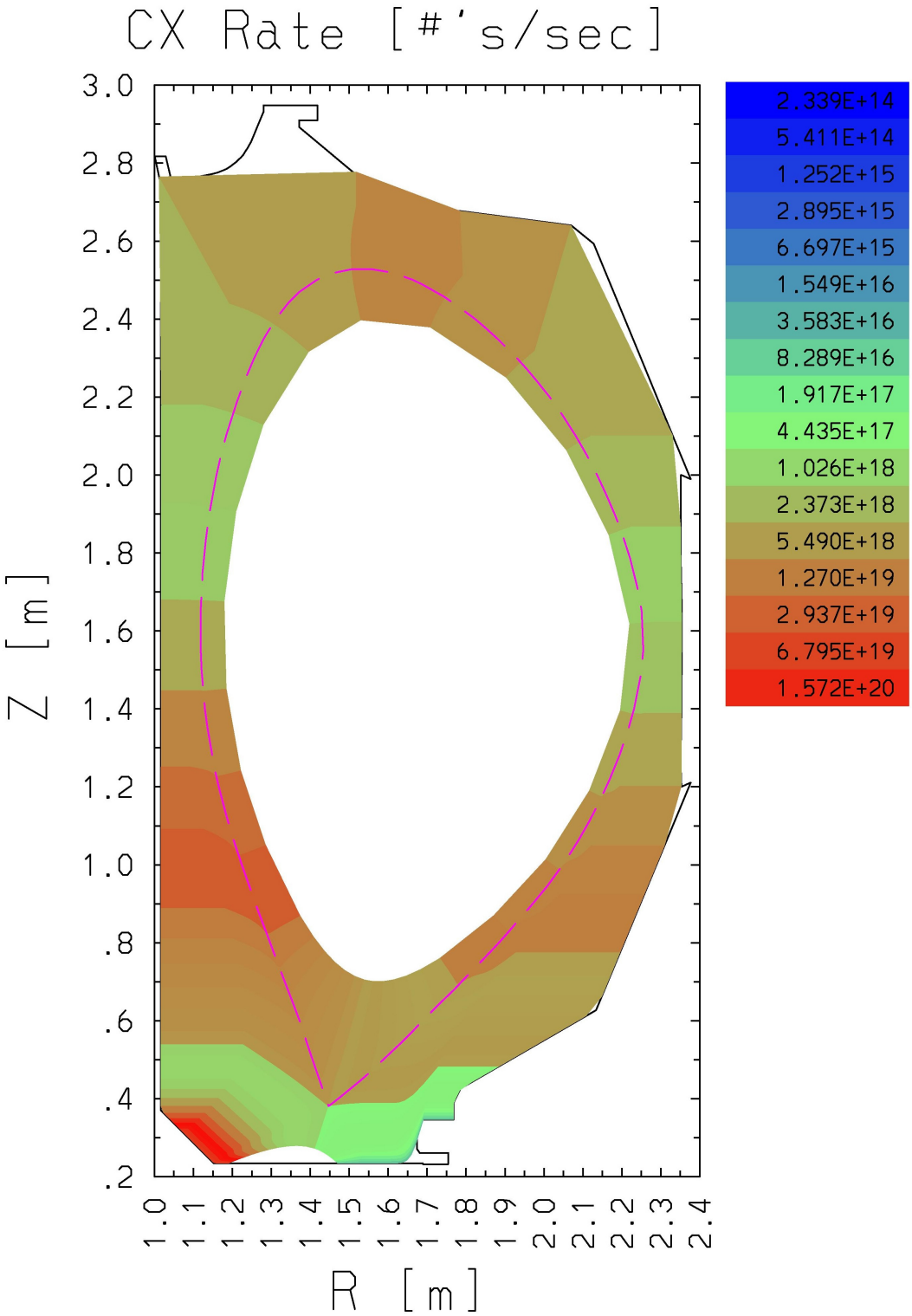

Figure 54: Charge Exchange Rates per Cell (Detached Case)

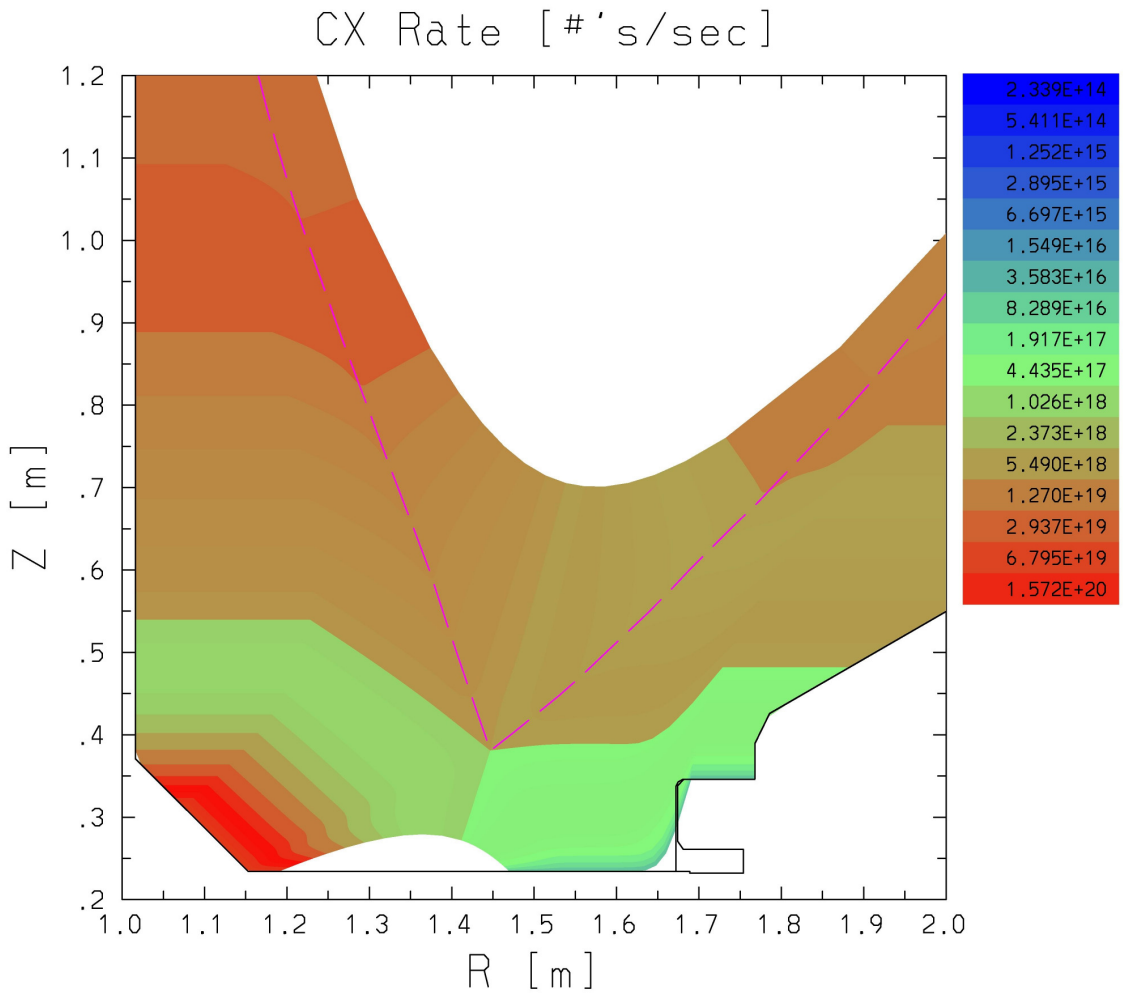

Figure 55: Charge Exchange Rates per Cell divertor view (Detached Case)

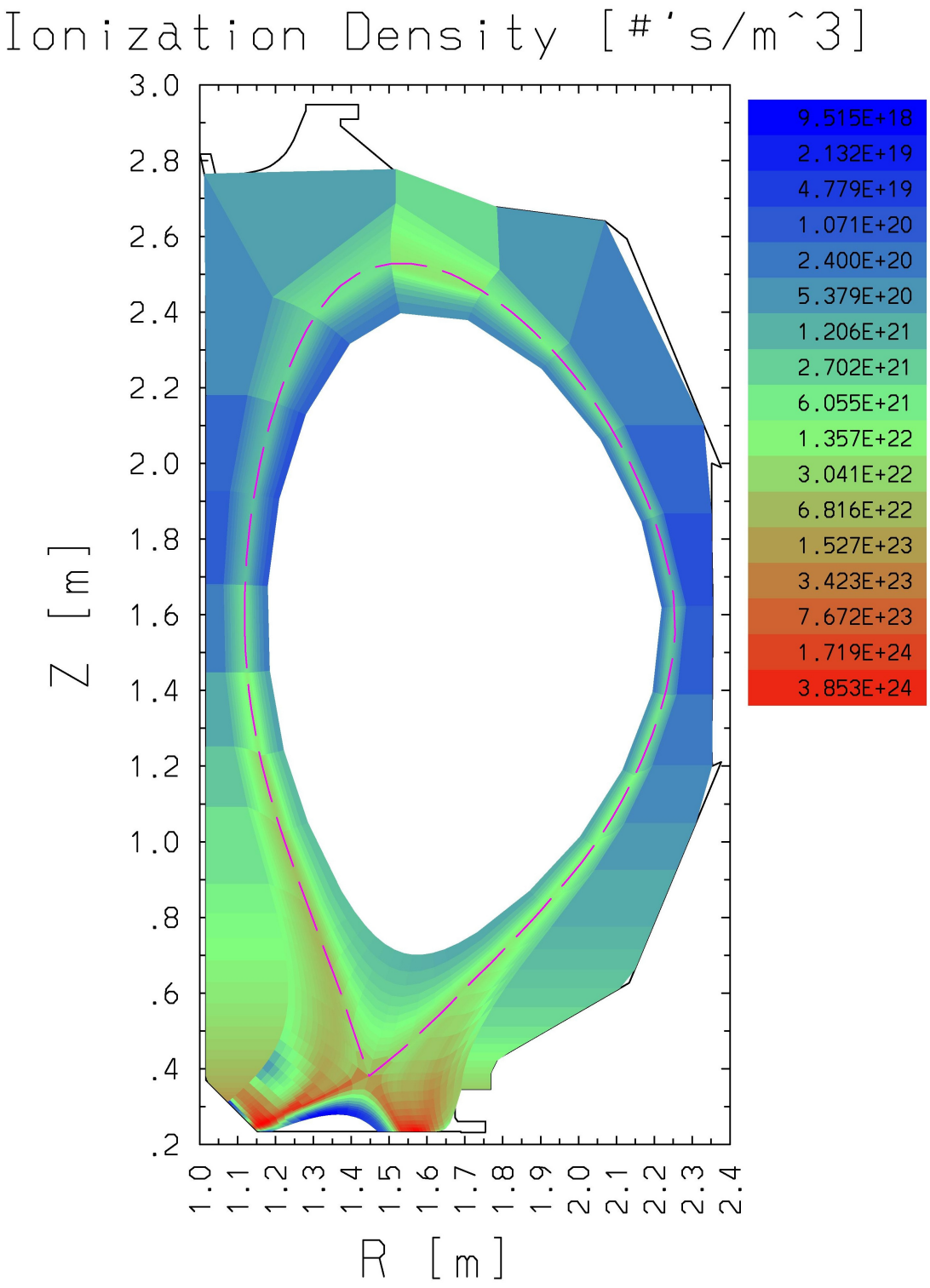

Figure 56: Ionization Density per Cell (Detached Case)

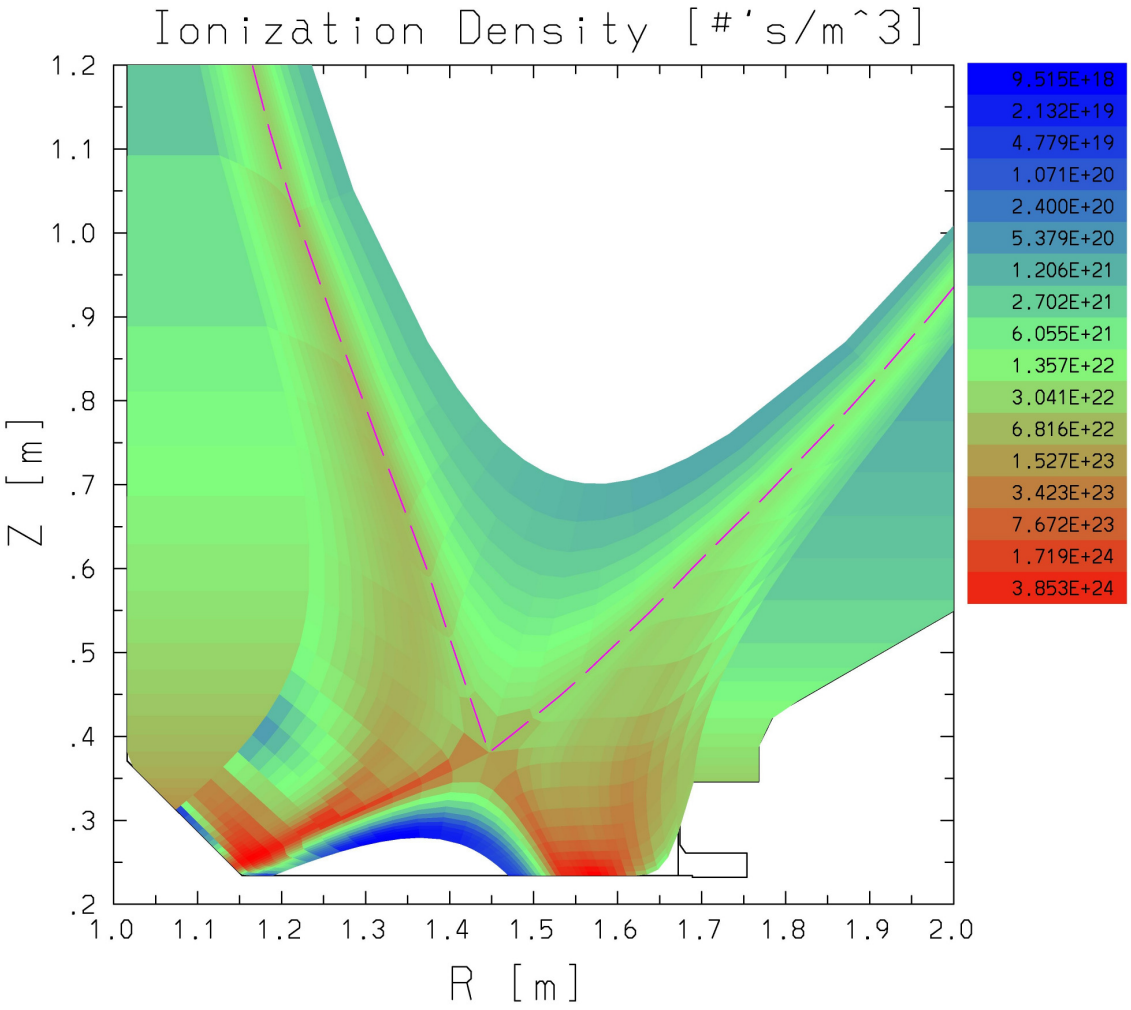

Figure 57: Ionization Density per Cell divertor view (Detached Case)

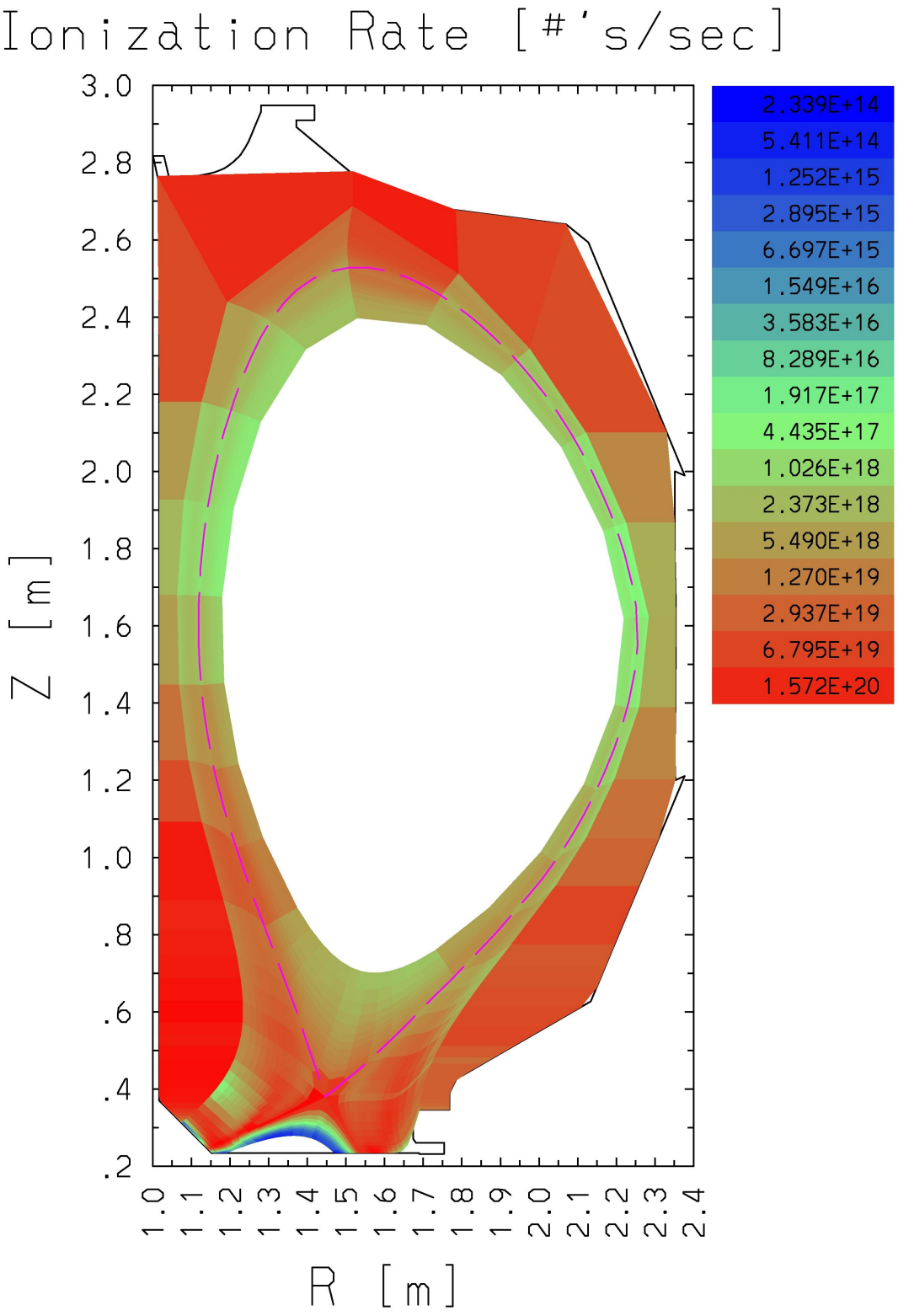

Figure 58: Ionization Rate per Cell (Detached Case)

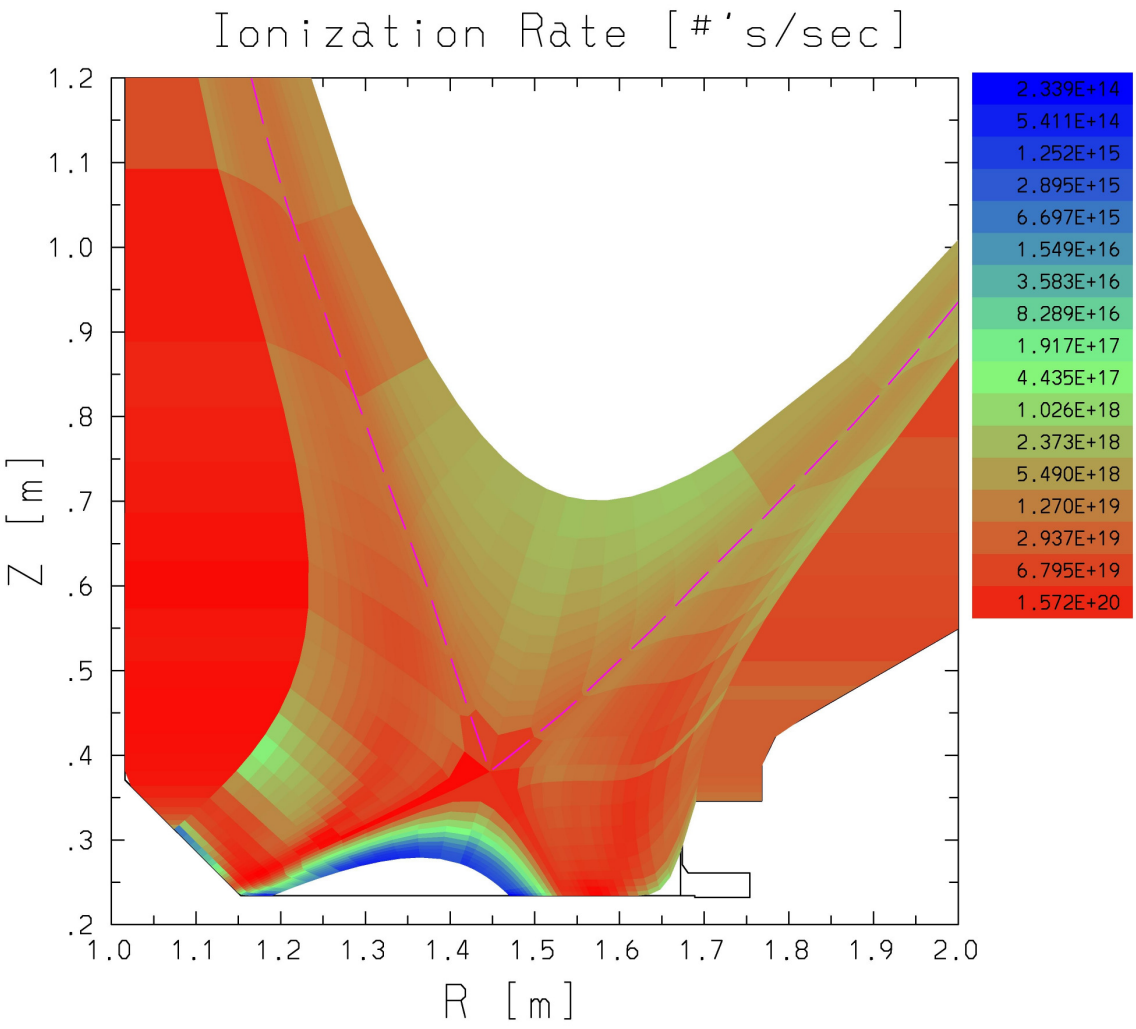

Figure 59: Ionization Rate per Cell divertor view (Detached Case)

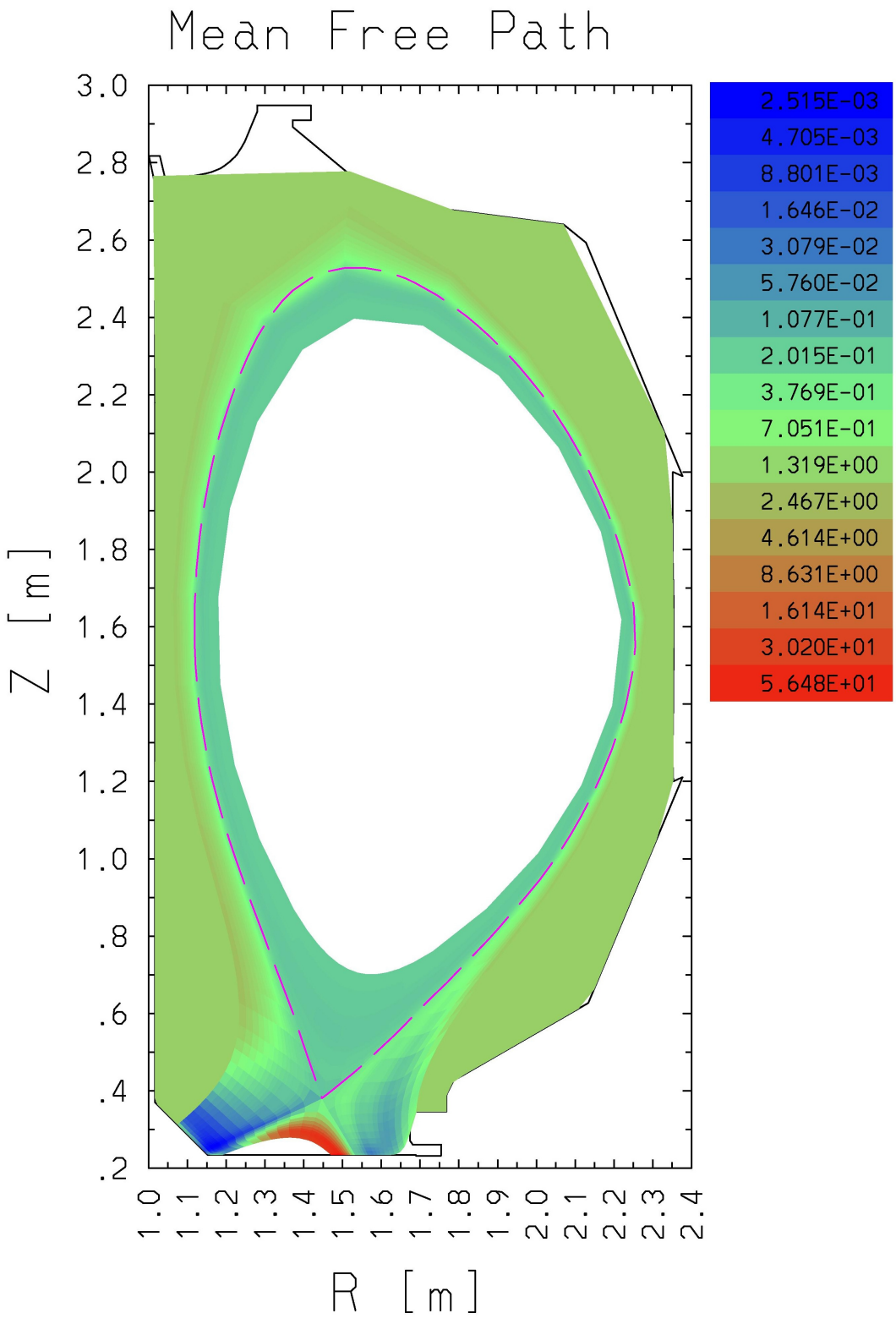

Figure 60: Mean Free Path per Cell (Detached Case)

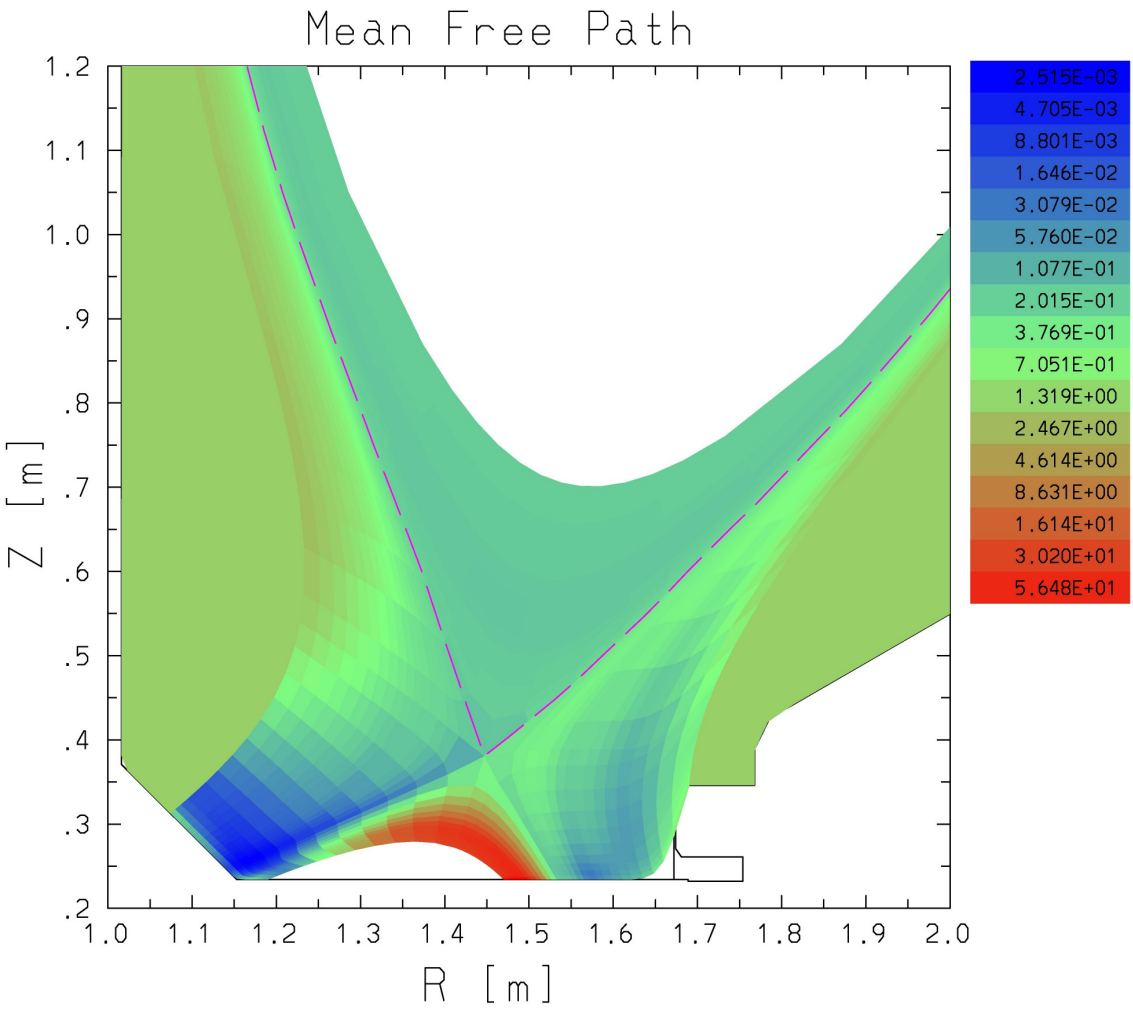

Figure 61: Mean Free Path per Cell divertor view (Detached Case)

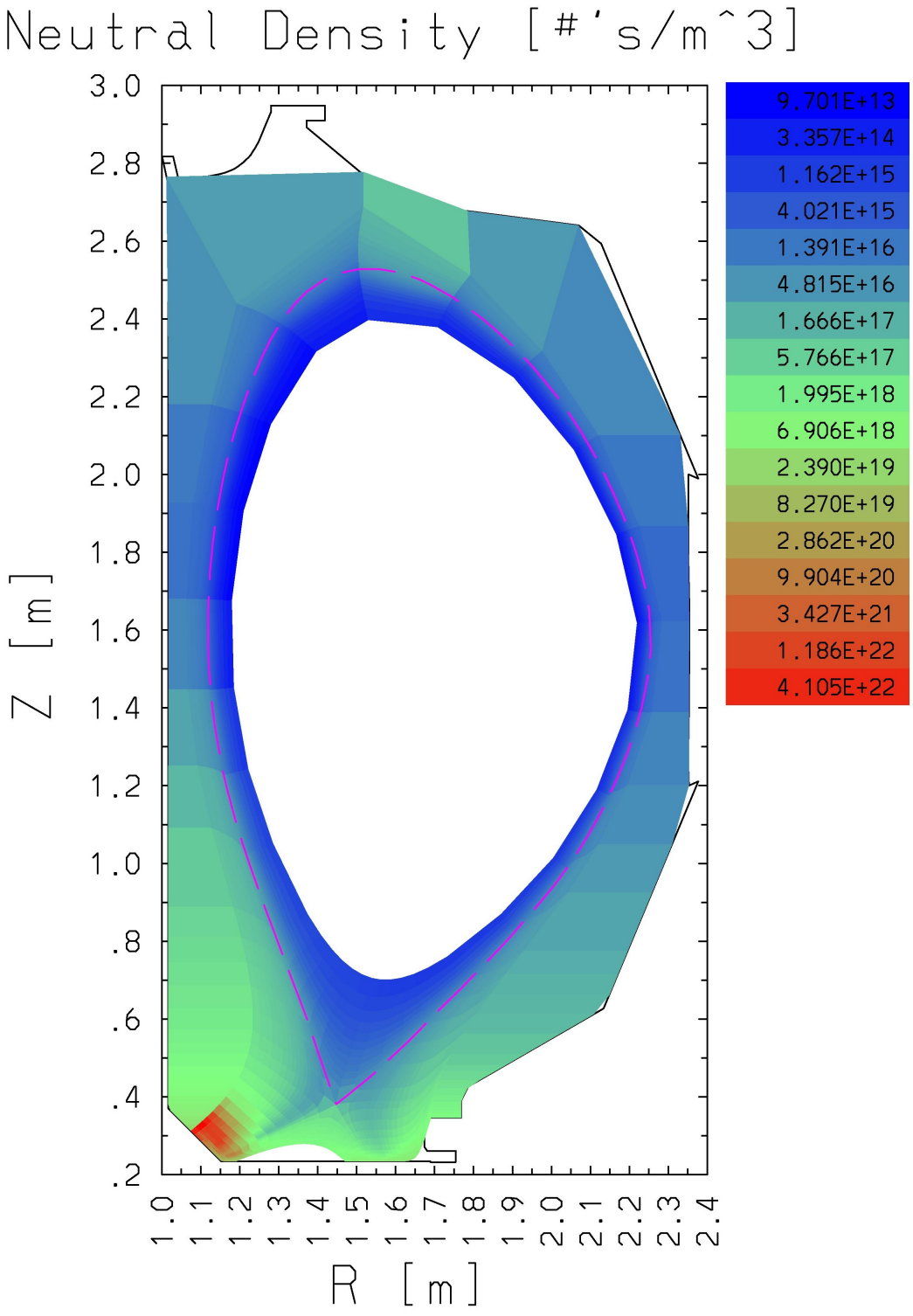

Figure 62: Neutral Density per Cell (Detached Case)

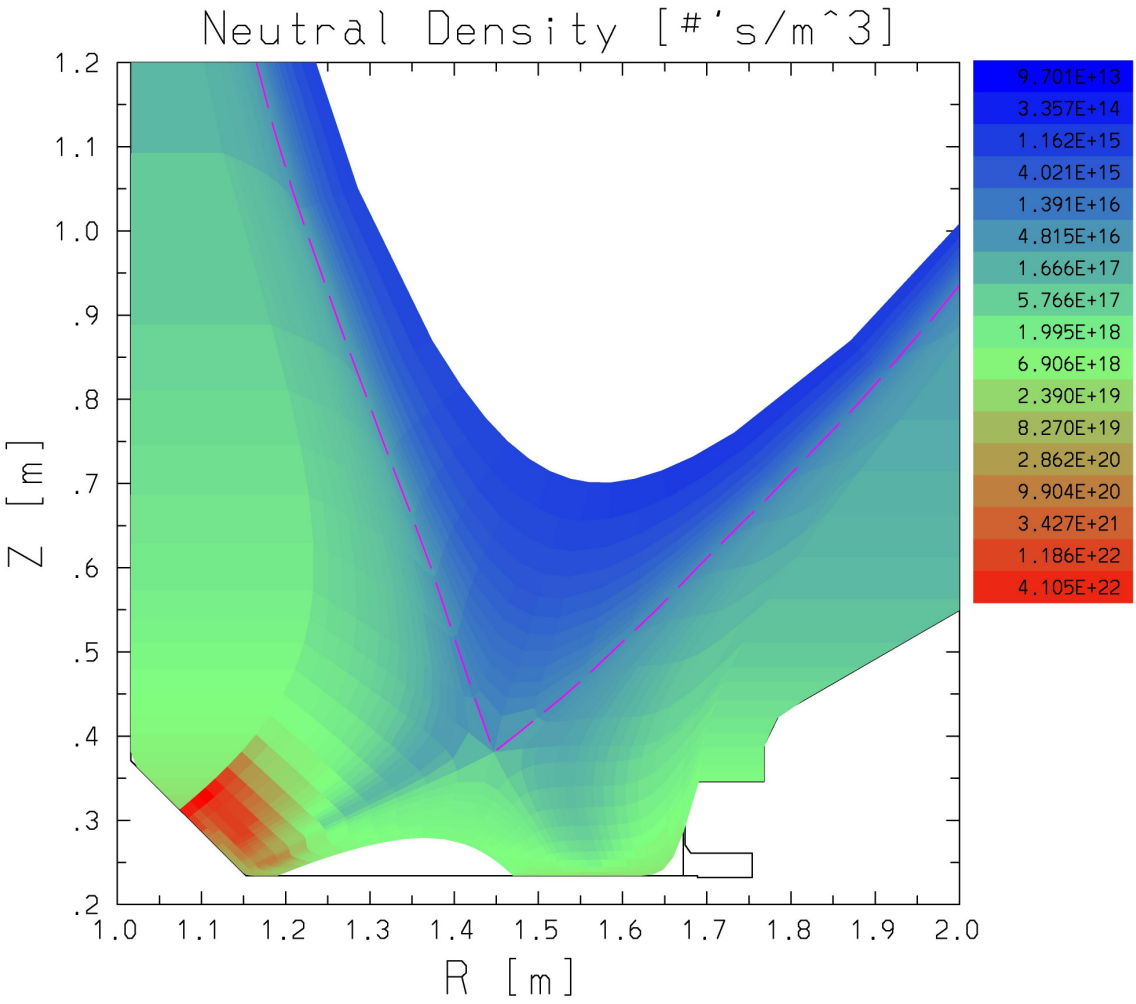

Figure 63: Neutral Density per Cell divertor view (Detached Case)

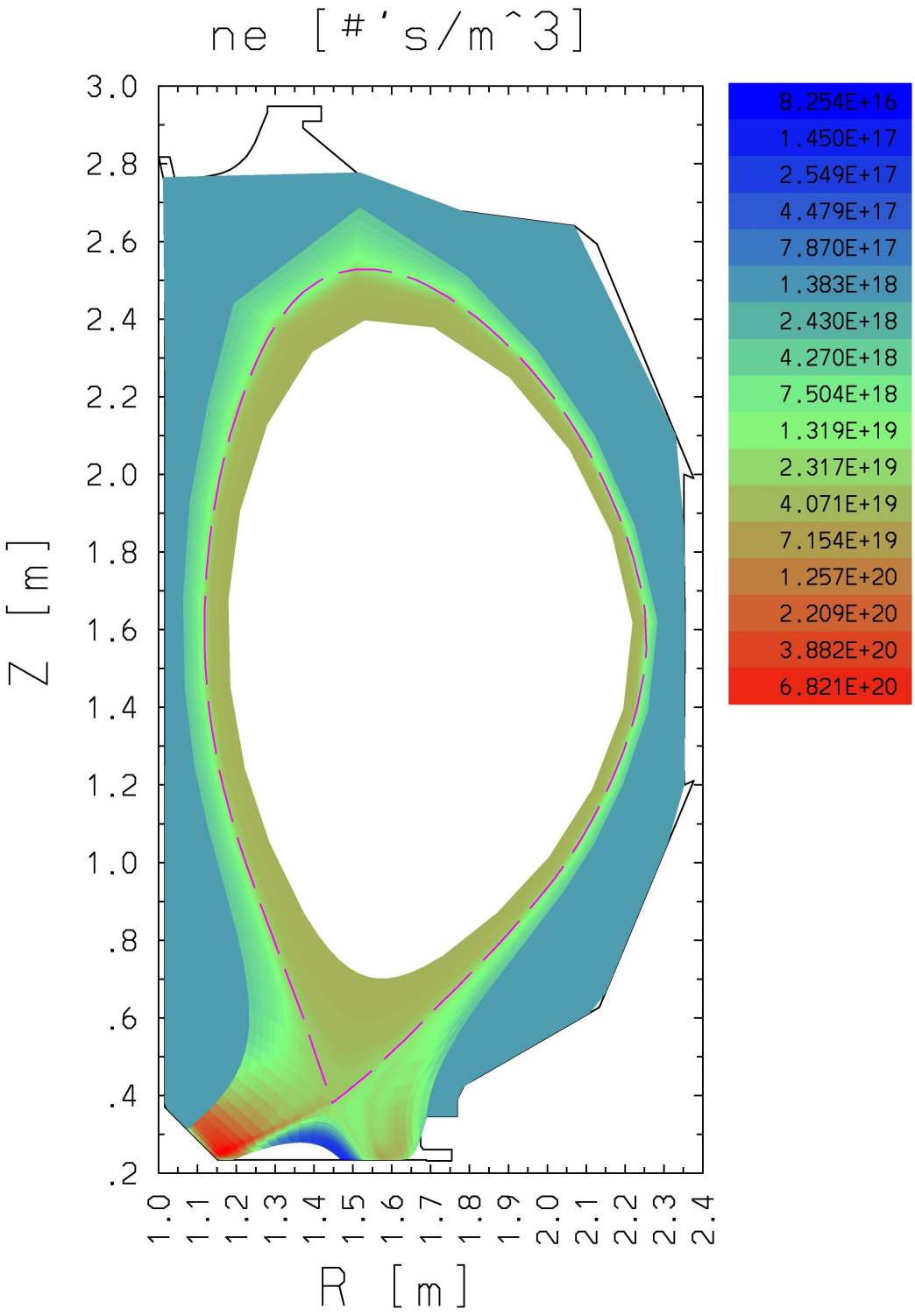

Figure 64: Electron Density per Cell (Detached Case)

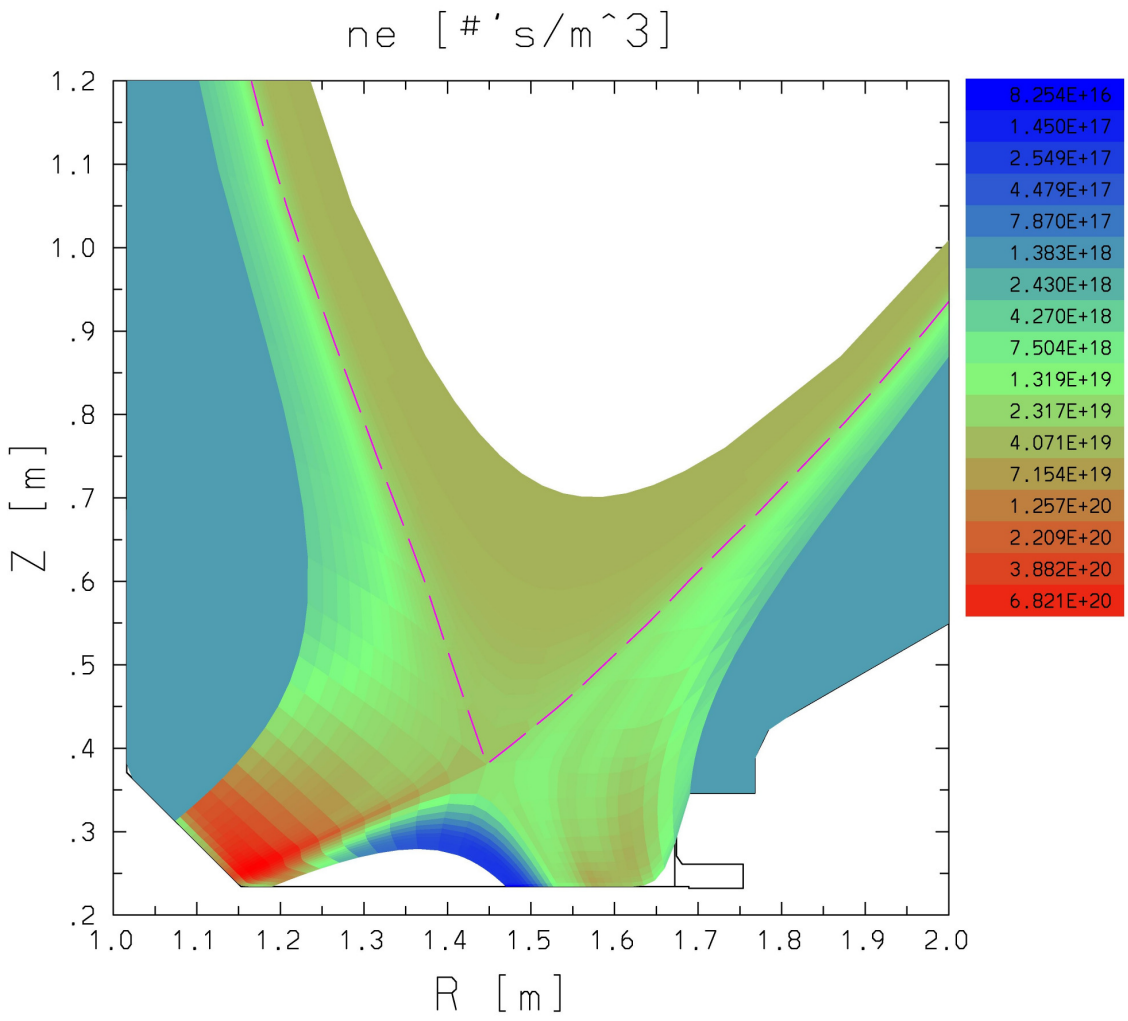

Figure 65: Electron Density per Cell divertor view (Detached Case)

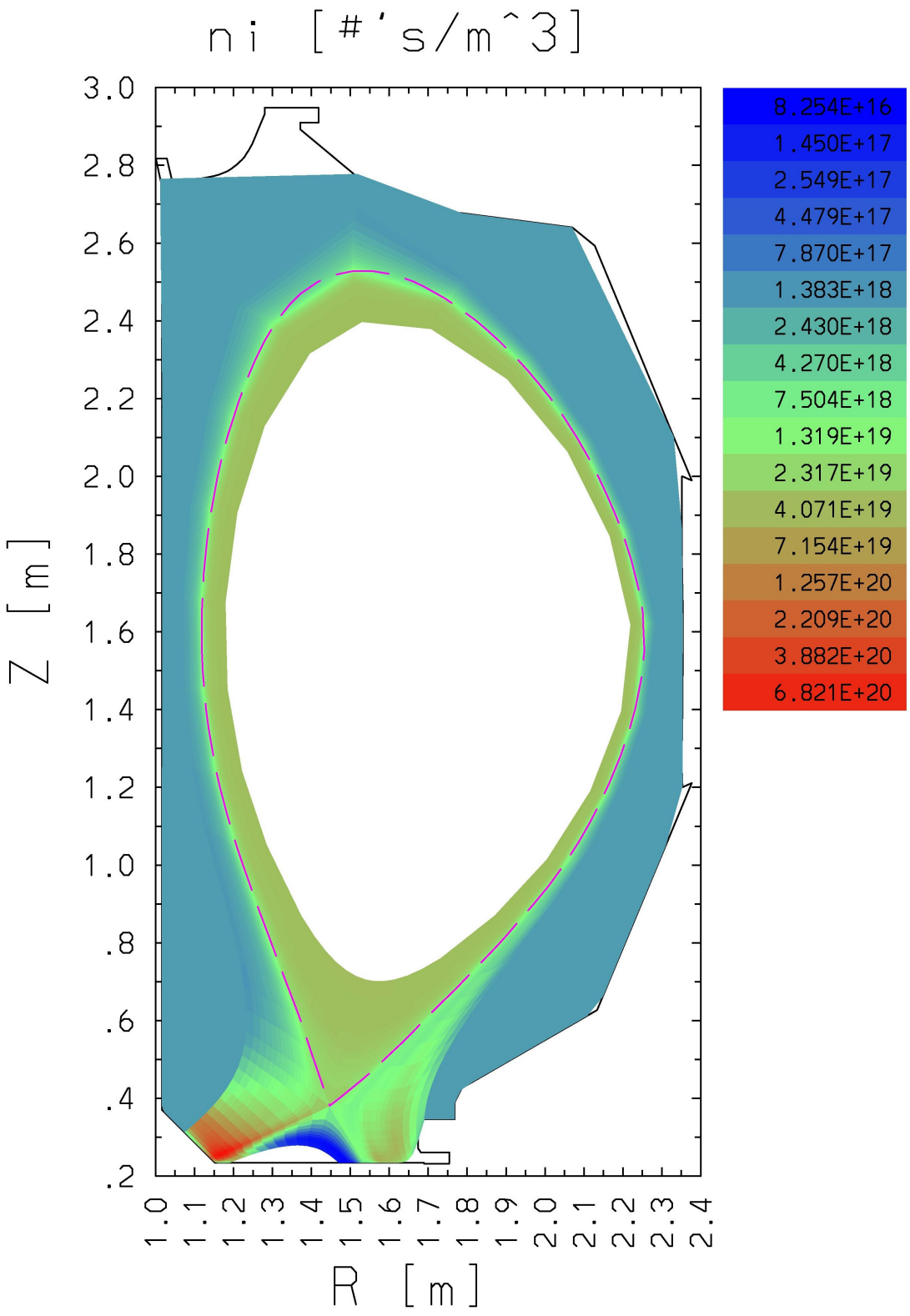

Figure 66: Ion Density per Cell (Detached Case)

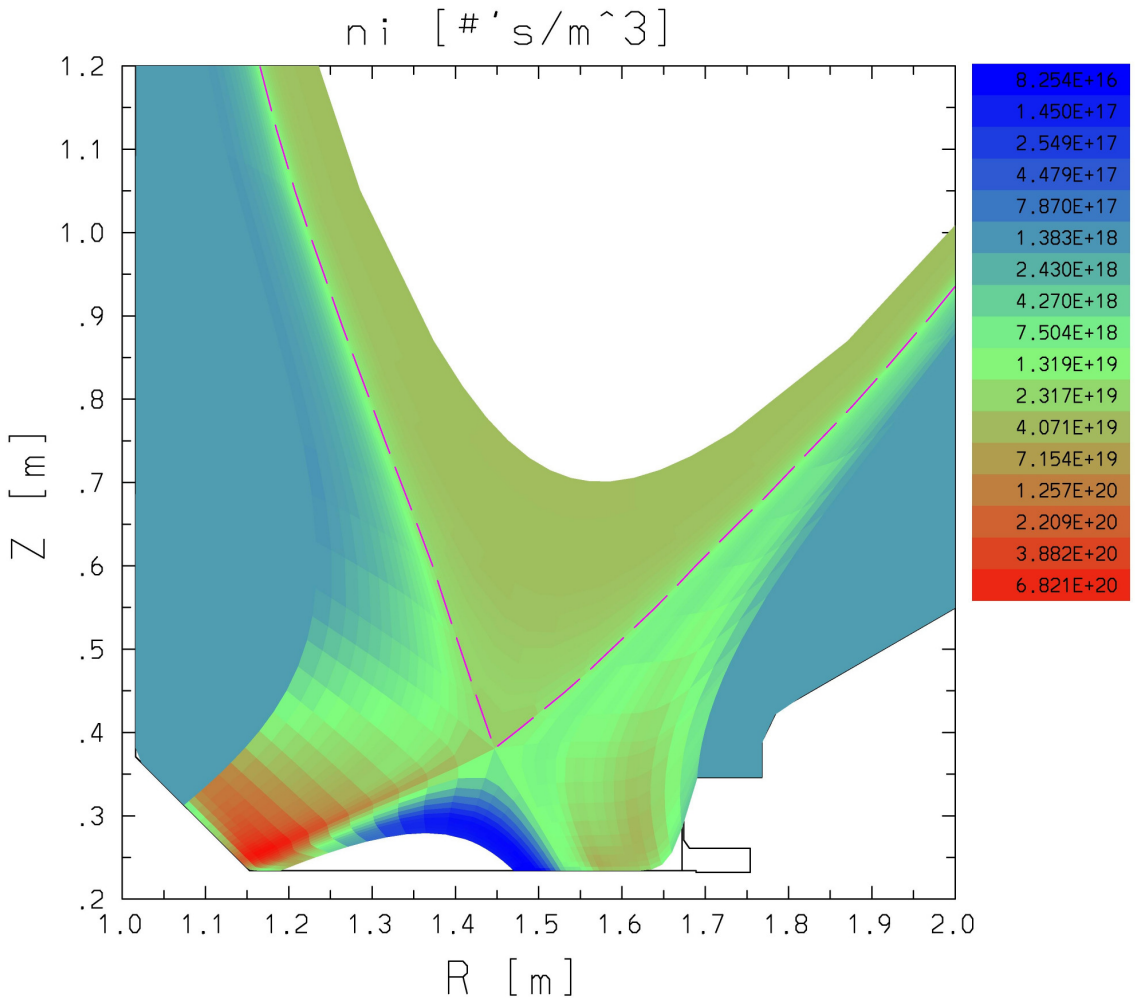

Figure 67: Ion Density per Cell divertor view (Detached Case)

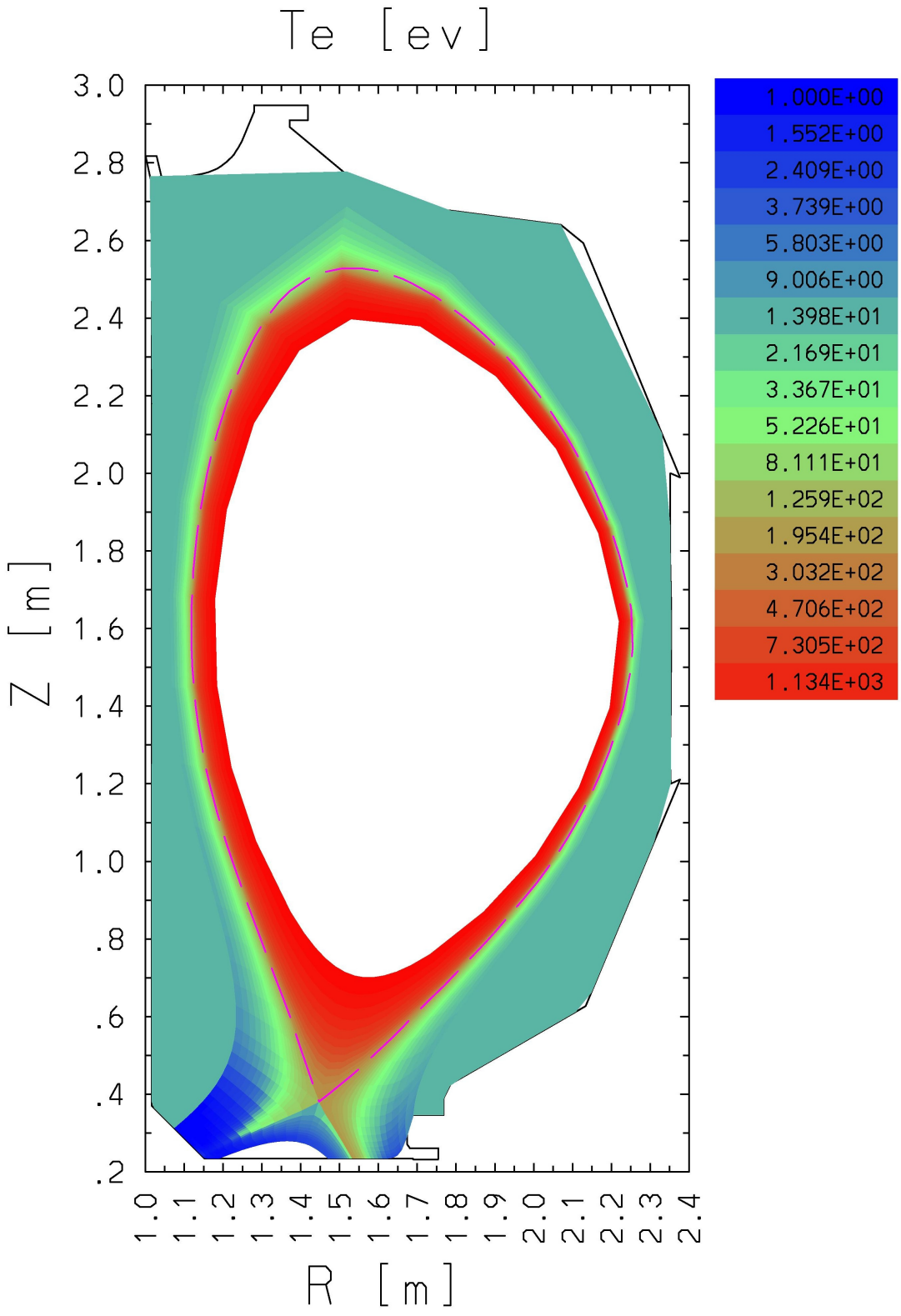

Figure 68: Electron Temperature per Cell (Detached Case)

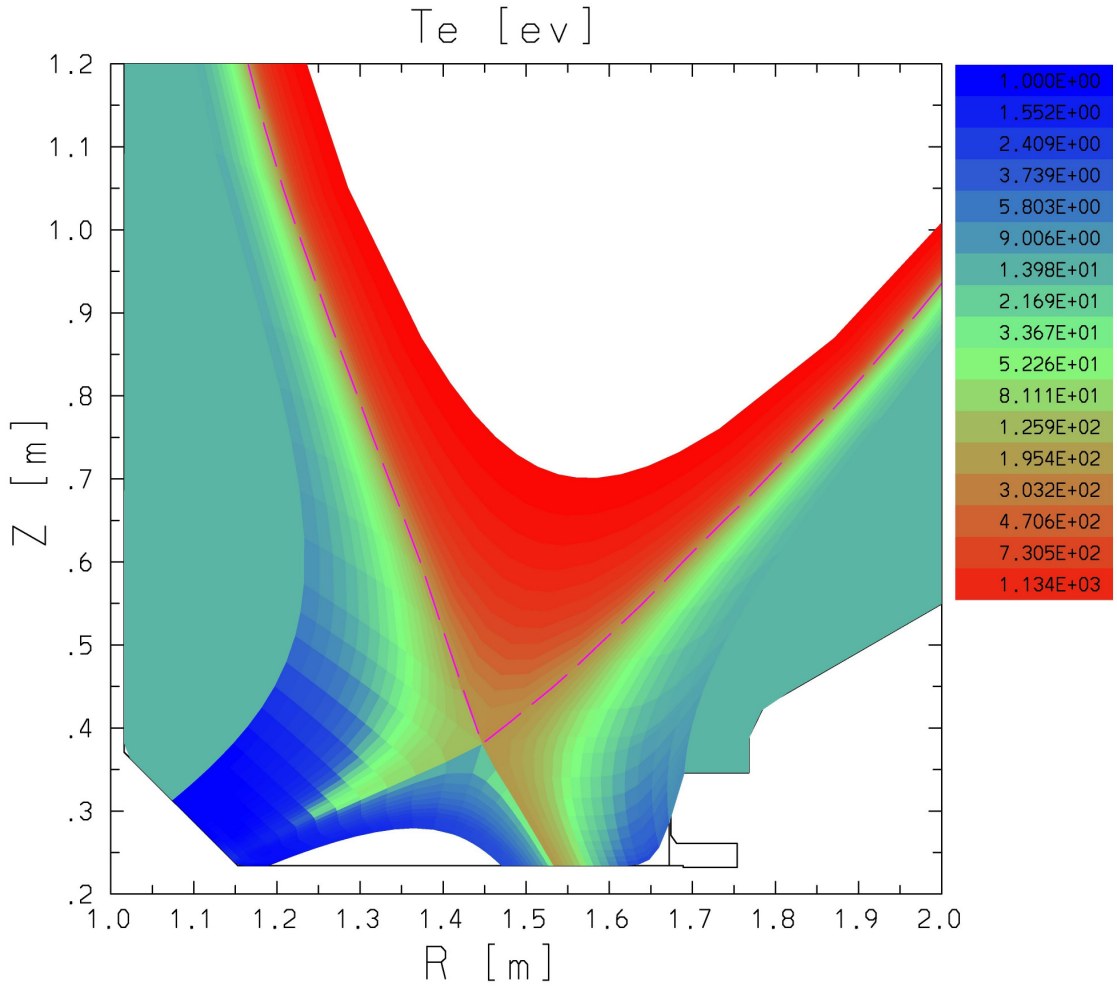

Figure 69: Electron Temperature per Cell divertor view (Detached Case)

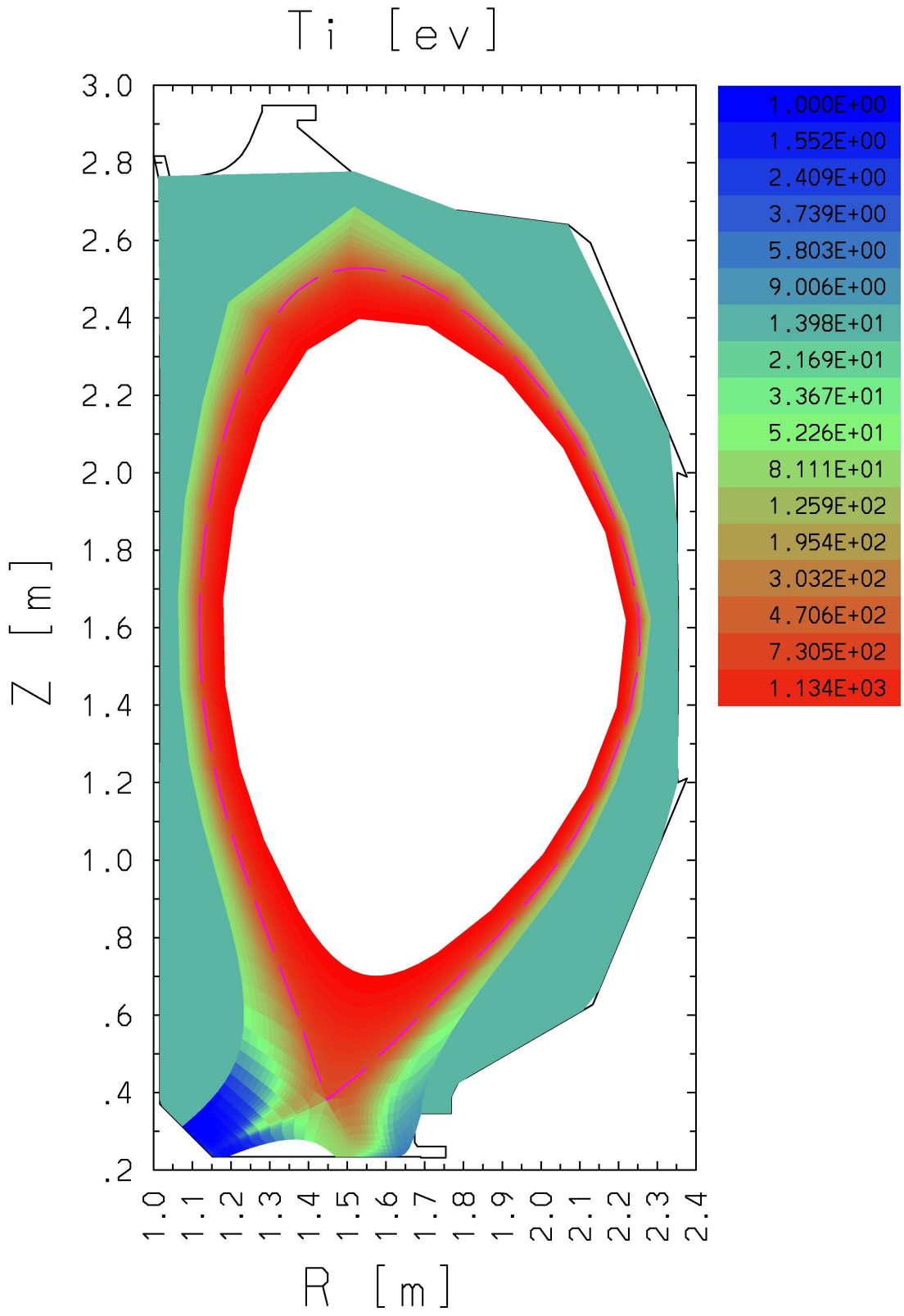

Figure 70: Ion Temperature per Cell (Detached Case)

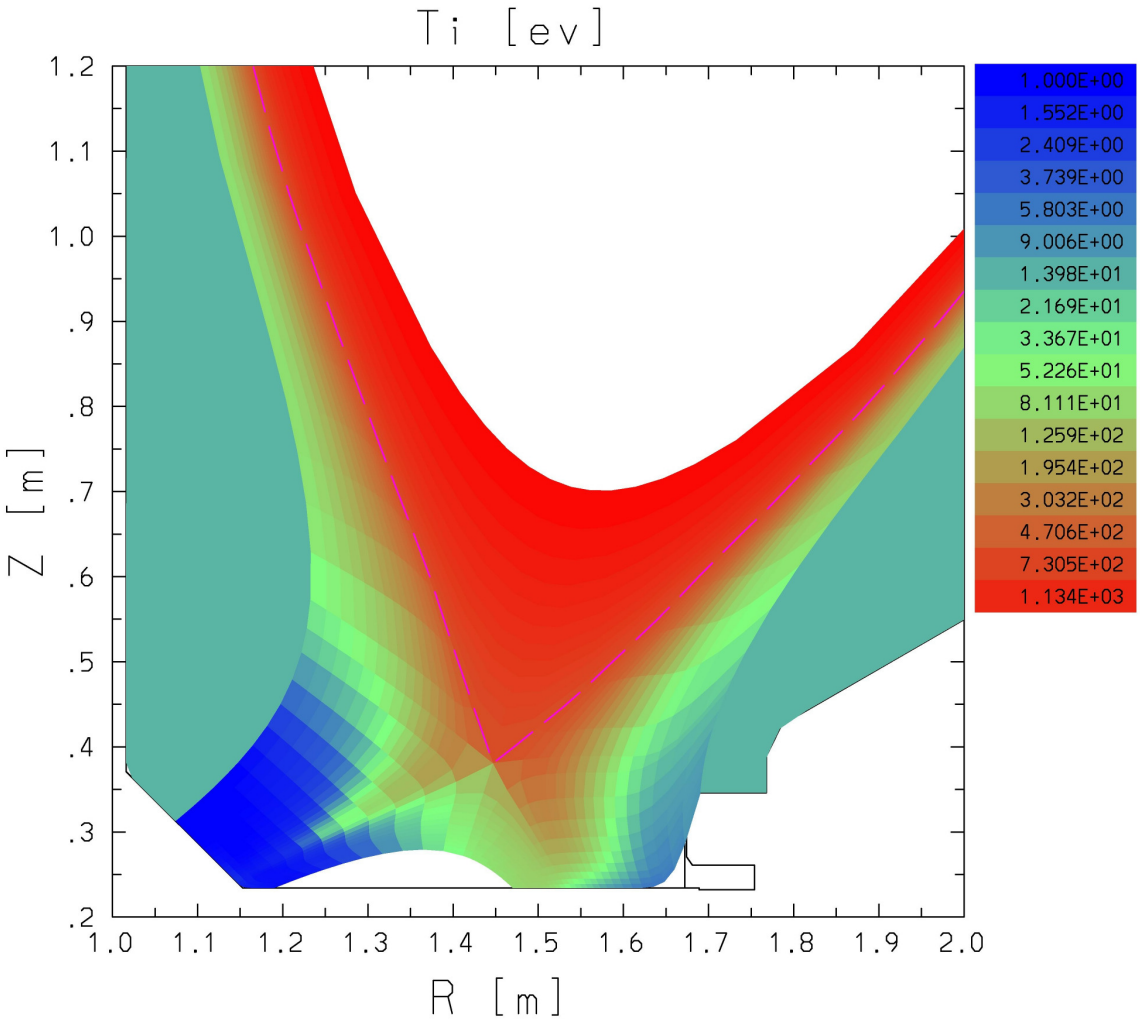

Figure 71: Ion Temperature per Cell divertor view(Detached Case)

Appendix C. ATTACHED CASE

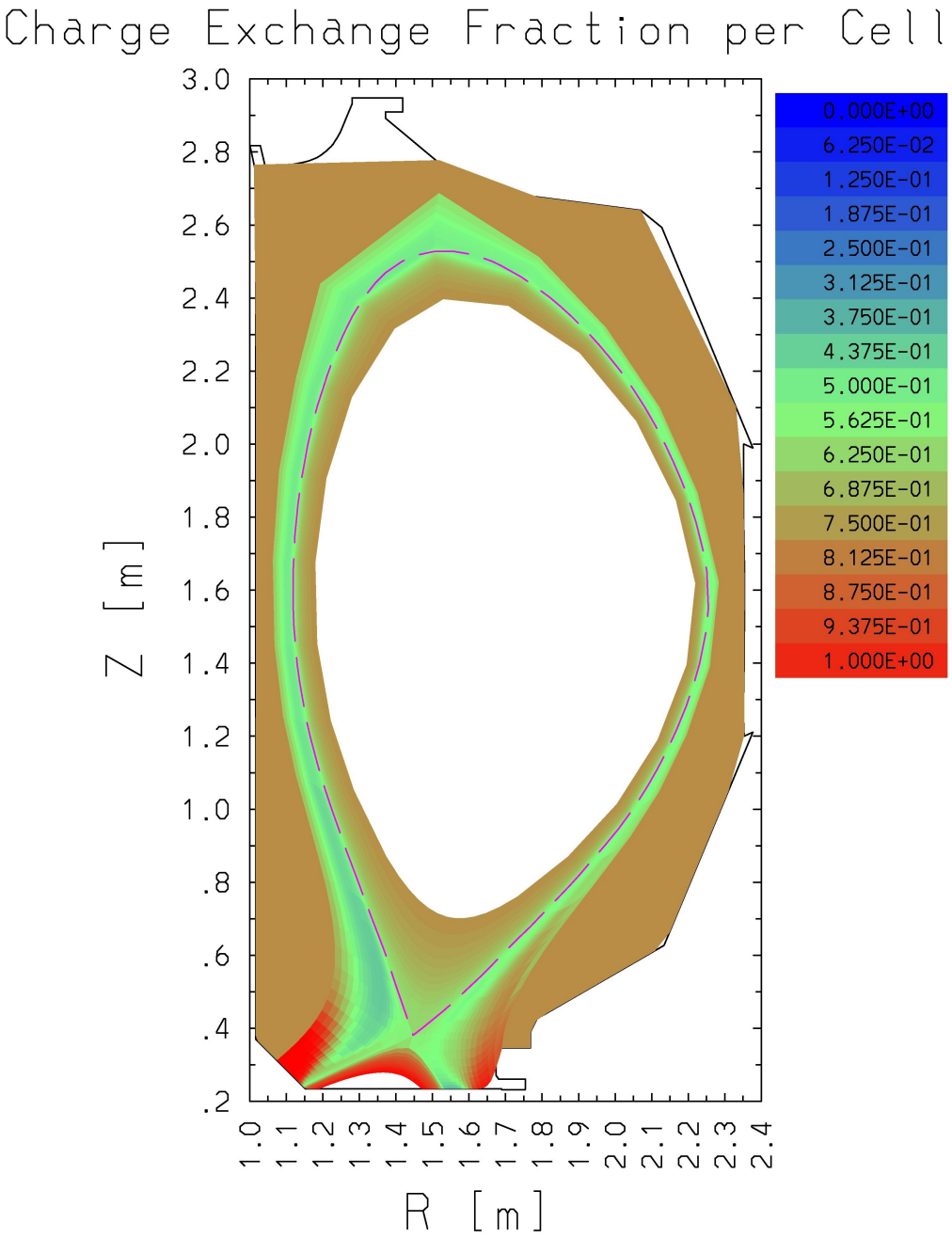

Figure 72: Charge Exchange Fraction per Cell (Attached Case)

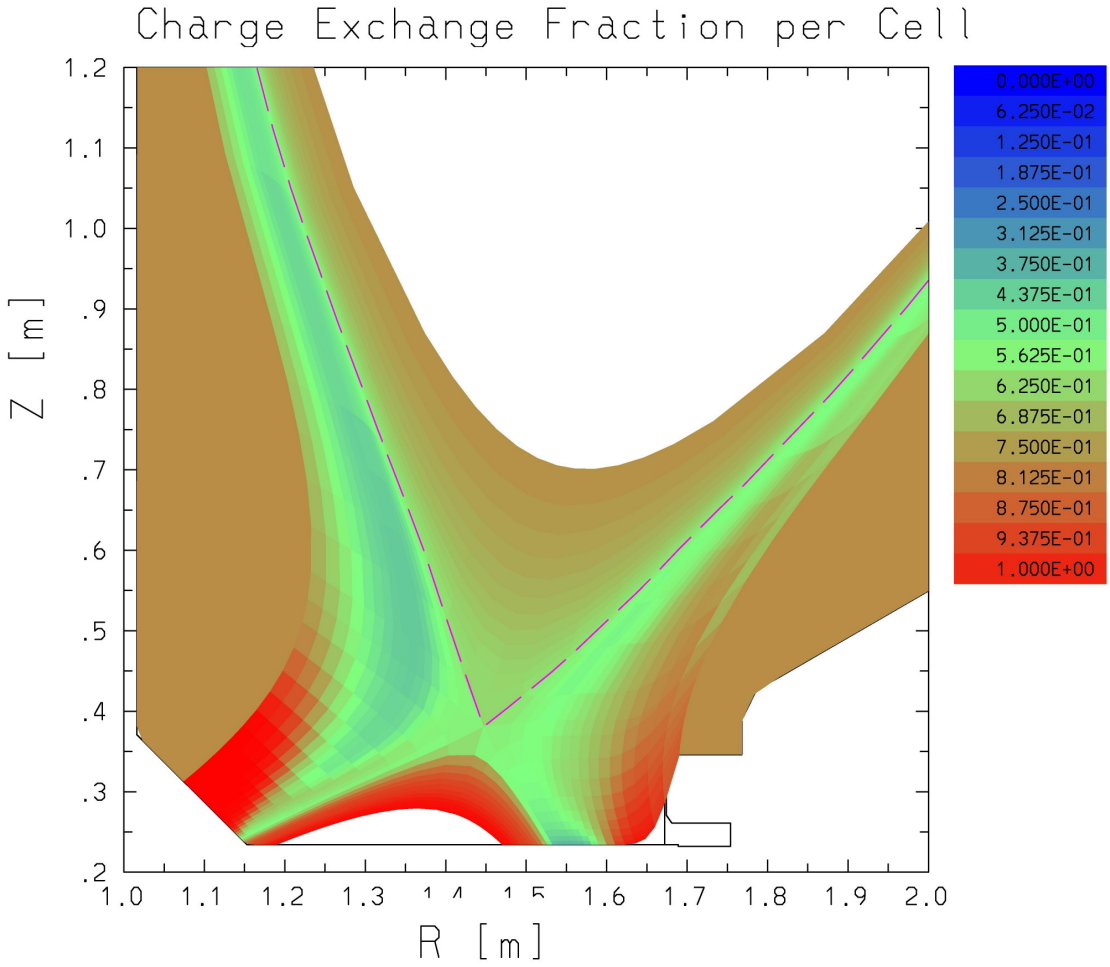

Figure 73: Charge Exchange Fraction per Cell divertor view (Attached Case)

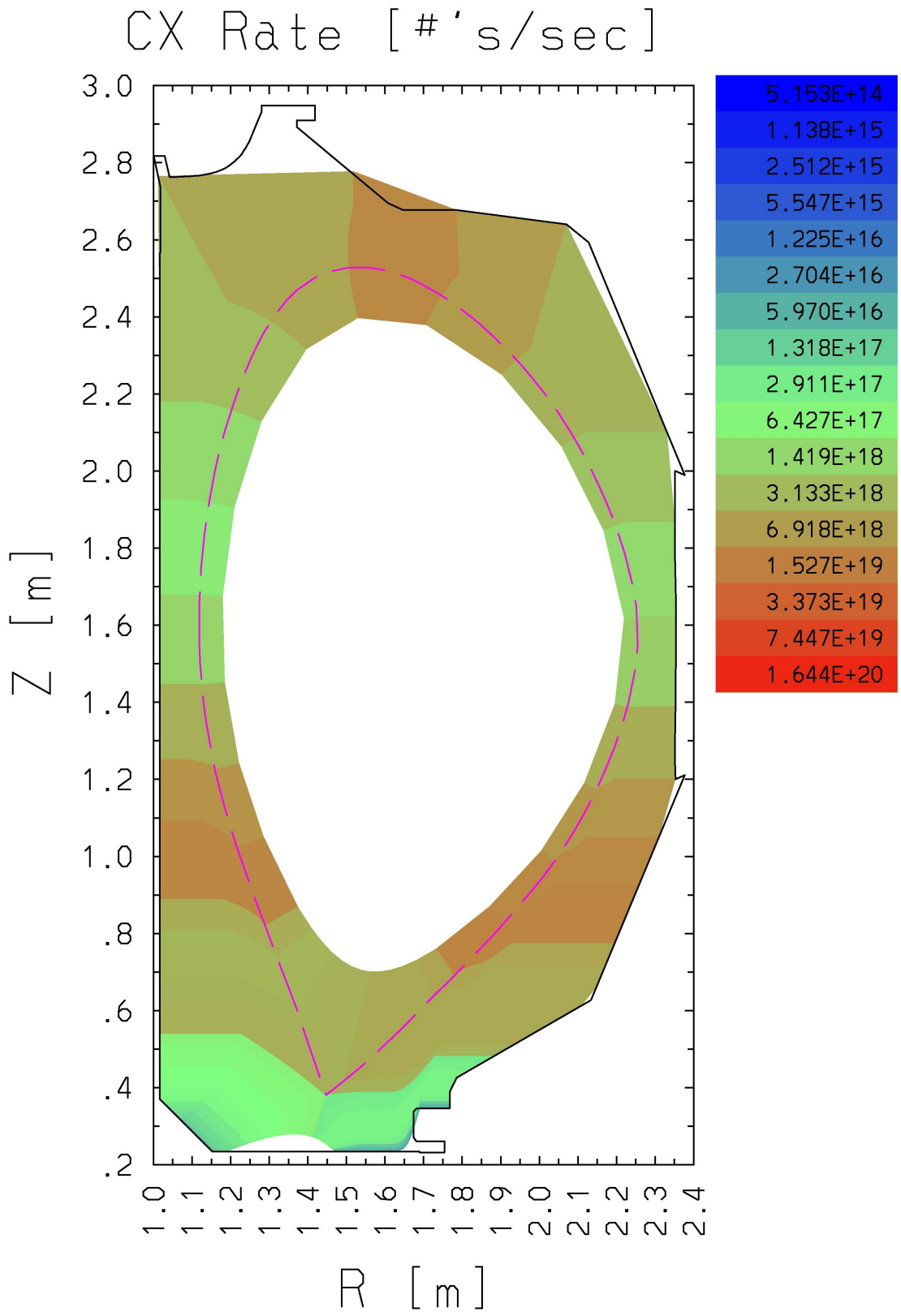

Figure 74: Charge Exchange Rates per Cell (Attached Case)

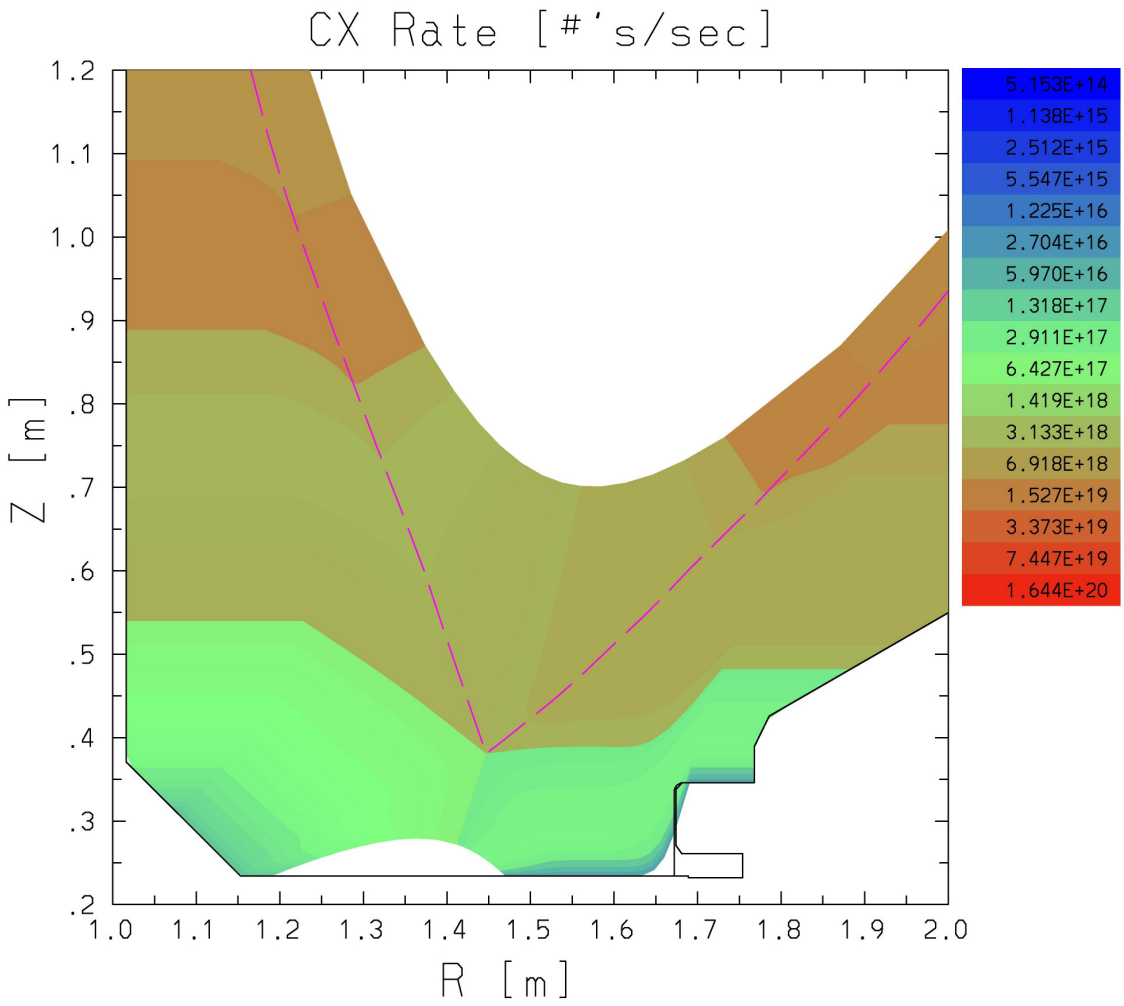

Figure 75: Charge Exchange Rates per Cell divertor view (Attached Case)

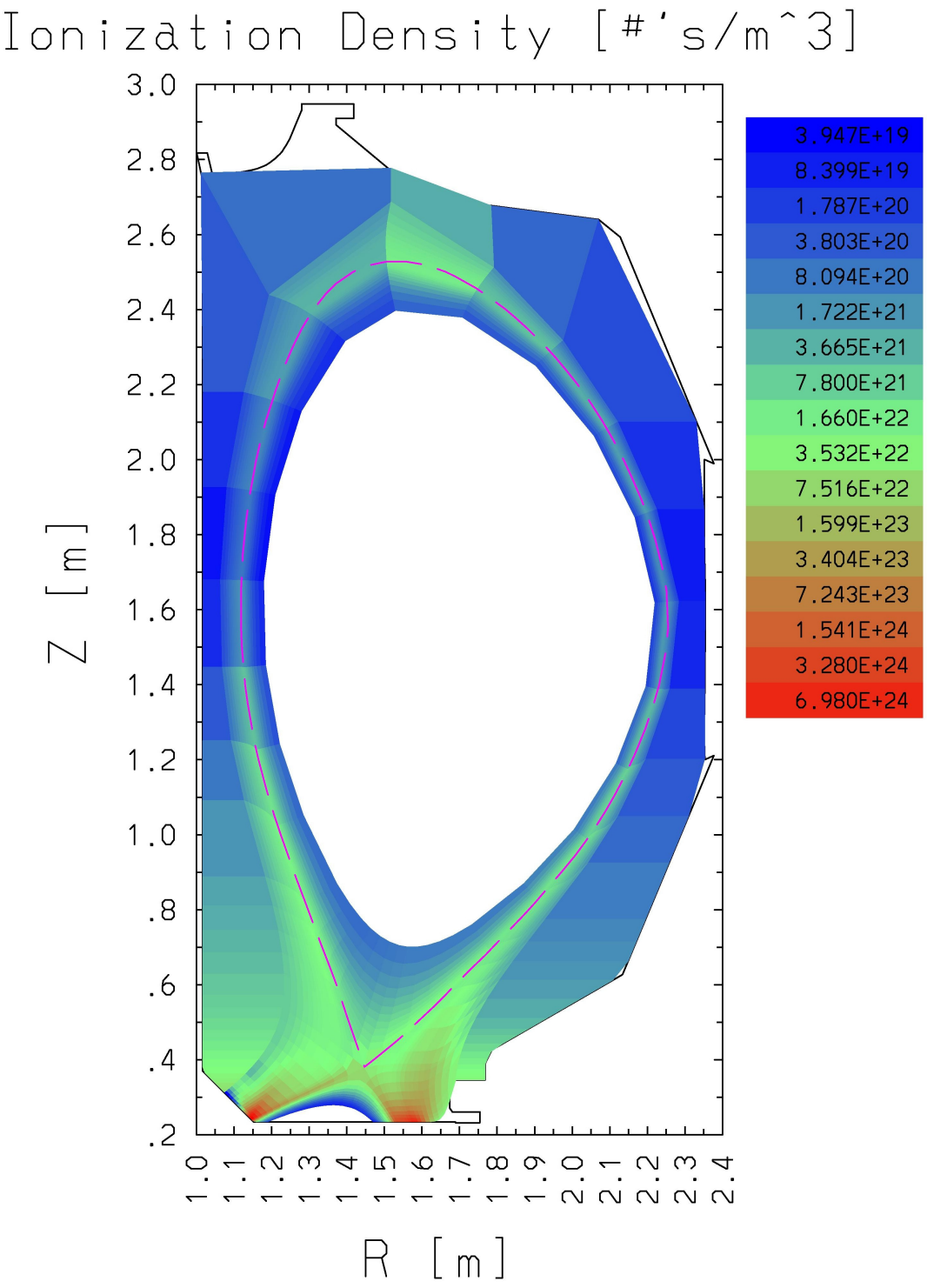

Figure 76: Ionization Density per Cell (Attached Case)

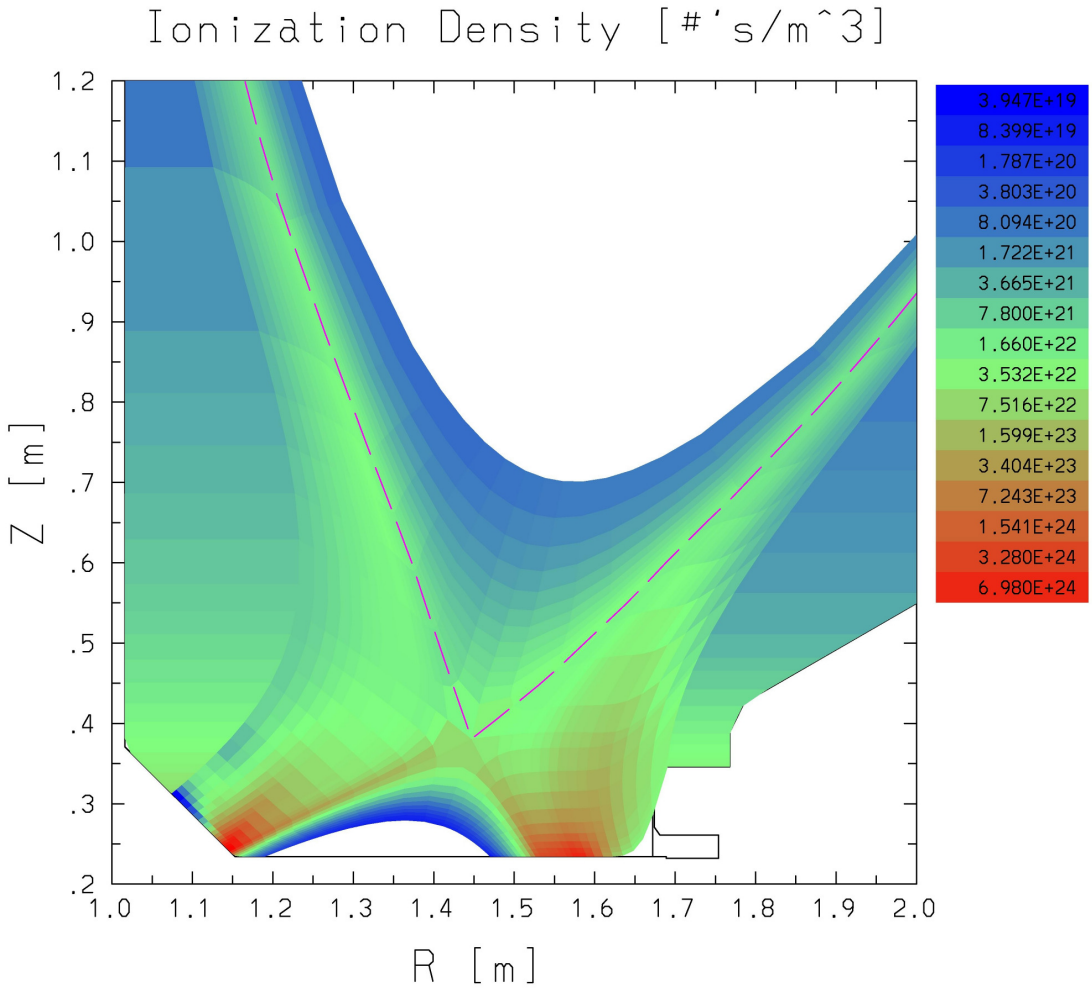

Figure 77: Ionization Density per Cell divertor view (Attached Case)

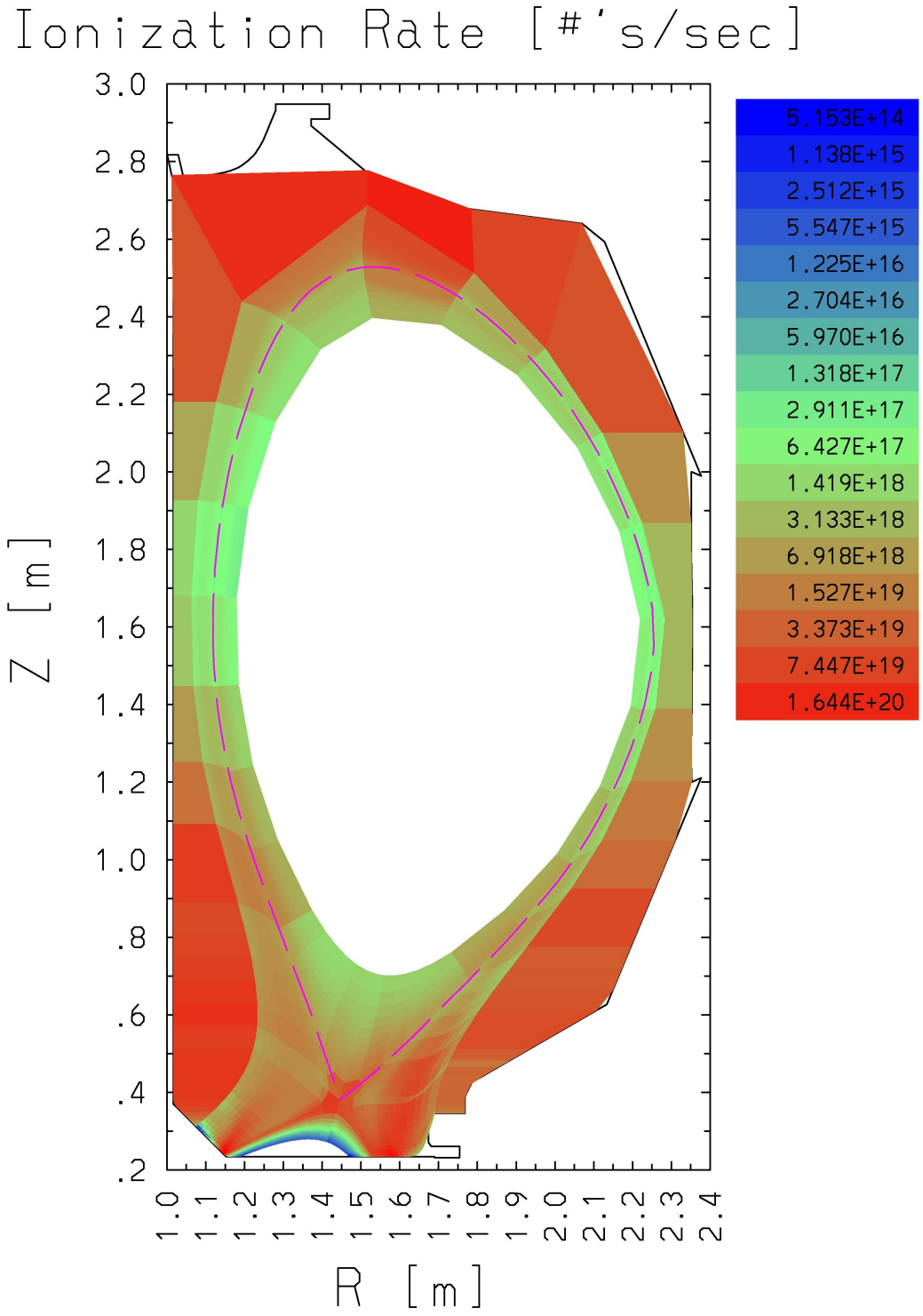

Figure 78: Ionization Rate per Cell (Attached Case)

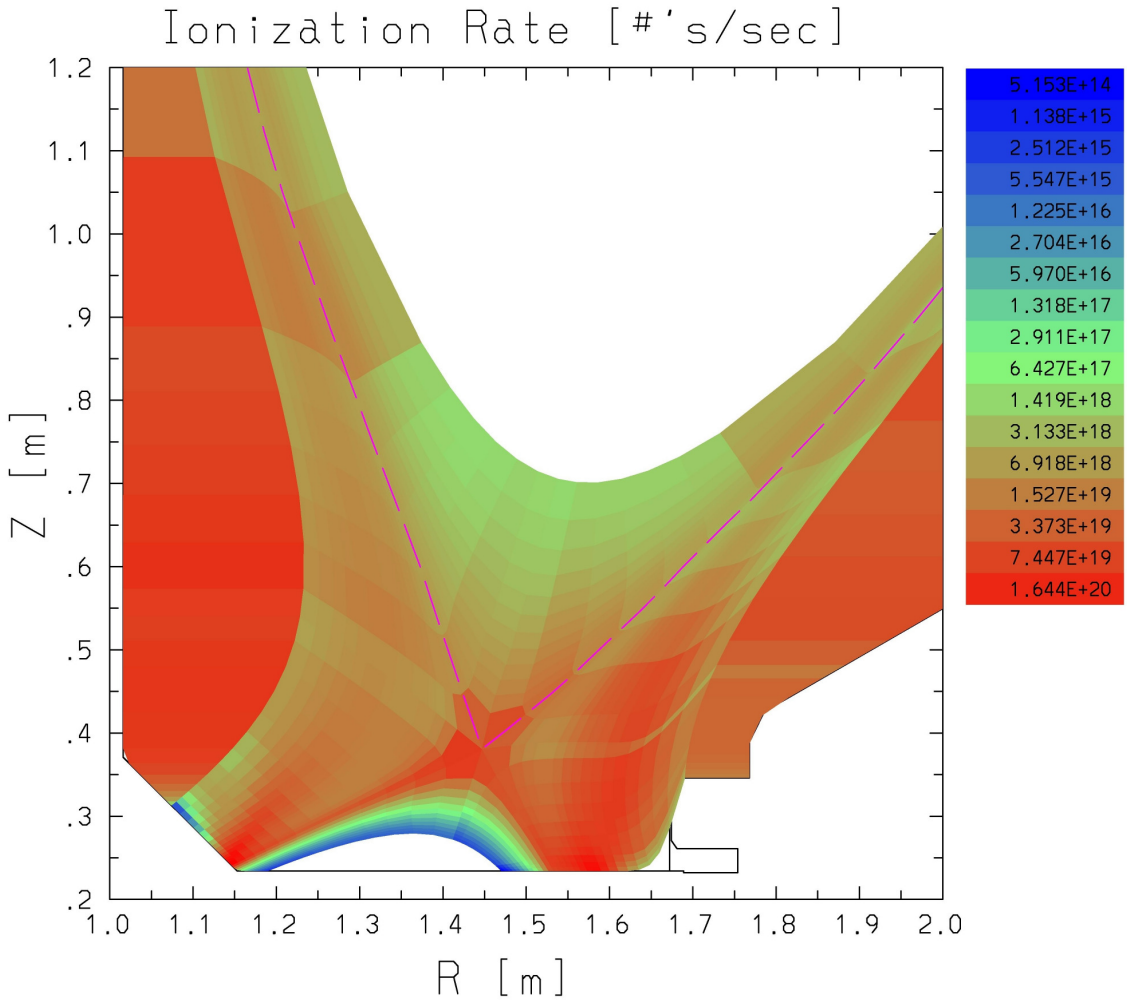

Figure 79: Ionization Rate per Cell divertor view (Attached Case)

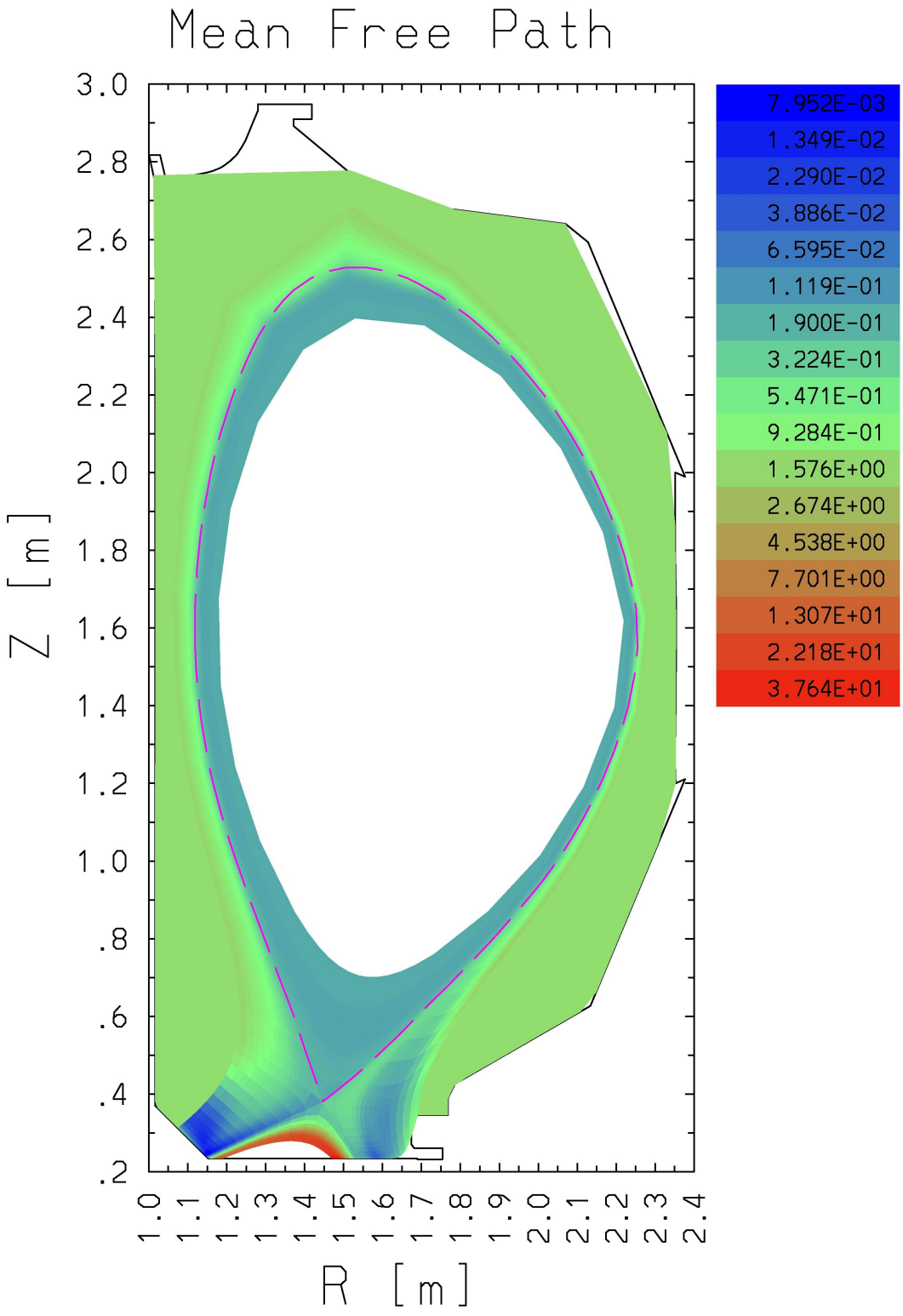

Figure 80: Mean Free Path per Cell (Attached Case)

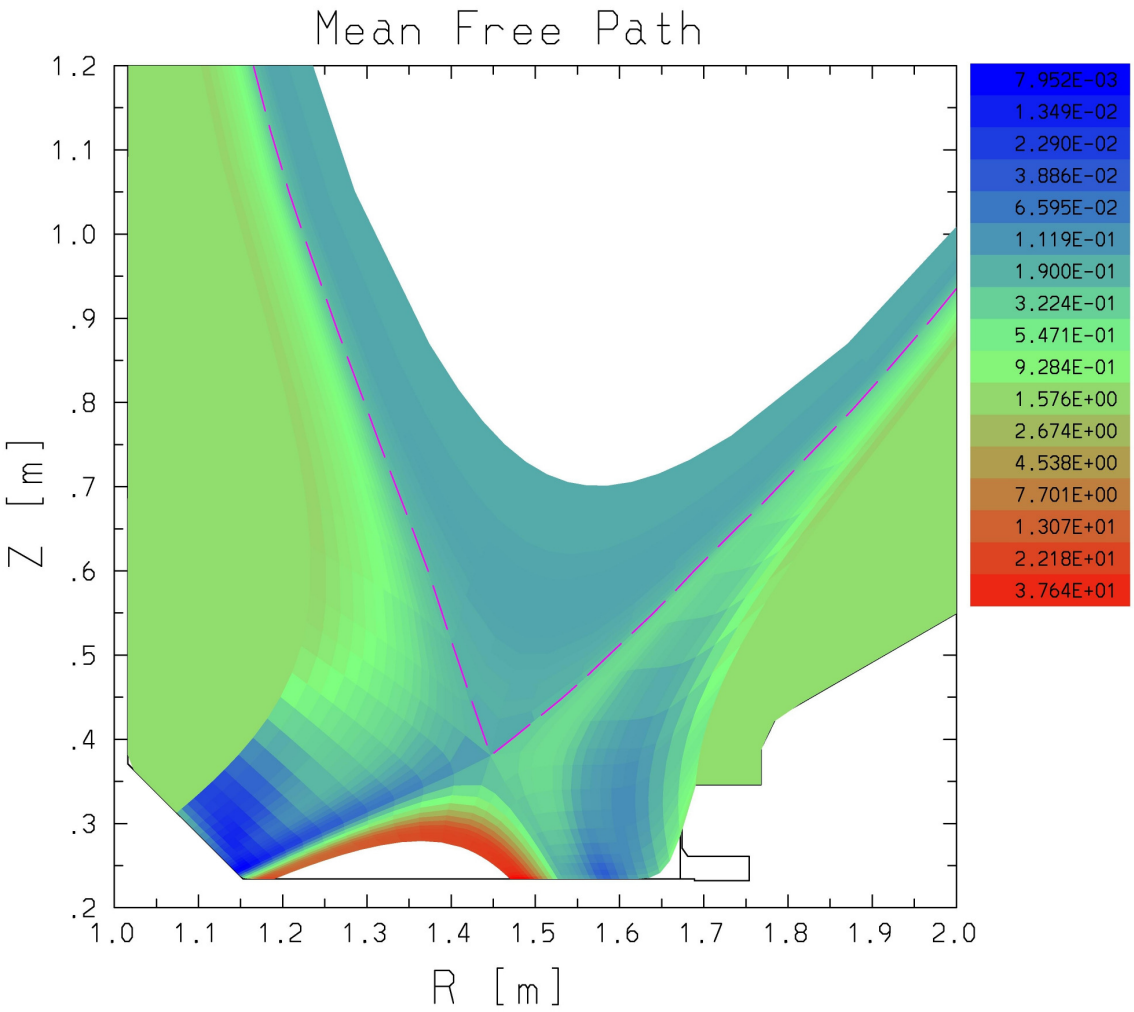

Figure 81: Mean Free Path per Cell divertor view (Attached Case)

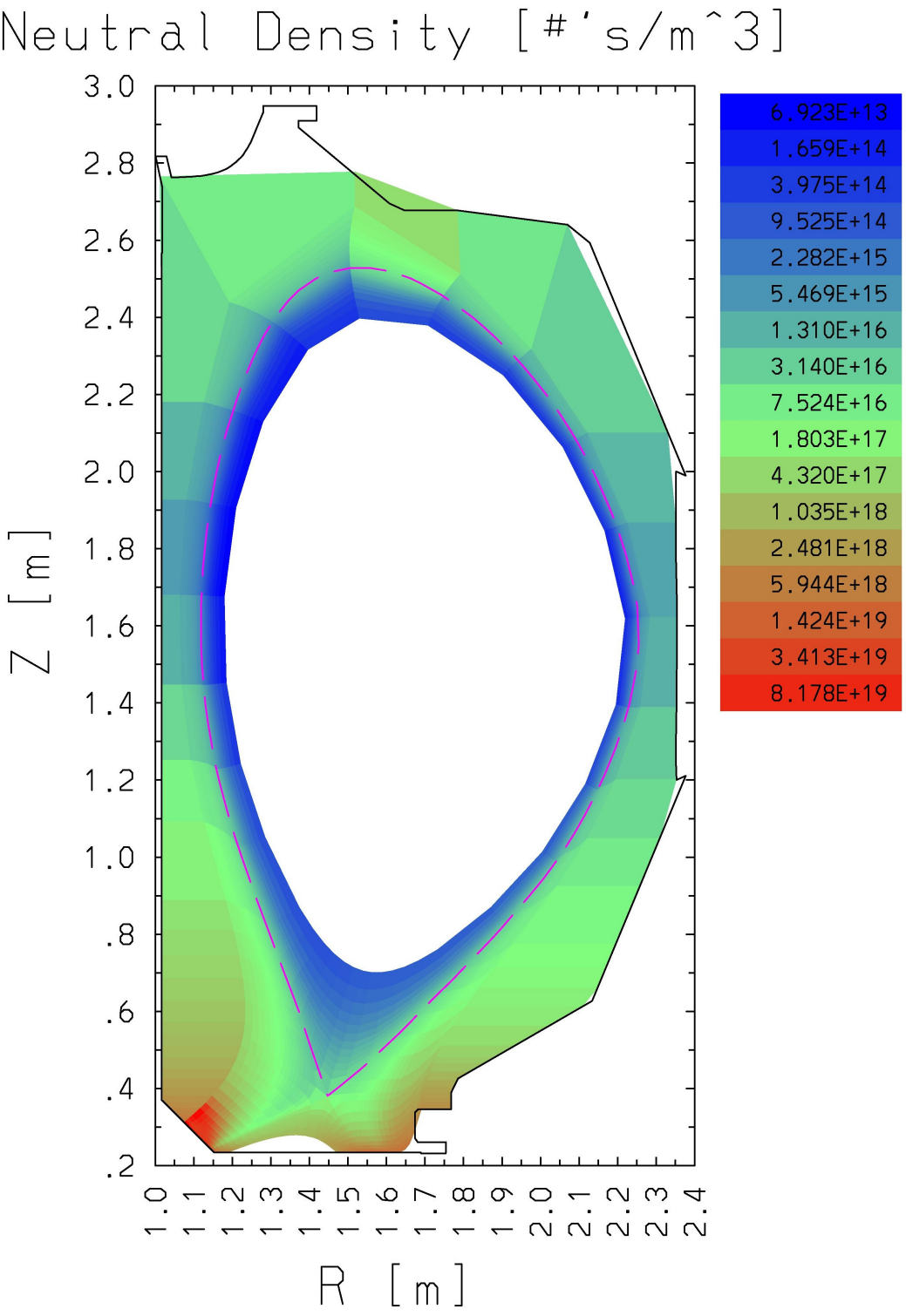

Figure 82: Neutral Density per Cell (Attached Case)

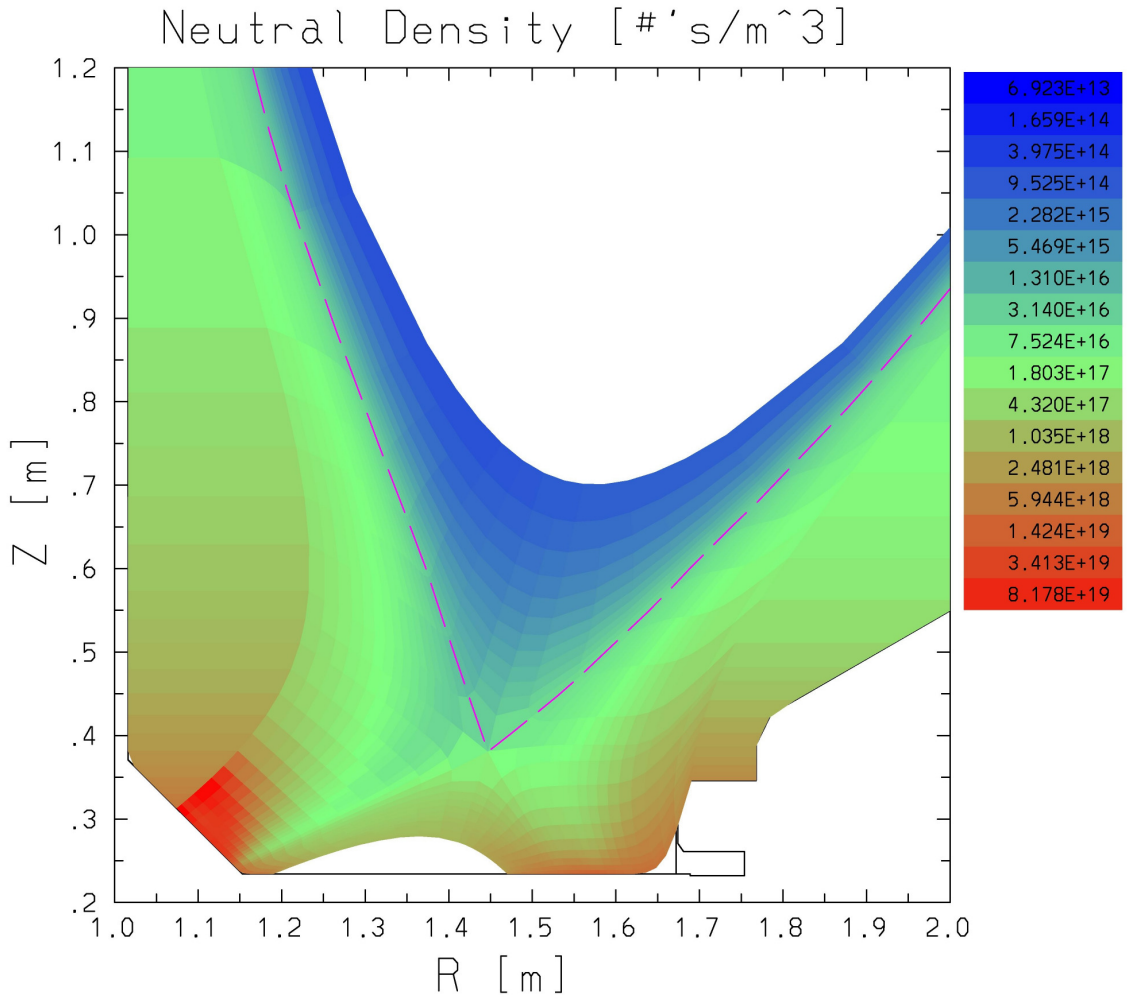

Figure 83: Neutral Density per Cell divertor view (Attached Case)

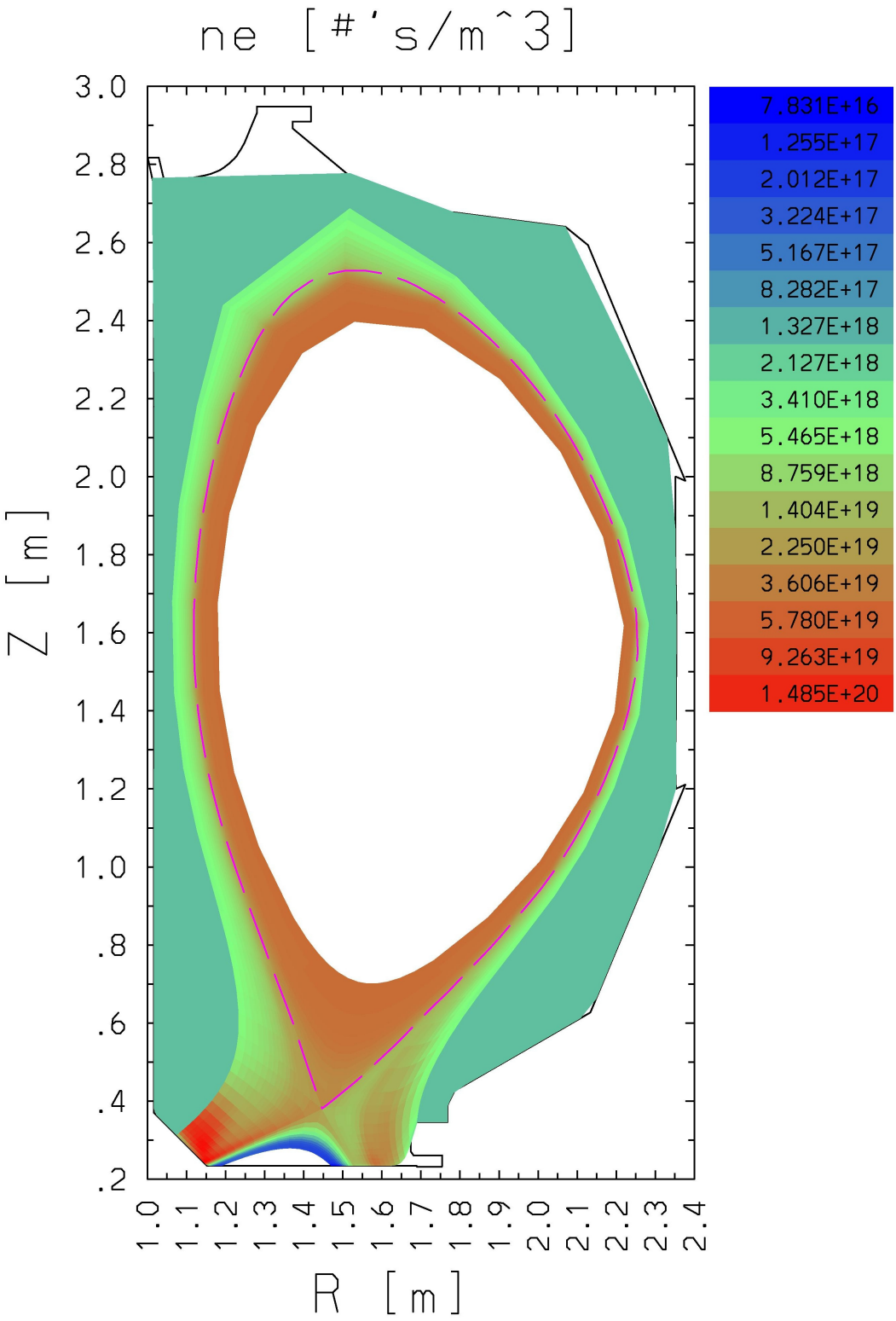

Figure 84: Electron Density per Cell (Attached Case)

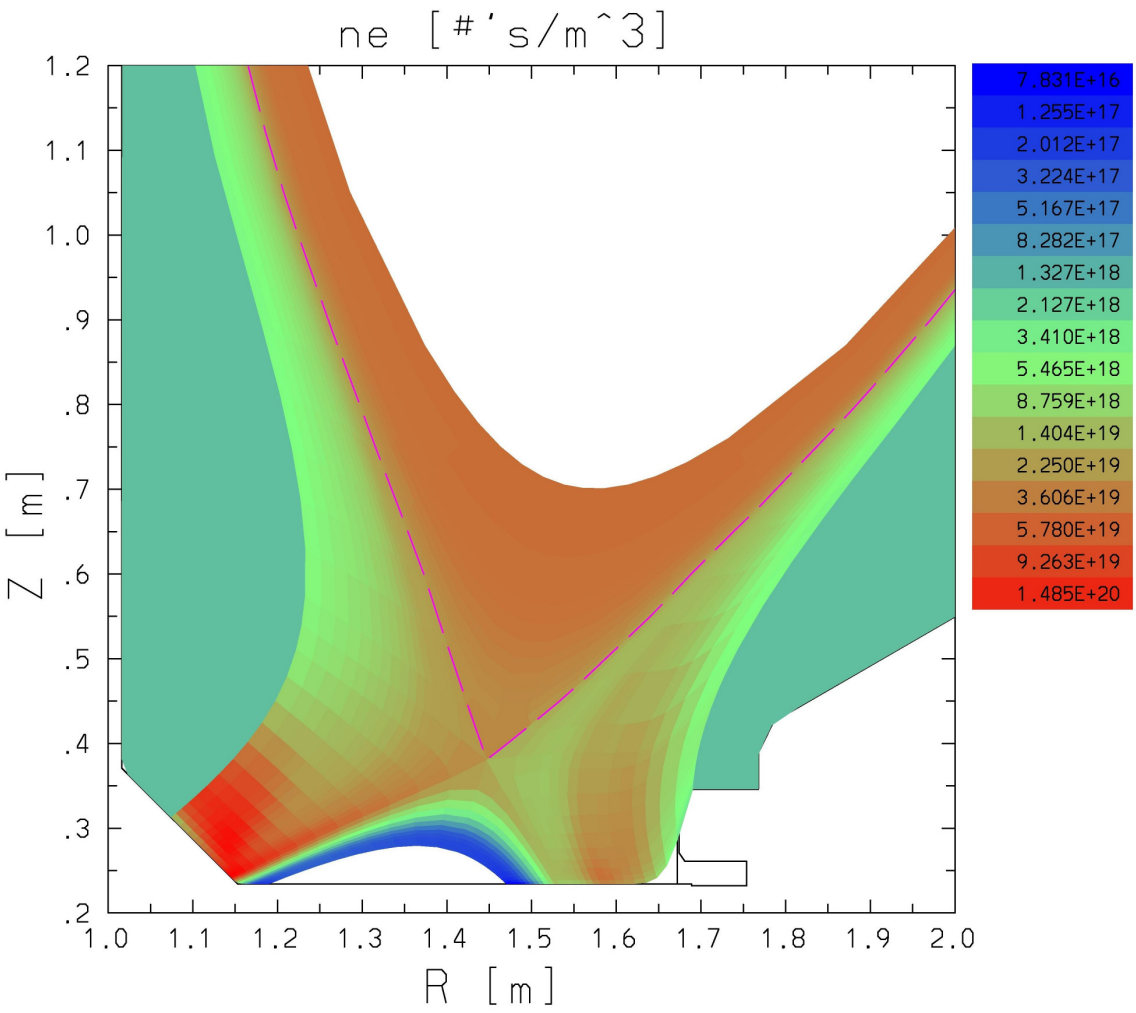

Figure 85: Electron Density per Cell divertor view (Attached Case)

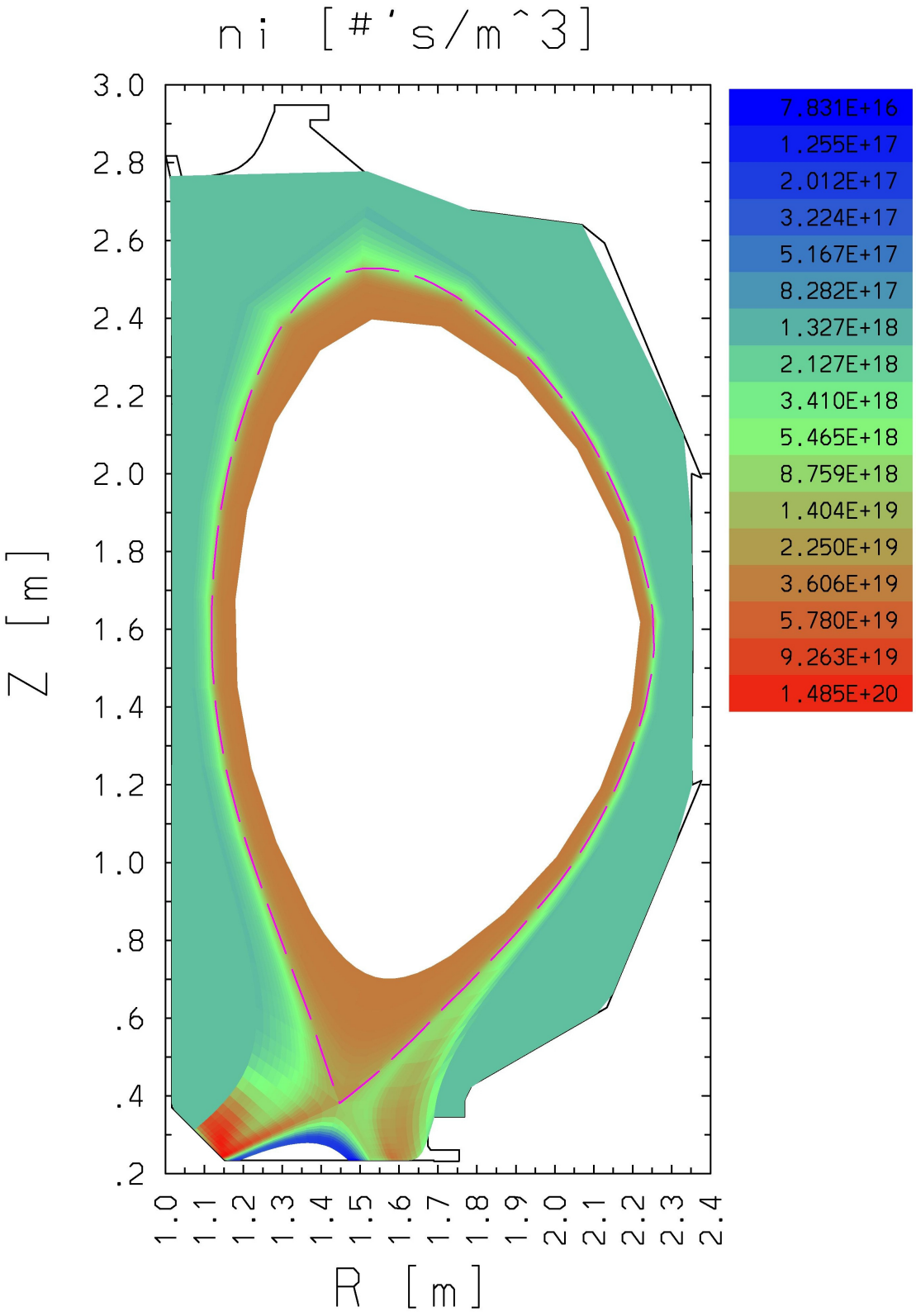

Figure 86: Ion Density per Cell (Attached Case)

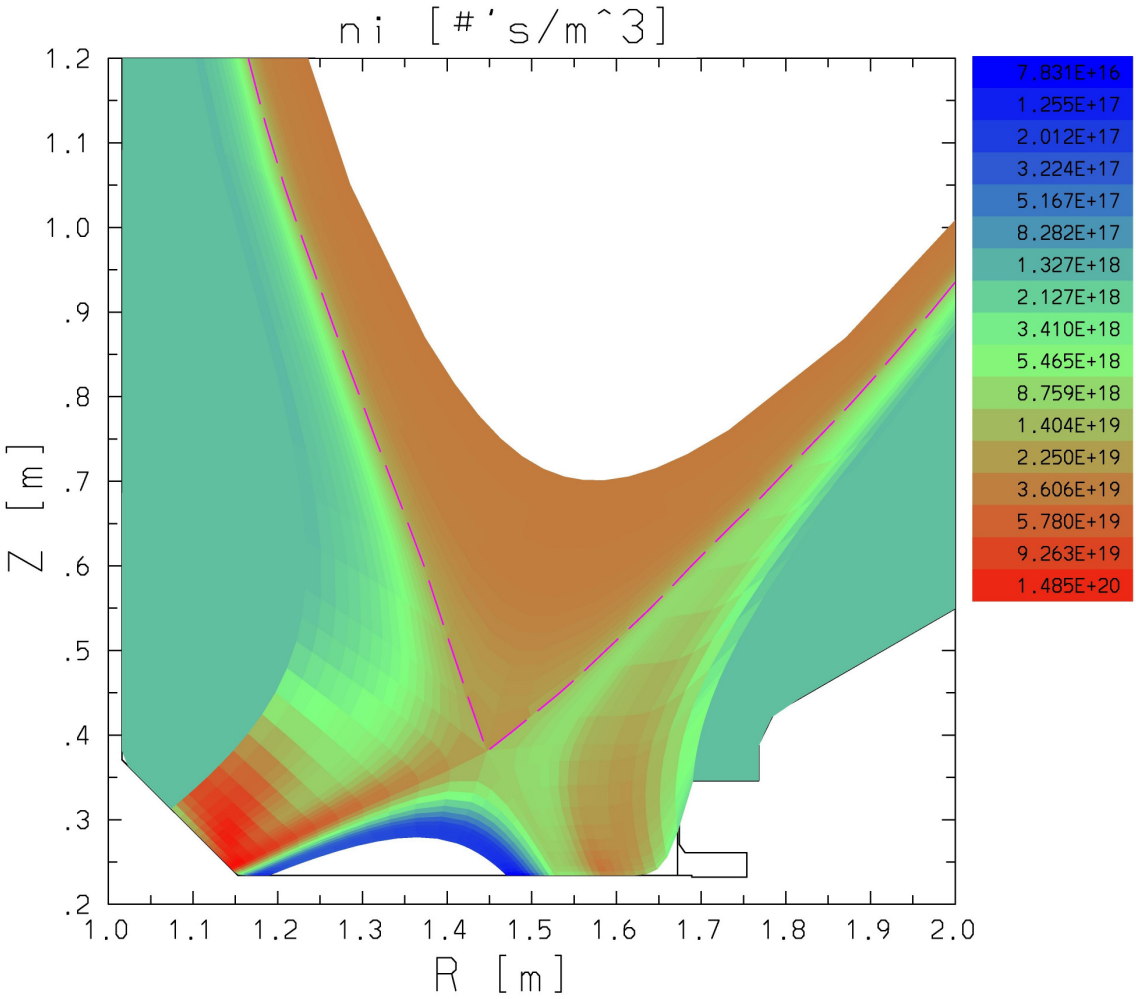

Figure 87: Ion Density per Cell divertor view (Attached Case)

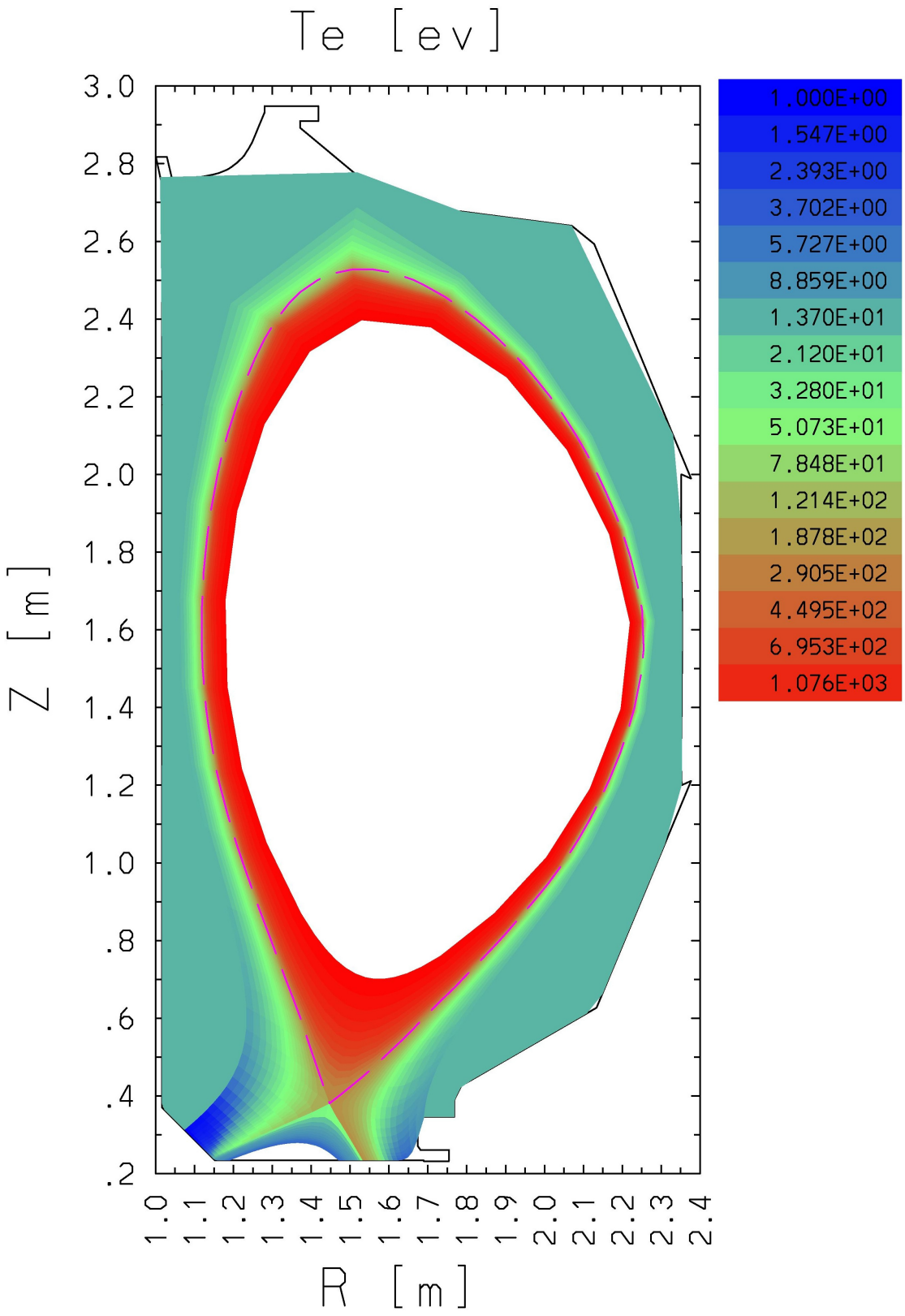

Figure 88: Electron Temperature per Cell (Attached Case)

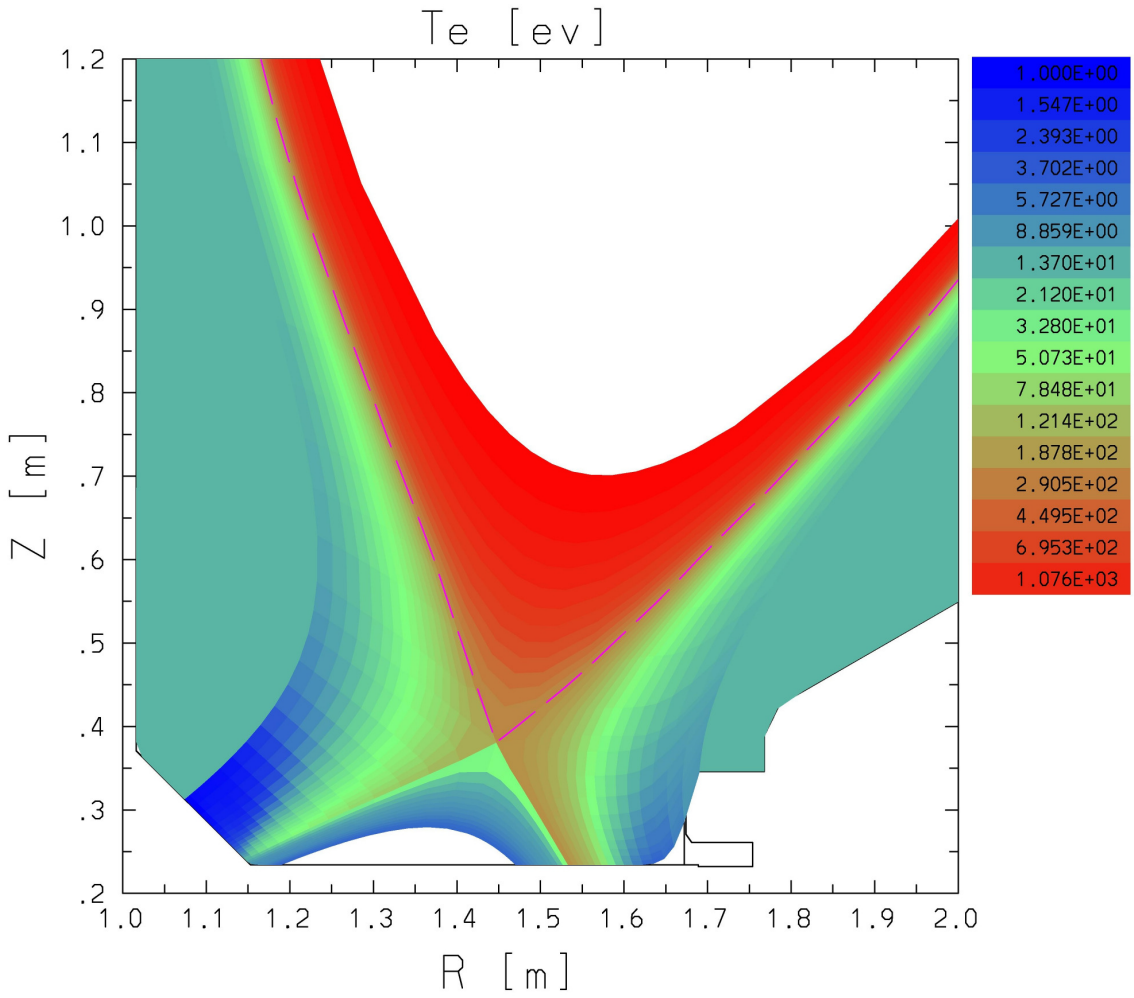

Figure 89: Electron Temperature per Cell divertor view (Attached Case)

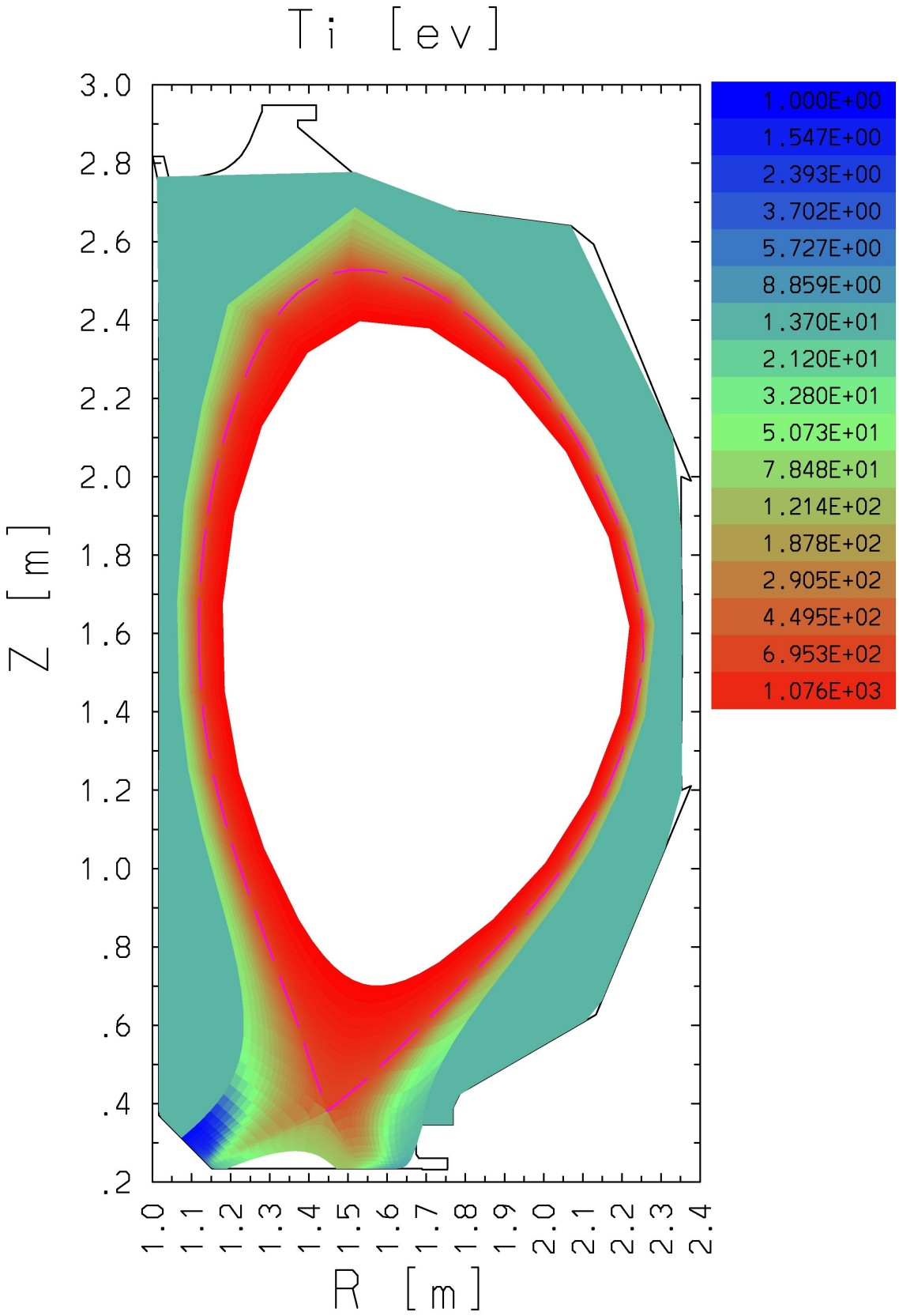

Figure 90: Ion Temperature per Cell (Attached Case)

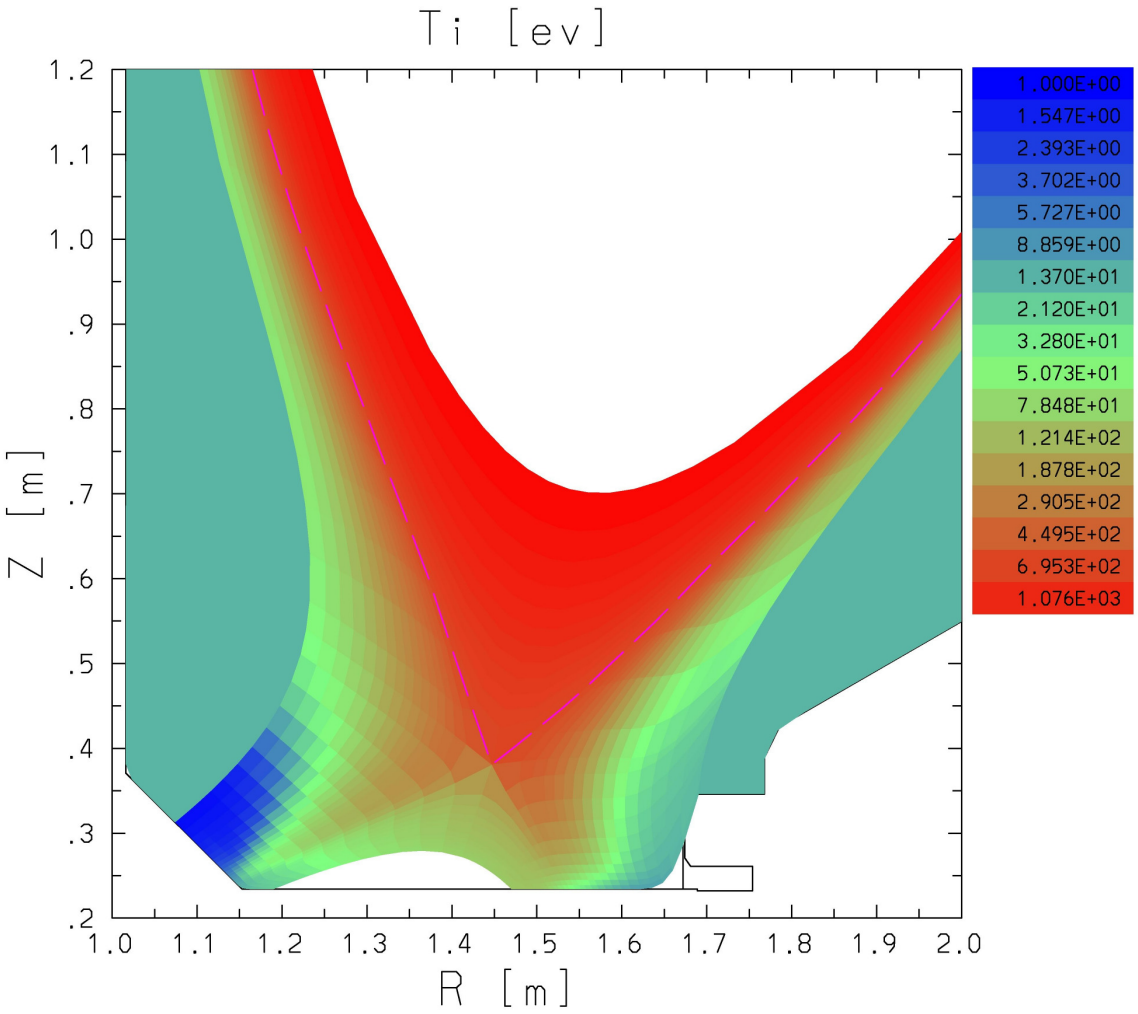

Figure 91: Ion Temperature per Cell divertor view(Attached Case)

Appendix D. “make_toneut” Code

The following appendix contains the actual “make_toneut” code used to create the geometry section of the toneut file. It is listed here incase the version on the General Atomics servers should somehow be deleted.

The code works by automatically extending the UEDGE mesh to the outer wall of the confinement vessel using simple geometry. The top of the GTNEUT mesh is determined by specific wall locations unlike the automated routines that define the base of the mesh. This was done because a GTNEUT mesh could not be automatically created to reproduce a mesh like that seen in the DEGAS2 code. The numbering schemes are incompatible. Modifications to specific wall locations like xlim(85) or ylim(85) can redefine the GTNEUT mesh.

The code is written in the BASIS scripting language used by UEDGE. It has similarities with the python language.

```
# This file defines a function to plot the UEDGE mesh, and
# then calls the function to plot the entire mesh.
# To use this file in a simple way, give the following commands:
#    read plotmesh
#    nf
# The function could then be used in a more sophisticated way
# to plot portions of the mesh, possibly with customized plot limits
# (by resetting any of r_min, r_max, z_min, and z_max):
#    call plotmesh(ixmn,ixmx,iymn,iymx)
#    nf
# where ixmn, ixmx, iymn, and iymx are integer variables or
# expressions.  Always give an "nf" command after reading the file
# plotmesh or calling the function plotmesh.

# DEFINE THE PLOT FUNCTION --

function createtoneut(ixmin,ixmax,iymin,iymax)
# Plot the cell boundaries for cell indices (ix,iy),
#             ixmin <= ix <= ixmax
#             iymin <= iy <= iymax
integer ix,iy,zachy,zachx,counter,indiv,outdiv,i,kk,hatleft,hatright
real r0(5),z0(5),r1(22),z1(22),rtop(2),rbottom(2),ztop(2),zbottom(2),rl(2),zl(2),rr(2),zr(2)
real wallr(ixmax,iymax,4),wallz(ixmax,iymax,4),rw(2),zw(2)
real denom,a1,c1,b1,b2,d1,d2,x1,x1,x3,x4,y1,y2,y3,y4,temp
real dcl,dct,dcr,dcb,acl,act,acr,acb,atot
frame r_min, r_max, z_min, z_max
integer nxmin,nxmax,nymin,nymax
integer ounit=basopen("toneut-cells","w")
integer walls=basopen("toneut-walls","w")
integer cores=basopen("toneut-cores","w")
integer rwall_gex=basopen("toneut-rwall_gex","w")
```

```
integer geometry=basopen("geometry.m","w")
integer flatflux=basopen("toneut-flatflux","w")
integer icn,icl,ict,icr,icb, plasmawall,cells,kk,plasmareg,wallreg,mm,pf1,pf2,pp,pfregionsides,ix1,iy1,qq,iter_pfr_in,iter_pfr_out,rwall
real dcl,dct,dcr,dcb,acl,act,acr,acb,atot,rcl(2),rcr(2),rct(2),rcb(2),zcl(2),zcr(2),zct(2),zcb(2),dcb1,acb1
real edense,idense,etemp,itemp,pfr_r,pfr_z,a,b,c,angc,divplt_d,divplt_t,divchan_d,divchan_t,sol_d,sol_t,deln,x_deln,nflux
real a1,a2,a3,a4,b1,b2,b3,b4,c1,c2,c3,c4,ang1,ang2,ang3,ang4
# icn = cell number of present cell
# icl = cell number of neighbor poloidally left (decreasing ix)
# ict = cell number of neighbor radially above (increasing iy)
# icr = cell number of neighbor poloidally right (increasing ix)
# icb = cell number of neighbor radially below (decreasing iy)
# dcl = length of line between icn and icl [meters}
# dct = length of line between icn and ict
# dcr = length of line between icn and icr
# dcb = length of line between icn and icb

# ll is for lower-left vertex
# ul is for upper-left vertex
# ur is for upper-right vertex
# lr is for lower-right vertex

attr labels=no     # don't label curves
attr scale=equal   # use equal horiz. & vert. grid spacing
counter = 1
titlet=runid
titleb="RADIAL POSITION (m)"
titlel="VERTICAL POSITION (m)"
indiv = (nxleg(1,1)+nxxpt)
outdiv= (nxleg(1,2)+nxxpt)
```

```
# Redefine gap to wall
#########################################################Inner Leg
do iy=iymax,iymax
do ix=ixmin,(nxleg(1,1)+nxxpt)+(nxcore(1,1)+nxxpt)-1
     x3=0
     y3=zm(ix,iy,1)
     x4=rm(ix,iy,1)
     y4=zm(ix,iy,1)
     if(zm(ix,iy,1)<ylim(85)) then
          x2=xlim(84)
          y2=ylim(84)
          x1=xlim(85)
          y1=ylim(85)
      else
          x2=xlim(85)
          y2=ylim(85)
          x1=xlim(10)
          y1=ylim(10)
      endif
     denom=(x1-x2)*(y3-y4)-(y1-y2)*(x3-x4)
     a1 = x1*y2-y1*x2
     c1 = x3*y4-y3*x4
     b1= x1-x2
     b2= y1-y2
     d1= x3-x4
     d2= y3-y4
     rm(ix,iy,3)=(a1*d1-b1*c1)/denom
     zm(ix,iy,3)=(a1*d2-b2*c1)/denom
  enddo
enddo
```

```
do iy=iymax,iymax
do ix=ixmin,((nxleg(1,1)+nxxpt)+nxxpt)+(nxcore(1,1)+nxxpt)-2
      x3=0
      y3=zm(ix,iy,2)
      x4=rm(ix,iy,2)
      y4=zm(ix,iy,2)
      if(zm(ix,iy,2)<ylim(85)) then
           x2=xlim(84)
           y2=ylim(84)
           x1=xlim(85)
           y1=ylim(85)
       else
           x2=xlim(85)
           y2=ylim(85)
           x1=xlim(10)
           y1=ylim(10)
       endif
      denom=(x1-x2)*(y3-y4)-(y1-y2)*(x3-x4)
      a1 = x1*y2-y1*x2
      c1 = x3*y4-y3*x4
      b1= x1-x2
      b2= y1-y2
      d1= x3-x4
      d2= y3-y4
      rm(ix,iy,4)=(a1*d1-b1*c1)/denom
      zm(ix,iy,4)=(a1*d2-b2*c1)/denom
   enddo
enddo

##########################################################outer Leg
do iy=iymax,iymax
```

```
do ix=(nxleg(1,1)+nxxpt)+(nxcore(1,1)+nxxpt)+1,ixmax
      x3=3
      y3=zm(ix,iy,1)
      x4=rm(ix,iy,1)
      y4=zm(ix,iy,1)

      do kk = 50,80
      if(zm(ix,iy,1)>ylim(kk+1) & zm(ix,iy,1)<ylim(kk)) then
           x2=xlim(kk)
           y2=ylim(kk)
           x1=xlim(kk+1)
           y1=ylim(kk+1)
       kk = 80
       else
       endif
      enddo

      denom=(x1-x2)*(y3-y4)-(y1-y2)*(x3-x4)
      a1 = x1*y2-y1*x2
      c1 = x3*y4-y3*x4
      b1= x1-x2
      b2= y1-y2
      d1= x3-x4
      d2= y3-y4
      rm(ix,iy,3)=(a1*d1-b1*c1)/denom
      zm(ix,iy,3)=(a1*d2-b2*c1)/denom
   enddo
enddo

do iy=iymax,iymax
do ix=(nxleg(1,1)+nxxpt)+(nxcore(1,1)+nxxpt)+1,ixmax
```

```
      x3=3
      y3=zm(ix,iy,2)
      x4=rm(ix,iy,2)
      y4=zm(ix,iy,2)

      do kk = 50,80
      if(zm(ix,iy,2)>ylim(kk+1) & zm(ix,iy,2)<ylim(kk)) then
           x2=xlim(kk)
           y2=ylim(kk)
           x1=xlim(kk+1)
           y1=ylim(kk+1)
       kk = 80
       else
       endif
      enddo

      denom=(x1-x2)*(y3-y4)-(y1-y2)*(x3-x4)
      a1 = x1*y2-y1*x2
      c1 = x3*y4-y3*x4
      b1= x1-x2
      b2= y1-y2
      d1= x3-x4
      d2= y3-y4
      rm(ix,iy,4)=(a1*d1-b1*c1)/denom
      zm(ix,iy,4)=(a1*d2-b2*c1)/denom
    enddo
  enddo

      rm(((nxleg(1,1)+nxxpt)+(nxcore(1,1)+nxxpt)-1),iymax,3)=xlim(12)
      zm(((nxleg(1,1)+nxxpt)+(nxcore(1,1)+nxxpt)-1),iymax,3)=ylim(12)
      rm(((nxleg(1,1)+nxxpt)+(nxcore(1,1)+nxxpt)-2),iymax,4)=xlim(12)
```

```
    zm(((nxleg(1,1)+nxxpt)+(nxcore(1,1)+nxxpt)-2),iymax,4)=ylim(12)


      x3=xlim(49)
         y3=ylim(49)
         x4=xlim(51)
         y4=ylim(51)
      x2=rm(((nxleg(1,1)+nxxpt)+(nxcore(1,1)+nxxpt)),iymax,3)
      y2=10
      x1=rm(((nxleg(1,1)+nxxpt)+(nxcore(1,1)+nxxpt)),iymax,3)
      y1=zm(((nxleg(1,1)+nxxpt)+(nxcore(1,1)+nxxpt)),iymax,3)

    denom=(x1-x2)*(y3-y4)-(y1-y2)*(x3-x4)
    a1 = x1*y2-y1*x2
    c1 = x3*y4-y3*x4
    b1= x1-x2
    b2= y1-y2
    d1= x3-x4
    d2= y3-y4
#     rm(ix,iy,3)=(a1*d1-b1*c1)/denom
#     zm(ix,iy,3)=(a1*d2-b2*c1)/denom


    rm(((nxleg(1,1)+nxxpt)+(nxcore(1,1)+nxxpt)),iymax,3)=(a1*d1-b1*c1)/denom
    zm(((nxleg(1,1)+nxxpt)+(nxcore(1,1)+nxxpt)),iymax,3)=(a1*d2-b2*c1)/denom
    rm(((nxleg(1,1)+nxxpt)+(nxcore(1,1)+nxxpt)-1),iymax,4)=(a1*d1-b1*c1)/denom
    zm(((nxleg(1,1)+nxxpt)+(nxcore(1,1)+nxxpt)-1),iymax,4)=(a1*d2-b2*c1)/denom

    rm(((nxleg(1,1)+nxxpt)+(nxcore(1,1)+nxxpt)+1),iymax,3)=xlim(53)
    zm(((nxleg(1,1)+nxxpt)+(nxcore(1,1)+nxxpt)+1),iymax,3)=ylim(53)
    rm(((nxleg(1,1)+nxxpt)+(nxcore(1,1)+nxxpt)),iymax,4)=xlim(53)
```

```
    zm(((nxleg(1,1)+nxxpt)+(nxcore(1,1)+nxxpt)),iymax,4)=ylim(53)

    rm(((nxleg(1,1)+nxxpt)+(nxcore(1,1)+nxxpt)+2),iymax,3)=xlim(54)
    zm(((nxleg(1,1)+nxxpt)+(nxcore(1,1)+nxxpt)+2),iymax,3)=ylim(54)
    rm(((nxleg(1,1)+nxxpt)+(nxcore(1,1)+nxxpt)+1),iymax,4)=xlim(54)
    zm(((nxleg(1,1)+nxxpt)+(nxcore(1,1)+nxxpt)+1),iymax,4)=ylim(54)

    rm(ixmax,iymax,4)=rm(ixmax-1,iymax,4)
    zm(ixmax,iymax,4)=zm(ixmax,iymax,2)
    rm(ixmax,iymax,3)=rm(ixmax-1,iymax,4)
    zm(ixmax,iymax,3)=zm(ixmax-1,iymax,4)



#%%%%%%%%%%%%%%%%%%%%%%%%%%%%%
##############################################
#THIS SECTION CREATES THE ACTUAL GTNEUT GEOMETRY
##############################################
plasmawall = 0
cells = ixmax * iymax +(nxxpt+nxleg(1,2))+(nxxpt+nxleg(1,1))
plasmareg = (nxxpt+nxcore(1,1))+(nxxpt+nxcore(1,2))
wallreg = ixmax+ 2 * iymax +1+1
ounit << " $inp"
ounit << " nCells = " << format((cells),6) << " nPlasmReg = " << format(plasmareg,6) <<  " nWallSegm = " << format(wallreg,6)
kk = 1
mm = (nxxpt+nxcore(1,1))+(nxxpt+nxcore(1,2))+cells
iter_pfr_in = 1
iter_pfr_out = (nxxpt+nxleg(1,1))
#nPlasmReg =  34  nWallSegm =  4

do iy = ixmin, iymax
```

```
   do ix = ixmin, ixmax
#  Compute cell number and surrounding neighbor numbers
   icn = ix + ixmax*(iy-1)
   icl = ixm1(ix,iy) + ixmax*(iy-1)
   if (ix == ixmin) icl = 0
   icr = ixp1(ix,iy) + ixmax*(iy-1)
   if (ix == ixmax) icr = 0
   icb = ix + ixmax*(iy-2)
   if (iy == iymin) icb = 0
   ict = ix + ixmax*iy
   if (iy == iymax) ict = 0
#PRIVATE FLUX REGION CELL NUMBER IS NY*NX+1
   if (iy == iymin & ix <= (nxxpt+nxleg(1,1))) then
   icb = iymax*ixmax + iter_pfr_in
   iter_pfr_in = iter_pfr_in + 1
   endif
   if (iy == iymin & ix >= ixmax - (nxxpt+nxleg(1,2))) then
   icb = iymax*ixmax + iter_pfr_out
   iter_pfr_out = iter_pfr_out + 1
   endif
#END PRIVATE FLUX REGION
   if (ix = ixmax) then
   icr = (cells+plasmareg+wallreg-1)-(iy)
   icl = icn - 1
   walls << "iType(" << format(icr,6) << " ) = 2  nSides(" << format(icr,6) << ") = 1 " << "adjCell(1," << format(icr,6) << ") = " <<
format(icn,6)
   endif
   if (ix = ixmin) then
   icl = cells+((nxxpt+nxcore(1,1))+(nxxpt+nxcore(1,2)))+iy
   walls << "iType(" << format(icl,6) << " ) = 2  nSides(" << format(icl,6) << ") = 1 " << "adjCell(1," << format(icl,6) << ") = " <<
format(icn,6)
```

```
   endif
   if (iy= iymax) then
   ict = cells+((nxxpt+nxcore(1,1))+(nxxpt+nxcore(1,2)))+ix+iy
   walls << "iType(" << format(ict,6) << " ) = 2  nSides(" << format(ict,6) << ") = 1 " << "adjCell(1," << format(ict,6) << ") = " <<
format(icn,6)
   endif

#########
#CORE REGION
   if (iy = iymin & ix > (nxxpt+nxleg(1,1)) & ix <= ixmax - (nxxpt+nxleg(1,2))) then
   icb = iymax*ixmax + (nxxpt+nxleg(1,2))+(nxxpt+nxleg(1,1)) + kk
   kk = kk + 1
cores << "iType(" << format(icb,6) << " ) = 1  nSides(" << format(icb,6) << ") = 1 " << "adjCell(1," << format(icb,6) << ") = " <<
format(icn,6)
   endif

#  Compute length of sides
   dcl = sqrt( (rm(ix,iy,3)-rm(ix,iy,1))**2 + (zm(ix,iy,3)-zm(ix,iy,1))**2 )
    b = dcl
   dct = sqrt( (rm(ix,iy,4)-rm(ix,iy,3))**2 + (zm(ix,iy,4)-zm(ix,iy,3))**2 )
   dcr = sqrt( (rm(ix,iy,2)-rm(ix,iy,4))**2 + (zm(ix,iy,2)-zm(ix,iy,4))**2 )
   dcb = sqrt( (rm(ix,iy,1)-rm(ix,iy,2))**2 + (zm(ix,iy,1)-zm(ix,iy,2))**2 )
    a = dcb
    c = sqrt( (rm(ix,iy,3)-rm(ix,iy,2))**2 + (zm(ix,iy,3)-zm(ix,iy,2))**2 )
    angc  =  acos((c**2 - (a**2+b**2))/(-1*2*a*b))
    angc = angc * (180/3.14159265358979)
    rcr=[rm(ix,iy,2),rm(ix,iy,4)]
    zcr=[zm(ix,iy,2),zm(ix,iy,4)]
    rcl=[rm(ix,iy,3),rm(ix,iy,1)]
    zcl=[zm(ix,iy,3),zm(ix,iy,1)]
    rcb=[rm(ix,iy,1),rm(ix,iy,2)]
```

```
      zcb=[zm(ix,iy,1),zm(ix,iy,2)]
      rct=[rm(ix,iy,4),rm(ix,iy,3)]
      zct=[zm(ix,iy,4),zm(ix,iy,3)]
    acl = acos(((rm(ix,iy,3)-rm(ix,iy,1))*(rm(ix,iy,2)-rm(ix,iy,1))+(zm(ix,iy,3)-zm(ix,iy,1))*(zm(ix,iy,2)-zm(ix,iy,1)))/(dcb*dcl))
    acl = acl * (180/3.14159265358979)
    act = acos(((rm(ix,iy,4)-rm(ix,iy,3))*(rm(ix,iy,1)-rm(ix,iy,3))+(zm(ix,iy,4)-zm(ix,iy,3))*(zm(ix,iy,1)-zm(ix,iy,3)))/(dcl*dct))
    act = act * (180/3.14159265358979)
    acr = acos(((rm(ix,iy,2)-rm(ix,iy,4))*(rm(ix,iy,3)-rm(ix,iy,4))+(zm(ix,iy,2)-zm(ix,iy,4))*(zm(ix,iy,3)-zm(ix,iy,4)))/(dct*dcr))
    acr = acr * (180/3.14159265358979)
    acb = acos(((rm(ix,iy,1)-rm(ix,iy,2))*(rm(ix,iy,4)-rm(ix,iy,2))+(zm(ix,iy,1)-zm(ix,iy,2))*(zm(ix,iy,4)-zm(ix,iy,2)))/(dcb*dcr))
    acb = acb * (180/3.14159265358979)
    atot = acb + acl + act + acr

    a1 = ((zm(ix,iy,3)-zm(ix,iy,4))**2+(rm(ix,iy,3)-rm(ix,iy,4))**2)**.5
    b1 = ((zm(ix,iy,4)-zm(ix,iy,2))**2+(rm(ix,iy,4)-rm(ix,iy,2))**2)**.5
    c1 = ((zm(ix,iy,3)-zm(ix,iy,2))**2+(rm(ix,iy,3)-rm(ix,iy,2))**2)**.5
    ang1 = acos((a1**2+b1**2-c1**2)/(2*a1*b1))
    ang1 =
ang1*(180/3.14159265358979323846264338327950288419716939937510582097494459230781640628620899862803482534211706
68)

    a2 = ((zm(ix,iy,4)-zm(ix,iy,2))**2+(rm(ix,iy,4)-rm(ix,iy,2))**2)**.5
    b2 = ((zm(ix,iy,1)-zm(ix,iy,2))**2+(rm(ix,iy,1)-rm(ix,iy,2))**2)**.5
    c2 = ((zm(ix,iy,4)-zm(ix,iy,1))**2+(rm(ix,iy,4)-rm(ix,iy,1))**2)**.5
    ang2 = acos((a2**2+b2**2-c2**2)/(2*a2*b2))
    ang2 =
ang2*(180/3.14159265358979323846264338327950288419716939937510582097494459230781640628620899862803482534211706
68)

    a3 = ((zm(ix,iy,1)-zm(ix,iy,2))**2+(rm(ix,iy,1)-rm(ix,iy,2))**2)**.5
    b3 = ((zm(ix,iy,1)-zm(ix,iy,3))**2+(rm(ix,iy,1)-rm(ix,iy,3))**2)**.5
```

```
   c3 = ((zm(ix,iy,3)-zm(ix,iy,2))**2+(rm(ix,iy,3)-rm(ix,iy,2))**2)**.5
   ang3 = acos((a3**2+b3**2-c3**2)/(2*a3*b3))
   ang3 =
ang3*(180/3.14159265358979323846264338327950288419716939937510582097494459230781640628620899862803482534211706
68)

   a4 = ((zm(ix,iy,1)-zm(ix,iy,3))**2+(rm(ix,iy,1)-rm(ix,iy,3))**2)**.5
   b4 = ((zm(ix,iy,4)-zm(ix,iy,3))**2+(rm(ix,iy,4)-rm(ix,iy,3))**2)**.5
   c4 = ((zm(ix,iy,4)-zm(ix,iy,1))**2+(rm(ix,iy,4)-rm(ix,iy,1))**2)**.5
   ang4 = acos((a4**2+b4**2-c4**2)/(2*a4*b4))
   ang4 =
ang4*(180/3.14159265358979323846264338327950288419716939937510582097494459230781640628620899862803482534211706
68)

#   Compute Angles

#   Write arrays to output file
ounit << "iType(" << format(icn,6) << " ) = 0  nSides(" << format(icn,6) << ") = 4"
ounit << "adjCell(1," << format(icn,6) << ") = " << format(ict,6) << " lside(1," << format(icn,6) << ") = " << format(a1,15,6,0) << \
        "  angle(1," << format(icn,6) << ") = " << format(ang1,15,6,0)
ounit << "adjCell(2," << format(icn,6) << ") = " << format(icr,6) << " lside(2," << format(icn,6) << ") = " << format(a2,15,6,0) << \
        "  angle(2," << format(icn,6) << ") = " << format(ang2,15,6,0)
ounit << "adjCell(3," << format(icn,6) << ") = " << format(icb,6) << " lside(3," << format(icn,6) << ") = " << format(a3,15,6,0) << \
        "  angle(3," << format(icn,6) << ") = " << format(ang3,15,6,0)
ounit << "adjCell(4," << format(icn,6) << ") = " << format(icl,6) << " lside(4," << format(icn,6) << ") = " << format(a4,15,6,0) << \
        "  angle(4," << format(icn,6) << ") = " << format(ang4,15,6,0)
geometry << "Cell.r1(" <<format(icn,6)<< ") ="  << format(rm(ix,iy,1),15,6,0)
geometry << "Cell.z1(" <<format(icn,6)<< ") ="  << format(zm(ix,iy,1),15,6,0)
geometry << "Cell.r2(" <<format(icn,6)<< ") ="  << format(rm(ix,iy,2),15,6,0)
geometry << "Cell.z2(" <<format(icn,6)<< ") ="  << format(zm(ix,iy,2),15,6,0)
geometry << "Cell.r3(" <<format(icn,6)<< ") ="  << format(rm(ix,iy,3),15,6,0)
```

```
geometry << "Cell.z3(" <<format(icn,6)<< ") ="  << format(zm(ix,iy,3),15,6,0)
geometry << "Cell.r4(" <<format(icn,6)<< ") ="  << format(rm(ix,iy,4),15,6,0)
geometry << "Cell.z4(" <<format(icn,6)<< ") ="  << format(zm(ix,iy,4),15,6,0)

  enddo
enddo
geometry << "NCELLS = "  << cells
   walls << "iType(" << format((cells+plasmareg+wallreg-1),6) << " ) = 2  nSides(" << format((cells+plasmareg+wallreg-1),6) << ")
= 1 " << "adjCell(1," << format((cells+plasmareg+wallreg-1),6) << ") = " << format((cells),6)
   walls << "iType(" << format((cells+plasmareg+wallreg),6) << " ) = 2  nSides(" << format((cells+plasmareg+wallreg),6) << ") = 1 "
<< "adjCell(1," << format((cells+plasmareg+wallreg),6) << ") = " << format((ixmax*iymax+1),6)
#################################################################
basclose(walls)
basclose(cores)
#################################################################
#THE PRIVATE FLUX REGION!!!
#!Assuming the Lower Null so...z is same
      pfr_z = zm(1,1,1)
      pfr_r = rm((nxxpt+nxleg(1,1)),1,2)

pfregionsides = (nxxpt+nxleg(1,2))+(nxxpt+nxleg(1,1))+1
qq = ixmax*iymax+1

do iy=iymin,iymin
      do ix=1,ixmax
            if(ix==((nxxpt+nxleg(1,1))+1)) ix = ixmax - (nxxpt+nxleg(1,2)) + 1
    icn = ix + ixmax*(iy-1)

    dcl = sqrt( (rm(ix,iy,1)-rm(ix,iy,2))**2 + (zm(ix,iy,1)-zm(ix,iy,2))**2 )
    dct = sqrt( (pfr_r-rm(ix,iy,2))**2 + (pfr_z-zm(ix,iy,2))**2 )
    dcb = sqrt( (rm(ix,iy,1)-pfr_r)**2 + (zm(ix,iy,1)-pfr_z)**2 )
```

```
    a = dct
    b = dcl
    c = dcb
    acl = acos((-1)*(a**2-(b**2+c**2))/(2*b*c))
    acl = acl * (180/3.14159265358979)
    act = acos((-1)*(b**2-(a**2+c**2))/(2*a*c))
    act = act * (180/3.14159265358979)
    acb = acos((-1)*(c**2-(b**2+a**2))/(2*b*a))
    acb = acb * (180/3.14159265358979)
    atot = acl + act + acb

    a1 = ((zm(ix,iy,1)-zm(ix,iy,2))**2+(rm(ix,iy,1)-rm(ix,iy,2))**2)**.5
    b1 = ((zm(ix,iy,2)-pfr_z)**2+(rm(ix,iy,2)-pfr_r)**2)**.5
    c1 = ((zm(ix,iy,1)-pfr_z)**2+(rm(ix,iy,1)-pfr_r)**2)**.5
    ang1 = acos((a1**2+b1**2-c1**2)/(2*a1*b1))
    ang1 =
ang1*(180/3.14159265358979323846264338327950288419716939937510582097494459230781640628620899862803482534211706
68)

    a2 = ((zm(ix,iy,2)-pfr_z)**2+(rm(ix,iy,2)-pfr_r)**2)**.5
    b2 = ((pfr_z-zm(ix,iy,1))**2+(pfr_r-rm(ix,iy,1))**2)**.5
    c2 = ((zm(ix,iy,1)-zm(ix,iy,2))**2+(rm(ix,iy,1)-rm(ix,iy,2))**2)**.5
    ang2 = acos((a2**2+b2**2-c2**2)/(2*a2*b2))
    ang2 =
ang2*(180/3.14159265358979323846264338327950288419716939937510582097494459230781640628620899862803482534211706
68)

    a3 = ((pfr_z-zm(ix,iy,1))**2+(pfr_r-rm(ix,iy,1))**2)**.5
    b3 = ((zm(ix,iy,1)-zm(ix,iy,2))**2+(rm(ix,iy,1)-rm(ix,iy,2))**2)**.5
    c3 = ((zm(ix,iy,2)-pfr_z)**2+(rm(ix,iy,2)-pfr_r)**2)**.5
    ang3 = acos((a3**2+b3**2-c3**2)/(2*a3*b3))
```

```
   ang3 =
ang3*(180/3.14159265358979323846264338327950288419716939937510582097494459230781640628620899862803482534211706
68)



   ict = qq +1
   icb = qq -1
   if(ix == ixmin) icb = cells + plasmareg + wallreg
   if(ix == ixmax) ict = cells + plasmareg + wallreg - 1

ounit << "iType(" << format(qq,6) << " ) = 0  nSides(" << format(qq,6) << ") = 3"

ounit << "adjCell(1," << format(qq,6) << ") = " << format(icn,6) << " lside(1," << format(qq,6) << ") = " << format(a1,15,6,0) << \
        "  angle(1," << format(qq,6) << ") = " << format(ang1,15,6,0)
ounit << "adjCell(2," << format(qq,6) << ") = " << format(ict,6) << " lside(2," << format(qq,6) << ") = " << format(a2,15,6,0) << \
        "  angle(2," << format(qq,6) << ") = " << format(ang2,15,6,0)
ounit << "adjCell(3," << format(qq,6) << ") = " << format(icb,6) << " lside(3," << format(qq,6) << ") = " << format(a3,15,6,0) << \
        "  angle(3," << format(qq,6) << ") = " << format(ang3,15,6,0)
geometry << "Cell.r1(" <<format(qq,6)<< ") ="  << format(rm(ix,iy,1),15,6,0)
geometry << "Cell.z1(" <<format(qq,6)<< ") ="  << format(zm(ix,iy,1),15,6,0)
geometry << "Cell.r2(" <<format(qq,6)<< ") ="  << format(rm(ix,iy,2),15,6,0)
geometry << "Cell.z2(" <<format(qq,6)<< ") ="  << format(zm(ix,iy,2),15,6,0)
geometry << "Cell.r3(" <<format(qq,6)<< ") ="  << format(pfr_r,15,6,0)
geometry << "Cell.z3(" <<format(qq,6)<< ") ="  << format(pfr_z,15,6,0)
geometry << "Cell.r4(" <<format(qq,6)<< ") ="  << format(pfr_r,15,6,0)
geometry << "Cell.z4(" <<format(qq,6)<< ") ="  << format(pfr_z,15,6,0)

qq = qq + 1
  enddo
enddo
```

```
###################################
basclose(ounit)
basclose(geometry)
###################################



################
rwall_gex << "zion =  1    aion =  2    aneut =  2    eneut = 0.002"
rwall_gex << "eneut_v = 0.003"
rwall_gex << "iquad=2"
rwall_gex << "icosn=0"
rwall_gex << "nph=21"
rwall_gex << "idbug =   0"
rwall_gex << "scalFact=1."
rwall_gex << "prntOrdr =  -1"
rwall_gex << "i_e0=3"
rwall_gex << "iatdat=1"
rwall_gex << "leh0=1"
rwall_gex << "ifrstcol = 0"
rwall_gex << "ifjsv=1"
rwall_gex << "irefl=1"
rwall_gex << "Rwall=" <<format((wallreg),3) <<"*0"
rwall_gex << "awall=" <<format((wallreg),3) <<"*12.0"
rwall_gex << "zwall=" <<format((wallreg),3) <<"*6.0"
rwall_gex << "twall=" <<format((wallreg),3) <<"*2.0e-3"
rwall_gex << "fwabsorb="<<format((wallreg),3) <<"*0"
rwall_gex << "idp=1"
rwall_gex << "isparsitr=10"
```

```
rwall_gex << "nd0=0"
rwall_gex << "neitr = 3"
rwall_gex << "nxleg1=" <<format((nxleg(1,1)),3)
rwall_gex << "nxleg2=" <<format((nxleg(1,2)),3)
rwall_gex << "nxcore1=" <<format((nxcore(1,1)),3)
rwall_gex << "nxcore2=" <<format((nxcore(1,2)),3)
rwall_gex << "nycore1=" <<format((nycore(1)),3)
rwall_gex << "nysol1=" <<format((nysol(1)),3)
rwall_gex << "nxxpt=" <<format((nxxpt),3)
rwall_gex << "nxmod=" <<format((nxmod),3)
rwall_gex << "$end"

flatflux << "elecTemp(   1)= " <<format((cells+plasmareg ),6) <<"*0.01 " <<"elecDens(   1)=" <<format((cells+plasmareg ),6)
<<"*2.0E+19"
flatflux << "ionTemp(   1) = " <<format((cells+plasmareg ),6) <<"*0.01 " <<"ionDens(   1)=" <<format((cells+plasmareg ),6)
<<"*2.0E+19"
flatflux << " g_ex(   2) =  0.63500E+19"


basclose(rwall_gex)
basclose(flatflux)

echo = oldecho
endf
```

```
# MAKE THE PLOT --

ezcshow=false      # don't advance frame after each plot command
ezclegfr=0.        # eliminate all space below plots for legends

real x2=sup(rm(,ny,4)), x1=inf(rm(,ny,4))
real r_min=.9
#0.9*x1
real r_max=x2+0.1*x1+.2
real ds=1.1*sup(zm)
real z_min=0.0
real z_max=z_min+ds+.2

call createtoneut(1+nxomit,nx,1,ny+1)
nf
```

References

1. Niemczewski, A., et al., Nucl. Fusion 37, 151-163 (1997).
2. Colchin, R.J., et al. , Nucl. Fusion 40, 175 (2000).
3. Stacey, W.M., et al., Phys. Plasmas 6, 3941 (1999).
4. Tokar, M.Z., et al., J. Nucl. Mater. 266-269, 958-963 (1999).
5. Groebner, R.J., et. al, Phys. Plasmas 9, 2134 (2002).
6. Stacey, W.M., Friis, Z.W., et al., Phys. Plasmas 12, 072518 (2005).
7. Tsuchiya, K., et al. , Plasma Phys. Control. Fusion 38, 1295 (1996).
8. Mahdavi, M.A., Phys. Plasmas 10, 3984 (2003).
9. Stacey, W.M., Groebner, R.J., Phys. Plasmas 10, 2412 (2003).
10. Stacey, W.M., Groebner, R.J., Phys. Plasmas 13, 012513 (2006).
11. Groth, M., et al. , J. Nucl. Mater. 337-339, 425 (2005).
12. Rensink, M.E., et al. , J. Nucl. Mater. 363-365, 816 (2007).
13. Leonard, A.W., et al. , J. Nucl. Mater. 363-365, 1066 (2007).
14. Lipschutlz, B.I., et al., Plasma Phys. Control. Fusion 47, 1559 (2005).
15. Whyte, D.G., et al., Plasma Phys. Control. Fusion 47, 1579 (2005).
16. Leonard, A.W., et al., J. Nucl. Mater. 390-391, 470 (2009).
17. Mandrekas, J., Computer Physics Communications 161, 36 (2004).
18. Zhang, D., et al. , Phys. Plasmas 13, 062509 (2006).
19. Stotler, D., et al. . *User's Guide for DEGAS2 CVS Revision:1.4*. 2007; Available from: http://w3.pppl.gov/degas2/Doc/degas2_all.pdf.
20. Reiter, D., Juelich KFA report (2005).
21. Callen, J.D., et al., *Analysis of Pedestal Transport*, in *Nucl. Fusion*. submitted 2009.
22. Rognlien, T. *Users Manual for the UEDGE Edge-Plasma Transport Code*. 2000; Available from: https://e-reports-ext.llnl.gov/pdf/246621.pdf.
23. Kadomtsev, B.B., Plasma Physics and Controlled Fusion 30, 2031-2049 (1988).
24. Pitts, R. *Tokamak basics*. Available from: http://physicsworld.com/cws/article/print/24295/1/PWfus3_03-06.
25. Stacey, W.M., *Fusion Plasma Physics*. 2005: WILEY-VCH. 557.
26. Garcia, R.D.M., et al., Phys. Plasmas 24, 903 (1982).
27. Tendler, M., Fusion Technol. 11, 289 (1987).
28. Heckmann, J., et al. , Phys. Plasmas 20 (1978).
29. Heifetz, D., et al. , J. Computational Physics 46 (1892).
30. Lehnert, B., Plasma Phys. Control. Fusion 26 (1984).
31. Stacey, W.M., Fusion Sci. Technol. 156, 99 (2006).
32. Helander, P., Phys. Plasmas 10, 4396-4404 (2003).
33. Rapp, J.e.a., J. Nucl. Mater., 1158-1154 (2001).
34. Guirlet, R., et al. *MARFE and Density Limit Detachment with the Tore Supra Actively Cooled Limiter*. in *29th EPS Conference on Plasma Phys. and Contr. Fusion Montreux*. 2002.
35. Fulop, T., et al., Phys. Plasmas 8, 5214 (2001).
36. Stacey, W.M., Phys. Plasmas 9, 3082 (2002).
37. Carreras, B.A., et al. , Phys. Plasmas 5, 2623 (1998).

38. Fukuda, T., Plasma Phys. Control. Fusion 40, 543-555 (1998).
39. Suttrop, W., et al., *Testing H-mode parameter similarity in JET and ASDEX Upgrade*, in *29th EPS Conference on Plasma Phys. and Contr. Fusion*. 2002: Montreux.
40. Helander, P., et al., Phys. Plasmas 4, 4218 (1997).
41. Stangeby, P., et al., Nucl. Fusion 30, 1225 (1991).
42. Friis, Z.W., *AN INVESTIGATION OF MARFE INDUCED H-L BACK TRANSITIONS*, in *Nuclear and Radiological Engineering*. 2005, Georgia Institute of Techology: Atlanta. p. 57.
43. Baker, D.R., et al. , Nucl. Fusion 22, 807 (1982).
44. Alladio, F., et al. , Phys. Lett. 90A, 405 (1982).
45. Kaye, S.M., et al. . in *Proc. 11th Euro. Conf. Control. Fusion Plasma Phys*. 1983. Aachen.
46. Niedermeyer, H., et al. in *Proc. 11th Euro. Conf. Control. Fusion Plasma Phys.* 1983. Aachen.
47. Petrie, T.W., et al., J. Nucl. Mater. 266-269, 642-647 (1999).
48. Liang, Y., et al., PRL 94, 105003 (2005).
49. Friis, Z.W., *Does the plasma flow effect the density limit in Tokamaks?* 2005, Institut für Plasmaphysik, Forschungszentrum Jülich,GmbH.
50. Drake, J.F., Plasma Phys. Control. Fusion 39, 1245-1258 (1997).
51. Stacey, W.M., et al., Plasma Phys. Control. Fusion 39, 1245–1258 (1997).
52. Stacey, W.M., Fusion Technol. 36, 269 (1999).
53. Stacey, W.M., Phys. Plasmas 9, 888 (2002).
54. Tokar, M.Z., et al., Phys. Plasmas 7, 2432 (2000).
55. Tokar, M.Z., et al., Phys. Plasmas 10, 4378 (2003).
56. Tokar, M.Z., et al., Phys. Plasmas 12, 052510 (2005).
57. Wesson, J., *Tokamaks*. 2004: Oxford Science Publications.
58. Greenwald, M. *DENSITY LIMITS IN TOROIDAL PLASMAS*. in *43rd Annual Meeting of the APS Division of Plasma Physics*. 2001. Long Beach, CA.
59. Rapp, J., et al., Nucl. Fusion 39, 765-776 (1999).
60. Groebner, R.J., et. al, Plasma Phys. Control. Fusion 44, A265 (2002).
61. Boivin, R.L., et al. , PSFC Preprints (1999).
62. Stacey, W.M., Phys. Plasmas 11, 4295 (2004).
63. Meghreblian, R.e.a., *Reactor Analysis*, ed. McGraw-Hill. 1969, New York.
64. Lewis, E., et al., *Computational Methods of Neutron Transport*, ed. J.W. Sons. 1984, New York.
65. Rubilar, R., PhD theses, *Neutral Particle Transport in the Plasma Edge and Divertor Region, in Nuclear Engineering*. 2000, Georgia Institute of Technology: Atlanta.
66. Bell, G., et al., *Nuclear Reactor Theory*, ed. V.N. Reinhold. 1970, New York.
67. Davison, B., *Neutron Transport Theory*, ed. O. University. 1957, London.
68. Duderstadt, J., et al., *Transport Theory*, ed. Wiley-Interscience. 19779, New York.
69. Greenspan, H., et al., *Computing Methods in Reactor Physics*, ed. J.W. Sons. 1968, New York.
70. Henry, A.F., *Nuclear Reactor Analysis*, ed. M. Press. 1975.

71. Williams, M., M.R., *Mathematical Methods in Particle Transport Theory*, ed. T.B. Group. 1971, London.
72. Stacey, W.M., et al., Nucl. Fusion 34, 1384 (1994).
73. Audenaerde, K., et al., J. Computational Physics 34, 268 (1980).
74. Stacey, W.M., Phys. Plasmas 4, 179 (1997).
75. Neubaur, O., et al., Fusion Sci. Technol. 47, 76-86 (2005).
76. Finken, K.H., et al., Nucl. Fusion 47, 179 (2007).
77. Antipenkov, A.B., et al., Fusion Engineering and Design 56-57, 233-238 (2001).
78. Koslowski, H.R., Meas. Sci. Technol 5, 91-102 (1994).
79. Koslowski, H.R., et al., Fusion Engineering and Design 56-57, 233-238 (1997).
80. Domier, C. *ECE Imaging Diagnostics*. 2009; Available from: http://tempest.das.ucdavis.edu/pdg/ECE/index.html.
81. De Bock, M., PhD theses, *Understanding and Controlling Plasma Rotation in Tokamaks*. 2007, Universiteit Eindhoven.
82. Isler, R.C., Plasma Phys. Control. Fusion 36, 171-208 (1994).
83. Hellermen, M., et al., Plasma Phys. Control. Fusion 37, 71-94 (1995).
84. Sergienko, G., *Personal Communication*.
85. Hutchinson, I.H., *Principles of Plasma Diagnostics*. ed. Cambridge University Press, 2002, Cambridge.
86. Liang, Y., *Personal Communication*.
87. Zhang, D., PhD theses, *NEUTRAL PARTICLE TRANSPORT IN PLASMA EDGE USING TRANSMISSION/ESCAPE PROBABILITY (TEP) METHOD*, in *Nuclear Engineering*. 2005, Georgia Institute of Technology: Atlanta. p. 168.
88. Davis, T.A., et al., *ACM Trans. Math. Software*. 1999.
89. Zhang, W., et al. , Plasma Phys. Control. Fusion 40, 335–346 (1998).
90. Braams, C.M.a.S., P.E., *Nuclear fusion: half a century of magnetic confinement fusion research*. 2002.
91. Brezinsek, S., et al., Physica Scripta T103, 51-55 (2003).
92. Janev, R.K., et al., *Elementary Processes in Hydrogen-Helium Plasmas*, ed. Springer-Verlag. 1987, Berlin.
93. Rognlien, T., *Personal Communication*.
94. Porter, G.D., et al., Phys. Plasmas 5, 4311 (1998).
95. Mandrekas, J., et al., Nucl. Fusion 43, 314 (2003).
96. Rubilar, R., et al., Nucl. Fusion 41, 1003-1019 (2001).
97. Stacey, W.M., et al., Fusion Sci. Technol. 40, 66 (2001).

Vita

Zachary Ward Friis was born in the plains of Wyoming on June 28th, 1979 to Hans Craig Friis and Judy Friis. He grew up in Valdosta, Georgia with his parents and younger sister Amber. Zach attended Lowndes High School and graduated in 1997. He stayed in Valdosta attending both Valdosta Technical College and Valdosta State University. He received a degree in Advanced Electronics Technology from Valdosta Tech and a Bachelor's of Science in Physics from Valdosta State. After graduating with high honors from Valdosta State, Zach matriculated into the graduate Nuclear and Radiological Engineering Program at the Georgia Institute of Technology. Zach received his Master's degree in Nuclear Engineering in 2005. He then received a fellowship from Argonne National Laboratory to be a visiting scientist at Forschungszentrum in Jülich, Germany. Upon completion of his studies abroad, Zach returned to Georgia Tech to pursue his Doctoral studies in Nuclear Engineering.